

Universiteit
Leiden
The Netherlands

# Cancer chess: molecular insights into PARP inhibitor resistance

Barazas, M.

**Citation**
Barazas, M. (2021, December 14). *Cancer chess: molecular insights into PARP inhibitor resistance*. Retrieved from https://hdl.handle.net/1887/3247064

| | |
|---|---|
| Version: | Publisher's Version |
| License: | Licence agreement concerning inclusion of doctoral thesis in the Institutional Repository of the University of Leiden |
| Downloaded from: | https://hdl.handle.net/1887/3247064 |

**Note:** To cite this publication please use the final published version (if applicable).

# Cancer Chess: Molecular Insights into PARP Inhibitor Resistance



*Marco Barazas*

# Cancer Chess: Molecular Insights into PARP Inhibitor Resistance

*Marco Barazas*

Cover illustration: “Family”, by Marga Barazas-Langeveld
Thesis lay-out: Marco Barazas & Margo Verduin
Printing: Gildeprint

The research described in this thesis was performed at the Division of Molecular Pathology of the Netherlands Cancer Institute – Antoni van Leeuwenhoek Hospital (NKI-AVL) and Oncode Institute, Amsterdam, The Netherlands, and was financially supported by the Dutch Cancer Society (KWF 2011-5220 and 2014-6532 to S. Rottenberg and J. Jonkers), the Netherlands Organization for Scientific Research (VICI 91814643, NGI 93512009, Cancer Genomics Netherlands, and a National Roadmap Grant for Large-Scale Research Facilities to J. Jonkers), the Swiss National Science Foundation (310030_179360 to S. Rottenberg), the Swiss Cancer League (KLS-4282-08-2017 to S. Rottenberg); and the European Union (ERC CoG-681572 to S. Rottenberg and ERC Synergy Grant 319661 to J. Jonkers).

The printing of the thesis was financially supported by the NKI-AVL and the University of Leiden.

© Copyright, Marco Barazas, 2021
ISBN: 978-94-6419-366-4
All rights reserved. No part of this book may be reproduced in any form or by any means without permission of the author.

# Cancer Chess: Molecular Insights into PARP Inhibitor Resistance

**Proefschrift**

ter verkrijging van de graad van doctor aan de Universiteit Leiden,
op gezag van rector magnificus prof.dr.ir. H. Bijl,
volgens besluit van het college voor promoties
te verdedigen op dinsdag 14 december 2021
klokke 11.15 uur

door
Marco Barazas

geboren te Hoorn, Nederland
in 1988

**Promotoren:**
Prof.dr. Jos Jonkers, promotor
Prof.dr. Sven Rottenberg, University of Bern, co-promotor

**Promotiecommissie:**
Prof.dr. H. Irth, chairman
Prof.dr. J.A. Bouwstra, secretary
Prof.dr. Haico van Attikum
Dr. Sylvie Noordermeer
Prof.dr. Marcel van Vugt, University of Groningen

## Table of Contents


| | | |
|---|---|---|
| | Preface | 6 |
| **Chapter 1** | General Introduction | 7 |
| **Chapter 2** | Genetic Dissection of Cancer Development, Therapy Response, and Resistance in Mouse Models of Breast Cancer<br>*Adapted from: Cold Spring Harb Symp Quant Biol. 81:141-150 (2016)* | 32 |
| **Chapter 3** | Brca-Deficient Mouse Mammary Tumor Organoids to Study Cancer Drug Resistance<br>*Adapted from: Nature Methods. 15(2):134-140 (2018)* | 50 |
| **Chapter 4** | The ASCIZ-DYNLL1 Axis Promotes 53BP1 Dependent Non-Homologous End Joining and PARP Inhibitor Sensitivity<br>*Adapted from: Nature Communications. 9(1):5406 (2018)* | 82 |
| **Chapter 5** | The Shieldin Complex Mediates 53BP1-Dependent DNA Repair<br>*Adapted from: Nature. 560(7716):117-121 (2018)* | 114 |
| **Chapter 6** | The CST Complex Mediates End Protection at Double-Strand Breaks and Promotes PARP Inhibitor Sensitivity in BRCA1-Deficient Cells<br>*Adapted from: Cell Reports.23(7):2107-2118 (2018)* | 160 |
| **Chapter 7** | Radiosensitivity Is an Acquired Vulnerability of PARPi-Resistant BRCA1-Deficient Tumors<br>*Adapted from: Cancer Research. 79(3):452-460 (2019)* | 196 |
| **Chapter 8** | General Discussion and Future Perspectives | 220 |
| **Addendum** | Summary | 244 |
| | Nederlandse Samenvatting | 247 |
| | List of Publications | 250 |
| | Curriculum Vitae | 252 |
| | Acknowledgements | 253 |

## Preface

Do you believe in coincidence? My instinct says 'no', and my scientific background strengthens me not to take coincidence for an answer. So why is it that in a room full of patients diagnosed with the same subtype of cancer, due to a defect in the same gene, and treated in the same way, some patients are faced with a relapsing tumor soon after treatment is initiated, while others live disease-free for many years? This intriguing question drives the motivation to the work presented in this thesis, which is focused on the subgroup of breast tumors that are hallmarked by a defect in BRCA1. Although this defect can be therapeutically targeted using PARP1 inhibitors, resistance to this treatment may develop. As a strong advocate of genetics, this work centers on identifying genetic interactions that may be able to explain why some of these tumors respond to PARP1 inhibition whereas others do not. At the same time, these studies have provided valuable insights in the regulation of DNA double-strand break repair. Insights which may interest not only the fundamental biologist, but may also serve a purpose in gene targeting and, hopefully, may be translated to improve cancer treatment. Indeed, the genetic alterations that were identified in this thesis not only render BRCA1-deficient tumor cells unresponsive to PARP1 inhibition, but also expose a new vulnerability that can be exploited.

# Cancer Chess:

## General Introduction

# Molecular Insights

# Into PARPi Resistance

## Chapter 1

## The Cancer Chess Analogy

From a more distant perspective, cancer treatment resembles a game of chess where the outcome is influenced by the choices that are made. At any given time, a number of chess pieces can be moved making it challenging to identify the right move for each situation. In response to each move, the opponent will set a tailored counter-move to prevent being driven into checkmate. While this might indeed neutralize the original strategy, it might at the same time open up a back door that can be taken advantage of. Moreover, since the number of possible moves is not endless it is theoretically possible to predict and have an adequate response for each move that can be made by the opponent. Thereby, with the right strategy one can stay in the driver's seat and force the opponent into a dead alley. In a similar fashion, tumors may be cornered by exploiting vulnerabilities that they acquire upon developing resistance to initial treatment.

This introduction elaborates on the rationale behind specific treatments for specific tumors, ultimately closing in on the function of and interaction between Breast Cancer 1 (BRCA1) and poly(ADP-ribose) polymerase (PARP)1. In addition, it describes the molecular mechanism thought to be at the basis of the successful clinical exploitation of the BRAC1-PARP1 interaction. The abundant role of DNA double-strand break (DSB) repair regulation is highlighted, as well as the unresolved questions that form the starting point for this thesis.

*Personalized medicine: a shift in focus*

The central dogma to cancer treatment is, and has been for many decades, to disentangle the heterogeneity in cancer and to find the optimal therapeutic strategy for each different type of cancer. While treatment choice has traditionally been guided by classifications based on the organ-of-origin and (histo)pathological characteristics (Fig. 1), the introduction of high-throughput sequencing (HTS) technology and collected efforts such as The Human Genome Project have made it possible to determine the genetic make-up and gene-expression profile for each tumor [1-3]. Therefore, the current interpretation of personalized medicine is aimed at improving cancer treatment by defining the genetic makeup of a tumor and tailoring the treatment to exploit tumor-specific vulnerabilities (Fig. 1). However, HTS has unequivocally shown that cancer genomes can be highly complex: tumor cells contain many genetic changes compared to normal cells, comprising single base changes, insertions, deletions, copy number changes and chromosome rearrangements [4-6]. Hence, it is evident that no tumor between two patients is completely identical, known as inter-tumor heterogeneity. This is further complicated by the realization that even within an individual tumor not all tumor cells are identical, known as intra-tumor heterogeneity [7]. Thus, while HTS theoretically allows sub-classifications to be made in unprecedented detail, it is not straightforward to use this information to guide treatment.

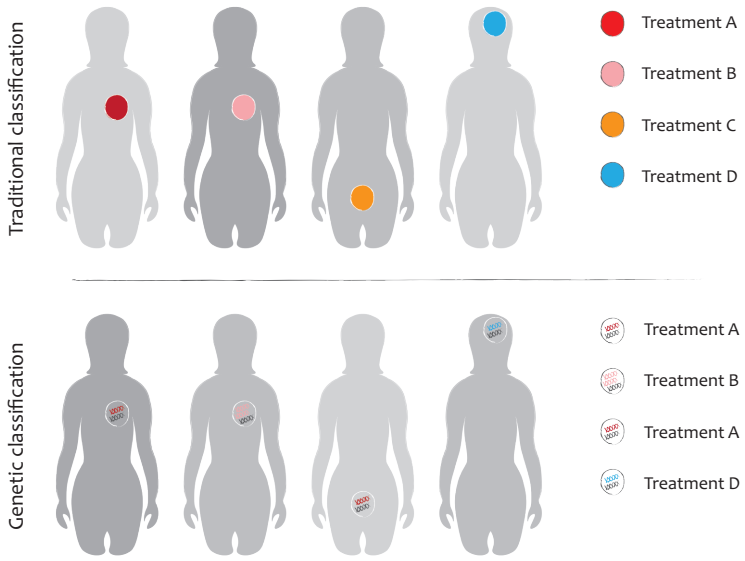



**FIGURE 1 |** Traditional classifications to guide treatment choice have been based on the organ-of-origin and (histo)pathological characteristics of the tumor. The development of NGS in principle allows this to be further refined with genetic classifications, using defined genetic alterations that may be targeted by a specific treatment irrespective of organ-of-origin.

*Lessons learned from targeting driver signaling pathways*

One approach in personalized medicine is to target the key signaling pathways that fuel tumor cell growth. For example, a subset of melanomas is driven by the BRAF V600E mutation, which leads to the constitutive activation of the MAPK signaling pathway [8]. BRAF V600E can be potently inhibited by the small molecule vemurafenib, which improved the survival of patients with this subset of melanoma while it had little effect in melanomas that are wild type for BRAF [9, 10]. This has provided a proof-of-principle for the concept of tailoring treatment to tumor-specific alterations. However, a subset of colon cancers that carried the same BRAF V600E mutation were not responsive to vemurafenib treatment [11]. This discordance was explained by the finding that colon cancers circumvent BRAF inhibition by feedback activation of EGFR. Strong synergistic effects were observed by the dual inhibition of BRAF (V600E) and EGFR. This was not required in melanoma cells since these cells naturally express low levels of EGFR. At the same time, it shows that pathway reactivation mitigates the inhibitory effect of BRAF inhibition and indeed, multiple mechanisms have been described to reactivate MAPK signaling and drive resistance to this targeted treatment [12]. Importantly, while EGFR feedback activation increased fitness in the presence of BRAF (V600E) inhibition, it was shown to be disadvantageous in the absence of the inhibitor [13]. Therefore, some relief was

found by withdrawing treatment in resistant cells, known as a "drug holiday". A drug holiday restored the resistant cancer cells to their original state, by which they regained sensitivity to V600E inhibition. While this strategy provided a temporary relief, it did not result in durable responses.

More recently, it was shown that MAPK reactivation increases the cellular levels of reactive oxygen species (ROS). This provides a back door that can be exploited by subsequent treatment with the histone deacetylase inhibitor vorinostat, which further boosts ROS levels to a lethal point selectively in drug-resistant cells [14]. The concept that drug-resistance might coincide with a fitness cost was first described in bacteria and is known as collateral sensitivity [15, 16]. Hereby, collateral sensitivity provides an opportunity to improve the outcome of targeted treatment in one-two punch treatment approaches that may drive resistant cancer cells into checkmate. At the same time, this exemplifies the importance to identify the molecular cause of resistance and the new vulnerability that it might expose.

*Exploiting synthetic lethality for cancer treatment*

While therapeutic targeting of key signaling pathways can be successful, there are also limitations to this approach. As illustrated in the previous section, reactivation of the targeted pathway is frequent and many different mechanisms have been described. Moreover, some tumor driver mutations are deemed undruggable, meaning that it is difficult to develop specific inhibitors for certain proteins. Examples include RAS mutations and MYC amplification, which are frequently found across cancer types [17,18]. In addition, cancer driver pathways are often important for the normal physiology of somatic cells, and therefore the therapeutic window may not be as large as one would hope.

Another promising approach in personalized medicine is to exploit the concept of synthetic lethality. A synthetic lethal (SL) interaction is an interaction between two genes which have no or little effect on cell viability when inactivated individually, while combined inactivation of these two genes is highly toxic to the cell (Fig. 2) [19]. This can be used for cancer treatment by identifying a tumor-specific disruption in a gene that takes part in a SL interaction, "Gene A". Disruption of another component, "Gene B", will be toxic selectively to tumor cells, since somatic cells have no defect in "Gene A". This can lead to a large therapeutic window and relatively few side effects. Hence, the challenge lies in identifying tumor-specific SL interactions that can be targeted by a drug. A famous success story is the acquired sensitivity of cells with a defect in BRCA1 or BRCA2 to chemical inhibition of PARP1/2 using PARP inhibitors (PARPi) such as olaparib [20].

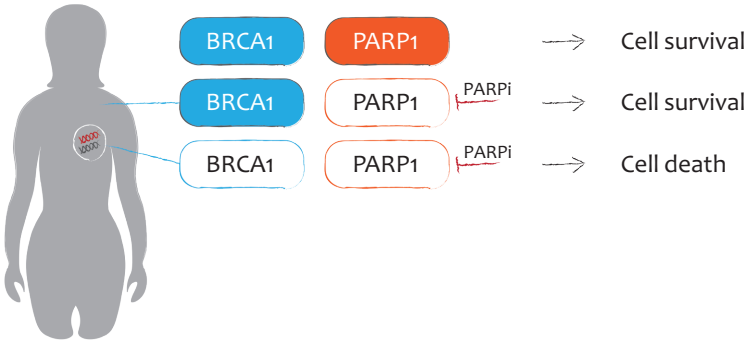



**FIGURE 2 |** Example of a synthetic lethal interaction exploited in patients. Inhibition of PARP1/2 is tolerated in somatic cells, but highly toxic to tumor cells in which BRCA1 is inactivated.

## The BRCA1/PARP Interaction

*The clinical side of BRCA1 and PARPi*

BRCA1 is a tumor suppressor protein which functions in the pathway that governs DNA double-strand break (DSB) repair via homologous recombination (HR) [21, 22]. Many pathogenic single-nucleotide polymorphisms (SNPs) in BRCA1 have been identified, and these were shown to disrupt the function of BRCA1 in HR [23]. Carriers of gene disrupting mutations in BRCA1 have an increased susceptibility for the development of cancer, primarily breast- or ovarian cancer [24, 25]. Breast tumors that arise in BRCA1 mutation carriers often show loss-of-heterozygosity (LOH) of the wild type allele resulting in a full BRCA1 defect [26, 27]. These tumors are associated with the basal-like and hormone-receptor negative breast cancer subtype [28]. On a genetic level, these tumors are characterized by a high extent of DNA copy-number alterations indicating that these tumors have unstable genomes [29]. The high level of genome instability is most likely tolerated due to the inactivation of the tumor suppressor protein p53, which is frequent in BRCA1 deficient tumors [30]. Besides familial breast- and ovarian cancer, inactivation of BRCA1, for example through promoter hyper-methylation and subsequent LOH, is also observed in sporadic breast- and ovarian cancer patients [31, 32]. Finally, defects in BRCA1 are not exclusive to breast- and ovarian cancer as HTS studies have reported on BRCA1 inactivation in prostate and pancreatic cancer [33, 34]. This potentially enlarges the population of patients that may benefit from PARPi treatment.

The use of PARPi for patients with BRCA1/2 deficient tumors is a promising strategy, because the defect is tumor-specific: somatic cells still carry at least one functional allele in both hereditary and sporadic cancer patients. Indeed, large therapeutic windows have been reported between BRCA1/2 proficient cells and BRCA1/2 deficient cells, which can be up to 1,000 fold [35, 36]. Moreover, the clinical

application of PARPi, such as olaparib, has relatively few side effects and the majority of germline BRCA1 mutant patients show clinical benefit from this treatment [37]. Since PARPi is well-tolerated, it can be administered as maintenance therapy in which patients receive daily treatment [38]. PARPi treatment reduced the risk of disease progression by 70% in patients that were newly diagnosed with advanced ovarian cancer carrying a BRCA1/2 mutation [39]. Moreover, a durable response was achieved in a fraction of patients demonstrating that PARPi treatment has curative potential. These clinical data confirm the synthetic lethality concept in cancer treatment. However, the majority of patients are eventually faced with a recurrent tumor that has become refractory to PARPi treatment (Fig. 3). Hence, resistance remains a major hurdle that must be overcome to achieve long-lasting responses in more patients, even when exploiting SL interactions. A more complete molecular understanding of PARPi's mechanism-of-action and resistance mechanisms may aid the design of rational treatment strategies to combat PARPi resistant tumors.

*Physiological functions of PARP1*

The PARP family of proteins catalyze the post-translational modification of target proteins by synthesizing branched homopolymer poly(ADP)-ribose (PAR) chains of up to 200-300 units, and are countered by the action of the PAR glycohydrolase (PARG) enzyme which degrades PAR. The best understood functions of ADP-ribosylation occur in response to stress, such as DNA damage, in which PARP1 and PARP2 play a major role (reviewed in [40]). Indeed, PARP1 and PARP2 have partially overlapping functions as their combined deletion is required to induce embryonic lethality in mice [41]. PARP1 is a highly conserved enzyme that contains N-terminal zinc finger motifs to detect damaged DNA, including single-strand DNA (ssDNA) nicks and ssDNA breaks (SSBs), bulky DNA lesions and DSBs [42, 43]. PARP1 binding to damaged DNA activates the C-terminal catalytic domain, which uses NAD+ as a substrate to impose negatively

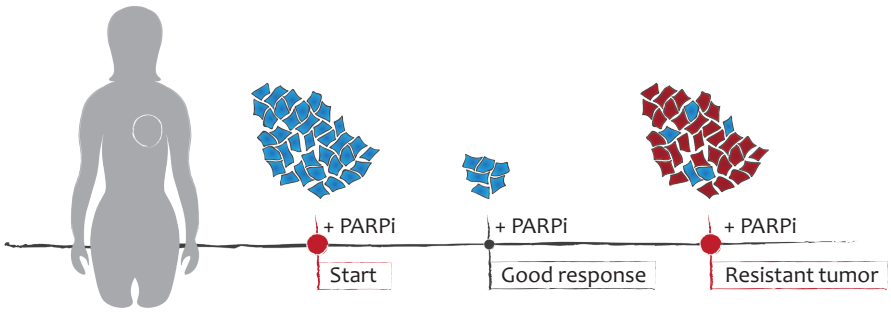



**FIGURE 3 |** Although the majority of BRCA1 mutant patients show clinical benefit from PARPi, eventually intrinsic or acquired resistance leads to tumor recurrence.

charged PAR chains (PARylation) onto target proteins. These target proteins include chromatin proteins to promote the recruitment of DNA repair effector proteins such as XRCC1 [44-46]. In addition, PARP1 also PARylates itself to mediate its release from the DNA after repair has been completed [47]. The PARylation of histone tails relaxes the chromatin environment by facilitating nucleosome eviction, which enhances the accessibility of damaged DNA [48, 49]. However, a major purpose of PARP1 (auto)-PARylation is to promote the recruitment of DNA damage response (DDR) proteins – which bind PAR non-covalently using PAR-binding motifs – in the presence of damaged DNA or when cells encounter replication stress.

The recognition of SSBs by PARP1 and subsequent PARP1/2 dependent recruitment of XRCC1 is well-described [40, 44, 45]. XRCC1 acts as a molecular scaffold for DNA polymerase β, bifunctional polynucleotide kinase 3′-phosphatase (PNKP) and DNA ligase 3 (LIG3) to efficiently repair SSBs. Additionally, PARP1 functions in the removal of covalent topoisomerase 1 (TOP1)-DNA cleavage complexes (TOP1cc) by tyrosyl-DNA phosphodiesterase 1 (TDP1) [50, 51]. TOP1cc is an intermediate that is formed to relax supercoiling ahead of the replication fork by making a ssDNA incision, but can also arise from endogenous or exogenous DNA lesions (reviewed in [52]). However, inadequate removal of TOP1cc induces DSB formation either directly by a subsequent cleavage event on the opposite strand, or indirectly when an incoming replication fork collides with TOP1cc. TDP1 hydrolyses the phosphodiester bond between the TOP1 tyrosyl moiety and the DNA 3'-end, but requires stabilization via PARP1 mediated PARylation for its activity. This subsequently exposes a nick that is a substrate for SSB repair. Indeed, recruitment of XRCC1 to TOP1cc is promoted by PARP1-TDP1 [50].

PARP1 has also been implicated in the response to replicative stress by stabilizing replication forks via a process termed replication fork reversal [53, 54]. Conceptually, this allows the sensing and repair of replication obstacles prior to their collision with incoming forks. Thereby, DSB formation as a consequence of replication fork collapse or run-off could be prevented. Mechanistically, fork reversal comprises the conversion of replication forks into so-called chicken-foot structures effectuated by annealing of the two nascent strands. While it remains unclear if and how this structure is formed under physiological conditions, a role for RECQ1 has been described in reversing four-way chicken-foot structures back into three-way structures using its helicase activity to mediate fork restart. The helicase activity of RECQ1 is inhibited by its interaction with PARylated PARP1 [55], whereby untimely restart is prevented until the lesion is removed. However, fork reversal inherently creates a one-sided DSB at the replication fork and thus requires protection from canonical DSB processing.

While it is well established that PARP1/2 orchestrates the maintenance of genome stability, its role herein is multifaceted and still not fully understood. The interest in PARP1/2, however, gained a significant boost when it was identified as a potent target for the treatment of tumors that are defective for HR due to a genetic defect in BRCA1 or BRCA2 [35, 36].

*Mechanism of action of PARPi*

The mechanism underlying the SL interaction between PARP1 and BRCA1/2 was initially explained by the effect of PARPi on inhibiting SSB repair [35, 36]. The inhibition of PARP1 mediated XRCC1 recruitment and its retention on SSBs impairs the repair of SSB intermediates formed during base excision repair (BER). These persistent SSBs subsequently drive the formation of DSBs during DNA replication, which require HR for accurate repair. In the absence of HR, these DSBs may be processed by error-prone mechanisms such as non-homologous end-joining (NHEJ). Since PARPi induced DSBs are one-sided, these repair activities drive the formation of non-viable chromatid rearrangements such as triradial and quadriradial chromosomes, ultimately resulting in cell death during mitosis [36, 56]. However, this model does not capture all available data, as it was found that depletion of XRCC1, a core factor in BER, did not induce equal synthetic lethality [57], suggesting that PARPi has additional effects that contribute to its toxicity in HR deficient cells. One of these was found to be the "trapping" of PARP1 on the DNA [58], a concept that is supported by several observations.

First, a number of PARP inhibitors have been developed, all of which inhibit the catalytic activity of PARP1 and PARP2 but with a different ability to trap PARP1 on the DNA. This trapping ability is correlated with its cytotoxicity: the most potent "trapper" has the strongest cytotoxic effect [59]. More direct evidence for the trapping concept comes from the finding that PARP1 retention at damage sites is extended by PARPi treatment [60]. Furthermore, PARP1 wildtype cells are more responsive to PARPi than to RNAi mediated depletion or genetic inactivation of PARP1 [61], and BRCA1 mutated cells were shown to become resistant to PARPi treatment by depleting PARP1 [62]. These studies show that the absence of PARP1 is less cytotoxic than the sole inhibition of its catalytic activity. Finally, PARPi cytotoxicity can be relieved by depleting PAR glycohydrolase (PARG) [63], the enzyme responsible for degrading PAR chains. Hereby, the residual catalytic activity of PARP1 - despite the presence of PARPi - is sufficient for the recruitment of downstream DDR factors and for its release from the DNA. These findings can be unified in a model in which PARP inhibition not only impairs SSB repair, but also invokes PARP1-DNA complexes [58]. Importantly, this implies that PARPi acts synergistically with processes that increase the load of DNA lesions on which PARP enzymes can become trapped. Indeed, additional DNA structures – besides the SSB intermediate formed during BER – that engage PARP1 have recently been identified [64, 65]. However, how these trapped complexes subsequently drive toxicity in HR deficient cells remains ambiguous. The accepted model is that ssDNA breaks are converted to one-sided DSBs during replication. Additionally, trapped PARP1-DNA complexes might induce replication fork stalling, ultimately leading to replication fork collapse and the formation of one-sided DSBs (Fig. 4) [20]. These replication-associated DSBs can be accurately repaired via HR in wild type cells, explaining why PARPi treatment is well-tolerated in patients. However, these DSBs become highly toxic to cells that have

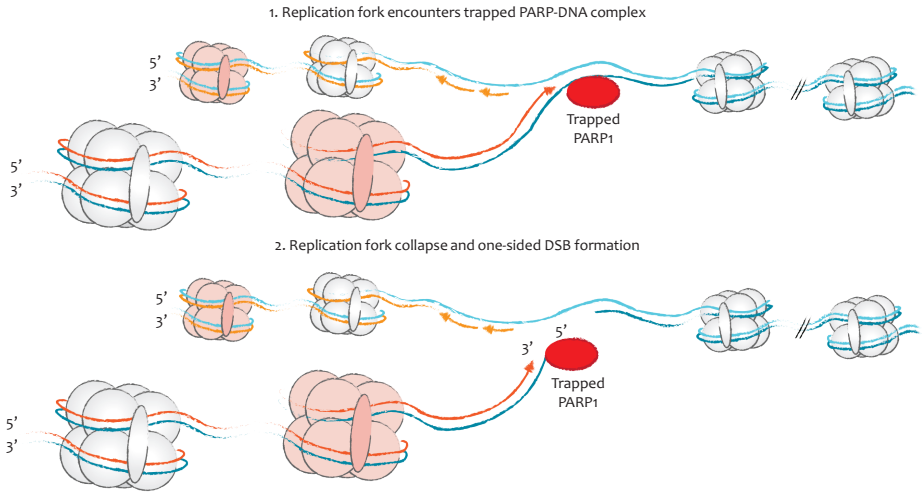



**FIGURE 4 |** The accepted model through which PARPi exerts its cytotoxic effects. During replication, unrepaired ssDNA breaks may be converted to one-sided DSBs, or trapped PARP1-DNA complexes might lead to replication fork stalling and subsequent replication fork collapse.

a defect in the HR pathway, such as cells that have lost BRCA1 or BRCA2 expression [35, 36]. It is this interaction between the formation of replication-associated DSBs by PARP inhibitors and the lack of an adequate DSB repair mechanism that is believed to be the mechanistic basis for the observed synthetic lethality in BRCA deficient cells. While it is still debated how trapped PARP1-DNA complexes induce toxicity (further discussed in Chapter 8), the notion that the HR pathway is paramount for its removal is supported by the findings that defects in other HR genes, such as PALB2, BRCA2, RAD51C or RAD51D also lead to PARPi sensitivity [58, 66, 67]. Tumors that are defective in one of these genes can acquire PARPi resistance by restoring protein function, for instance via reversion mutations [68-73]. Moreover, *in vitro* and *in vivo* model systems indicate that mechanisms that restore HR activity independent of BRCA1 restoration are prominent drivers of PARPi resistance in BRCA1 deficient cells. In the years hereafter, restoration of HR activity and resistance to PARPi in BRCA1 deficient cells have been powerful readouts to significantly advance the understanding of DSB repair regulation.

## Bringing Double-Strand Breaks to a Close

*Two pathways for DSB repair*

A single persistent DSB is thought to be sufficient to drive a cell to lethality. DSB repair mechanisms have evolved to resolve DSBs that occur in a variety of cellular contexts to preserve genome integrity. The two most studied and fundamentally different

pathways are non-homologous end joining (NHEJ) and HR, which are highlighted below. Additionally, several backup mechanisms have been described, presumably to complete repair if NHEJ or HR fail. These mechanisms include theta-mediated end-joining (TMEJ) [74-76] and single-strand annealing (SSA) [77].

Simplistically, NHEJ is the sequence-independent fusion of two DSB ends. In reality, this apparently simple mechanism requires the action of a complex signaling cascade to recognize DSBs, make the chromatin accessible, and modify the DSB ends prior to their ligation (reviewed in [78]). Depending on the complexity of the DSB end, these steps may comprise the limited resection of DNA ends, fill-in of DNA gaps, or the removal of blocking end groups. Thus, NHEJ can resolve a large variety of DSB substrates. This capacity is further enhanced by LIG4, which retains DNA ligase activity on incompatible ends [79]. As a consequence, NHEJ is active throughout the cell cycle [80], but comes with an increased risk of introducing genome alterations in the form of small deletions, insertions or even translocations. The latter may be formed when two distant DSB ends are ligated together.

In contrast to NHEJ, HR uses a homologous DNA sequence as a template for DSB repair, making this the most accurate DSB repair mechanism (reviewed in [81]). The repair template is preferentially provided by the sister chromatid on replicated regions. Hence, HR is primarily active during S and G2 phases of the cell cycle [80]. A critical step in HR is the initiation of extensive 5' to 3' end resection on the DSB end to generate a 3' single-stranded DNA (ssDNA) overhang. Resection occurs in a two-step model, in which the endonuclease and 3' to 5' exonuclease activity of the Mre11, Rad50, Nbs1 (MRN) complex generates short stretches of ssDNA and removes DNA-bound proteins from the DSB termini, most notably Ku (reviewed in [82]). The second step involves more extensive end resection, which requires the action of 5' to 3' exonucleases, such as EXO1 or DNA2 [83], and is promoted by CtIP [84]. Following resection, the ssDNA overhang is protected from the formation of secondary structures by the binding of replication protein A (RPA). The subsequent replacement of RPA with RAD51 requires the action of mediators, such as BRCA2 [85]. The resulting RAD51-ssDNA nucleofilament searches for and pairs with homologous sequences [86-88]. Upon pairing, the homologous sequence serves as a template for DNA synthesis, by which the invading strand is extended across the original break site. This process of strand invasion produces a displacement D-loop, which is resolved in the final step of HR.

While repair of DSBs via the HR pathway is generally preferred due to its higher fidelity, a regulatory mechanism is required to restrict its activity to DSBs that arise during or post-replication, while at the same time allowing NHEJ activity on the remaining DSBs. The differential requisite to inhibit or initiate end resection commits DSB repair to the NHEJ or HR pathway, respectively, and it is this step that is tightly controlled by several mechanisms – often referred to as 'pathway choice'. Critical in this process are the opposing roles of 53BP1 and BRCA1, which favor repair via NHEJ or HR, respectively (discussed below).

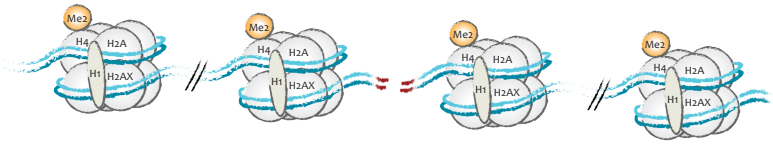
*Regulating the End Problem: 53BP1*

Upon recognition of a DSB, a signaling cascade is initiated which changes the chromatin environment around the break site (reviewed in [89-91]) (Fig. 5). One of these changes is the phosphorylation of histone H2AX (γ-H2AX) by ATM, which serves as a molecular signal to ensure local recruitment of DNA response factors, including MDC1. Subsequently, MDC1 recruits the E3 ubiquitin ligases RNF8 and RNF168, which together with the E2 ubiquitin-conjugating enzyme 13 (UBC13) catalyze the formation of Lys63-linked ubiquitin chains on H2AK13 and H2AK15 [92]. This local ubiquitylation is required for the retention of 53BP1 and BRCA1 [93]. The accumulation of 53BP1 is further dependent on mono- and di-methylated H4K20 [94]. Di-methylated H4K20 (H4K20me2) is a widespread mark that "primes" the chromatin for 53BP1 binding. The specificity towards DSBs is thought to arise by masking H4K20me2 from 53BP1 binding in undamaged DNA; the exposure of which is coordinated by RNF8 and RNF168 [95]. While the methylation state is rather stable, the dynamic acetylation of H4K16 negatively influences the binding of 53BP1 to H4K20me2 as another regulatory mechanism to fine-tune DSB repair pathway choice [96, 97]. Ultimately, these marks are integrated to locally accumulate 53BP1 near the break site where the 53BP1 pathway protects DSB ends from resection and facilitates repair via NHEJ.

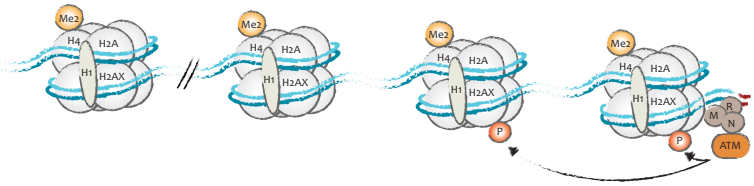
The role of 53BP1 in end protection and facilitating the NHEJ pathway has been demonstrated in a number of cellular contexts. One compelling example occurs in activated mature B-cells, which are restricted to the production of antibodies (immunoglobulins) of the IgM or IgD isotype. The controlled induction of a DSB at conserved motifs – switch regions - in the heavy chain locus (IgH) is followed by a recombination event in the heavy chain exon clusters, Cμ, Cγ, Cα and Cε. This process of class switch recombination (CSR) is required for the production of antibodies of a different isotype, such as IgG, IgA or IgE [98]. CSR is stimulated by the activity of activation-induced (cytidine) deaminase (AID), which produces deoxyuracils by deaminating deoxycytosines [98-100]. Due to the high density and staggered position of deoxyuracils in switch regions, the repair process leads to the formation of DSBs and subsequent repair by NHEJ activity. DSB induction in switch regions is not affected by the absence of 53BP1; rather, 53BP1 plays a major role to ensure correct ligation. Indeed, the knockout of 53BP1 impairs isotype switching and results in a severe CSR defect [101, 102]. The role of 53BP1 is less pronounced in V(D)J recombination, which occurs during the maturation of B-cells. V(D)J recombination is the driving force to generate diversity in the antigen binding domain of immunoglobulins and T cell receptors. The assembly of exons from the variable (V), diversity (D) and joining (J) gene segments follows an ordered pattern of DSB induction by the RAG1/2

**FIGURE 5 |** A (simplified) schematic overview of the signaling cascade leading to DSB repair via the 53BP1 pathway. Key activities are exerted by MRN, ATM, RNF8, RNF168, 53BP1, RIF1 and REV7, which are highlighted. The connections that are still unresolved are depicted by a dashed line.

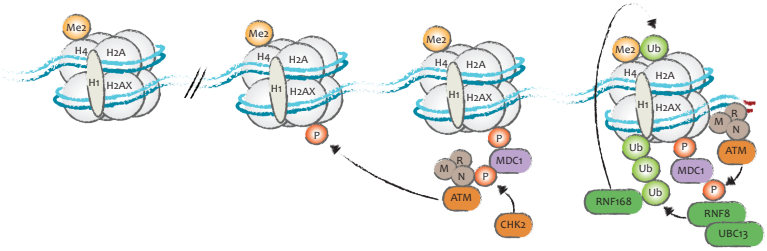
1. DSB formation



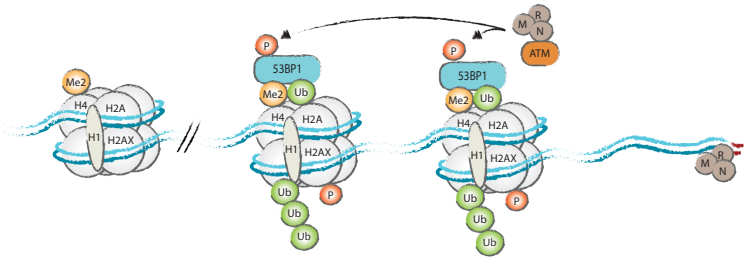

2. Break recognition and ATM mediated phosphorylation of H2AX



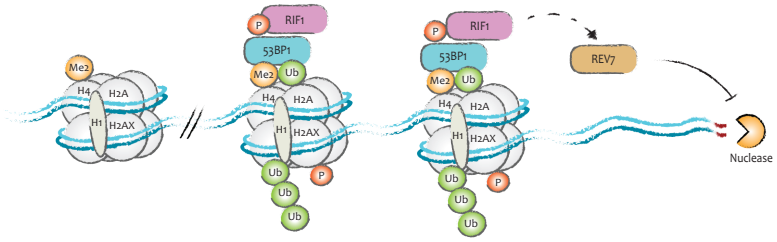

3. Recruitment of MDC1 and RNF8/168 ultimately lead to exposure of H4K20Me2



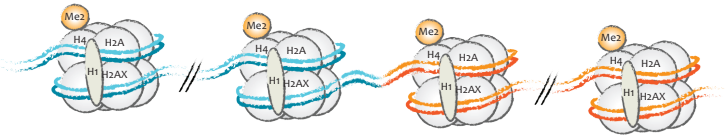

4. Recruitment of 53BP1, which also gets phosphorylated by ATM




5. Nuclease activity inhibition by 53BP1 through RIF1 and REV7, favoring NHEJ




6. Potential for toxic repair by joining distant DSBs



nuclease and is followed by repair via NHEJ (reviewed in [103]). Interestingly, while inactivation of core NHEJ factors such as LIG4 severely impairs V(D)J recombination [104, 105], 53BP1 knockout exclusively impairs distal V(D)J joining [106]. The function of 53BP1 is also demonstrated in the context of dysfunctional telomeres. The telomeric ends of chromosomes resemble DSBs and are sheltered from invoking a DDR by a process known as telomere capping (reviewed in [107]). Mechanistically, the repetitive nature of telomeric sequences (TTAGGG in vertebrates) allows the formation of a T-loop, a loop structure by which a telomeric 3' overhang folds back into the DNA [108, 109]. The protein complex that mediates the formation of T-loops is the Shelterin complex, in which TRF2 is an essential component. The absence of TRF2 leads to telomere uncapping and triggers DSB repair signaling [110]. Since these misrecognized DSBs are one-sided, the activity of NHEJ induces chromosomal fusions. Indeed, this phenotype is driven by NHEJ as it was shown to be rescued by the depletion of core NHEJ components such as LIG4, as well as by the depletion of 53BP1 [111, 112]. A role for 53BP1 in the repair of DSBs arising from exogenous sources has also been demonstrated. Knockout of 53BP1 in DT40 cells induced an intermediate sensitivity to ionizing radiation (IR) compared to knockout of LIG4 or KU70 [113, 114]. Moreover, the double knockout did not further enhance IR sensitivity, suggesting that 53BP1 acts on a subset of the DSB substrates that are repaired by NHEJ. Together, these studies are consistent with a role of 53BP1 in promoting DSB repair by NHEJ, rather than being an essential component of the NHEJ pathway itself or playing a role in an alternative repair pathway.

Soon after the identification of 53BP1 it was shown that RIF1 and PTIP are two downstream proteins in the 53BP1 pathway [114-119] (Fig. 5). The interaction with 53BP1 depends on specific phosphoresidues on the N-terminus of 53BP1, which are phosphorylated by ATM. Both RIF1 and PTIP phenocopy 53BP1 as the loss of either protein was shown to facilitate repair via NHEJ of dysfunctional telomeres and cause radiosensitivity. However, while RIF1 plays an essential role in CSR, the role of PTIP is dispensable in this context suggesting the existence of additional layers of regulation depending on the DSB substrate. The 53BP1 pathway was further extended by the identification of REV7/MAD2L2, which function downstream of RIF1 [120, 121]. Importantly, all of these factors are present in the nucleus throughout the cell cycle. Thus, a mechanism needs to be in place to inhibit the 53BP1 pathway in S-phase to allow repair via the HR pathway.

*Regulating the end problem: BRCA1*

The notion that BRCA1 functions in HR originates from the finding that BRCA1 colocalizes with RAD51 [22]. The BRCA1 gene contains an N-terminal RING domain, two nuclear localization signals (NLS), a coiled-coil (CC) motif and a C-terminal BRCT domain. The RING domain interacts with a similar domain in BARD1, and this interaction is required for the ubiquitin E3 ligase activity of BRCA1 [122-124]. BRCA1

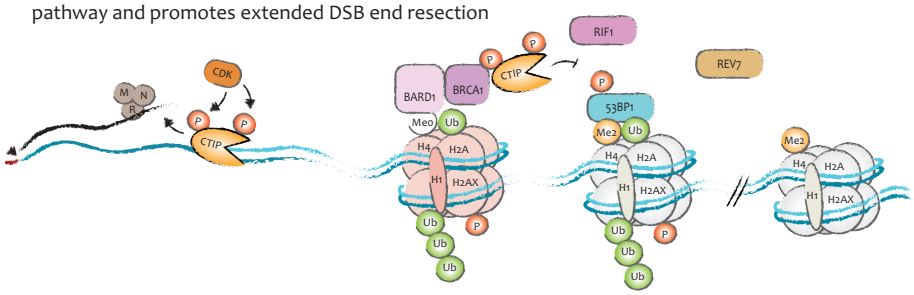
directly partners with PALB2 through its CC motif to facilitate the accumulation of BRCA2, thereby linking BRCA1 to downstream proteins in the HR pathway [125, 126]. The BRCT domain allows phosphorylation-dependent binding to a number of proteins, including Abraxas, BACH1/BRIP1 and CtIP (forming the BRCA1-A, BRCA1-B and BRCA1-C complexes, respectively) [127-131]. Thereby, BRCA1 can take part in a number of protein complexes, each with different functions in DNA repair. The BRCA1-C complex, together with MRE11-RAD50-NBS (MRN), facilitates 5' end resection to promote homologous recombination [84, 129, 132, 133].

Importantly, the RING, CC and BRCT domains are all important for the physiological function of BRCA1 and mutations in these regions are often deleterious. Indeed, cancer-predisposing pathogenic mutations tend to cluster in these domains and impair the function of BRCA1 in HR [23]. BRCA1 deficient cells show a defect in the localization of PALB2, BRCA2 and RAD51 into nuclear foci at DSBs, which is most likely caused by the impaired 5' end resection of DSBs in the absence of BRCA1, as evidenced by decreased loading of pRPA [133].

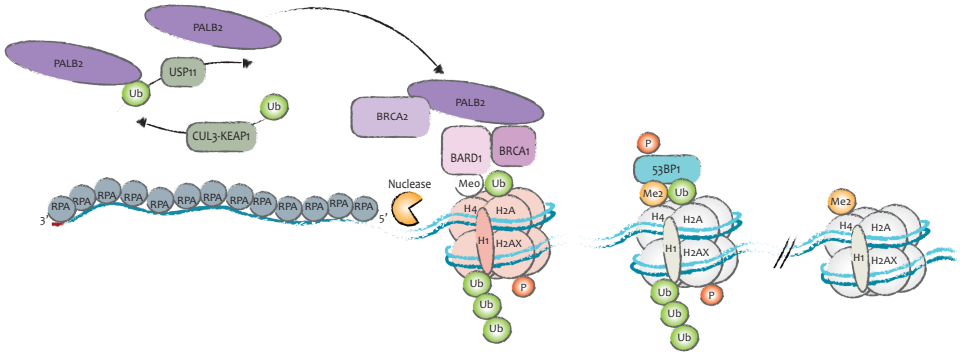
*Releasing the break on DSB resection*

The outcome of DSB repair pathway choice is influenced by the cell cycle phase (Fig. 6). Paradoxically, 53BP1 is recruited to DSBs irrespective of the cell cycle phase, demonstrating that DSBs are initially primed for repair via NHEJ. Rather, 53BP1 is actively occluded from the core of the break site and gets redistributed to the periphery during S phase [134]. The repositioning of 53BP1 coincides with the recruitment of BRCA1 and is diminished in the absence of BRCA1. BRCA1 has a more striking effect on RIF1 recruitment: while RIF1 recruitment is largely restricted to G1 cells, its localization in S/G2 cells can be restored by depletion of BRCA1 [114]. This unequivocally shows the antagonistic relation between the 53BP1 pathway and BRCA1. Like 53BP1, recruitment of BRCA1 to DSBs depends on a chromatin environment marked by γ-H2AX and the ubiquitin cascade imposed by RNF8 and RNF168 activity. Integration with the cell cycle comes from the BRCT dependent interaction between BRCA1 and CtIP. Both this interaction and the activity of CtIP to promote end resection are mediated by CDK dependent phosphorylation of specific residues on CtIP, S327 and T847 respectively [129, 132, 135]. These phosphorylation events were shown to be required to antagonize RIF1 localization to DSBs in S/G2 [114]. Moreover, the localization of RIF1 to DSBs in G1 cells can be reduced by the expression of a phosphomimicking mutant of CtIP that is constitutively active (CtIP-T847E). Thus, CDK activity regulates a 'switch' to inhibit the 53BP1 pathway specifically in S phase. Together, these data demonstrate a regulatory circuit of 53BP1-RIF1 and BRCA1-CTIP to control DSB pathway choice. Another cell cycle regulatory step is the interaction between BRCA1 and PALB2. It was shown that this interaction is inhibited by the ubiquitylation of Lys20 on PALB2 by the CUL3-KEAP1 E3 ligase [136]. The PALB2Lys20 mark requires removal by the deubiquitylase USP11, which

1. BRCA1/BARD1 are recruited to post-replicative DSBs through recognition of the H4oK20meo chromatin mark. CDK mediated phosphorylation on BRCA1 and CTIP antagonizes the 53BP1 pathway and promotes extended DSB end resection




2. ssDNA exposed by end resection is bound by RPA.
Formation of the BRCA1-PALB2-BRCA2 complex is under cell cycle control through USP11.




3. BRCA2 replaces RPA with RAD51 and repair proceeds via HR

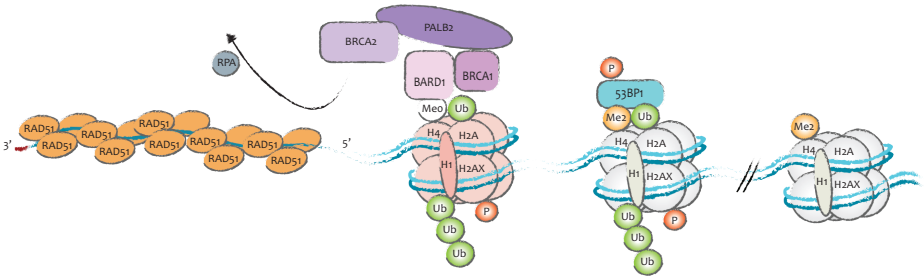



**FIGURE 6 |** A schematic overview of the first steps of the HR pathway, in which BRCA1 and BRCA2 play a pivotal role. Several cell cycle regulatory mechanisms that antagonize the 53BP1 pathway and restrict HR to post-replicative regions are depicted.

is controlled by a CRL4 complex that targets USP11 for degradation upon DNA damage in G1. Loss of 53BP1, artificial stimulation of CtIP by expression of CtIP-T847E, plus depletion of KEAP1 lead to (partial) HR activation even in G1 phase cells demonstrating that these factors normally function to restrict HR to S phase cells.

The regulation is likely more complex as in early S phase not all the DNA has been replicated and therefore not all DSBs that occur in S phase cells are suitable for repair via HR. Recent insights to this regulatory requirement suggest a role for the H4K20me2 mark, which is required for the recruitment of 53BP1. The histones that are newly incorporated during replication do not yet carry this mark, which dilutes the concentration of H4K20me2 on post-replicative regions [137, 138]. It is conceivable that the lower concentration of H4K20me2 or potentially other chromatin marks facilitates the redistribution of 53BP1 specifically on DSBs for which a sister-chromatid is available. In conjunction, the recently shown recognition of H4K20me0 by BARD1 provides an elegant mechanism by which BRCA1 may be specifically recruited to post-replicative regions [139].

## The Interplay of 53BP1 and BRCA1 on PARPi Sensitivity

The antagonistic relation between 53BP1 and BRCA1 is especially evident from the phenotypes in BRCA1 deficient cells that are rescued by the depletion of 53BP1. Loss of BRCA1 in otherwise wild type cells induces cell cycle arrest and subsequent apoptosis, presumably due to the genomic instability that arises in these cells. This cellular response can be overcome by the depletion of P53 to allow cell survival in *Brca1*$^{\Delta 11/\Delta 11}$ cells [140]. However, this did not rescue the underlying BRCA1 defect as *Brca1*$^{\Delta 11/\Delta 11}$*;p53*$^{-/-}$ mice are hallmarked by a high degree of genomic instability and are prone to tumor development and premature aging. In contrast, mice in which *Trp53bp1* was inactivated in the *Brca1*$^{\Delta 11/\Delta 11}$ background had a low incidence of tumor development and showed a near normal lifespan [141]. Two landmark studies independently demonstrated that the concurrent loss of 53BP1 in *Brca1*$^{\Delta 11/\Delta 11}$ or BRCA1 null cells coincides with a (partial) restoration of homologous recombination activity [142, 143]. While inhibition of 53BP1 had previously been shown to enhance HR [144], these studies demonstrated that BRCA1 function is not essential for HR, as HR is reactivated in the absence of 53BP1. Strikingly, the loss of 53BP1 was shown to drive PARPi resistance in BRCA1 deficient cells, presumably due to the restoration of HR activity. Indeed, HR activity and PARPi resistance could be reversed by inhibition of ATM signaling supporting the notion that the HR defect is the primary source driving PARPi sensitivity [142]. Similar phenotypes have been described upon depletion of the downstream factors PTIP, RIF1 or REV7/MAD2L2 [115-117, 119-121]. While the significance of 53BP1 pathway inactivation as a driver of PARPi resistance in BRCA1 deficient cancer patients requires further study, the occurrence of mutations in TRP53BP1 and REV7/MAD2L2 has been described [145]. These data have put the 53BP1 pathway at the center of attention due to its potential clinical implications for successful PARPi treatment.

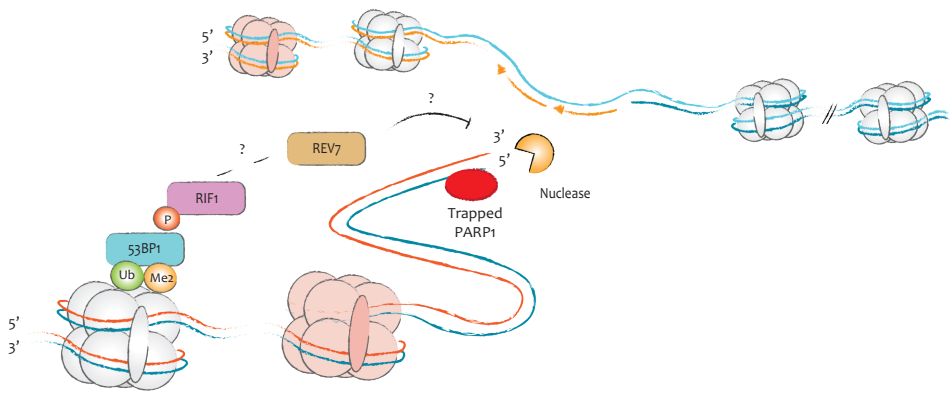



**FIGURE 7 |** The 53BP1 pathway is believed to protect PARPi induced one-sided DSBs from resection by nucleases. Steps that are incompletely understood are depicted with a '?'.

## Scope of This Thesis

The BRCA1/PARP1 paradigm exploits the HR defect of BRCA1 deficient cells and has great potential for cancer treatment. However, durable responses are infrequent as most tumors eventually become resistant to PARPi treatment. Thus, resistance is a hurdle that must be overcome in order to maximally exploit this synthetic lethal interaction in the clinic. In reference to the cancer chess analogy, we are now beginning to grasp the counter-moves that may be played by resistant tumors as the molecular mechanisms that underlie PARPi resistance are being mapped at an increasing pace. Reactivation of HR activity through restoration of functional BRCA1 expression is one class of such mechanisms; however, it is clear that resistance may also develop while BRCA1 remains inactivated. A prominent route towards BRCA1 independent PARPi resistance is the reactivation of HR activity owing to the inactivation of the 53BP1 pathway. The 53BP1 pathway normally antagonizes resection at DSB ends and it has been shown that the removal of this "brake" allows DSB ends to be resected with sufficient efficiency to restore HR. However, several aspects of this class of resistance mechanisms and its implications for cancer treatment remain unexplained, which is the focus of this thesis.

Mechanistically, there is an incomplete understanding of how the 53BP1 pathway protects DSB ends from resection, since neither 53BP1, RIF1 nor REV7/MAD2L2 has direct DNA binding capabilities (Fig. 7). Two models exist to explain this discrepancy: (i) the 53BP1 pathway changes the chromatin environment to block nuclease access, or (ii) the 53BP1 pathway recruits yet unidentified factors with DNA binding capacity. The second model implies the existence of additional proteins that may be inactivated in cancer cells to withstand treatment, thus suggesting that our view on the BRCA1/PARP1 chessboard is still incomplete. With this second model in mind, several

CRISPR/Cas9 based high-throughput loss-of-function screens were performed to identify such factors. Chapter 3 describes an advance in technology to accelerate the *in vivo* validation of putative resistance factors by combining CRISPR/Cas9 technology and 3D tumor organoid culture protocols. The identification and validation of multiple factors of the 53BP1 pathway are described in Chapters 4-6, thus providing support for the second model.

From a translational perspective, the question is whether inactivation of the 53BP1 pathway puts the patient and clinician checkmate, or if a new synthetic lethal interaction is acquired upon the loss of the 53BP1 pathway, thus allowing for one-two punch approaches. The 53BP1 pathway has a physiological function in DSB repair and it is therefore conceivable that its inactivation is disadvantageous in specific contexts. One such context was identified and exploited as described in Chapter 7 of this thesis.

Together, this thesis aims to further the molecular understanding of the 53BP1 pathway and its role in driving PARP inhibitor resistance in the absence of BRCA1; and to identify new vulnerabilities of these resistant cells that can be exploited.

## References

1. Venter JC, Adams MD, Myers EW, Li PW, Mural RJ, Sutton GG, et al. The sequence of the human genome. Science (New York, NY). 2001; 291: 1304-51.
2. Wang Z, Gerstein M, Snyder M. RNA-Seq: a revolutionary tool for transcriptomics. Nature reviews Genetics. 2009; 10: 57-63.
3. Stratton MR, Campbell PJ, Futreal PA. The cancer genome. Nature. 2009; 458: 719-24.
4. Nik-Zainal S, Davies H, Staaf J, Ramakrishna M, Glodzik D, Zou X, et al. Landscape of somatic mutations in 560 breast cancer whole-genome sequences. Nature. 2016; 534: 47-54.
5. Nik-Zainal S, Van Loo P, Wedge DC, Alexandrov LB, Greenman CD, Lau KW, et al. The life history of 21 breast cancers. Cell. 2012; 149: 994-1007.
6. Stephens PJ, Tarpey PS, Davies H, Van Loo P, Greenman C, Wedge DC, et al. The landscape of cancer genes and mutational processes in breast cancer. Nature. 2012; 486: 400-4.
7. Gerlinger M, Rowan AJ, Horswell S, Math M, Larkin J, Endesfelder D, et al. Intratumor heterogeneity and branched evolution revealed by multiregion sequencing. N Engl J Med. 2012; 366: 883-92.
8. Davies H, Bignell GR, Cox C, Stephens P, Edkins S, Clegg S, et al. Mutations of the BRAF gene in human cancer. Nature. 2002; 417: 949.
9. Chapman PB, Hauschild A, Robert C, Haanen JB, Ascierto P, Larkin J, et al. Improved survival with vemurafenib in melanoma with BRAF V600E mutation. N Engl J Med. 2011; 364: 2507-16.
10. Chapman JR, Taylor MR, Boulton SJ. Playing the end game: DNA double-strand break repair pathway choice. Mol Cell. 2012; 47: 497-510.
11. Prahallad A, Sun C, Huang S, Di Nicolantonio F, Salazar R, Zecchin D, et al. Unresponsiveness of colon cancer to BRAF(V600E) inhibition through feedback activation of EGFR. Nature. 2012; 483: 100-3.
12. Manzano JL, Layos L, Buges C, de Los Llanos Gil M, Vila L, Martinez-Balibrea E, et al. Resistant mechanisms to BRAF inhibitors in melanoma. Annals of translational medicine. 2016; 4: 237.
13. Seghers AC, Wilgenhof S, Lebbé C, Neyns B. Successful rechallenge in two patients with BRAF-V600-mutant melanoma who experienced previous progression during treatment with a selective BRAF inhibitor. 2012; 22: 466-72.
14. Wang L, Leite de Oliveira R, Huijberts S, Bosdriesz E, Pencheva N, Brunen D, et al. An Acquired Vulnerability of Drug-Resistant Melanoma with Therapeutic Potential. Cell. 2018; 173: 1413-25.e14.
15. Hutchison DJ. Cross Resistance and Collateral Sensitivity Studies in Cancer Chemotherapy. Advances in cancer research: Academic Press; 1963. p. 235-350.

16. Muller FL, Aquilanti EA, DePinho RA. Collateral Lethality: A new therapeutic strategy in oncology. Trends in cancer. 2015; 1: 161-73.
17. Cox AD, Fesik SW, Kimmelman AC, Luo J, Der CJ. Drugging the undruggable RAS: Mission Possible? Nature Reviews Drug Discovery. 2014; 13: 828.
18. Chen H, Liu H, Qing G. Targeting oncogenic Myc as a strategy for cancer treatment. Signal Transduction and Targeted Therapy. 2018; 3: 5.
19. Kaelin WG, Jr. The concept of synthetic lethality in the context of anticancer therapy. Nature reviews Cancer. 2005; 5: 689-98.
20. Lord CJ, Ashworth A. PARP inhibitors: Synthetic lethality in the clinic. Science (New York, NY). 2017; 355: 1152-8.
21. Moynahan ME, Chiu JW, Koller BH, Jasin M. Brca1 controls homology-directed DNA repair. Mol Cell. 1999; 4: 511-8.
22. Scully R, Chen J, Plug A, Xiao Y, Weaver D, Feunteun J, et al. Association of BRCA1 with Rad51 in Mitotic and Meiotic Cells. Cell. 1997; 88: 265-75.
23. Anantha RW, Simhadri S, Foo TK, Miao S, Liu J, Shen Z, et al. Functional and mutational landscapes of BRCA1 for homology-directed repair and therapy resistance. eLife. 2017; 6: e21350.
24. Ford D, Easton DF, Bishop DT, Narod SA, Goldgar DE. Risks of cancer in BRCA1-mutation carriers. The Lancet. 1994; 343: 692-5.
25. Struewing JP, Hartge P, Wacholder S, Baker SM, Berlin M, McAdams M, et al. The Risk of Cancer Associated with Specific Mutations of BRCA1 and BRCA2 among Ashkenazi Jews. 1997; 336: 1401-8.
26. Smith SA, Easton DF, Evans DG, Ponder BA. Allele losses in the region 17q12-21 in familial breast and ovarian cancer involve the wild-type chromosome. Nat Genet. 1992; 2: 128-31.
27. Cornelis RS, Neuhausen SL, Johansson O, Arason A, Kelsell D, Ponder BA, et al. High allele loss rates at 17q12-q21 in breast and ovarian tumors from BRCAl-linked families. The Breast Cancer Linkage Consortium. Genes, chromosomes & cancer. 1995; 13: 203-10.
28. Foulkes WD, Stefansson IM, Chappuis PO, Bégin LR, Goffin JR, Wong N, et al. Germline BRCA1 Mutations and a Basal Epithelial Phenotype in Breast Cancer. JNCI: Journal of the National Cancer Institute. 2003; 95: 1482-5.
29. Tirkkonen M, Johannsson O, Agnarsson BA, Olsson H, Ingvarsson S, Karhu R, et al. Distinct somatic genetic changes associated with tumor progression in carriers of BRCA1 and BRCA2 germ-line mutations. Cancer research. 1997; 57: 1222-7.
30. Greenblatt MS, Chappuis PO, Bond JP, Hamel N, Foulkes WD. TP53 Mutations in Breast Cancer Associated with BRCA1 or BRCA2 Germ-line Mutations. Distinctive Spectrum and Structural Distribution. 2001; 61: 4092-7.
31. Russell PA, Pharoah PD, De Foy K, Ramus SJ, Symmonds I, Wilson A, et al. Frequent loss of BRCA1 mRNA and protein expression in sporadic ovarian cancers. International journal of cancer. 2000; 87: 317-21.
32. Esteller M, Silva JM, Dominguez G, Bonilla F, Matias-Guiu X, Lerma E, et al. Promoter Hypermethylation and BRCA1 Inactivation in Sporadic Breast and Ovarian Tumors. JNCI: Journal of the National Cancer Institute. 2000; 92: 564-9.
33. Robinson D, Van Allen EM, Wu YM, Schultz N, Lonigro RJ, Mosquera JM, et al. Integrative Clinical Genomics of Advanced Prostate Cancer. Cell. 2015; 162: 454.
34. Waddell N, Pajic M, Patch AM, Chang DK, Kassahn KS, Bailey P, et al. Whole genomes redefine the mutational landscape of pancreatic cancer. Nature. 2015; 518: 495-501.
35. Bryant HE, Schultz N, Thomas HD, Parker KM, Flower D, Lopez E, et al. Specific killing of BRCA2-deficient tumours with inhibitors of poly(ADP-ribose) polymerase. Nature. 2005; 434: 913-7.
36. Farmer H, McCabe N, Lord CJ, Tutt ANJ, Johnson DA, Richardson TB, et al. Targeting the DNA repair defect in BRCA mutant cells as a therapeutic strategy. Nature. 2005; 434: 917.
37. Fong PC, Boss DS, Yap TA, Tutt A, Wu P, Mergui-Roelvink M, et al. Inhibition of poly(ADP-ribose) polymerase in tumors from BRCA mutation carriers. N Engl J Med. 2009; 361: 123-34.
38. Ledermann J, Harter P, Gourley C, Friedlander M, Vergote I, Rustin G, et al. Olaparib maintenance therapy in platinum-sensitive relapsed ovarian cancer. N Engl J Med. 2012; 366: 1382-92.
39. Moore K, Colombo N, Scambia G, Kim BG, Oaknin A, Friedlander M, et al. Maintenance Olaparib in Patients with Newly Diagnosed Advanced Ovarian Cancer. N Engl J Med. 2018.

40. Schreiber V, Dantzer F, Ame J-C, de Murcia G. Poly(ADP-ribose): novel functions for an old molecule. Nature Reviews Molecular Cell Biology. 2006; 7: 517.
41. Menissier de Murcia J, Ricoul M, Tartier L, Niedergang C, Huber A, Dantzer F, et al. Functional interaction between PARP-1 and PARP-2 in chromosome stability and embryonic development in mouse. The EMBO journal. 2003; 22: 2255-63.
42. Langelier MF, Planck JL, Roy S, Pascal JM. Structural basis for DNA damage-dependent poly(ADP-ribosylation by human PARP-1. Science (New York, NY). 2012; 336: 728-32.
43. Kameshita I, Matsuda Z, Taniguchi T, Shizuta Y. Poly (ADP-Ribose) synthetase. Separation and identification of three proteolytic fragments as the substrate-binding domain, the DNA-binding domain, and the automodification domain. The Journal of biological chemistry. 1984; 259: 4770-6.
44. Masson M, Niedergang C, Schreiber V, Muller S, Menissier-de Murcia J, de Murcia G. XRCC1 is specifically associated with poly(ADP-ribose) polymerase and negatively regulates its activity following DNA damage. Molecular and cellular biology. 1998; 18: 3563-71.
45. El-Khamisy SF, Masutani M, Suzuki H, Caldecott KW. A requirement for PARP-1 for the assembly or stability of XRCC1 nuclear foci at sites of oxidative DNA damage. Nucleic Acids Res. 2003; 31: 5526-33.
46. Okano S, Lan L, Caldecott KW, Mori T, Yasui A. Spatial and temporal cellular responses to single-strand breaks in human cells. Molecular and cellular biology. 2003; 23: 3974-81.
47. Satoh MS, Lindahl T. Role of poly(ADP-ribose) formation in DNA repair. Nature. 1992; 356: 356.
48. Poirier GG, de Murcia G, Jongstra-Bilen J, Niedergang C, Mandel P. Poly(ADP-ribosyl)ation of polynucleosomes causes relaxation of chromatin structure. Proceedings of the National Academy of Sciences of the United States of America. 1982; 79: 3423-7.
49. Kim MY, Mauro S, Gévry N, Lis JT, Kraus WL. NAD+-dependent modulation of chromatin structure and transcription by nucleosome binding properties of PARP-1. Cell. 2004; 119: 803-14.
50. Das BB, Huang SY, Murai J, Rehman I, Ame JC, Sengupta S, et al. PARP1-TDP1 coupling for the repair of topoisomerase I-induced DNA damage. Nucleic Acids Res. 2014; 42: 4435-49.
51. Plo I, Liao ZY, Barcelo JM, Kohlhagen G, Caldecott KW, Weinfeld M, et al. Association of XRCC1 and tyrosyl DNA phosphodiesterase (Tdp1) for the repair of topoisomerase I-mediated DNA lesions. DNA repair. 2003; 2: 1087-100.
52. Pommier Y. Drugging topoisomerases: lessons and challenges. ACS chemical biology. 2013; 8: 82-95.
53. Ray Chaudhuri A, Hashimoto Y, Herrador R, Neelsen KJ, Fachinetti D, Bermejo R, et al. Topoisomerase I poisoning results in PARP-mediated replication fork reversal. Nature Structural &Amp; Molecular Biology. 2012; 19: 417.
54. Ray Chaudhuri A, Nussenzweig A. The multifaceted roles of PARP1 in DNA repair and chromatin remodelling. Nature reviews Molecular cell biology. 2017; 18: 610-21.
55. Berti M, Ray Chaudhuri A, Thangavel S, Gomathinayagam S, Kenig S, Vujanovic M, et al. Human RECQ1 promotes restart of replication forks reversed by DNA topoisomerase I inhibition. Nat Struct Mol Biol. 2013; 20: 347-54.
56. Schoonen PM, Talens F, Stok C, Gogola E, Heijink AM, Bouwman P, et al. Progression through mitosis promotes PARP inhibitor-induced cytotoxicity in homologous recombination-deficient cancer cells. Nature communications. 2017; 8: 15981.
57. Patel AG, Sarkaria JN, Kaufmann SH. Nonhomologous end joining drives poly(ADP-ribose) polymerase (PARP) inhibitor lethality in homologous recombination-deficient cells. 2011; 108: 3406-11.
58. Murai J, Huang SY, Das BB, Renaud A, Zhang Y, Doroshow JH, et al. Trapping of PARP1 and PARP2 by Clinical PARP Inhibitors. Cancer research. 2012; 72: 5588-99.
59. Murai J, Huang SY, Renaud A, Zhang Y, Ji J, Takeda S, et al. Stereospecific PARP trapping by BMN 673 and comparison with olaparib and rucaparib. Molecular cancer therapeutics. 2014; 13: 433-43.
60. Aleksandrov R, Dotchev A, Poser I, Krastev D, Georgiev G, Panova G, et al. Protein Dynamics in Complex DNA Lesions. Molecular Cell. 69: 1046-61.e5.
61. Pettitt SJ, Rehman FL, Bajrami I, Brough R, Wallberg F, Kozarewa I, et al. A genetic screen using the PiggyBac transposon in haploid cells identifies Parp1 as a mediator of olaparib toxicity. PloS one. 2013; 8: e61520.
62. Pettitt SJ, Krastev DB, Brandsma I, Drean A, Song F, Aleksandrov R, et al. Genome-wide and high-density CRISPR-Cas9 screens identify point mutations in PARP1 causing PARP inhibitor resistance. Nature communications. 2018; 9: 1849.

63. Gogola E, Duarte AA, de Ruiter JR, Wiegant WW, Schmid JA, de Bruijn R, et al. Selective Loss of PARG Restores PARylation and Counteracts PARP Inhibitor-Mediated Synthetic Lethality. Cancer Cell. 2018; 33: 1078-93.e12.
64. Hanzlikova H, Kalasova I, Demin AA, Pennicott LE, Cihlarova Z, Caldecott KW. The Importance of Poly(ADP-Ribose) Polymerase as a Sensor of Unligated Okazaki Fragments during DNA Replication. Mol Cell. 2018; 71: 319-31.e3.
65. Zimmermann M, Murina O, Reijns MAM, Agathanggelou A, Challis R, Tarnauskaite Z, et al. CRISPR screens identify genomic ribonucleotides as a source of PARP-trapping lesions. Nature. 2018; 559: 285-9.
66. McCabe N, Turner NC, Lord CJ, Kluzek K, Bialkowska A, Swift S, et al. Deficiency in the repair of DNA damage by homologous recombination and sensitivity to poly(ADP-ribose) polymerase inhibition. Cancer research. 2006; 66: 8109-15.
67. Buisson R, Dion-Cote AM, Coulombe Y, Launay H, Cai H, Stasiak AZ, et al. Cooperation of breast cancer proteins PALB2 and piccolo BRCA2 in stimulating homologous recombination. Nat Struct Mol Biol. 2010; 17: 1247-54.
68. Kondrashova O, Nguyen M, Shield-Artin K, Tinker AV, Teng NNH, Harrell MI, et al. Secondary Somatic Mutations Restoring RAD51C and RAD51D Associated with Acquired Resistance to the PARP Inhibitor Rucaparib in High-Grade Ovarian Carcinoma. Cancer discovery. 2017; 7: 984-98.
69. Barber LJ, Sandhu S, Chen L, Campbell J, Kozarewa I, Fenwick K, et al. Secondary mutations in BRCA2 associated with clinical resistance to a PARP inhibitor. The Journal of pathology. 2013; 229: 422-9.
70. Norquist B, Wurz KA, Pennil CC, Garcia R, Gross J, Sakai W, et al. Secondary somatic mutations restoring BRCA1/2 predict chemotherapy resistance in hereditary ovarian carcinomas. Journal of clinical oncology : official journal of the American Society of Clinical Oncology. 2011; 29: 3008-15.
71. Sakai W, Swisher EM, Jacquemont C, Chandramohan KV, Couch FJ, Langdon SP, et al. Functional Restoration of BRCA2 Protein by Secondary BRCA2 Mutations in BRCA2-Mutated Ovarian Carcinoma. 2009; 69: 6381-6.
72. Swisher EM, Sakai W, Karlan BY, Wurz K, Urban N, Taniguchi T. Secondary BRCA1 mutations in BRCA1-mutated ovarian carcinomas with platinum resistance. Cancer research. 2008; 68: 2581-6.
73. Goodall J, Mateo J, Yuan W, Mossop H, Porta N, Miranda S, et al. Circulating Cell-Free DNA to Guide Prostate Cancer Treatment with PARP Inhibition. Cancer discovery. 2017; 7: 1006-17.
74. Yousefzadeh MJ, Wood RD. DNA polymerase POLQ and cellular defense against DNA damage. DNA repair. 2013; 12: 1-9.
75. Wood RD, Doublié S. DNA polymerase θ (POLQ), double-strand break repair, and cancer. DNA repair. 2016; 44: 22-32.
76. Schimmel J, van Schendel R, den Dunnen JT, Tijsterman M. Templated Insertions: A Smoking Gun for Polymerase Theta-Mediated End Joining. Trends in Genetics. 2019; 35: 632-44.
77. Her J, Bunting SF. How cells ensure correct repair of DNA double-strand breaks. The Journal of biological chemistry. 2018; 293: 10502-11.
78. Davis AJ, Chen DJ. DNA double strand break repair via non-homologous end-joining. Translational cancer research. 2013; 2: 130-43.
79. Gu J, Lu H, Tippin B, Shimazaki N, Goodman MF, Lieber MR. XRCC4:DNA ligase IV can ligate incompatible DNA ends and can ligate across gaps. The EMBO journal. 2007; 26: 1010-23.
80. Rothkamm K, Krüger I, Thompson LH, Löbrich M. Pathways of DNA double-strand break repair during the mammalian cell cycle. Molecular and cellular biology. 2003; 23: 5706-15.
81. Moynahan ME, Jasin M. Mitotic homologous recombination maintains genomic stability and suppresses tumorigenesis. Nature reviews Molecular cell biology. 2010; 11: 196-207.
82. Paull TT. 20 Years of Mre11 Biology: No End in Sight. Molecular Cell. 2018; 71: 419-27.
83. Zhu Z, Chung W-H, Shim EY, Lee SE, Ira G. Sgs1 Helicase and Two Nucleases Dna2 and Exo1 Resect DNA Double-Strand Break Ends. Cell. 2008; 134: 981-94.
84. Sartori AA, Lukas C, Coates J, Mistrik M, Fu S, Bartek J, et al. Human CtIP promotes DNA end resection. Nature. 2007; 450: 509-14.
85. Yang H, Li Q, Fan J, Holloman WK, Pavletich NP. The BRCA2 homologue Brh2 nucleates RAD51 filament formation at a dsDNA-ssDNA junction. Nature. 2005; 433: 653-7.
86. Baumann P, Benson FE, West SC. Human Rad51 protein promotes ATP-dependent homologous pairing and strand transfer reactions in vitro. Cell. 1996; 87: 757-66.

87. Chen Z, Yang H, Pavletich NP. Mechanism of homologous recombination from the RecA-ssDNA/dsDNA structures. Nature. 2008; 453: 489-4.
88. Forget AL, Kowalczykowski SC. Single-molecule imaging of DNA pairing by RecA reveals a three-dimensional homology search. Nature. 2012; 482: 423-7.
89. Lukas J, Lukas C, Bartek J. More than just a focus: The chromatin response to DNA damage and its role in genome integrity maintenance. Nature cell biology. 2011; 13: 1161.
90. Zimmermann M, de Lange T. 53BP1: pro choice in DNA repair. Trends in Cell Biology. 2014; 24: 108-17.
91. Panier S, Boulton SJ. Double-strand break repair: 53BP1 comes into focus. Nature reviews Molecular cell biology. 2014; 15: 7-18.
92. Mattiroli F, Vissers Joseph HA, van Dijk Willem J, Ikpa P, Citterio E, Vermeulen W, et al. RNF168 Ubiquitinates K13-15 on H2A/H2AX to Drive DNA Damage Signaling. Cell. 2012; 150: 1182-95.
93. Fradet-Turcotte A, Canny MD, Escribano-Diaz C, Orthwein A, Leung CC, Huang H, et al. 53BP1 is a reader of the DNA-damage-induced H2A Lys 15 ubiquitin mark. Nature. 2013; 499: 50-4.
94. Botuyan MV, Lee J, Ward IM, Kim JE, Thompson JR, Chen J, et al. Structural basis for the methylation state-specific recognition of histone H4-K20 by 53BP1 and Crb2 in DNA repair. Cell. 2006; 127: 1361-73.
95. Mallette FA, Mattiroli F, Cui G, Young LC, Hendzel MJ, Mer G, et al. RNF8- and RNF168-dependent degradation of KDM4A/JMJD2A triggers 53BP1 recruitment to DNA damage sites. The EMBO journal. 2012; 31: 1865-78.
96. Tang J, Cho NW, Cui G, Manion EM, Shanbhag NM, Botuyan MV, et al. Acetylation limits 53BP1 association with damaged chromatin to promote homologous recombination. Nat Struct Mol Biol. 2013; 20: 317-25.
97. Hsiao KY, Mizzen CA. Histone H4 deacetylation facilitates 53BP1 DNA damage signaling and double-strand break repair. Journal of molecular cell biology. 2013; 5: 157-65.
98. Xu Z, Zan H, Pone EJ, Mai T, Casali P. Immunoglobulin class-switch DNA recombination: induction, targeting and beyond. Nature Reviews Immunology. 2012; 12: 517.
99. Muramatsu M, Kinoshita K, Fagarasan S, Yamada S, Shinkai Y, Honjo T. Class switch recombination and hypermutation require activation-induced cytidine deaminase (AID), a potential RNA editing enzyme. Cell. 2000; 102: 553-63.
100. Honjo T, Kinoshita K, Muramatsu M. Molecular Mechanism of Class Switch Recombination: Linkage with Somatic Hypermutation. 2002; 20: 165-96.
101. Manis JP, Morales JC, Xia Z, Kutok JL, Alt FW, Carpenter PB. 53BP1 links DNA damage-response pathways to immunoglobulin heavy chain class-switch recombination. Nature immunology. 2004; 5: 481-7.
102. Ward IM, Reina-San-Martin B, Olaru A, Minn K, Tamada K, Lau JS, et al. 53BP1 is required for class switch recombination. The Journal of cell biology. 2004; 165: 459-64.
103. Schatz DG, Ji Y. Recombination centres and the orchestration of V(D)J recombination. Nature Reviews Immunology. 2011; 11: 251.
104. Grawunder U, Zimmer D, Fugmann S, Schwarz K, Lieber MR. DNA ligase IV is essential for V(D)J recombination and DNA double-strand break repair in human precursor lymphocytes. Mol Cell. 1998; 2: 477-84.
105. Grawunder U, Zimmer D, Kulesza P, Lieber MR. Requirement for an interaction of XRCC4 with DNA ligase IV for wild-type V(D)J recombination and DNA double-strand break repair in vivo. The Journal of biological chemistry. 1998; 273: 24708-14.
106. Difilippantonio S, Gapud E, Wong N, Huang CY, Mahowald G, Chen HT, et al. 53BP1 facilitates long-range DNA end-joining during V(D)J recombination. Nature. 2008; 456: 529-33.
107. Palm W, de Lange T. How shelterin protects mammalian telomeres. Annual review of genetics. 2008; 42: 301-34.
108. Griffith JD, Comeau L, Rosenfield S, Stansel RM, Bianchi A, Moss H, et al. Mammalian telomeres end in a large duplex loop. Cell. 1999; 97: 503-14.
109. Nikitina T, Woodcock CL. Closed chromatin loops at the ends of chromosomes. The Journal of cell biology. 2004; 166: 161-5.
110. Konishi A, de Lange T. Cell cycle control of telomere protection and NHEJ revealed by a ts mutation in the DNA-binding domain of TRF2. Genes Dev. 2008; 22: 1221-30.
111. Smogorzewska A, Karlseder J, Holtgreve-Grez H, Jauch A, de Lange T. DNA ligase IV-dependent NHEJ of deprotected mammalian telomeres in G1 and G2. Current biology : CB. 2002; 12: 1635-44.

112. Dimitrova N, Chen YC, Spector DL, de Lange T. 53BP1 promotes non-homologous end joining of telomeres by increasing chromatin mobility. Nature. 2008; 456: 524-8.
113. Nakamura K, Sakai W, Kawamoto T, Bree RT, Lowndes NF, Takeda S, et al. Genetic dissection of vertebrate 53BP1: a major role in non-homologous end joining of DNA double strand breaks. DNA repair. 2006; 5: 741-9.
114. Escribano-Diaz C, Orthwein A, Fradet-Turcotte A, Xing M, Young JT, Tkac J, et al. A cell cycle-dependent regulatory circuit composed of 53BP1-RIF1 and BRCA1-CtIP controls DNA repair pathway choice. Mol Cell. 2013; 49: 872-83.
115. Callen E, Di Virgilio M, Kruhlak MJ, Nieto-Soler M, Wong N, Chen HT, et al. 53BP1 mediates productive and mutagenic DNA repair through distinct phosphoprotein interactions. Cell. 2013; 153: 1266-80.
116. Chapman JR, Barral P, Vannier JB, Borel V, Steger M, Tomas-Loba A, et al. RIF1 is essential for 53BP1-dependent nonhomologous end joining and suppression of DNA double-strand break resection. Mol Cell. 2013; 49: 858-71.
117. Di Virgilio M, Callen E, Yamane A, Zhang W, Jankovic M, Gitlin AD, et al. Rif1 prevents resection of DNA breaks and promotes immunoglobulin class switching. Science (New York, NY). 2013; 339: 711-5.
118. Wang J, Aroumougame A, Lobrich M, Li Y, Chen D, Chen J, et al. PTIP associates with Artemis to dictate DNA repair pathway choice. Genes Dev. 2014; 28: 2693-8.
119. Zimmermann M, Lottersberger F, Buonomo SB, Sfeir A, de Lange T. 53BP1 regulates DSB repair using Rif1 to control 5' end resection. Science (New York, NY). 2013; 339: 700-4.
120. Xu G, Chapman JR, Brandsma I, Yuan J, Mistrik M, Bouwman P, et al. REV7 counteracts DNA double-strand break resection and affects PARP inhibition. Nature. 2015; 521: 541-4.
121. Boersma V, Moatti N, Segura-Bayona S, Peuscher MH, van der Torre J, Wevers BA, et al. MAD2L2 controls DNA repair at telomeres and DNA breaks by inhibiting 5' end resection. Nature. 2015; 521: 537-40.
122. Meza JE, Brzovic PS, King MC, Klevit RE. Mapping the functional domains of BRCA1. Interaction of the ring finger domains of BRCA1 and BARD1. The Journal of biological chemistry. 1999; 274: 5659-65.
123. Hashizume R, Fukuda M, Maeda I, Nishikawa H, Oyake D, Yabuki Y, et al. The RING heterodimer BRCA1-BARD1 is a ubiquitin ligase inactivated by a breast cancer-derived mutation. The Journal of biological chemistry. 2001; 276: 14537-40.
124. Morris JR, Solomon E. BRCA1 : BARD1 induces the formation of conjugated ubiquitin structures, dependent on K6 of ubiquitin, in cells during DNA replication and repair. Human Molecular Genetics. 2004; 13: 807-17.
125. Sy SM, Huen MS, Chen J. PALB2 is an integral component of the BRCA complex required for homologous recombination repair. Proceedings of the National Academy of Sciences of the United States of America. 2009; 106: 7155-60.
126. Zhang F, Ma J, Wu J, Ye L, Cai H, Xia B, et al. PALB2 links BRCA1 and BRCA2 in the DNA-damage response. Current biology : CB. 2009; 19: 524-9.
127. Yu X, Chini CCS, He M, Mer G, Chen J. The BRCT Domain Is a Phospho-Protein Binding Domain. 2003; 302: 639-42.
128. Manke IA, Lowery DM, Nguyen A, Yaffe MB. BRCT repeats as phosphopeptide-binding modules involved in protein targeting. Science (New York, NY). 2003; 302: 636-9.
129. Yu X, Chen J. DNA damage-induced cell cycle checkpoint control requires CtIP, a phosphorylation-dependent binding partner of BRCA1 C-terminal domains. Molecular and cellular biology. 2004; 24: 9478-86.
130. Cantor SB, Bell DW, Ganesan S, Kass EM, Drapkin R, Grossman S, et al. BACH1, a novel helicase-like protein, interacts directly with BRCA1 and contributes to its DNA repair function. Cell. 2001; 105: 149-60.
131. Wang B, Matsuoka S, Ballif BA, Zhang D, Smogorzewska A, Gygi SP, et al. Abraxas and RAP80 form a BRCA1 protein complex required for the DNA damage response. Science (New York, NY). 2007; 316: 1194-8.
132. Huertas P, Jackson SP. Human CtIP mediates cell cycle control of DNA end resection and double strand break repair. The Journal of biological chemistry. 2009; 284: 9558-65.
133. Cruz-Garcia A, Lopez-Saavedra A, Huertas P. BRCA1 accelerates CtIP-mediated DNA-end resection. Cell Rep. 2014; 9: 451-9.
134. Ross Chapman J, J Sossick A, Boulton S, P Jackson S. BRCA1-associated exclusion of 53BP1 from DNA: Damage sites underlies temporal control of DNA repair; 2012.
135. Huertas P, Cortes-Ledesma F, Sartori AA, Aguilera A, Jackson SP. CDK targets Sae2 to control DNA-end resection and homologous recombination. Nature. 2008; 455: 689-92.

136. Orthwein A, Noordermeer SM, Wilson MD, Landry S, Enchev RI, Sherker A, et al. A mechanism for the suppression of homologous recombination in G1 cells. Nature. 2015; 528: 422-6.
137. Simonetta M, de Krijger I, Serrat J, Moatti N, Fortunato D, Hoekman L, et al. H4K20me2 distinguishes pre-replicative from post-replicative chromatin to appropriately direct DNA repair pathway choice by 53BP1-RIF1-MAD2L2. Cell cycle (Georgetown, Tex). 2018: 1-13.
138. Pellegrino S, Michelena J, Teloni F, Imhof R, Altmeyer M. Replication-Coupled Dilution of H4K20me2 Guides 53BP1 to Pre-replicative Chromatin. Cell Rep. 2017; 19: 1819-31.
139. Nakamura K, Saredi G, Becker JR, Foster BM, Nguyen NV, Beyer TE, et al. H4K20me0 recognition by BRCA1-BARD1 directs homologous recombination to sister chromatids. Nature cell biology. 2019.
140. Xu X, Qiao W, Linke SP, Cao L, Li WM, Furth PA, et al. Genetic interactions between tumor suppressors Brca1 and p53 in apoptosis, cell cycle and tumorigenesis. Nat Genet. 2001; 28: 266-71.
141. Cao L, Xu X, Bunting SF, Liu J, Wang RH, Cao LL, et al. A selective requirement for 53BP1 in the biological response to genomic instability induced by Brca1 deficiency. Mol Cell. 2009; 35: 534-41.
142. Bunting SF, Callen E, Wong N, Chen HT, Polato F, Gunn A, et al. 53BP1 inhibits homologous recombination in Brca1-deficient cells by blocking resection of DNA breaks. Cell. 2010; 141: 243-54.
143. Bouwman P, Aly A, Escandell JM, Pieterse M, Bartkova J, van der Gulden H, et al. 53BP1 loss rescues BRCA1 deficiency and is associated with triple-negative and BRCA-mutated breast cancers. Nat Struct Mol Biol. 2010; 17: 688-95.
144. Xie A, Hartlerode A, Stucki M, Odate S, Puget N, Kwok A, et al. Distinct roles of chromatin-associated proteins MDC1 and 53BP1 in mammalian double-strand break repair. Mol Cell. 2007; 28: 1045-57.
145. Bruna A, Rueda OM, Greenwood W, Batra AS, Callari M, Batra RN, et al. A Biobank of Breast Cancer Explants with Preserved Intra-tumor Heterogeneity to Screen Anticancer Compounds. Cell. 2016; 167: 260-74.e22

## Abstract

The cancer genomics revolution has rapidly expanded the inventory of somatic mutations characterizing human malignancies, highlighting a previously underappreciated extent of molecular variability between and within patients. Also in breast cancer, the most commonly diagnosed malignancy in women, this heterogeneity complicates the understanding of the stepwise sequence of pathogenic events and the design of effective and long-lasting target therapies. To disentangle this complexity and pinpoint which molecular perturbations are crucial to hijack the cellular machinery and lead to tumorigenesis and drug resistance, functional studies are needed in model systems that faithfully and comprehensively recapitulate all the salient aspects of their cognate human counterparts. Mouse models of breast cancer have been instrumental for the study of tumor initiation and drug response but also involve cost and time limitations that represent serious bottlenecks in translational research. To keep pace with the overwhelming amount of hypotheses that warrant *in vivo* testing, continuous refinement of current breast cancer models and implementation of new technologies is crucial. In this review, we summarize the current state of the art in modeling human breast cancer in mice, and we put forward our vision for future developments.

# Cancer Chess:

## Genetic Dissection of Cancer

# Molecular Insights

## Development, Therapy Response,

# Into PARPi Resistance

## and Resistance in Mouse Models

## of Breast Cancer

# Chapter 2

*Adapted from:*
*Stefano Annunziato, **Marco Barazas**, Sven Rottenberg, Jos Jonkers.*
*Cold Spring Harb Symp Quant Biol. 81:141-150 (2016)*

## Main Text

Breast cancer is the most commonly diagnosed invasive cancer worldwide, with more than 1.6 million new cases each year. Rather than a single disease, it represents a spectrum of malignancies, encompassing several distinct biological entities and subtypes, each associated with specific histopathological and molecular characteristics, responses to therapy, and clinical outcomes. Multiple taxonomies have been developed to divide breast cancer cases into different categories. Histopathological classification comprises several morphological and immunohistochemical phenotypes that can be further divided into different grades. Among the various morphologies, advanced mammary tumors mostly fall into the class of invasive ductal carcinomas (IDCs), followed by invasive lobular carcinomas (ILCs). Molecular classification based on gene expression patterns distinguishes five major subtypes of breast cancer: luminal A and B, ErbB2$^{+}$, basal-like, and claudin-low [1]. Although these distinctions have proven useful for clinical decision-making, there are limitations in predicting disease prognosis and response to therapy. For example, a recent prospective, randomized phase III study showed that nearly half of the women with early breast cancer who are at high risk based on standard clinicopathological parameters might not require adjuvant chemotherapy [2]. The additional use of a 70-gene expression signature may help to identify breast cancer patients who do not require adjuvant chemotherapy, but the identification of molecular signatures that reliably predict chemotherapy response remains elusive. Moreover, sequencing studies have shown that even within the same molecular subtype an extreme heterogeneity in the mutational landscape exists, which may account for discrepancies in prognosis and therapy response between different patients [3-5]. Another complicating factor is intratumoral heterogeneity. Individual tumors are mosaics of multiple clones of neoplastic cells, each characterized by a distinct genetic makeup and differential responses to the selective pressures to which they are exposed, making the tumor mass not static but continuously shaped by a branching evolutionary process resembling Darwinian evolution. Distinguishing causal disease variants (driver mutations) from background alterations (passenger mutations) is a major goal in breast cancer research, as it can pinpoint evolutionary conserved processes that mammary tumor cells apply during stepwise transformation and to which they might be addicted. To exploit these potential Achilles' heels, we require a comprehensive knowledge of how these signaling networks physiologically function, how they become aberrant, and how they can be directly or indirectly disrupted.

Given this complexity, genetically engineered mouse models (GEMMs) of breast cancer, together with patient-derived tumor xenografts (PDXs) and GEMM-derived tumor allografts, have proven valuable resources for deepening our understanding of how mammary tumors initiate, progress, metastasize, and respond to therapy in a physiologically relevant *in vivo* setting [6]. These mouse models are increasingly being used in longitudinal preclinical studies for translation of novel therapies to clinical testing.

Moreover, GEMMs provide unique opportunities to infer cause–effect relationships on de novo induced malignancies growing in intact organisms, rather than correlative observations on end-stage patient tumor samples.

Over the past 15 years, our research has been focused on the generation and characterization of mouse models for two breast cancer subtypes: ILCs and basal-like IDCs. To achieve this, we engineered a number of tumor-specific driver mutations in the relevant target cells of mouse models, recapitulating the key dependencies of the resulting lesions to the corresponding deranged signaling pathways. In this review, we will discuss how these models can be used for functional dissection of tumorigenic cascades, unraveling new therapeutic vulnerabilities and mechanisms of therapy resistance—in particular, in light of the advent of new technologies such as clustered regularly interspersed short palindromic repeat (CRISPR)–Cas9 gene editing, which are opening new avenues in breast cancer modeling in mice.

*Invasive lobular breast carcinoma (ILC) models*

ILC accounts for 8%–14% of all breast cancer cases and is hallmarked at the morphological level by tumor cells growing in single "Indian files" within a dense fibrous stroma. This phenotype can be explained at the molecular level by loss of integrity of cell adherens junctions because of mutations or methylation of the *CDH1* gene, which encodes the transmembrane protein E-cadherin [7-11]. To our surprise, we found that mammary gland–specific Cre-mediated inactivation of *Cdh1* alleles in mice was insufficient to induce mammary tumors, probably because normal cells undergo apoptosis and are counterselected when E-cadherin is lost [12-14]. This prompted us to investigate which cooperating oncogenic events are required for malignant transformation of E-cadherin-deficient mammary epithelial cells. We have found that multifocal ILC formation is promoted by dual mammary-specific loss of E-cadherin and p53 [13, 14] or E-cadherin and PTEN (phosphatase and tensin homolog) [15], with tumor architecture and molecular profiles closely resembling their human ILC counterparts (Table 1). However, it remains elusive which biological processes are rescued by codepletion of E-cadherin with one of these factors. To identify novel candidate cancer genes and networks that collaborate with E-cadherin loss in mammary tumorigenesis, we used the *Sleeping Beauty* (SB) transposon system [16, 17] to perform an insertional mutagenesis screen in *WAPcre;Cdh1*$^{F/F}$ mice [18]. Retrieval of recurrent integrations in SB-induced *WAPcre;Cdh1*$^{F/F}$ mammary tumors identified common insertion sites in several genes, some known to be mutated in human ILC, suggesting that mutagenesis of these genes leads to malignant transformation. Moreover, analysis of enriched targeted pathways and mutually exclusive insertions revealed the regulation of the actin cytoskeleton as a completely novel oncogenic pathway in both mouse and human ILC.

Furthermore, recent genomic studies on collections of human ILCs have unveiled that, in addition to somatic inactivation of E-cadherin, activation of phosphoinositide 3-kinase (PI3K)/AKT signaling appears to be a common event in this breast cancer subtype [19-21]. To validate these findings, we developed GEMMs of ILC that combine mammary gland – specific ablation of E-cadherin and activation of different oncogenic *Pik3ca* or *Akt* mutants (MHAM van Miltenburg, et al., in prep.). To rapidly generate breast cancer models carrying these allelic variants, we used a novel strategy for fast-track production of GEMMs, called GEMM-ESC, which is based on Flp-recombinase-mediated introduction of additional mutant alleles into the *Col1a1* locus of embryonic stem cells (ESCs) derived from existing GEMMs [22]. Interestingly, the resulting mice showed rapid development of tumors with strong resemblance to human ILC in terms of morphology, gene expression, and invasiveness, on which we are now testing a panel of anticancer therapeutics to identify promising genotype-specific drug sensitivities.

*Basal-like breast cancer models*

Basal-like breast cancers represent a heterogeneous class of malignancies with poor clinical outcome that accounts in total for 10%–15% of all breast cancer cases [1, 23]. The majority of basal-like tumors lack expression of estrogen receptor (ER), progesterone receptor (PR), and human epidermal growth factor receptor 2 (HER2) and are therefore referred to as triple-negative breast cancers. These tumors are not targetable with hormonal therapy or HER2 inhibitors, which leaves clinicians with only few effective options for therapeutic intervention.

Approximately 50% of basal-like breast cancers display a dysfunctional BRCA pathway because of germline or somatic mutations in *BRCA1/2* or *BRCA1* promoter hypermethylation [3, 5]. Also a fraction of non-basal-like tumors are BRCA-deficient, mostly because of germline mutations in *BRCA2*. As these genes are crucial in the error-free repair of DNA double-strand breaks (DSBs) by homologous recombination (HR), BRCA defects are associated with chromosomal instability and hypersensitivity to DNA DSB-inducing drugs such as alkylating agents, poly ADP ribose polymerase inhibitors (PARPi), and radiotherapy [24-26]. However, drug resistance mechanisms have been described in both clinical and preclinical studies of BRCA-associated tumors, posing serious concerns, as no other therapies are currently available for relapsing patients.

To study tumorigenesis and drug resistance mechanisms, we developed several conditional mouse models for BRCA1- and BRCA2-associated breast cancer [27, 28]. In our *K14cre;Brca1*$^{F/F}$*;p53*$^{F/F}$ (KB1P) and *K14cre;Brca2*$^{F/F}$*;p53*$^{F/F}$ (KB2P) models, mammary inactivation of *Brca1/2* is accompanied by loss of p53, as mutations in this tumor suppressor frequently co-occur with *BRCA1/2* mutations in breast cancer [29, 30]. These mice develop mammary tumors after a latency period of 6–8 months, suggesting that additional mutations are required for tumorigenesis (Table 1). However, in contrast to ILC, in which point mutations are the most common somatic alterations,

**TABLE 1 | Characteristics of human ILC and BRCA1-associated breast cancer and the corresponding GEMMs developed in our laboratory**

| Invasive lobular carcinoma | Human | *WAPcre;Cdh1$^{F/F}$;Pten$^{F/F}$* mouse model |
|---|---|---|
| Morphology | Lobular | Lobular |
| Invasive | Yes | Yes |
| Grade | Low | Low |
| Mitotic index | Low | Low |
| ER expression | Yes | Yes |
| Molecular subtype | Luminal | Luminal |
| Collagen deposition | Yes | Yes |
| Stroma-rich | Yes | Yes |
| **BRCA1-associated breast cancer** | **Human** | ***K14cre;Brca1$^{F/F}$;p53$^{F/F}$* mouse model** |
| Morphology | Ductal | Ductal |
| Invasive | Yes | Yes |
| Grade | High | High |
| Mitotic index | High | High |
| ER/PR expression | No | No |
| Molecular subtype | Basal-like | Basal-like |
| Genomically instable | Yes | Yes |
| HR-deficient | Yes | Yes |

ILC, invasive lobular carcinoma; BRCA1, breast cancer gene 1; GEMMs, genetically engineered mouse models; ER, estrogen receptor; PR, progesterone receptor; HR, homologous recombination.

*BRCA*-mutated breast cancers are characterized by complex patterns of DNA copy number aberrations (CNAs), including translocations and gains/losses of entire chromosome arms [31]. Using cross-species oncogenomics, we identified *MYC* amplification and *RB1* loss as recurrent CNAs in both mouse and human *BRCA1/2*-mutated breast cancers [32]. Exploiting the GEMM-ESC strategy, we could model conditional overexpression of MYC in our *WAPcre;Brca1$^{F/F}$;p53$^{F/F}$* (WB1P) mouse model and found that mammary tumor development was indeed strongly accelerated compared to the original line [33]. Moreover, we observed that the number of CNAs in WB1P-MYC tumors was markedly reduced compared to WB1P tumors, showing only few recurrent CNAs that most likely harbor additional cancer drivers that collaborate with MYC overexpression and loss of BRCA1/p53 in breast tumorigenesis. We are currently performing cross-species comparisons of the recurrent CNAs in WB1P-MYC tumors with CNA profiles from human breast cancers to identify candidate cancer genes, which will be validated in the WB1P-MYC model. We believe that this iterative CNA profiling approach in progressively complex GEMMs will be instrumental for deciphering the key driver events in BRCA1-associated breast cancer and for uncovering novel therapeutic vulnerabilities.

*Preclinical trials in Brca-associated breast cancer models*

Although phase-I and -II clinical trials are mostly carried out in heavily pretreated volunteer patients who suffer from end-stage metastatic cancer, mouse models provide the opportunity to initiate treatment on naïve tumors in a clinically relevant *in vivo* setting. Treatment of mammary tumor-bearing KB1P mice with a panel of DSB-inducing agents showed heterogeneous responses between individual tumors but also marked differences in tumors treated with doxorubicin or docetaxel and those treated with cisplatin [34]. Although KB1P tumors eventually developed resistance to doxorubicin and

docetaxel, no acquired resistance was observed for cisplatin. Even though these tumors could never be completely eradicated by maximum tolerated dose concentrations of cisplatin, the relapsing tumors remained responsive to subsequent treatments, resulting in a typical sawtooth tumor response. A major breakthrough came when it was found that spontaneous KB1P and KB2P tumors could be orthotopically allografted in syngeneic mice while maintaining their genetic characteristics and drug sensitivity profile. This approach reduced the time to produce cohorts of tumor-bearing mice from 7–9 mo to 4–6 wk, and enabled large-scale intervention studies in which the response of a single donor to different chemotherapeutic strategies could be compared, ruling out any intertumor heterogeneity (Fig. 1). Intervention studies with the PARP inhibitor olaparib in KB1P tumor allografts led to the development of carboplatin and olaparib switch-maintenance therapy for *Brca1*-mutated breast cancer [35]. This preclinical concept was confirmed in a clinical trial with olaparib maintenance therapy in *BRCA*-mutation carriers with platinum-sensitive ovarian cancer [36, 37] and eventually led to clinical approval of olaparib [38]. Similarly, intervention studies in KB2P tumor allografts showed that alkylators such as nimustine could induce complete tumor eradication [39]. Eradication of *BRCA*-mutated and BRCA-like cancer by high-dose alkylating chemotherapy was subsequently confirmed by retrospective analysis of data from clinical trials [40-42]. These and other studies illustrate the utility of GEMMs of human cancer in translational cancer medicine.

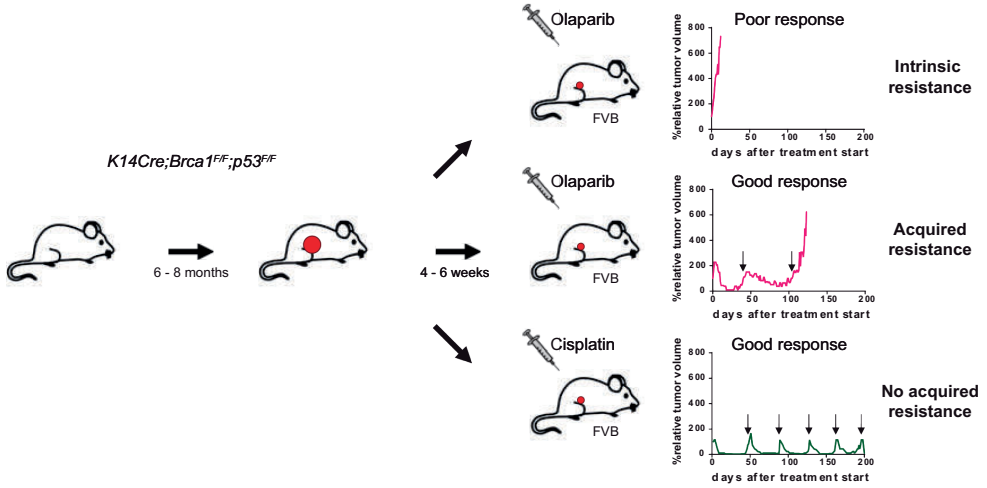



**FIGURE 1 | Large-scale intervention studies using breast cancer gene (BRCA)-deficient orthotopic allografts.** Spontaneous tumors develop with a latency of 6–8 months in *K14cre;Brca1$^{F/F}$;p53$^{F/F}$* (KB1P) or *K14cre;Brca2$^{F/F}$;p53$^{F/F}$* (KB2P) genetically engineered mouse models (GEMMs). Retransplantation of spontaneous tumors in syngeneic FVB wild-type mice highlighted intertumor heterogeneity in treatment response. In the case of olaparib, some tumors displayed intrinsic resistance, whereas others displayed initial good response followed by the emergence of acquired resistance. In contrast, resistance never developed in cisplatin-treated animals, despite multiple consecutive rounds of treatment (indicated by black arrows).

*PARPi resistance mechanisms in Brca-associated breast cancer models*

In addition to accelerating preclinical trials, the KB1P and KB2P allograft platforms also enabled large-scale induction of acquired resistance to a drug of choice and subsequent identification of the underlying resistance mechanisms. The power of this approach was demonstrated with the PARP inhibitor olaparib, which was described to display selective toxicity against BRCA1/2-deficient cells [40-44]. Indeed, KB1P tumor allografts initially responded well to treatment but eventually relapsed and developed stable resistance [35]. This has provided a valuable collection of matched treatment-naïve and treatment-resistant tumors, which could be analyzed using next-generation sequencing or (phospho)-proteomics, thereby taking advantage of the clean genetic background of inbred mice and the known genetic profile of treatment-naïve tumors. We found that *Abcb1a* and *Abcb1b*, encoding P-glycoprotein (P-gp) efflux pumps, were up-regulated in resistant tumors and we confirmed that P-gp played an important role in mediating export of olaparib from tumor cells (Fig. 2A; [35]). Resistance could be reversed when P-gp-mediated drug efflux was inhibited by coadministration of tariquidar. Although the clinical relevance of P-gp up-regulation as cause of drug resistance remains controversial [45], expression of *MDR1*, the human counterpart of *Abcb1*, was recently found to be inversely correlated to olaparib response in human ovarian cancer cells [46]. Such increased expression may result from complex genomic rearrangements that fuse a distant promoter to the *MDR1* gene and thereby bypass the *MDR1* promoter methylation [47]. The case of P-gp shows that a thorough mechanistic understanding is instrumental to combat resistant tumors — for example, by coadministration of tariquidar or by switching treatment to chemotherapeutics that are poor substrates for P-gp [48].

To dissect P-gp-independent mechanisms of PARPi resistance, the KB1P mouse model was refined through germline genetic deletion of *Mdr1* resulting in the *K14cre;Brca1*$^{F/F}$*;p53*$^{F/F}$*;Mdr1a/b*$^{-/-}$ (KB1PM) model [48]. Alternatively, KB1P tumors were treated with the PARP inhibitor AZD2461, which is a poor substrate for P-gp [49]. PARPi resistance developed in these models despite the exclusion of P-gp-related mechanisms. To identify the underlying resistance mechanisms, next-generation sequencing data from treatment-naïve and PARPi-resistant tumors were combined with data from unbiased functional genetic screens *in vitro*. Through an insertional mutagenesis screen in conditional BRCA1-knockout mouse ESCs, we found that loss of 53BP1 rescues the proliferation defect, HR deficiency, and PARPi hypersensitivity of BRCA1-deficient cells by enhancing DSB end resection (Fig. 2B; [50]). This work from our laboratory and similar studies from the Nussenzweig laboratory [51] have led to novel mechanistic insights in DSB repair and to date several downstream effector proteins of 53BP1 have been shown to suppress HR in BRCA1-deficient cells, including RIF1 [52-55], PTIP [56], Artemis [57], and REV7/MAD2L2 [58, 59]. Thorough analysis of mutational status and expression levels of 53BP1 and REV7 in PARPi-resistant KB1P(M) tumors confirmed that loss of 53BP1 or REV7 causes *in vivo* resistance

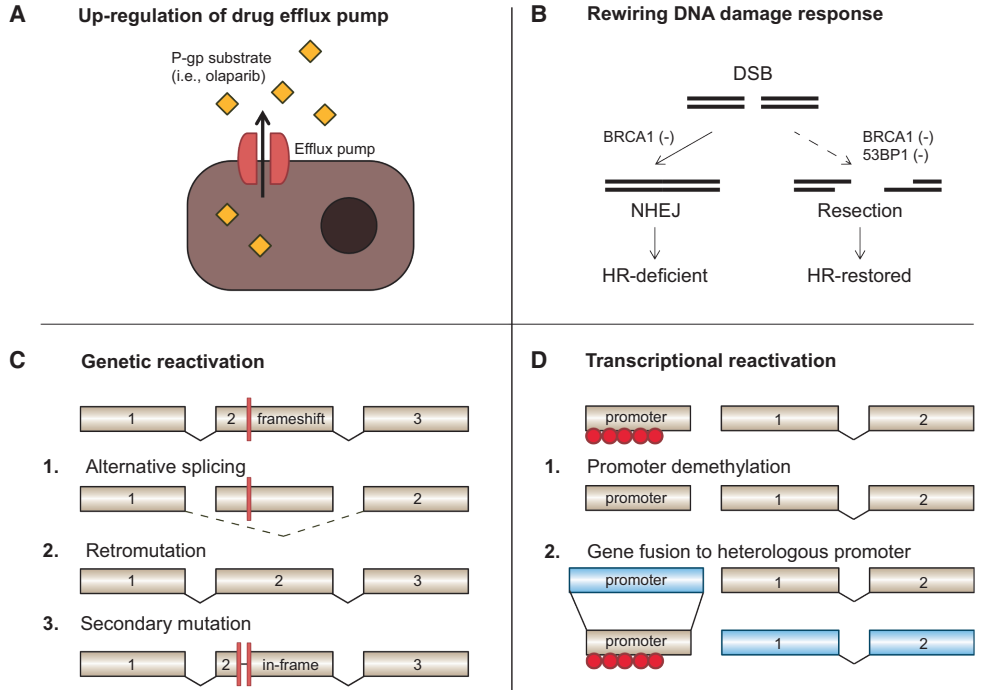



**FIGURE 2 | Overview of resistance mechanisms identified using mouse models of breast cancer gene (BRCA)-deficient breast cancer.** (*A*) Up-regulation of drug efflux pumps (i.e., MDR1) reduces intracellular drug concentration. (*B*) The DNA damage response pathway can be rewired to restore homologous recombination (HR), in this case by loss of 53BP1. (*C*) Genetic reactivation of *BRCA1*-mutated alleles can occur because of alternative splicing, retromutations, or secondary mutations restoring the *BRCA1* reading frame. (*D*) Transcription of silenced *BRCA1* alleles can be restored upon promoter demethylation or gene fusions to distant promoters. P-gp, P-glycoprotein; DSB, double-strand break; NHEJ, nonhomologous end joining; HR, homologous recombination.

to PARPi [48, 59]. Interestingly, although KB1P(M) tumors with 53BP1 loss are cross-resistant to topotecan and doxorubicin, they are still responsive to cisplatin, suggesting that platinum drugs may be a useful salvage therapy for this class of PARPi-resistant tumors [48].

Although the majority of KB1P(M) tumors acquired PARPi resistance through restoration of HR, a substantial fraction of PARPi-resistant tumors remained defective in the formation of ionizing radiation-induced nuclear RAD51 foci (RAD51-IRIFs), which are a hallmark of HR. Moreover, when we analyzed the BRCA2-deficient KB2P tumors with acquired PARPi resistance, none of these showed restoration of HR as measured by RAD51-IRIF assays [60]. This suggests the existence of alternative resistance mechanisms. It was recently shown that chemoresistance in BRCA2-deficient cells might be mediated through protection of replication forks (RFs) — for instance, by depletion of PAX transcription activation domain interacting protein (PTIP) [61].

It will be important to investigate whether RF protection is a common feature of PARPi-resistant KB1P(M) and KB2P tumors.

In patients, mutated BRCA1 or BRCA2 proteins are often still expressed in tumors. Therefore, the large intragenic *Brca1/2* deletions present in KB1P(M) and KB2P tumors — although instrumental in genetic studies — might not fully recapitulate the biology of BRCA-associated tumors in mutation carriers. To this end, we generated several mouse models mimicking pathogenic *BRCA1* variants that are often encountered in the clinic [62, 63]. These models provided evidence that the type and location of the *BRCA1* mutation can have significant implications for the response of these tumors to DSB-inducing agents and PARPi. It was found that tumor cells harboring the *BRCA1185delAG* allelic variant, which was modeled in mice by a *Brca1185stop* allele, can use a downstream alternative start site leading to the expression of a RING-less BRCA1 protein [63]. This RING-less BRCA1 protein maintains hypomorphic HR activity, which is sufficient to induce a poor response to platinum drugs or olaparib. These results illustrate the importance of testing *BRCA1* allelic variants not only for genetic counseling but also for providing adequate treatment.

PDX models provide a solution to narrow the gap between mouse and human cancer biology and as such represent a novel *in vivo* platform for studying therapy response and resistance. Although PDX models have been relatively difficult to generate in the past, recent advances have made it possible to generate PDX biobanks covering a heterogeneous population of tumors [64]. Once the (epi)genetic landscape of a PDX model is characterized, this provides an effective tool to study the drug response of a specific tumor and to predict which resistance mechanisms might evolve during treatment. We recently demonstrated the feasibility of such an approach by treatment of PDX models of BRCA1-deficient breast cancer with alkylating agents or olaparib [65]. Similar to the GEMM tumors, these PDX tumors generally responded well to treatment, but eventually developed resistance. The underlying mechanism was dependent on the type of *BRCA1* inactivation: Whereas therapy-resistant *BRCA1*-methylated PDX tumors frequently showed *BRCA1* promoter demethylation, *BRCA1*-mutated tumors acquired resistance via genetic reversion through secondary mutations that restored the *BRCA1* reading frame (Fig. 2C-D). These events have also been known to mediate resistance in ovarian cancer patients [47, 66], showing the predictive potential of PDX models. The PDX models also revealed a novel resistance mechanism involving gene fusions that placed *BRCA1* under transcriptional control of a heterologous promoter. It is intriguing that resistance mechanisms in PDX tumors are mainly centered on re-expression of functional BRCA1 protein rather than inactivation of 53BP1 or related factors, highlighting the strong selective pressure on complete restoration of BRCA1 function when BRCA1-deficient tumor cells are exposed to DSB-inducing therapy. However, a fraction of tumors acquired resistance in the absence of BRCA1 reexpression, showing that alternative resistance mechanisms also occur in PDX models.

Taken together, these studies illustrate the power of mouse models in unraveling resistance mechanisms before their emergence in patients. It will be important to investigate to what extent these play a role in the clinic. This is not trivial, as they likely occur in a limited group of *BRCA* patients and thus require careful patient selection. It is noteworthy that resistance caused by mutations in additional DNA repair genes such as 53BP1 or REV7 might expose new treatment vulnerabilities (e.g., sensitivity to combined PARP and ataxia telangiectasia mutated [ATM] inhibition [51]). It will therefore be important to determine if and how each resistance mechanism can be exploited therapeutically. Ultimately, this may provide a framework for oncologists to combat resistance in the clinic.

*Non-germline GEMMs of breast cancer*

Large-scale cancer genome sequencing studies and forward genetic screens have jointly boosted the discrimination between passenger and driver mutations and the identification of genetic determinants of drug sensitivity and resistance in breast cancer. The systematic translation of these long catalogs of structural aberrations into functional information requires the assessment of the pathophysiological impact of candidate gene perturbations in reliable preclinical models. This inevitably poses a practical challenge for *in vivo* validation experiments, because of the considerable costs and time requirements associated with establishing new breast cancer GEMMs. Novel technologies, especially CRISPR–Cas9-based methods, are revolutionizing the genetic engineering field by providing fast ways for precise and efficient ESC manipulation and GEMM development [67]. However, as sequencing expenses of human tumors keep decreasing, research will shift from testing oncogenicity of single driver alleles to investigating the impact of multiple allelic variants on tumor development and therapy response. At the same time, forward genetics strategies will evolve from genome-wide approaches based on simple gene (in)activation to more refined chemical mutagenesis and gene-based CRISPR screens capable of identifying novel hypomorphic, dominant-negative, and separation-of-function mutants at the base pair level. We foresee that the number of testable hypotheses will far exceed the capacity of transgenic facilities, warranting the development of new *in vivo* platforms for systematic, multiplexed interrogation of putative cancer drivers. Ideally, such models should sort out current temporal and economical limitations of GEMM establishment and bypass extensive mouse husbandry but also allow a high degree of manipulability and flexibility by enabling spatiotemporal control of tumor initiation and progression.

To develop such a platform for breast cancer, we explored the possibility of nongermline modeling of mammary tumors by exploiting intraductal injection in the nipple of adult female mice as a way to deliver high-titer lentiviral or adenoviral preparations to mammary epithelium and achieve somatic genome engineering. We have shown that intraductally injected lentiviruses can target tumor-initiating cells

of both the basal and the luminal compartment, allowing modeling of both ILC and basal-like tumors in mice with the corresponding set of relevant predisposing alleles. For example, intraductal injection of Cre-encoding lentiviruses in *Cdh1*$^{F/F}$;*Pten*$^{F/F}$ mice induced the formation of ILCs that were undistinguishable from the ILCs arising in the original *WAPcre;Cdh1*$^{F/F}$; *Pten*$^{F/F}$ model [68]. Somatic Cre delivery may more accurately recapitulate sporadic tumor initiation by allowing titratable and spatiotemporally controlled delivery of viruses to mammary tissue. Moreover, targeting specificity can be modulated by using viruses with cell type–specific promoters and/or posttranscriptional control elements [69].

Importantly, the potential of nongermline modeling extends far beyond simple exogenous administration of Cre to established GEMMs. A diverse array of viral and nonviral constructs can be employed to achieve desired permutations of specific candidate genes even in the absence of germline conditional alleles: (a) vectors for overexpression of wild-type, truncated, or mutated cDNAs; (b) vectors for shRNA-mediated down-regulation or CRISPR-mediated (epi)genetic manipulation of single or multiple endogenous genes [70]; (c) CRISPR vectors for modeling large chromosomal rearrangements [71]; and (d) vectors for tagging and imaging of tumors (Fig. 3). Regarding CRISPR-based *in vivo* editing approaches, we and others have shown that somatic delivery of the bacterial Cas9 protein has the considerable drawback of eliciting strong and specific immune responses in immunocompetent

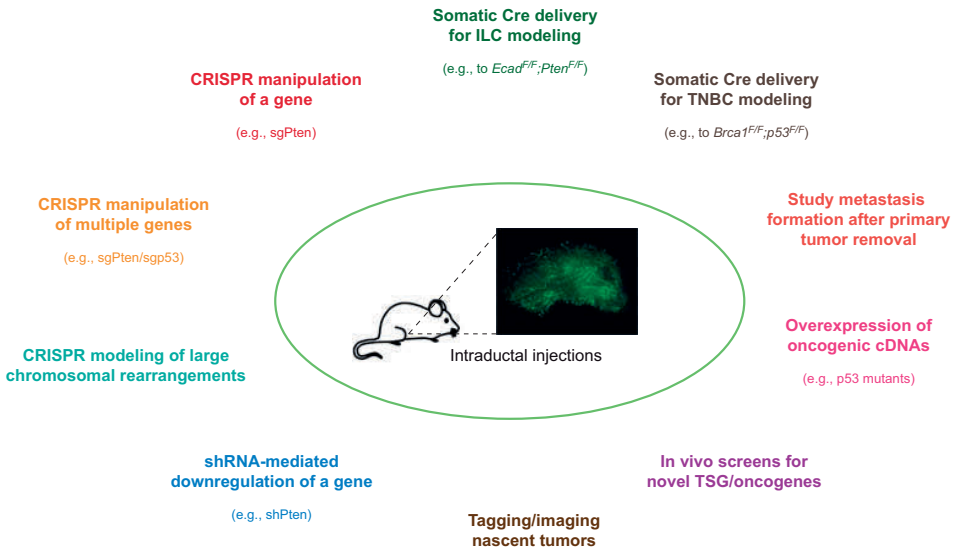



**FIGURE 3 |** Multiple applications for somatic genome engineering of the mammary tissue via intraductal injection to study tumor biology. ILC, invasive lobular carcinoma; TNBC, triple-negative breast cancer; sgPten, single-guide phosphatase and tensin homolog; shPTEN, short-hairpin phosphatase and tensin homolog; TSG, tumor suppressor gene.

animals [68, 72]. This problem can be overcome by employing knock-in models that are tolerant to Cas9 because of constitutive or conditional expression of Cas9 or catalytically inactive dCas9-effector fusions (which allow for transcriptional silencing/activation of endogenous alleles) [73, 74]. We have recently reported somatic induction of oncogenic loss-of-function mutations in mice with mammary-specific expression of Cas9 by intraductal injection of single-guide RNA (sgRNA)-encoding lentiviruses, which eventually led to ILC formation [68].

*Mammary tumor organoids*

Another exciting technological breakthrough came from the possibility to derive organotypic 3D culture models of normal and malignant mammary tissue. Human and murine tumor organoid cultures retain key features of donor tumors, including cellular heterogeneity and molecular characteristics [75, 76]. Compared to the laborious and time-consuming establishment of 2D cell lines, which requires adaptation to monolayer growth on plastic surfaces, tumor organoid cultures are much easier to derive, can be expanded indefinitely *ex vivo*, and upon xenografting/allografting undergo polyclonal expansion and efficiently produce tumors that preserve the cellular heterogeneity and drug response profiles of the original tumors [77]. For example, we found the differential olaparib sensitivity of isogenic treatment-naïve and PARPi-resistant KB1P mammary tumors to be stable upon organoid derivation and subsequent retransplantation. Using CRISPR–Cas9 technology, we were able to introduce *Trp53bp1* frameshift mutations in the treatment-naïve KB1P organoid line and demonstrate that this permutation rendered the organoid-derived tumors refractory to olaparib. We are exploiting the KB1P tumor organoid platform to test additional candidate drug resistance genes for their *in vivo* relevance, including candidates retrieved from forward genetic screens and from sequencing of drug-resistant tumors (Fig. 4). Moreover, given the short latency period and polyclonal tumor outgrowth, GEMM and PDX tumor organoids are particularly amenable for *in vivo* genetic screens using short-hairpin RNA (shRNA), CRISPR, CRISPRi, and CRISPRa libraries.

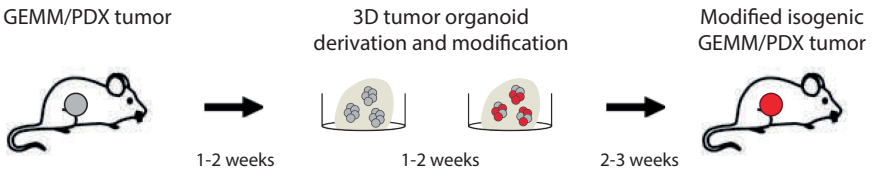



**FIGURE 4 |** 3D tumor organoid cultures can be rapidly derived from established genetically engineered mouse model (GEMM)/patient-derived xenograft (PDX) tumors, modified *ex vivo* with desired genetic permutations and retransplanted in mice to evaluate *in vivo* treatment responses.

## Conclusion

A number of known and unknown biological discrepancies inevitably exist between mouse models and humans. Moreover, refinements in mouse modeling should be compliant with practical and ethical issues associated with model establishment. Nevertheless, the systematic and synergistic deployment of complementary *in vitro* and *in vivo* platforms (GEMMs, PDX models, organoids, nongermline models) is envisioned to provide a quantum leap in the oncology arena and in breast cancer research in particular. Cutting-edge mouse cancer clinics will enable so-called coclinical trials, in which clinical studies will be paralleled by preclinical intervention studies in mouse avatars. This will allow clinicians to infer in real-time genotype-specific drug response profiles from mouse models and design more effective and long-lasting patient-tailored treatment schemes. The emergence of drug resistance is an invariable and intrinsic consequence of Darwinian tumor growth dynamics, but instead of "whack-a-mole" treatment schedules, coclinical trials could assist in the design of more sophisticated and personalized regimens in which tumors are forced through evolutionary bottlenecks that render them exquisitely sensitive to secondary therapies. Reiteration of this adaptive process is possible only by the use of ever-smarter mouse models, which will ultimately lead to improved long-term management of this devastating disease.

## Acknowledgements

We are grateful to Peter Bouwman for critical reading of the manuscript. Research in the Jonkers and Rottenberg laboratories described in this review has been supported by grants from the Dutch Cancer Society (NKI 2007-3772, NKI 2008-4116, NKI 2009-4303, NKI 2011-5197, NKI 2011-5220, NKI 2012-5220, NKI 2014-6532, NKI 2015-7877, EMCR 2014-7048), the Netherlands Organization for Scientific Research (NWO), Cancer Genomics Netherlands (CGCNL), Cancer Systems Biology Center (CSBC), NGI Zenith 93512009, VIDI 91711302, VICI 91814643, the Swiss National Science Foundation (310030-156869), the Swiss Cancer Research Foundation (MD-PhD-3446-01-2014), the European Union Seventh Framework Programme (EurocanPlatform project 260791, Infrafrontier-I3 project 312325, CHEMORES project 037665), and the European Research Council (ERC SyG CombatCancer, ERC CoG-681572). Additional support is provided by the Mouse Clinic for Cancer and Aging (MCCA), financed by NWO as part of the National Roadmap for Large-Scale Research Facilities.

## References

1. Perou CM, Sørlie T, Eisen MB, van de Rijn M, Jeffrey SS, Rees CA, et al. Molecular portraits of human breast tumours. Nature. 2000; 406: 747-52.
2. Cardoso F, van't Veer LJ, Bogaerts J, Slaets L, Viale G, Delaloge S, et al. 70-Gene Signature as an Aid to Treatment Decisions in Early-Stage Breast Cancer. New England Journal of Medicine. 2016; 375: 717-29.

3. Comprehensive molecular portraits of human breast tumours. Nature. 2012; 490: 61-70.
4. Stephens PJ, Tarpey PS, Davies H, Van Loo P, Greenman C, Wedge DC, et al. The landscape of cancer genes and mutational processes in breast cancer. Nature. 2012; 486: 400-4.
5. Nik-Zainal S, Davies H, Staaf J, Ramakrishna M, Glodzik D, Zou X, et al. Landscape of somatic mutations in 560 breast cancer whole-genome sequences. Nature. 2016; 534: 47-54.
6. Vargo-Gogola T, Rosen JM. Modelling breast cancer: one size does not fit all. Nat Rev Cancer. 2007; 7: 659-72.
7. Martinez V, Azzopardi JG. Invasive lobular carcinoma of the breast: incidence and variants. Histopathology. 1979; 3: 467-88.
8. Borst MJ, Ingold JA. Metastatic patterns of invasive lobular versus invasive ductal carcinoma of the breast. Surgery. 1993; 114: 637-41; discussion 41-2.
9. Moll R, Mitze M, Frixen UH, Birchmeier W. Differential loss of E-cadherin expression in infiltrating ductal and lobular breast carcinomas. Am J Pathol. 1993; 143: 1731-42.
10. Vos CB, Cleton-Jansen AM, Berx G, de Leeuw WJ, ter Haar NT, van Roy F, et al. E-cadherin inactivation in lobular carcinoma in situ of the breast: an early event in tumorigenesis. British journal of cancer. 1997; 76: 1131-3.
11. Droufakou S, Deshmane V, Roylance R, Hanby A, Tomlinson I, Hart IR. Multiple ways of silencing E-cadherin gene expression in lobular carcinoma of the breast. Int J Cancer. 2001; 92: 404-8.
12. Boussadia O, Kutsch S, Hierholzer A, Delmas V, Kemler R. E-cadherin is a survival factor for the lactating mouse mammary gland. Mechanisms of Development. 2002; 115: 53-62.
13. Derksen PW, Braumuller TM, van der Burg E, Hornsveld M, Mesman E, Wesseling J, et al. Mammary-specific inactivation of E-cadherin and p53 impairs functional gland development and leads to pleomorphic invasive lobular carcinoma in mice. Dis Model Mech. 2011; 4: 347-58.
14. Derksen PW, Liu X, Saridin F, van der Gulden H, Zevenhoven J, Evers B, et al. Somatic inactivation of E-cadherin and p53 in mice leads to metastatic lobular mammary carcinoma through induction of anoikis resistance and angiogenesis. Cancer cell. 2006; 10: 437-49.
15. Boelens MC, Nethe M, Klarenbeek S, de Ruiter JR, Schut E, Bonzanni N, et al. PTEN Loss in E-Cadherin-Deficient Mouse Mammary Epithelial Cells Rescues Apoptosis and Results in Development of Classical Invasive Lobular Carcinoma. Cell Rep. 2016; 16: 2087-101.
16. Collier LS, Carlson CM, Ravimohan S, Dupuy AJ, Largaespada DA. Cancer gene discovery in solid tumours using transposon-based somatic mutagenesis in the mouse. Nature. 2005; 436: 272-6.
17. Dupuy AJ, Akagi K, Largaespada DA, Copeland NG, Jenkins NA. Mammalian mutagenesis using a highly mobile somatic Sleeping Beauty transposon system. Nature. 2005; 436: 221-6.
18. Kas SM, de Ruiter JR, Schipper K, Annunziato S, Schut E, Klarenbeek S, et al. Insertional mutagenesis identifies drivers of a novel oncogenic pathway in invasive lobular breast carcinoma. Nat Genet. 2017; 49: 1219-30.
19. Ciriello G, Gatza ML, Beck AH, Wilkerson MD, Rhie SK, Pastore A, et al. Comprehensive Molecular Portraits of Invasive Lobular Breast Cancer. Cell. 2015; 163: 506-19.
20. Desmedt C, Zoppoli G, Gundem G, Pruneri G, Larsimont D, Fornili M, et al. Genomic Characterization of Primary Invasive Lobular Breast Cancer. J Clin Oncol. 2016; 34: 1872-81.
21. Michaut M, Chin SF, Majewski I, Severson TM, Bismeijer T, de Koning L, et al. Integration of genomic, transcriptomic and proteomic data identifies two biologically distinct subtypes of invasive lobular breast cancer. Sci Rep. 2016; 6: 18517.
22. Huijbers IJ, Bin Ali R, Pritchard C, Cozijnsen M, Kwon MC, Proost N, et al. Rapid target gene validation in complex cancer mouse models using re-derived embryonic stem cells. EMBO Mol Med. 2014; 6: 212-25.
23. Badve S, Dabbs DJ, Schnitt SJ, Baehner FL, Decker T, Eusebi V, et al. Basal-like and triple-negative breast cancers: a critical review with an emphasis on the implications for pathologists and oncologists. Mod Pathol. 2011; 24: 157-67.
24. Jaspers JE, Rottenberg S, Jonkers J. Therapeutic options for triple-negative breast cancers with defective homologous recombination. Biochimica et Biophysica Acta (BBA) - Reviews on Cancer. 2009; 1796: 266-80.
25. Bouwman P, Jonkers J. The effects of deregulated DNA damage signalling on cancer chemotherapy response and resistance. Nat Rev Cancer. 2012; 12: 587-98.

26. Barazas M, Gasparini A, Huang Y, Küçükosmanoğlu A, Annunziato S, Bouwman P, et al. Radiosensitivity Is an Acquired Vulnerability of PARPi-Resistant BRCA1-Deficient Tumors. Cancer research. 2019; 79: 452-60.
27. Bouwman P, Jonkers J. Mouse models for BRCA1 associated tumorigenesis: from fundamental insights to preclinical utility. Cell Cycle. 2008; 7: 2647-53.
28. Evers B, Jonkers J. Mouse models of BRCA1 and BRCA2 deficiency: past lessons, current understanding and future prospects. Oncogene. 2006; 25: 5885-97.
29. Jonkers J, Meuwissen R, van der Gulden H, Peterse H, van der Valk M, Berns A. Synergistic tumor suppressor activity of BRCA2 and p53 in a conditional mouse model for breast cancer. Nat Genet. 2001; 29: 418-25.
30. Liu X, Holstege H, van der Gulden H, Treur-Mulder M, Zevenhoven J, Velds A, et al. Somatic loss of BRCA1 and p53 in mice induces mammary tumors with features of human BRCA1-mutated basal-like breast cancer. Proc Natl Acad Sci U S A. 2007; 104: 12111-6.
31. Vollebergh MA, Jonkers J, Linn SC. Genomic instability in breast and ovarian cancers: translation into clinical predictive biomarkers. Cell Mol Life Sci. 2012; 69: 223-45.
32. Holstege H, van Beers E, Velds A, Liu X, Joosse SA, Klarenbeek S, et al. Cross-species comparison of aCGH data from mouse and human BRCA1- and BRCA2-mutated breast cancers. BMC Cancer. 2010; 10: 455.
33. Annunziato S, de Ruiter JR, Henneman L, Brambillasca CS, Lutz C, Vaillant F, et al. Comparative oncogenomics identifies combinations of driver genes and drug targets in BRCA1-mutated breast cancer. Nat Commun. 2019; 10: 397.
34. Rottenberg S, Nygren AO, Pajic M, van Leeuwen FW, van der Heijden I, van de Wetering K, et al. Selective induction of chemotherapy resistance of mammary tumors in a conditional mouse model for hereditary breast cancer. Proc Natl Acad Sci U S A. 2007; 104: 12117-22.
35. Rottenberg S, Jaspers JE, Kersbergen A, van der Burg E, Nygren AO, Zander SA, et al. High sensitivity of BRCA1-deficient mammary tumors to the PARP inhibitor AZD2281 alone and in combination with platinum drugs. Proc Natl Acad Sci U S A. 2008; 105: 17079-84.
36. Ledermann J, Harter P, Gourley C, Friedlander M, Vergote I, Rustin G, et al. Olaparib Maintenance Therapy in Platinum-Sensitive Relapsed Ovarian Cancer. New England Journal of Medicine. 2012; 366: 1382-92.
37. Ledermann J, Harter P, Gourley C, Friedlander M, Vergote I, Rustin G, et al. Olaparib maintenance therapy in patients with platinum-sensitive relapsed serous ovarian cancer: a preplanned retrospective analysis of outcomes by BRCA status in a randomised phase 2 trial. Lancet Oncol. 2014; 15: 852-61.
38. Deeks ED. Olaparib: first global approval. Drugs. 2015; 75: 231-40.
39. Evers B, Schut E, van der Burg E, Braumuller TM, Egan DA, Holstege H, et al. A high-throughput pharmaceutical screen identifies compounds with specific toxicity against BRCA2-deficient tumors. Clinical cancer research : an official journal of the American Association for Cancer Research. 2010; 16: 99-108.
40. Schouten PC, Marmé F, Aulmann S, Sinn HP, van Essen HF, Ylstra B, et al. Breast cancers with a BRCA1-like DNA copy number profile recur less often than expected after high-dose alkylating chemotherapy. Clinical cancer research : an official journal of the American Association for Cancer Research. 2015; 21: 763-70.
41. Vollebergh MA, Lips EH, Nederlof PM, Wessels LF, Wesseling J, Vd Vijver MJ, et al. Genomic patterns resembling BRCA1- and BRCA2-mutated breast cancers predict benefit of intensified carboplatin-based chemotherapy. Breast Cancer Res. 2014; 16: R47.
42. Vollebergh MA, Lips EH, Nederlof PM, Wessels LFA, Schmidt MK, van Beers EH, et al. An aCGH classifier derived from BRCA1-mutated breast cancer and benefit of high-dose platinum-based chemotherapy in HER2-negative breast cancer patients. Ann Oncol. 2011; 22: 1561-70.
43. Bryant HE, Schultz N, Thomas HD, Parker KM, Flower D, Lopez E, et al. Specific killing of BRCA2-deficient tumours with inhibitors of poly(ADP-ribose) polymerase. Nature. 2005; 434: 913-7.
44. Farmer H, McCabe N, Lord CJ, Tutt AN, Johnson DA, Richardson TB, et al. Targeting the DNA repair defect in BRCA mutant cells as a therapeutic strategy. Nature. 2005; 434: 917-21.
45. Amiri-Kordestani L, Basseville A, Kurdziel K, Fojo AT, Bates SE. Targeting MDR in breast and lung cancer: discriminating its potential importance from the failure of drug resistance reversal studies. Drug Resist Updat. 2012; 15: 50-61.

46. Vaidyanathan A, Sawers L, Gannon A-L, Chakravarty P, Scott AL, Bray SE, et al. ABCB1 (MDR1) induction defines a common resistance mechanism in paclitaxel- and olaparib-resistant ovarian cancer cells. British journal of cancer. 2016; 115: 431-41.
47. Patch AM, Christie EL, Etemadmoghadam D, Garsed DW, George J, Fereday S, et al. Whole-genome characterization of chemoresistant ovarian cancer. Nature. 2015; 521: 489-94.
48. Jaspers JE, Kersbergen A, Boon U, Sol W, van Deemter L, Zander SA, et al. Loss of 53BP1 causes PARP inhibitor resistance in Brca1-mutated mouse mammary tumors. Cancer Discov. 2013; 3: 68-81.
49. Oplustil O'Connor L, Rulten SL, Cranston AN, Odedra R, Brown H, Jaspers JE, et al. The PARP Inhibitor AZD2461 Provides Insights into the Role of PARP3 Inhibition for Both Synthetic Lethality and Tolerability with Chemotherapy in Preclinical Models. Cancer research. 2016; 76: 6084-94.
50. Bouwman P, Aly A, Escandell JM, Pieterse M, Bartkova J, van der Gulden H, et al. 53BP1 loss rescues BRCA1 deficiency and is associated with triple-negative and BRCA-mutated breast cancers. Nat Struct Mol Biol. 2010; 17: 688-95.
51. Bunting SF, Callén E, Wong N, Chen HT, Polato F, Gunn A, et al. 53BP1 inhibits homologous recombination in Brca1-deficient cells by blocking resection of DNA breaks. Cell. 2010; 141: 243-54.
52. Chapman JR, Barral P, Vannier JB, Borel V, Steger M, Tomas-Loba A, et al. RIF1 is essential for 53BP1-dependent nonhomologous end joining and suppression of DNA double-strand break resection. Mol Cell. 2013; 49: 858-71.
53. Di Virgilio M, Callen E, Yamane A, Zhang W, Jankovic M, Gitlin AD, et al. Rif1 prevents resection of DNA breaks and promotes immunoglobulin class switching. Science. 2013; 339: 711-5.
54. Escribano-Díaz C, Orthwein A, Fradet-Turcotte A, Xing M, Young JT, Tkáč J, et al. A cell cycle-dependent regulatory circuit composed of 53BP1-RIF1 and BRCA1-CtIP controls DNA repair pathway choice. Mol Cell. 2013; 49: 872-83.
55. Zimmermann M, Lottersberger F, Buonomo SB, Sfeir A, de Lange T. 53BP1 regulates DSB repair using Rif1 to control 5' end resection. Science. 2013; 339: 700-4.
56. Callen E, Di Virgilio M, Kruhlak MJ, Nieto-Soler M, Wong N, Chen HT, et al. 53BP1 mediates productive and mutagenic DNA repair through distinct phosphoprotein interactions. Cell. 2013; 153: 1266-80.
57. Wang J, Aroumougame A, Lobrich M, Li Y, Chen D, Chen J, et al. PTIP associates with Artemis to dictate DNA repair pathway choice. Genes Dev. 2014; 28: 2693-8.
58. Boersma V, Moatti N, Segura-Bayona S, Peuscher MH, van der Torre J, Wevers BA, et al. MAD2L2 controls DNA repair at telomeres and DNA breaks by inhibiting 5' end resection. Nature. 2015; 521: 537-40.
59. Xu G, Chapman JR, Brandsma I, Yuan J, Mistrik M, Bouwman P, et al. REV7 counteracts DNA double-strand break resection and affects PARP inhibition. Nature. 2015; 521: 541-4.
60. Gogola E, Duarte AA, de Ruiter JR, Wiegant WW, Schmid JA, de Bruijn R, et al. Selective Loss of PARG Restores PARylation and Counteracts PARP Inhibitor-Mediated Synthetic Lethality. Cancer cell. 2018; 33: 1078-93.e12.
61. Ray Chaudhuri A, Callen E, Ding X, Gogola E, Duarte AA, Lee JE, et al. Replication fork stability confers chemoresistance in BRCA-deficient cells. Nature. 2016; 535: 382-7.
62. Drost R, Bouwman P, Rottenberg S, Boon U, Schut E, Klarenbeek S, et al. BRCA1 RING function is essential for tumor suppression but dispensable for therapy resistance. Cancer cell. 2011; 20: 797-809.
63. Drost R, Dhillon KK, van der Gulden H, van der Heijden I, Brandsma I, Cruz C, et al. BRCA1185delAG tumors may acquire therapy resistance through expression of RING-less BRCA1. J Clin Invest. 2016; 126: 2903-18.
64. Hidalgo M, Amant F, Biankin AV, Budinská E, Byrne AT, Caldas C, et al. Patient-derived xenograft models: an emerging platform for translational cancer research. Cancer Discov. 2014; 4: 998-1013.
65. Ter Brugge P, Kristel P, van der Burg E, Boon U, de Maaker M, Lips E, et al. Mechanisms of Therapy Resistance in Patient-Derived Xenograft Models of BRCA1-Deficient Breast Cancer. J Natl Cancer Inst. 2016; 108.
66. Swisher EM, Sakai W, Karlan BY, Wurz K, Urban N, Taniguchi T. Secondary BRCA1 mutations in BRCA1-mutated ovarian carcinomas with platinum resistance. Cancer research. 2008; 68: 2581-6.
67. Wang H, Yang H, Shivalila CS, Dawlaty MM, Cheng AW, Zhang F, et al. One-step generation of mice carrying mutations in multiple genes by CRISPR/Cas-mediated genome engineering. Cell. 2013; 153: 910-8.
68. Annunziato S, Kas SM, Nethe M, Yücel H, Del Bravo J, Pritchard C, et al. Modeling invasive lobular breast carcinoma by CRISPR/Cas9-mediated somatic genome editing of the mammary gland. Genes Dev. 2016; 30: 1470-80.

69. Tao L, van Bragt MP, Laudadio E, Li Z. Lineage tracing of mammary epithelial cells using cell-type-specific cre-expressing adenoviruses. Stem Cell Reports. 2014; 2: 770-9.
70. Sander JD, Joung JK. CRISPR-Cas systems for editing, regulating and targeting genomes. Nature Biotechnology. 2014; 32: 347-55.
71. Maddalo D, Manchado E, Concepcion CP, Bonetti C, Vidigal JA, Han YC, et al. In vivo engineering of oncogenic chromosomal rearrangements with the CRISPR/Cas9 system. Nature. 2014; 516: 423-7.
72. Wang D, Mou H, Li S, Li Y, Hough S, Tran K, et al. Adenovirus-Mediated Somatic Genome Editing of Pten by CRISPR/Cas9 in Mouse Liver in Spite of Cas9-Specific Immune Responses. Hum Gene Ther. 2015; 26: 432-42.
73. Platt RJ, Chen S, Zhou Y, Yim MJ, Swiech L, Kempton HR, et al. CRISPR-Cas9 knockin mice for genome editing and cancer modeling. Cell. 2014; 159: 440-55.
74. Sánchez-Rivera FJ, Jacks T. Applications of the CRISPR-Cas9 system in cancer biology. Nat Rev Cancer. 2015; 15: 387-95.
75. Clevers H. Modeling Development and Disease with Organoids. Cell. 2016; 165: 1586-97.
76. Fatehullah A, Tan SH, Barker N. Organoids as an in vitro model of human development and disease. Nat Cell Biol. 2016; 18: 246-54.
77. Duarte AA, Gogola E, Sachs N, Barazas M, Annunziato S, J RdR, et al. BRCA-deficient mouse mammary tumor organoids to study cancer-drug resistance. Nat Methods. 2018; 15: 134-40.

## Abstract

Poly(ADP-ribose) polymerase inhibition (PARPi) is a promising new therapeutic approach for the treatment of cancers that show homologous recombination deficiency (HRD). Despite the success of PARPi in targeting HRD in tumors that lack the tumor suppressor function of BRCA1 or BRCA2, drug resistance poses a major obstacle. We developed three-dimensional cancer organoids derived from genetically engineered mouse models (GEMMs) for BRCA1- and BRCA2-deficient cancers. Unlike conventional cell lines or mammospheres, organoid cultures can be efficiently derived and rapidly expanded *in vitro*. Orthotopically transplanted organoids give rise to mammary tumors that recapitulate the epithelial morphology and preserve the drug response of the original tumor. Notably, GEMM-tumor-derived organoids can be easily genetically modified, making them a powerful tool for genetic studies of tumor biology and drug resistance.

# Cancer Chess:

## BRCA-Deficient Mouse Mammary

# Molecular Insights

## Tumor Organoids to Study

# Into PARPi Resistance

## Cancer Drug Resistance

# Chapter 3

*Adapted from:*

*Alexandra A Duarte, Ewa Gogola, Norman Sachs,* ***Marco Barazas****, Stefano Annunziato, et al.*

*Nature Methods. 15(2):134-140 (2018)*

## Introduction

We have previously demonstrated that mammary adenocarcinomas that arise in *K14cre;Brca1$^{F/F}$;p53$^{F/F}$* (KB1P), *K14cre;Brca1$^{F/F}$; p53$^{F/F}$;Mdr1a/b$^{-/-}$* (KB1PM) and *K14cre;Brca2$^{F/F}$; p53$^{F/F}$* (KB2P) mouse models of BRCA-associated hereditary breast cancer recapitulate key features of the human disease [1, 2], including morphology, expression of basal markers, genomic instability and hypersensitivity to DNA-targeting therapy [3]. These features are preserved following orthotopic transplantation of tumor fragments into syngeneic mice [4]. This transplantation model has proven to be useful for studying mechanisms of drug resistance, particularly to PARP inhibitors [5-10]. To perform detailed analyses of drug resistance mechanisms, we derived two-dimensional (2D) cell lines from KB1P(M) and KB2P mammary tumors [6, 11]. Although these cell lines are useful, they exhibit limitations such as phenotypic and genetic uniformity and divergence from the primary tumor during adaptation to *in vitro* growth.

Recently, *in vitro* culture methods have been developed for efficient derivation of three-dimensional (3D) organoids from normal and malignant tissue [12, 13]. Organoid cultures preserve important features of the original tumor, such as cellular heterogeneity and self-renewal capacity. We developed a panel of KB1P(M) and KB2P tumor-derived organoid lines that provide more physiological models in which to study drug resistance than 2D cultures. We used pairs of PARPi-sensitive and PARPi-resistant BRCA1- and BRCA2-deficient tumors to test whether organoid cultures can be used to predict the drug response of the original tumor both *in vitro* and after orthotopic transplantation into mice.

## Results

*Generation of mammary tumor organoids*

We adapted a previously described culture system [12] to both fresh and cryopreserved mammary tumor tissues, yielding mammary tumor organoid cultures that could be rapidly expanded and cultured *in vitro* (Supplementary Fig. 1A). The success rate for establishing organoid lines was high for both KB1P(M) and KB2P donor tumors, whereas previous attempts to derive 2D cell lines or 3D mammospheres were much less efficient (Fig. 1A). Similar success rates were obtained for the *K14cre;p53$^{F/F}$* (KP) and *K14cre;p53$^{F/F}$;Mdr1a/b$^{-/-}$* (KPM) models, which were used as a BRCA-proficient control. Stable organoid lines could be obtained in 2–3 weeks, whereas 2D cell lines required 3–6 months to adapt to *in vitro* conditions. Moreover, KB1P(M)/KB2P organoid lines could be cultured under normal oxygen conditions, whereas BRCA1- and BRCA2-deficient cell lines require a 3% oxygen environment. The success rate of orthotopic transplantation of KB1P(M)/KB2P organoids was high: we observed tumor outgrowth for all of the organoid lines tested (nine KB1P(M) and ten KB2P organoid lines; data not shown).

To assess the potential of mammary carcinoma organoids to form tumors *in vivo*, we performed a limiting dilution experiment in which we injected 100–1,000,000 cells (as organoids) of the PARPi-naive KB1P4 organoid line (ORG-KB1P4N.1) in the mammary fat pad of wild-type mice. We observed consistent tumor development in animals transplanted with as few as 1,000 cells (Fig. 1A), demonstrating the high tumorigenic potential of these cells compared with conventional cell lines that require transplantation of 0.5–1 × $10^6$ cells [6]. Tumor latency of transplanted organoids correlated with the number of cells transplanted, suggesting that organoids undergo polyclonal expansion *in vivo* (Supplementary Table 1). The tumorigenic potential of KB1P(M) and KB2P organoids did not result from *in vitro* transformation, as organoids isolated from healthy mammary tissue (Supplementary Fig. 1B) did not give rise to mammary tumors following transplantation (Supplementary Table 1), despite the fact that normal mammary organoids and tumor organoids showed similar proliferation rates *in vitro* (Supplementary Fig. 1C).

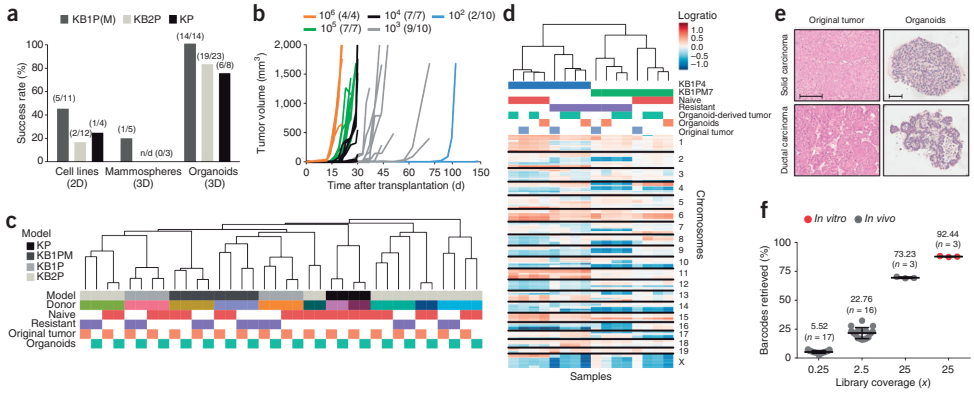



**FIGURE 1 | Generation and characterization of mouse mammary tumor organoids.** *(A)* Success rates for establishing 2D and 3D *in vitro* models from the indicated mammary tumors. Values in brackets indicate the number of donor tumors from which models were successfully derived versus the total number of donor tumors. n.d., no data. *(B)* Tumorigenic potential of organoids *in vivo*. Animals were transplanted with $10^2$–$10^6$ organoid cells and tumor growth was monitored. Values in brackets indicate the number of tumors obtained versus the total number of mammary fat pads injected. *(C)* Unsupervised hierarchical clustering based on DNA copy number profiles of a panel of 18 organoid lines and their respective original GEMM tumors (correlation distance, average linkage). Tested models and individual donors are represented by different colors (Supplementary Fig. 3A). *(D)* Unsupervised hierarchical clustering based on DNA copy number profiles of a representative panel of four original KB1P(M) tumors, organoids and organoid-derived tumors (correlation distance, complete linkage). *(E)* Tumor-derived organoids preserve the morphology of the donor tumor. Scale bars represent 100 µm. *(F)* Quantification of barcodes retrieved from ORG-KB1PM7N.1 organoid cells transduced with a lentiviral library of 20,000 barcodes (*in vitro* sample) and tumors obtained following organoid transplantation (*in vivo* samples). The fraction of barcodes retrieved by genomic sequencing is represented as a function of the theoretical library coverage. The average library fraction retrieved is indicated. *in vitro*: *n* represents the number of replicates (samples); *in vivo*: *n* represents the number of tumors.

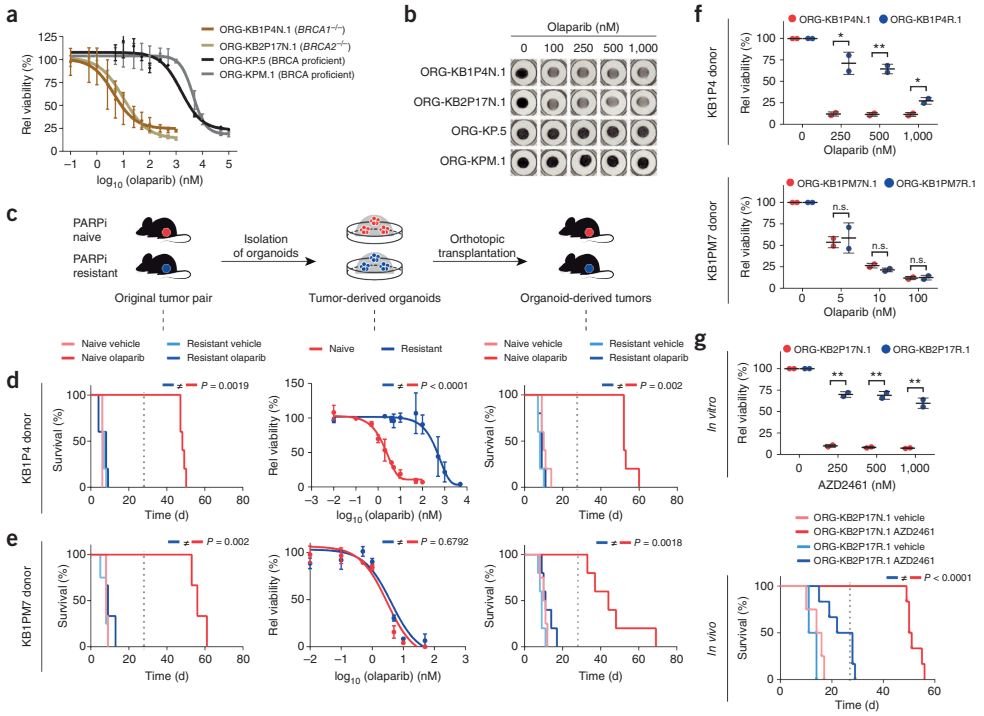



**FIGURE 2 | Comparison of PARPi response of original GEMM tumors, tumor-derived organoids and organoid-derived tumors.** *(A-B) In vitro* responses of BRCA-deficient and BRCA-proficient organoids to the PARP inhibitor olaparib. Quantification *A* and representative images of stained wells *B* are shown. Data represent two independent experiments. *(C)* General outline. *(D-E) In vivo* and *in vitro* PARPi response of models derived from KB1P4 *D* and KB1PM7 *E* donor tumors. Left, Kaplan–Meier curves showing the survival of mice bearing the original tumors treated with either vehicle or Olaparib for 28 consecutive days (KB1P4 donor: *n* = 2 for naive vehicle, *n* = 5 for other treatment groups; KB1PM7 donor: *n* = 4 for resistant vehicle, *n* = 3 for other treatment groups). End of treatment is indicated by a dotted grid line. *P* values were calculated by log-rank test (Mantel–Cox). Middle, *in vitro* olaparib response of ORG-KB1P4N.1/R.1 and ORG-KB1PM7N.1/R.1 organoids, as determined by a viability assay. Data are presented as mean ± s.d. for two independent replicates; value was calculated with extra sum-square F test. Right, Kaplan–Meier curves showing survival of mice transplanted with the same organoids (*n* = 5 per treatment group) (Supplementary Fig. 6). *(F) In vitro* PARPi toxicity in ORG-KB1P4N.1/R.1 (top) and ORG-KB1PM7N.1/R.1 (bottom) organoids as determined using a long-term clonogenic assay. Data are presented as the mean ± s.d. of two independent experiments. **P* < 0.01, ***P* < 0.001 (*t* test); n.s., not significant. *(G) In vitro* and *in vivo* responses of organoids derived from KB2P17 donor tumors to the PARPi AZD2461. Top, long-term clonogenic assay, data represented and analyzed as in *F*. Bottom, Kaplan–Meier survival curves, *P* value – log-rank Mantel–Cox test. Treatment of mice and survival analysis was carried out as described above (*n* = 4 for vehicle, *n* = 6 for AZD2461).

We next performed genetic and histological characterization of KB1P(M)/KB2P organoids and the corresponding tumor outgrowths to determine whether they retained the essential features of the parental GEMM tumors. As expected, deletions of *Brca1*, *Brca2*, *p53* and *Mdr1a* were conserved in both organoids and organoid-derived tumors, as confirmed by genotyping PCR (Supplementary Fig. 2). Given that BRCA-deficiency is strongly associated with high genomic instability [14], we generated DNA

copy number profiles for a panel of 18 organoid lines and their respective original tumors. Unsupervised hierarchical clustering revealed a high similarity between the patterns of genetic aberrations of organoids and their original donors (Fig. 1C and Supplementary Fig. 3A). As expected, BRCA-proficient KP tumors and organoid lines carried a substantially lower number of genetic aberrations than those lacking BRCA1 or BRCA2 function [15]. Moreover, the resemblance to the parental tumor was higher for organoids than for the 2D cell lines isolated from the same tumor (Supplementary Fig. 3B). We extended this analysis to organoid-derived tumors and observed that the genetic fingerprint of the organoids was maintained following transplantation (Fig. 1D). In addition, the epithelial phenotype that characterizes the KB1P(M) and KB2P tumor models was preserved following transplantation, as determined by morphology and immunohistochemistry (Fig. 1E and Supplementary Fig. 4).

To examine the cellular fitness of organoids *in vivo* and the clonal evolution of organoid-derived tumors, we barcoded individual cells in organoids by lentiviral transduction. Using transduction with a GFP-encoding lentivirus, we found that a multiplicity of infection (MOI, the number of viral particles per cell) of 1 resulted in about 30% of cells expressing GFP (Supplementary Fig. 5). This value increased to 68% when we applied an MOI of 5. We introduced a lentiviral library of 20,000 barcodes in the PARPi-naive KB1PM7 organoid line (ORG-KB1PM7N.1) at an MOI of 1. After puromycin selection, the barcoded organoids were transplanted into syngeneic wild-type mice at different cell numbers, corresponding to a theoretical library coverage of 0.25 to 25 (number of cells = theoretical coverage × library complexity). After outgrowth of the tumors, we purified and amplified the barcode-containing DNA. Using massive parallel sequencing, we quantified the barcodes to determine the fraction of the library present in the tumor cell population (Fig. 1F). After puromycin selection and before transplantation, an average of 92% of the barcodes could be retrieved from the organoid culture at a coverage of 25x. In the tumors that grew out, we still found 73% of the barcodes, indicating that a substantial fraction of the barcodes was preserved. At a coverage of 2.5x and 0.25x, this value decreased to approximately 23% and 6%, respectively. Taken together, these data suggest that GEMM-tumor-derived organoids exhibit high clonal heterogeneity *in vivo* and give rise to tumors that preserve the cellular complexity of the parental organoid population. We conclude that these models are suitable for studying the effects of intratumoral heterogeneity *in vivo* and are particularly compatible with *in vivo* screening approaches.

*Analysis of PARPi response in vivo and in vitro*

We determined the PARPi sensitivity of organoid cultures using a standard cytotoxicity assay. Consistent with the concept of synthetic lethal interaction between PARP1 inhibition and BRCA1 and BRCA2 deficiency [16], organoids derived from KB1P/KB2P tumors were more sensitive to treatment with the clinical PARP inhibitor olaparib

than homologous recombination (HR)-proficient KP(M) organoids (Fig. 2A-B). We next studied the *in vitro* and *in vivo* olaparib response of ORG-KB1P4N.1/R.1 and ORG-KB1PM7N.1/R.1 organoids, which were derived from two matched pairs of PARPi-naive and resistant tumors (Fig. 2C). For both KB1P4 and KB1PM7 donors, we found olaparib resistance to be stable following re-transplantation of the original tumor (Fig. 2D-E and Supplementary Fig. 6A-C). We examined the olaparib response in organoid lines *in vitro* and in parallel we transplanted the organoid lines orthotopically into wild-type animals and tested the olaparib response of the organoid-derived mammary tumors. Similar to the original KB1P4 olaparib-naive and olaparib-resistant tumors, ORG-KB1P4N.1 and its resistant derivative retained their differential sensitivities to PARPi treatment both *in vitro* and *in vivo* (Fig. 2D and Supplementary Fig. 6B). Tumors arising from ORG-KB1PM7N.1 and ORG-KB1PM7R.1 organoids also reproduced the respective olaparib-sensitive and olaparib-resistant phenotypes described for the donor tumors, demonstrating that organoid-derived tumors can recapitulate the PARPi response of the original tumors (Fig. 2E and Supplementary Fig. 6D). However, we did not observe a difference in olaparib sensitivity between ORG-KB1PM7N.1 and ORG-KB1PM7R.1 *in vitro* (Fig. 2E).

To investigate the long-term cytotoxic effects of PARPi treatment on organoid cultures, we performed an *in vitro* clonogenic assay. Although ORG-KB1P4N.1 and ORG-KB1P4R.1 exhibited significantly different olaparib responses, ORG-KB1PM7N.1 and ORG-KB1PM7R.1 failed to do so (Fig. 2F). In addition, we extended our analysis to ORG-KB2P17N.1/R.1 organoids derived from a matched pair of PARPi-naive and PARPi-resistant KB2P tumors that have been shown to preserve their drug response after re-transplantation [10]. Similar to KB1P4-derived organoids, following treatment with the PARPi AZD2461, ORG-KB2P17N.1/R.1 organoids recapitulated the PARPi-phenotype both *in vitro* and *in vivo* (Fig. 2G).

Given the low olaparib $IC_{50}$ of the ORG-KB1PM7R.1 organoid line, the data suggest that these organoids are sensitized to PARPi *in vitro*. To exclude a potential effect of the WNT and EGFR pathways, which are activated by the organoid culture medium, we examined the drug response of ORG-KB1PM7N.1/R.1 and ORG-KB1P4N.1/R.1 organoids cultured in medium depleted of the critical growth factors R-spondin 1, Noggin and EGF. The PARPi-resistance phenotype of both organoid pairs was unaffected by the growth-factor-depleted medium (Supplementary Fig. 7A-B). These results were confirmed in two additional organoid pairs, ORG-KB1PM7N.2/R.2, which was independently isolated from the original KB1PM7N/R tumors (thereby excluding a possible clonal artifact), and ORG-KB1PM7N.3/R.3, which were both isolated from the vehicle-treated tumors that arose from transplantation of ORG-KB1PM7N.1/R.1 and which faithfully recapitulated the phenotype of the original donor tumors (Supplementary Fig. 7C). These findings demonstrate that some mechanisms of PARPi resistance in KB1P(M), and possibly KB2P, tumors are not effectively recapitulated by *in vitro* viability assays with tumor-derived organoids.

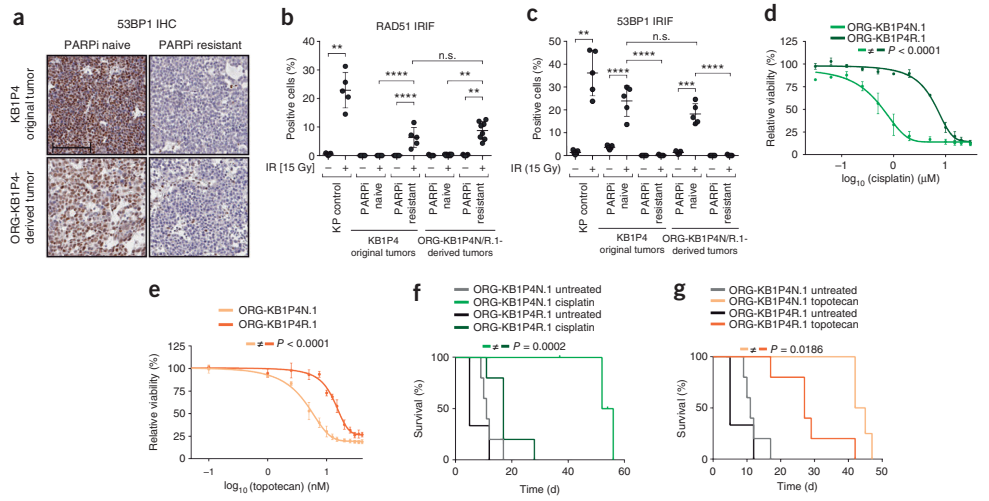



**FIGURE 3 | PARPi-resistant GEMM-derived cancer organoids preserve functional properties of the original tumors.** *(A)* Representative 53BP1 staining of the indicated tumors. Scale bar represents 100 μm. *(B) In situ* analysis of RAD51 IRIF formation in indicated tumors. KP tumor was used as a positive control. Cells with >5 nuclear foci were considered positive; each data point represents a single area of the tumor analyzed (>50 cells per area); ***P* < 0.001, ****P* < 0.0005, *****P* < 0.0001, *t* test. (**c**) 53BP1 IRIF formation assay, analyzed as described in *B*. *(D-E) In vitro* response of ORG-KB1P4N.1/R.1 organoids to cisplatin *D* and topotecan *E*. Data are presented as the mean ± s.d. of two independent repeats; *P* value, extra-sum square F test. *(F-G)* Overall survival (Kaplan–Meier curves) of mice transplanted with ORG-KB1P4N.1/R.1 organoids, untreated (ORG-KB1P4N.1/R.1, *n* = 5 and *n* = 3, respectively), or treated with cisplatin (ORG-KB1P4N.1/R.1, *n* = 5) *F* or topotecan (ORG-KB1P4N.1/R.1, *n* = 4 and *n* = 5, respectively) *G*. Cisplatin (6 mg/kg) was administered at days 0 and 14 and topotecan (4 mg/kg) was administered at days 0–4 and 14-18; *P* value, log-rank (Mantel–Cox) test.

### *Functional analysis of drug-resistance mechanisms*

The tumors from which the PARPi-resistant organoid lines ORG-KB1P4R.1 and ORG-KB1PM7R.1 are derived differ in their mechanism of resistance. As we established by RAD51/53BP1 ionizing-radiation-induced foci (IRIF) formation assays and we confirmed by immunohistochemistry (Fig. 3A-C and Supplementary Fig. 8A), PARPi resistance in the KB1P4R tumor is likely caused by loss of 53BP1 protein expression, a well-defined mechanism of HR restoration [6, 17, 18]. In contrast, we did not detect HR restoration in the olaparib-resistant KB1PM7R tumor (data not shown). Tumors derived from transplantation of ORG-KB1P4R.1 organoids also lack 53BP1 expression and maintain the capacity to form RAD51 IRIF, indicating that organoid-derived tumors preserve the mechanism of PARPi resistance of the donor tumors (Fig. 3A-C and Supplementary Fig. 8A).

We and others have previously shown that 53BP1 loss and consequent restoration of HR activity reduces the hypersensitivity of BRCA1-deficient cells to other DNA-damaging agents, such as cisplatin and topotecan [6]. We therefore examined the response of ORG-KB1P4N.1/R.1 organoids to these anticancer drugs, both *in vitro* and

*in vivo*. As expected, 53BP1-deficient ORG-KB1P4R.1 organoids were less sensitive to both agents (Fig. 3D-G and Supplementary Fig. 8B-C). Together, these data indicate that GEMM-derived mammary tumor organoid models can be employed to study the response to multiple cytotoxic drugs and establish cross-resistance profiles.

*Genome editing for in vivo analysis of drug response*

Finally, we explored the utility of GEMM-derived mammary tumor organoids for rapid *in vivo* validation of candidate mediators of drug resistance. We employed the CRISPR/Cas9 system, which has already been successfully used for genetic manipulation of organoids derived from mouse intestine and kidney [19-22]. As a proof-of-concept demonstration, we inactivated *Trp53bp1* in PARPi-naive BRCA1-deficient mouse mammary tumor organoids (ORG-KB1PM7N.1) and examined the response to olaparib treatment *in vivo*. We targeted the murine *Trp53bp1* locus in ORG-KB1PM7N.1 organoids by simultaneous co-transduction with lentiviruses expressing Cas9 and a doxycycline-regulated single guide RNA (sgRNA) against *Trp53bp1*. The frequencies of insertions

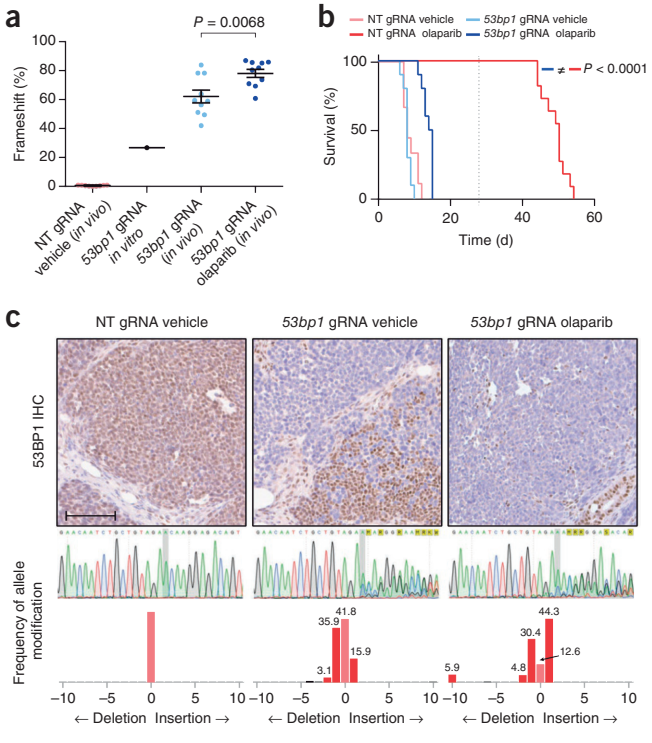



**FIGURE 4 | Mouse mammary cancer organoids for *in vivo* validation of PARPi resistance factors.** (*A*) Frequency of frameshift indels in *Trp53bp1* in manipulated organoids and organoid-derived tumors. *P* value was determined using the Student's *t* test. (*B*) Kaplan–Meier curves showing the survival of mice bearing tumors derived from ORG-KB1PM7N.1 organoids modified by CRISPR/Cas9 using a gRNA targeting *Trp53bp1* or a NT gRNA. Animals were treated with vehicle or olaparib for 28 consecutive days ($n$ = 10 per treatment group). End of treatment is indicated by a dotted grid line (Supplementary Fig. 9). *P* value was calculated by log-rank test (Mantel–Cox). (*C*) Immunohistochemistry analysis of 53BP1 expression in tumors derived from the indicated organoids. Representative 53BP1 staining of tumors from each treatment group are shown with corresponding allele modification frequencies indicating the predicted indel size (bottom). Scale bar represents 100 µm.

and deletions (indels) were measured using the tracking of indels by decomposition (TIDE) method [23]. This analysis was performed after 7 days of doxycycline induction and revealed an indel frequency of 31% in *Trp53bp1*-targeted cells (data not shown), with a high proportion (27%) of *Trp53bp1* alleles carrying frameshift disruptions (Fig. 4A). As expected, tumors derived from transplantation of *Trp53bp1*-targeted ORG-KB1PM7N.1 organoids exhibited a limited response to olaparib compared with the control tumors (derived from ORG-KB1PM7N.1 organoids transduced with a non-targeting (NT) guide RNA (gRNA), which were highly sensitive (Fig. 4B and Supplementary Fig. 9). Frameshift mutations in the *Trp53bp1* locus were strongly enriched in vehicle-treated tumors (Fig. 4A), indicating that a loss of 53BP1 expression produces a substantial selective advantage in KB1PM tumor cells, even in the absence of PARPi treatment. We observed a further enrichment in *Trp53bp1* frameshift mutations following olaparib treatment, and immunohistochemical analysis confirmed the depletion of 53BP1-positive tumor cells (Fig. 4C). These data are consistent with the known role of 53BP1 loss in PARPi resistance. Notably, these results demonstrate that GEMM-derived mammary tumor organoids can be efficiently modified by the
CRISPR/Cas9 system to target a gene of interest. Moreover, *in vivo* characterization of targeted organoids can be readily performed as a result of the short latency period and efficient tumor outgrowth.

## Discussion

We successfully combined our well-defined genetic mouse models of *BRCA1*- and *BRCA2*-mutated breast cancer with organoid culture technology. Preclinical models for BRCA1- and BRCA2-associated cancers have provided insight into mechanisms of drug resistance resulting from hypomorphic BRCA1 activity or genetic reversion of *BRCA1* and *BRCA2* genes (reviewed in [24]). Nevertheless, it is clear that restoration of BRCA1 and BRCA2 explains only some of the cases of therapy resistance in the clinic [25, 26]. The KB1P(M)/KB2P-derived mammary tumor organoids that we established here preserve the irreversible inactivation of BRCA1 and BRCA2 function. Thus, they are a powerful tool for studying and validating BRCA1- and BRCA2-independent mechanisms of anticancer drug resistance.

We previously generated unique and extensive panels of KB1P(M) and KB2P PARPi-resistant tumors with the potential to represent the tumor heterogeneity that is observed in human breast cancer [5, 6] (Gogola et al., unpublished data). Analyses of these tumor panels have elucidated previously unknown mechanisms of PARPi resistance, including increased ABCB1- and MDR1-mediated drug efflux and rewiring of the DNA repair machinery as a result of a loss of 53BP1 or REV7 and MAD2L2 [5-7]. Recent sequencing efforts of large panels of ovarian and breast cancers have shown that genetic alterations of ABCB1 and MDR1, 53BP1, and REV7 and MAD2L2 are indeed found in drug-resistant human tumors [26, 27]. In addition to their potential clinical

implications, studies using KB1P(M) and KB2P models also provide new insights into the basic mechanisms of DNA repair, as illustrated by a recent description of a previously unknown role for REV7 as a factor involved in NHEJ [8]. The study of organoids derived from these resistant tumors may be useful for identifying and targeting new vulnerabilities to overcome drug resistance.

As we demonstrated using CRISPR/Cas9-mediated inactivation of *Trp53bp1*, organoid lines derived from drug-naive tumors provide a rapid and straightforward model for testing candidate drug targets and therapy resistance genes. An increasing number of studies are employing high-throughput sequencing technologies to compile comprehensive descriptions of genetic aberrations in tumors. For example, whole-genome sequencing of 560 breast cancers identified a large number of somatic mutations in protein-coding cancer genes in tumors that show a mutational signature associated with BRCA1 or BRCA2 deficiency [15]. The effect of these somatic mutations on response to therapy could be systematically tested in our panel of KB1P(M) and KB2P tumor organoids.

As recently reviewed [28], 2D disease models have provided valuable knowledge on many cellular processes in cancer. However, clinical translation of drug candidates that show activity in 2D cancer cell lines has been poor, which is in part a result of the limitations of these *in vitro* models. GEMM-derived mammary tumor organoids retain critical characteristics of the original tumors and combine the ease of genetic manipulation with engraftment efficiency in syngeneic mice. These features render organoids especially suitable for genetic and pharmacologic screens *in vivo*.

Notably, in one case we found that organoids derived from a PARPi-resistant tumor displayed *in vitro* sensitivity to PARPi, whereas tumors derived from these organoids perfectly recapitulated the PARPi response observed in the original tumors *in vivo*. This finding points to the limitations of current 3D cancer organoids for studying drug resistance *in vitro* and highlights the need for additional studies to further improve 3D culture systems. The observed discrepancy between *in vitro* and *in vivo* responses to PARPi could be a result of a protective effect of the *in vivo* tumor microenvironment, which has been found to influence treatment response in breast cancer (reviewed in [29]). Thus, *in vivo* models remain important for studying therapy resistance. For this purpose, the generation of 3D cancer organoids and their genetic modification before orthotopic transplantation provides a unique tool for rapidly testing mechanisms of drug resistance *in vivo*.

## Materials and Methods

A detailed step-by-step protocol, including the primary *in vitro* procedures with mouse mammary tumor organoids, is available through Protocol Exchange [30].

*Establishment and maintenance of mammary tumor organoid lines*

Fresh or cryopreserved mammary tumor pieces were minced and digested in Advanced DMEM/F12 medium (AdDMEM/F12, Gibco) supplemented with 5% FBS (vol/vol, Gibco), 2 mg/ml collagenase type IV (Gibco), 2 mg/ml trypsin (Difco), 5 µg/ml gentamicin (Invitrogen) and 5 µg/ml insulin (Sigma) for 30 min at 37 °C with gentle shaking. After centrifugation at 1,500 rpm for 10 min, the collagenase solution was discarded and the pellet was washed in AdDMEM/F12. The suspension was pelleted again, resuspended in 20 U/ml DNase (Roche) solution in AdDMEM/F12 and mixed by vortexing for 5 min. The DNase solution was discarded after centrifugation as before and the pellet was resuspended in AdDMEM/F12. The suspension was passed through a 70-µm cell strainer (Falcon), and washed once in AdDMEM/F12. Organoids were separated from single cells through multiple brief centrifugations at 1,500 rpm. Organoids were embedded in Cultrex Reduced Growth Factor Basement Membrane Extract Type 2 (BME, Trevigen), seeded on 24-well suspension plates (Greiner Bio-One) and cultured in complete mouse mammary gland organoid media (AdDMEM/F12 supplemented with 1 M HEPES (Sigma), GlutaMAX (Invitrogen), penicillin/streptomycin (Gibco), B27 (Gibco), 125 µM N-acetyl-l-cysteine (Sigma), 50 ng/ml murine epidermal growth factor (EGF, Invitrogen), 10% Rspo1-conditioned medium (vol/vol, kindly provided by C. Kuo, Stanford University) and 10% Noggin-conditioned medium[12] (vol/vol)). Organoids from healthy mammary tissue were isolated in a similar manner and cultured as described previously [31], with modifications. Healthy organoids were cultured in AdDMEM/F12 supplemented with 1 M HEPES, GlutaMAX, penicillin/streptomycin, 1% insulin-transferrin-selenium (vol/vol, Gibco) and 2.5 nM FGF2 (Sigma). Removal of FGF2 or incubation with tumor organoid media did not support growth of healthy organoids (data not shown).

Passaging of organoids was performed either via mechanical disruption using a fire-polished glass Pasteur pipet or by dissociation with TrypLE (Gibco). Passaging was performed weekly in a 1:2–1:6 ratio. For long-term storage, organoid cultures were dissociated and mixed with Recovery Cell Culture Freezing Medium (Gibco) and frozen following the standard procedures. When required, the organoids were thawed using standard thawing procedures, embedded in BME and cultured as described above.

*Mice, generation of mammary tumors and orthotopic transplantations*

All animal experiments were approved by the Animal Ethics Committee of The Netherlands Cancer Institute and performed in accordance with the Dutch Act on Animal Experimentation (November 2014). KP(M), KB1P(M) and KB2P mouse mammary tumors were generated as previously described [1, 5-7, 10]. Briefly, KP, KPM, KB1P, KB1PM and KB2P mammary tumors were generated in *K14cre;p53*$^{F/F}$, *K14cre;p53*$^{F/F}$*; Mdr1a/b*$^{-/-}$, *K14cre;Brca1*$^{F/F}$*;p53*$^{F/F}$, *K14cre;Brca1*$^{F/F}$*;p53*$^{F/F}$*; Mdr1a/b*$^{-/-}$ and *K14cre;Brca2*$^{F/F}$*;p53*$^{F/F}$ female mice, respectively. To generate PARPi-resistant tumors, KB1P(M) and KB2P tumors

were genotyped and orthotopically transplanted in wild-type FVB/N and FVB/Ola129 F1 mice, respectively. Mammary tumor size was determined by caliper measurements (length and width in millimeters), and tumor volume (in $mm^3$) was calculated by using the following formula: 0.5 × length × $width^2$. Upon KB1P tumor outgrowth to approximately 200 $mm^3$ (100%), mice were treated with vehicle, AZD2461 (100 mg/kg orally) or olaparib (50 mg/kg intraperitoneally) for 28 consecutive days. KB1PM tumor-bearing mice were similarly treated with olaparib and KB2P tumor-bearing mice were treated with AZD2461. Mice with a relapsing tumor received another treatment cycle when the tumor was 100% of the original size at treatment start. Animals were sacrificed with $CO_2$ when the tumor reached a volume of 1,500 $mm^3$.

For the transplantation of organoid lines, organoids were used at a size corresponding to an average of 150–200 cells per organoid. Organoid suspensions containing a total of $10^4$ (KB1P(M)) or 5 × $10^4$ (KB2P) cells were injected in the fourth right mammary fat pad of wild-type FVB/N (KB1P(M)) or NMRI nude (KB2P) mice. CRISPR/Cas9-manipulated organoids were transplanted in NMRI nude mice to prevent an immune response against Cas9 protein [32, 33]. Organoids were transplanted in complete mouse media/BME mixture (1:1).

*Drugs and treatment of tumor-bearing mice*

Treatment of mice transplanted with tumor pieces was initiated when tumors reached a size of approximately 200 $mm^3$. In animals transplanted with organoids, treatment was initiated when tumors reached a size of 75 $mm^3$ due to the accelerated growth of these tumors. Olaparib (100 mg/kg intraperitoneally) or AZD2461 (100 mg/kg orally) was administered for 28 consecutive days. To assess cross-resistance, mice were given a single treatment regimen of topotecan (4 mg/kg intraperitoneally, days 0–4 and 14–18) or cisplatin (6 mg/kg intravenously, days 0 and 14). Control mice were dosed with vehicle only. Mammary tumor size was determined as described above. Animals were sacrificed with $CO_2$ when the tumor volume reached 1,500 $mm^3$, unless otherwise stated. In addition to sterile collection of multiple tumor pieces for grafting experiments (as described above), tumor samples were frozen in dry ice and fixed in 4% formaldehyde solution in PBS (wt/vol).

*Genotyping*

Genomic DNA extraction from tumor and organoid samples was performed according to the standard phenol:chloroform extraction protocol. Genotyping of *Brca1*$^F$, *Brca1*, *Brca2*$^F$, *Brca2*, *p53* and *Mdr1a/b*$^{-/-}$ alleles was performed as previously described[1,2,6]. The *p53*$^F$ allele was detected by PCR amplification with oligos Fwd-5'-GGGGAAGTTTCAAGCCTTCAT-3' and Rev-5'-TCTGAGAATCAGTTTATCCTCCCT-3', yielding products of 225 bp and 370 bp for the wild-type and *loxP*-flanked alleles, respectively.

The PCR reaction mix contained 100 ng of template DNA, 0.4 µM oligos and 5 µL MyTaq HS Red Mix (Bioline) in 10 µl total volume. Thermocycling conditions consisted of 30 s at 94 °C and 3 min at 60 °C.

*Immunohistochemistry*

Staining of E-cadherin, Vimentin, Keratin-14 and 53BP1 was performed on formalin-fixed paraffin-embedded (FFPE) tissue. Samples were boiled in Tris-EDTA pH 9.0 or citrate buffer pH 6.0 (53BP1) for antigen retrieval. Next, we used 3% $H_2O_2$ (vol/vol) in methanol to block endogenous peroxidase activity, and 10% milk (wt/vol, E-cadherin) or 4% BSA (wt/vol) plus 5% normal goat serum in PBS (vol/vol, Vimentin, 53BP1) as blocking buffer. Primary antibodies were diluted in 1.25% normal goat serum plus 1% BSA (wt/vol) in PBS. For detection and visualization, labeled polymer-HRP (horseradish peroxidase) anti-rabbit Envision (K4011, Dako), DAB (D5905, Sigma), $H_2O_2$ (A-31642, Sigma, 1:1,250) and hematoxylin counterstaining were applied. For staining, organoids were recovered from BME by washing with ice-cold PBS followed by centrifugation at 4 °C at 600 rpm for 5 min. After fixation in formalin, organoids were pelleted and embedded in 2% low-melting agarose (in PBS, Sigma). Staining was then performed as described above.

*RAD51 and 53BP1 IRIF formation assay*

For the analysis of RAD51 and 53BP1 IRIF, tumor pieces or organoids were transplanted into syngeneic mice. When tumors reached approximately 500 $mm^3$ in volume, the animals were either irradiated (15Gy) using a CT-guided high precision cone beam micro-irradiator (X-RAD 225Cx) or left untreated. 2 h after irradiation the tumors were taken out and fixed in 4% formalin. Immunofluorescent staining, foci visualization and analysis were carried out as described before [8]. A homologous recombination-proficient *K14cre;p53*$^{F/F}$ (KP) mammary tumor was used as positive control.

*Antibodies*

Primary antibodies: rabbit anti-E-cadherin (3195, Cell Signaling, 1:200); rabbit anti-Vimentin (5741, Cell Signaling, 1:200); rabbit anti-Keratin-14 (ab181595, Abcam, 1:6,000); rabbit anti-53BP1 (for immunohistochemistry, A300-272A, Bethyl Laboratories, 1:1,000; for immunofluorescence, ab21083, Abcam, 1:1,000); rabbit anti-RAD51 (kindly provided by R. Kanaar, Erasmus University Rotterdam).

*Generation of DNA copy number profiles and data analysis*

DNA copy number profiles were generated from whole exome sequencing (Fig. 1D and Supplementary Fig. 3B) or CNV-Seq data (Fig. 1C and Supplementary Fig. 3A). For

whole-exome sequencing, genomic DNA was sheared to approximately 300-bp fragments by sonication (Covaris S2), and 500–1,000 ng of sheared DNA was used as input for a six-cycle PCR to construct a fragmented library using the KAPA HTP Library Preparation Kit (Kapa). Exome enrichment was done using SureSelectXT2 Mouse All Exon kit (Agilent Technologies). The manufacturer's protocol (protocol G9630-90000) was followed except for the following steps: (1) the capture was diluted 1:1 and (2) six indexed samples were pooled before hybridization. Samples were sequenced on an Illumina HiSeq2500 (Illumina). DNA copy number profiles were generated from whole-exome sequencing data using CopyWriteR which uses off-target reads from the exome capture to estimate DNA copy number profiles [34]. DNA copy number profiles were generated using a bin size of 20,000 nucleotides. The $\log_2$-transformed read counts from CopyWriteR were used to cluster the samples using unsupervised hierarchical clustering (correlation distance, complete linkage). For visualization purposes, the heatmaps were drawn by down-sampling the original read counts to a bin size of 10,000,000 nucleotides; however, distances between samples were calculated using the original bin size of 20,000 nucleotides.

To perform CNV-Seq, the amount of double stranded DNA in the genomic DNA samples was quantified by using the Qubit dsDNA HS Assay Kit (Invitrogen, cat no Q32851). Up to 2,000 ng of double stranded genomic DNA were fragmented by Covaris shearing to obtain fragment sizes of 160–180 bp. Samples were purified using 1.8X Agencourt AMPure XP PCR Purification beads according to manufacturer's instructions (Beckman Coulter, cat no A63881). The sheared DNA samples were quantified and qualified on a BioAnalyzer system using the DNA7500 assay kit (Agilent Technologies cat no. 5067-1506). With a input of maximum 1 µg sheared DNA, library preparation for Illumina sequencing was performed using the KAPA HTP Library Preparation Kit (KAPA Biosystems, KK8234). During library enrichment 4–6 PCR cycles were used to obtain enough yield for sequencing. After library preparation, the libraries were cleaned up using 1× AMPure XP beads. All DNA libraries were analyzed on a BioAnalyzer system using the DNA7500 chips for determining the molarity. Up to 11 uniquely indexed samples were mixed together by equimolar pooling, in a final concentration of 10 nM, and subjected to sequencing on an Illlumina HiSeq2500 machine in one lane of a single-read 65-bp run, according to manufacturer's instructions. The resulting reads were aligned to the GRCm38 reference genome using BWA-MEM [35]. After the alignment, sample read counts were generated by counting aligned reads with a mapping quality ≥ 37 within 20-kb bins along the reference genome. These counts were then first corrected for GC bias using a nonlinear loess fit and second also corrected for mappability of the bins using a linear fit. Bins that overlapped regions blacklisted by Encode [36] or had a mappability below 0.2 were excluded from the final counts. Log ratios were determined by calculating the $\log_2$ ratio of each samples counts compared to a common reference count. This reference count was calculated using an in-silico simulated data set, in which simulated reads from the GRCm38 reference genome were

mapped and counted using the previously described approach and conditions. Finally, the samples were clustered by the $\log_2$ ratios using unsupervised hierarchical clustering (correlation distance, average linkage). For visualization purposes, the heatmaps were drawn by down-sampling the original read counts to a bin size of 10,000,000 nucleotides; however, distances between samples were calculated using the original bin size of 20,000 nucleotides.

*Cell viability assay*



For cell viability assays, organoids were dissociated into single cells as described above, and 50,000–100,000 cells were seeded per well in 40 µl complete mouse media/BME mixture on 24-well suspension plates and cultured for 7/14 (short/ long-term assay) days in the presence of a concentration range of olaparib, AZD2461, cisplatin or topotecan, as indicated. Cell viability was assessed by one of two methods: 1) using the resazurin-based Cell Titer Blue assay following manufacturer's protocol (Promega); or 2) via the ability of cellular oxidoreductase enzymes to reduce 3-(4,5-dimethylthiazol-2-yl)-2,5-diphenyltetrazolium bromide (MTT) to its insoluble, purple-colored formazan as previously described [37]. Briefly, MTT (Sigma) solution was added to the organoid culture to a final concentration of 500 mg/ml. After incubation for 2–3 h at 37 °C, the medium was discarded and 2% SDS (wt/vol, Biosolve) solution in PBS (Gibco) was added for 2 h to solubilize the BME matrix followed by addition of DMSO for 1 h to solubilize the reduced MTT. The OD was measured on a microplate absorbance reader (Tecan Infinite 200 PRO) at 562 nm. To assess cell proliferation, organoids were dissociated into single cells and seeded at 100,000 cells per well as described above; the Cell Titer Blue assay was performed at the indicated time points. All cell viability experiments were performed at least in duplicate and data were analyzed with GraphPad Prism statistical software using nonlinear regression and extra sum-of-squares F-test.

*Organoid transduction*

pLenti6-GFP (Invitrogen) was used as a transduction control. iKRUNC-Puro vector was created as described before [38], but instead of blasticidin resistance, a puro-mycin resistance ORF replaced the GFP ORF of FH1tUTG. The library of 20,000 barcodes was cloned into the iKRUNC-Puro vector (described elsewhere; Annunziato and Jonkers, unpublished data). The pGSC_Cas9_Neo vector was a kind gift from B. Evers (Netherlands Cancer Institute). For targeting of the murine *Tr53bp1* gene, the oligos Fwd-5'-CGAGGAACAATCTGCTGTAGAACA-3' and Rev-5'-AAACTGTTCTACAGCAGATTGTTC-3' were annealed and ligated to BfuAI-digested iKRUNC construct. The non-targeting gRNA was similarly cloned using the oligos Fwd-5'-CGAGTGATTGGGGGTCGTTCGCCA-3' and Rev-5'-AAACTGGCGAACGACCCCCAATCA-3'. All vectors were verified by Sanger sequencing and validated in KB1P tumor-derived cells (data not shown).

HEK293FT cells were used to generate cell-free viral supernatants. HEK293FT cells were cultured in IMDM (Sigma) supplemented with 10% FBS, 2 mM glutamine, and 50 U/ml penicillin/streptomycin. Lentiviral stocks, pseudotyped with the VSV-G envelope, were produced by transient co-transfection of four plasmids as previously described [39]. Viral titers were determined using qPCR Lentivirus Titration Kit (Applied Biological Materials).

For infection, organoids were incubated with TripLE at 37 °C for 10 min and then dissociated into single cells with a fire-polished glass pipette. Cells were pelleted at 1,200 rpm for 5 min, resuspended in virus suspension (in complete mouse media) and supplemented with 8 µg/ml Polybrene (Millipore). Viral transduction was performed by spinoculation as previously described [40]. For the barcode-labeled organoid experiment, the medium was refreshed twenty-four hours after infection and supplemented with 2 µg/ml puromycin (Gibco). For *Tr53bp1* knockout experiments, the medium was supplemented with 2 µg/ml puromycin and 500 µg/ml G418 (Gibco). Expression of sgRNAs was induced by treatment with 3 µg/ml doxycycline (Sigma) for 7 days.

*Tr53bp1 sequence analysis*

For validation of target modification, genomic DNA was isolated from tumor and organoid samples using Gentra Puregene (Qiagen) according to the manufacturer's recommendations. Following PCR amplification of *Tr53bp1* (Fwd-5'-TGAGAAATGGAGGCAACACCA-3' and Rev-5'-TGCAAATGTGGGCTACTGGG-3'), PCR products were sequenced (5'-CTCGATCTCACACTTCCGCC-3'). Allele modification frequencies were determined with the online Tracking of Indels by Decomposition (TIDE) software available at http://tide.nki.nl [23] using untransduced organoids as a reference sequence. The indel size ranges were set to 15 nucleotides upstream and downstream of the *Tr53bp1* target sequence.

*Library representation analysis*

To ensure single integration events following lentiviral transduction, the lentiviral titer was adjusted to yield 25% transduced cells (as determined by flow cytometry analysis following transduction with Lenti-GFP). Puromycin-resistant organoids were transplanted at different cell numbers per flank to achieve library coverage of 0.25*x*, 2.5*x* or 25*x* (cell number = library coverage × complexity). When tumors reached 1,000 $mm^3$ in volume, animals were sacrificed and whole tumors were snap frozen (dry ice). Following genomic DNA extraction (phenol:chloroform method), barcodes were retrieved by two rounds of PCR amplification using the following conditions: (1) 98 °C, 30 s, (2) 16 cycles of 98 °C for 10 s, 60 °C for 20 s and 72 °C for 1 min, (3) 72 °C, 5 min. Reaction mix consisted of 1.5 µl DMSO, 10 µl GC Phusion Buffer 5×, 1 µl 2 mM dNTPs,

0.25 µl 100 µM Fwd oligo, 0.25 µl 100 µM Rev oligo, 0.5µl Phusion polymerase in 50 µl total volume. As a template for PCR1, 12 µg of genomic DNA was used per sample (1 µg per reaction, 12 replicates per sample). Following PCR1 all replicates were pooled and 2.5µl was used as input for PCR2. Oligos used for PCR1: Fwd-5'-ACACTCTTTCCCTACACGACGCTCTTCCGATCTNNNNNNGGCTTTATATATCTTGTGGAAAGGACG-3', Rev-5'-GTGACTGGAGTTCAGACGTGTGCTCTTCCGATCTACTGACGGGCACCGGAGCCAATTCC-3' and PCR2: Fwd-5'-AATGATACGGCGACCACCGAGATCTACACTCTTTCCCTACACGACGCTCTTCCGATCT-3', Rev-5'-CAAGCAGAAGACGGCATACGAGATNNNNNNGTGACTGGAGTTCAGACGTGTGCTCTTCCGATCT-3'. NNNNNN represents one of the following six-nucleotide barcodes: CGTGAT, ACATCG, GCCTAA, TGGTCA, CACTGT, ATTGGC, GATCTG, TCAAGT, CTGATC, AAGCTA, GTAGCC, TACAAG, TTGACT, GGAACT, TGACAT, GGACGG, CTCTAC, GCGGAC, TTTCAC. Next, PCR2 products were purified using MinElute PCR Purification Kit (Qiagen) and sequenced (Illumina Sequencing 2500). Sequencing reads were aligned to the reference sequences using edgeR software (Bioconductor) [41].

*Statistics*

The following statistics were used for the indicated figures: Figures 2D,E,G (Kaplan-Meier curves), 3F,G and 4B, a log-rank Mantel-Cox test; Figures 2D,E and 3D,E and Supplementary Figure 7 (*in vitro* cytotoxic assays), nonlinear regression model was applied and *P* values were determined with extra sum-square F test; Figures 2F,G, 3B,C and 4A, a paired two-tailed *t*-test was used. All statistical analyses were performed with GraphPad Prism 6 software.

Statistics were calculated based on the following sample size: Figure 2D,E (left panel), KB1P4 donor: $n = 2$ for naive vehicle, $n = 5$ for other treatment groups, KB1PM7 donor: $n = 4$ for resistant vehicle, $n = 3$ for other treatment groups; Fig. 2D,E (right panel), ORG-KB1P4 and ORG-KB1PM7 donors: $n = 5$ per treatment group; Figure 2G (lower panel), ORG-KB2P17 donor: $n = 4$ for vehicle, $n = 6$ for AZD2461); Figure 3F,G, ORG-KB1P4 naive, $n = 5$ for vehicle, $n = 5$ for cisplatin and $n = 4$ for topotecan, ORG- KB1P4 resistant, $n = 3$ for vehicle, $n = 5$ for cisplatin and $n = 5$ for topotecan; Figure 4B, $n = 10$ per treatment group; Figures 2D,E (middle panel), 2F,G (upper panel), and 3D,E and Supplementary Figure 7, data are presented for two independent experiments (performed in duplicate).

*Life Sciences Reporting Summary*

Further information on experimental design is available in the Life Sciences Reporting Summary.

*Data availability*

The data that support the findings of this study not included as source data in this publication are available from the corresponding authors upon request. The deep sequencing data generated in this study are available in the European Nucleotide Archive (ENA) under accession number PRJEB22990 Source data for Figures 1–4 and Supplementary 1 and 7 are available online.

## Acknowledgements

We wish to thank the members of the Preclinical Intervention Unit of the Mouse Clinic for Cancer and Ageing (MCCA) at the Netherlands Cancer Institute (NKI), N. Domanitskaia, N. Gerhards, G. Lakner, O. Levionnois, N. Regenscheit and M. Siffert (Vetsuisse Bern) for their technical support with the animal experiments. We are grateful to B. Evers (NKI) for providing the iKRUNC-Puro vector, H. van der Gulden (NKI) for her assistance with the genotyping procedure, and the NKI animal facility, animal pathology facility, flow cytometry facility and genomics core facility for their excellent service. Financial support came from the Dutch Cancer Society (KWF 2011-5220 and 2014-6532 to S.R. and J.J.), the Netherlands Organization for Scientific Research (VICI 91814643, Cancer Genomics Netherlands and a National Roadmap grant for Large-Scale Research Facilities to J.J., VENI 916.15.182 to N.S.), the Netherlands Genomics Initiative Zenith (93512009 to J.J.), the Swiss National Science Foundation (310030_156869 to S.R.), the Swiss Cancer Research Foundation (MD-PhD-3446-01-2014 to S.B.) and the European Union (ERC CoG-681572 to S.R. and ERC synergy grant 319661 COMBATCANCER to J.J.).

## Author contributions

S.R., A.A.D. and E.G. conceived and designed the study. A.A.D., E.G. and N.S. developed and validated the mammary tumor organoid model with input from H.C. and help from J.M.H. For this purpose, they designed and conducted the experiments, and interpreted the results together with P.B., J.J. and S.R. M.B. and S.A. designed and performed the *in vivo* validation experiment using CRISPR/ Cas9-mediated targeting of 53BP1, analyzed the data and contributed to the figures. J.R.d.R. and A.V. carried out the bioinformatical analyses and provided the corresponding figures. S.B. and M.v.d.V. helped with animal studies. P.B., J.J. and S.R. supervised the project. A.A.D. and E.G. prepared the manuscript with input from all of the authors.

## Disclosure of Potential Conflicts of Interest

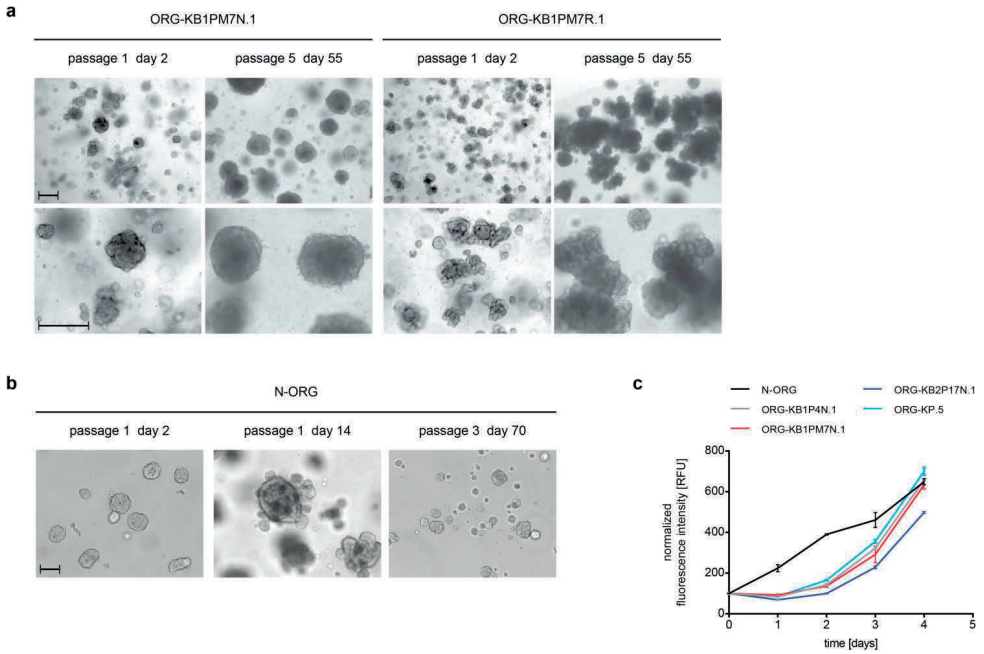
The authors declare that they have no competing financial interests.

## References

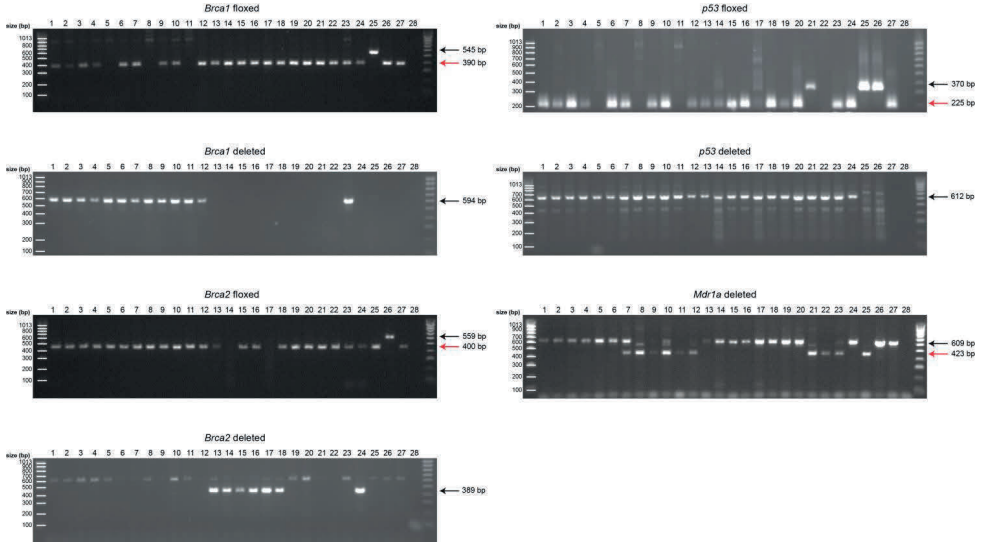

1. Jonkers J, Meuwissen R, van der Gulden H, Peterse H, van der Valk M, Berns A. Synergistic tumor suppressor activity of BRCA2 and p53 in a conditional mouse model for breast cancer. Nat Genet. 2001; 29: 418-25.
2. Liu X, Holstege H, van der Gulden H, Treur-Mulder M, Zevenhoven J, Velds A, et al. Somatic loss of BRCA1 and p53 in mice induces mammary tumors with features of human BRCA1-mutated basal-like breast cancer. Proc Natl Acad Sci U S A. 2007; 104: 12111-6.
3. Rottenberg S, Borst P. Drug resistance in the mouse cancer clinic. Drug Resist Updat. 2012; 15: 81-9.
4. Rottenberg S, Nygren AO, Pajic M, van Leeuwen FW, van der Heijden I, van de Wetering K, et al. Selective induction of chemotherapy resistance of mammary tumors in a conditional mouse model for hereditary breast cancer. Proc Natl Acad Sci U S A. 2007; 104: 12117-22.
5. Rottenberg S, Jaspers JE, Kersbergen A, van der Burg E, Nygren AO, Zander SA, et al. High sensitivity of BRCA1-deficient mammary tumors to the PARP inhibitor AZD2281 alone and in combination with platinum drugs. Proc Natl Acad Sci U S A. 2008; 105: 17079-84.
6. Jaspers JE, Kersbergen A, Boon U, Sol W, van Deemter L, Zander SA, et al. Loss of 53BP1 causes PARP inhibitor resistance in Brca1-mutated mouse mammary tumors. Cancer Discov. 2013; 3: 68-81.
7. Jaspers JE, Sol W, Kersbergen A, Schlicker A, Guyader C, Xu G, et al. BRCA2-deficient sarcomatoid mammary tumors exhibit multidrug resistance. Cancer research. 2015; 75: 732-41.
8. Xu G, Chapman JR, Brandsma I, Yuan J, Mistrik M, Bouwman P, et al. REV7 counteracts DNA double-strand break resection and affects PARP inhibition. Nature. 2015; 521: 541-4.
9. Tkáč J, Xu G, Adhikary H, Young JTF, Gallo D, Escribano-Díaz C, et al. HELB Is a Feedback Inhibitor of DNA End Resection. Mol Cell. 2016; 61: 405-18.
10. Ray Chaudhuri A, Callen E, Ding X, Gogola E, Duarte AA, Lee JE, et al. Replication fork stability confers chemoresistance in BRCA-deficient cells. Nature. 2016; 535: 382-7.
11. Evers B, Drost R, Schut E, de Bruin M, van der Burg E, Derksen PW, et al. Selective inhibition of BRCA2-deficient mammary tumor cell growth by AZD2281 and cisplatin. Clinical cancer research : an official journal of the American Association for Cancer Research. 2008; 14: 3916-25.
12. Sato T, Stange DE, Ferrante M, Vries RG, Van Es JH, Van den Brink S, et al. Long-term expansion of epithelial organoids from human colon, adenoma, adenocarcinoma, and Barrett's epithelium. Gastroenterology. 2011; 141: 1762-72.
13. Sato T, Vries RG, Snippert HJ, van de Wetering M, Barker N, Stange DE, et al. Single Lgr5 stem cells build crypt-villus structures in vitro without a mesenchymal niche. Nature. 2009; 459: 262-5.
14. Turner N, Tutt A, Ashworth A. Hallmarks of 'BRCAness' in sporadic cancers. Nat Rev Cancer. 2004; 4: 814-9.
15. Nik-Zainal S, Davies H, Staaf J, Ramakrishna M, Glodzik D, Zou X, et al. Landscape of somatic mutations in 560 breast cancer whole-genome sequences. Nature. 2016; 534: 47-54.
16. Ashworth A. A synthetic lethal therapeutic approach: poly(ADP) ribose polymerase inhibitors for the treatment of cancers deficient in DNA double-strand break repair. J Clin Oncol. 2008; 26: 3785-90.
17. Bouwman P, Aly A, Escandell JM, Pieterse M, Bartkova J, van der Gulden H, et al. 53BP1 loss rescues BRCA1 deficiency and is associated with triple-negative and BRCA-mutated breast cancers. Nat Struct Mol Biol. 2010; 17: 688-95.
18. Bunting SF, Callén E, Wong N, Chen HT, Polato F, Gunn A, et al. 53BP1 inhibits homologous recombination in Brca1-deficient cells by blocking resection of DNA breaks. Cell. 2010; 141: 243-54.
19. Schwank G, Koo BK, Sasselli V, Dekkers JF, Heo I, Demircan T, et al. Functional repair of CFTR by CRISPR/Cas9 in intestinal stem cell organoids of cystic fibrosis patients. Cell Stem Cell. 2013; 13: 653-8.
20. Matano M, Date S, Shimokawa M, Takano A, Fujii M, Ohta Y, et al. Modeling colorectal cancer using CRISPR-Cas9-mediated engineering of human intestinal organoids. Nat Med. 2015; 21: 256-62.
21. Drost J, van Jaarsveld RH, Ponsioen B, Zimberlin C, van Boxtel R, Buijs A, et al. Sequential cancer mutations in cultured human intestinal stem cells. Nature. 2015; 521: 43-7.
22. Freedman BS, Brooks CR, Lam AQ, Fu H, Morizane R, Agrawal V, et al. Modelling kidney disease with CRISPR-mutant kidney organoids derived from human pluripotent epiblast spheroids. Nat Commun. 2015; 6: 8715.

23. Brinkman EK, Chen T, Amendola M, van Steensel B. Easy quantitative assessment of genome editing by sequence trace decomposition. Nucleic Acids Res. 2014; 42: e168.
24. Annunziato S, Barazas M, Rottenberg S, Jonkers J. Genetic Dissection of Cancer Development, Therapy Response, and Resistance in Mouse Models of Breast Cancer. Cold Spring Harb Symp Quant Biol. 2016; 81: 141-50.
25. Ang JE, Gourley C, Powell CB, High H, Shapira-Frommer R, Castonguay V, et al. Efficacy of chemotherapy in BRCA1/2 mutation carrier ovarian cancer in the setting of PARP inhibitor resistance: a multi-institutional study. Clinical cancer research : an official journal of the American Association for Cancer Research. 2013; 19: 5485-93.
26. Patch AM, Christie EL, Etemadmoghadam D, Garsed DW, George J, Fereday S, et al. Whole-genome characterization of chemoresistant ovarian cancer. Nature. 2015; 521: 489-94.
27. Bruna A, Rueda OM, Greenwood W, Batra AS, Callari M, Batra RN, et al. A Biobank of Breast Cancer Explants with Preserved Intra-tumor Heterogeneity to Screen Anticancer Compounds. Cell. 2016; 167: 260-74.e22.
28. Horvath P, Aulner N, Bickle M, Davies AM, Nery ED, Ebner D, et al. Screening out irrelevant cell-based models of disease. Nat Rev Drug Discov. 2016; 15: 751-69.
29. McMillin DW, Negri JM, Mitsiades CS. The role of tumour-stromal interactions in modifying drug response: challenges and opportunities. Nat Rev Drug Discov. 2013; 12: 217-28.
30. Duarte AA, Gogola E, Sachs N, Barazas M, Annunziato S, J RdR, et al. BRCA-deficient mouse mammary tumor organoids to study cancer-drug resistance. Nat Methods. 2018; 15: 134-40.
31. Ewald AJ, Brenot A, Duong M, Chan BS, Werb Z. Collective epithelial migration and cell rearrangements drive mammary branching morphogenesis. Dev Cell. 2008; 14: 570-81.
32. Annunziato S, Kas SM, Nethe M, Yücel H, Del Bravo J, Pritchard C, et al. Modeling invasive lobular breast carcinoma by CRISPR/Cas9-mediated somatic genome editing of the mammary gland. Genes Dev. 2016; 30: 1470-80.
33. Wang D, Mou H, Li S, Li Y, Hough S, Tran K, et al. Adenovirus-Mediated Somatic Genome Editing of Pten by CRISPR/Cas9 in Mouse Liver in Spite of Cas9-Specific Immune Responses. Hum Gene Ther. 2015; 26: 432-42.
34. Kuilman T, Velds A, Kemper K, Ranzani M, Bombardelli L, Hoogstraat M, et al. CopywriteR: DNA copy number detection from off-target sequence data. Genome Biology. 2015; 16: 49.
35. Li HW. Aligning sequence reads, clone sequences and assembly contigs with BWA-MEM. arXiv: Genomics. 2013.
36. An integrated encyclopedia of DNA elements in the human genome. Nature. 2012; 489: 57-74.
37. Grabinger T, Luks L, Kostadinova F, Zimberlin C, Medema JP, Leist M, et al. Ex vivo culture of intestinal crypt organoids as a model system for assessing cell death induction in intestinal epithelial cells and enteropathy. Cell Death & Disease. 2014; 5: e1228-e.
38. Prahallad A, Heynen GJ, Germano G, Willems SM, Evers B, Vecchione L, et al. PTPN11 Is a Central Node in Intrinsic and Acquired Resistance to Targeted Cancer Drugs. Cell Rep. 2015; 12: 1978-85.
39. Follenzi A, Ailles LE, Bakovic S, Geuna M, Naldini L. Gene transfer by lentiviral vectors is limited by nuclear translocation and rescued by HIV-1 pol sequences. Nat Genet. 2000; 25: 217-22.
40. Koo BK, Stange DE, Sato T, Karthaus W, Farin HF, Huch M, et al. Controlled gene expression in primary Lgr5 organoid cultures. Nat Methods. 2011; 9: 81-3.
41. Robinson MD, McCarthy DJ, Smyth GK. edgeR: a Bioconductor package for differential expression analysis of digital gene expression data. Bioinformatics. 2010; 26: 139-40.

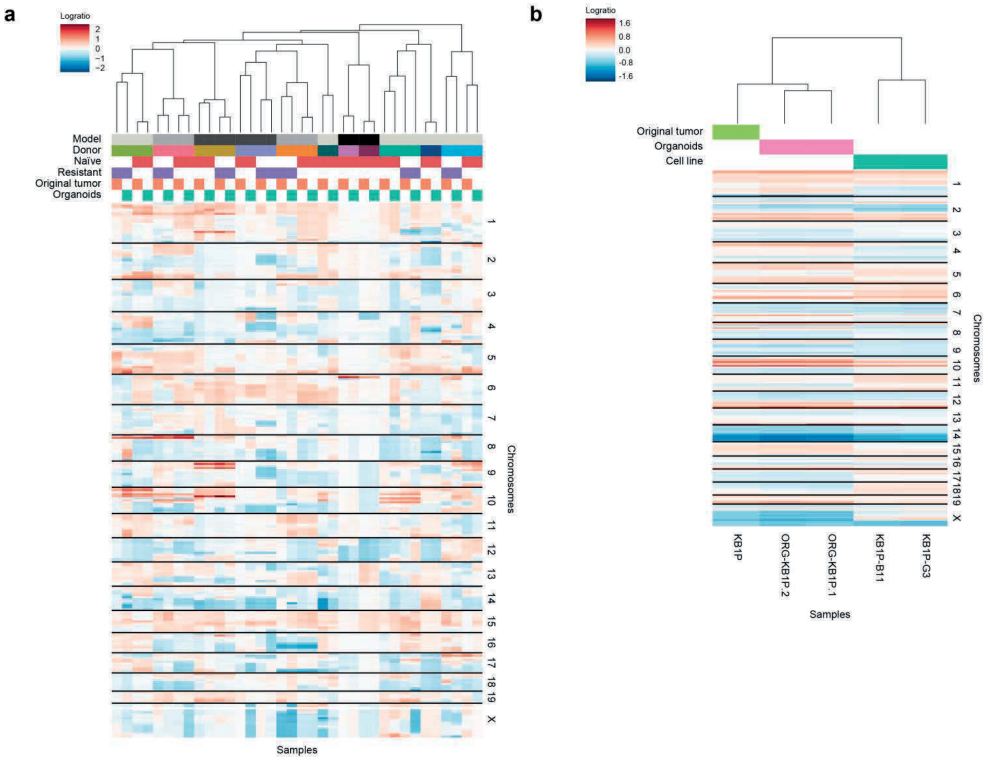
## Supplementary Figures and Table



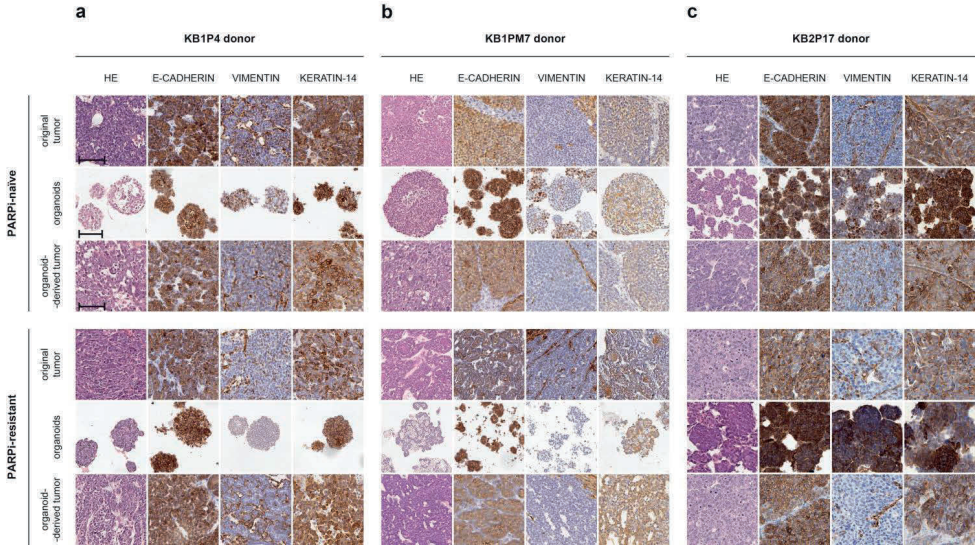

**SUPPLEMENTARY FIGURE 1 | Comparison of mouse mammary organoids derived from malignant and healthy tissues.** *(A)* Brightfield images of ORG-KB1PM7N.1/R.1 organoid cultures embedded in Basement Membrane Extract 2 days (passage 1) and 55 days (passage 5) following isolation. Scale bar, 100 µm. *(B)* Brightfield images of *in vitro* cultures of organoids derived from healthy mammary tissue (N-ORG) at the indicated time points. Scale bar, 100 µm. *(C) In vitro* proliferation of tumor (ORG-KP.5, ORG- KB1P4N.1, ORG-KB1PM7N.1 and KB2P17N.1) and healthy (N-ORG) mammary organoids, as determined by a cell viability assay.



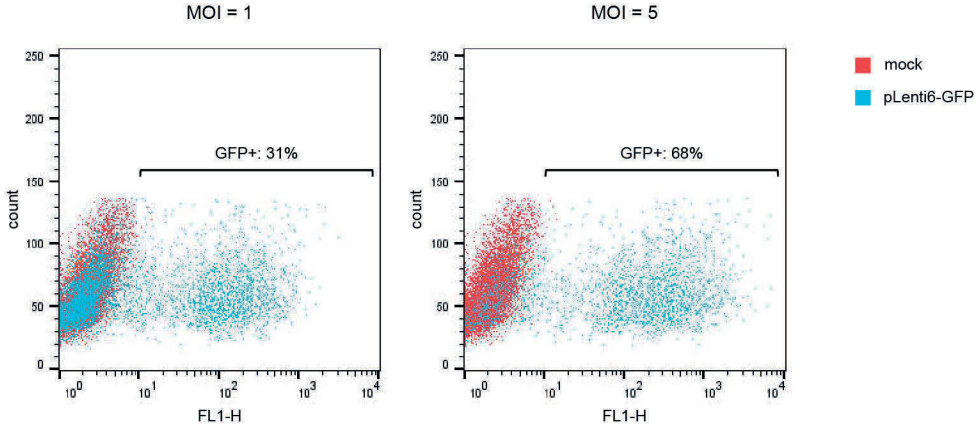

**SUPPLEMENTARY FIGURE 2 | Genetic characterization of mouse mammary tumor organoids**. Genotyping PCR of genomic DNA from KB1PM7, KB1P4, KB2P17, KP.5 and KPM.1 GEMM tumors, tumor-derived organoids and organoid-derived tumors. Wild-type bands are indicated by red arrows and floxed or deletion bands are indicated by black arrows. Wild- type bands indicate the presence of stromal cells from the syngeneic wild-type mice in which tumors were transplanted. Spleen DNA from KB1PM or KB2P mice was used as a positive control for the floxed PCR products and liver DNA from a wildtype animal was used as a positive control for the wild-type PCR products. Sample annotations: (1) KB1P4 naïve original tumor, (2) ORG-KB1P4N.1, (3) ORG-KB1P4N.1-derived tumor, (4) KB1P4 PARPi-resistant original tumor, (5) ORG-KB1P4R.1, (6) ORG-KB1P4R.1-derived tumor, (7) KB1PM7 PARPi-naïve original tumor, (8) ORG-KB1PM7N.1, (9) ORG-KB1PM7N.1-derived tumor, (10) KB1PM7 PARPi-resistant original tumor, (11) ORG-KB1PM7R.1, (12) ORG-KB1PM7R.1-derived tumor, (13) KB2P17 PARPi-naïve original tumor, (14) ORG-KB2P17N.1, (15) ORG-KB2P17N.1-derived tumor, (16) KB2P17 PARPi-resistant original tumor, (17) ORG-KB2P17R.1, (18) ORG-KB2P17R.1-derived tumor, (19) KP.5 original tumor, (20) ORG-KP.5, (21) KPM.1 original spontaneous tumor, (22) ORG-KPM.1, (23) KB1PM tumor (positive control), (24) KB2P tumor (positive control), (25) KB1PM spleen (floxed control), (26) KB2P spleen (floxed control), (27) wild-type liver (wild-type control), (28) negative control (no DNA input).



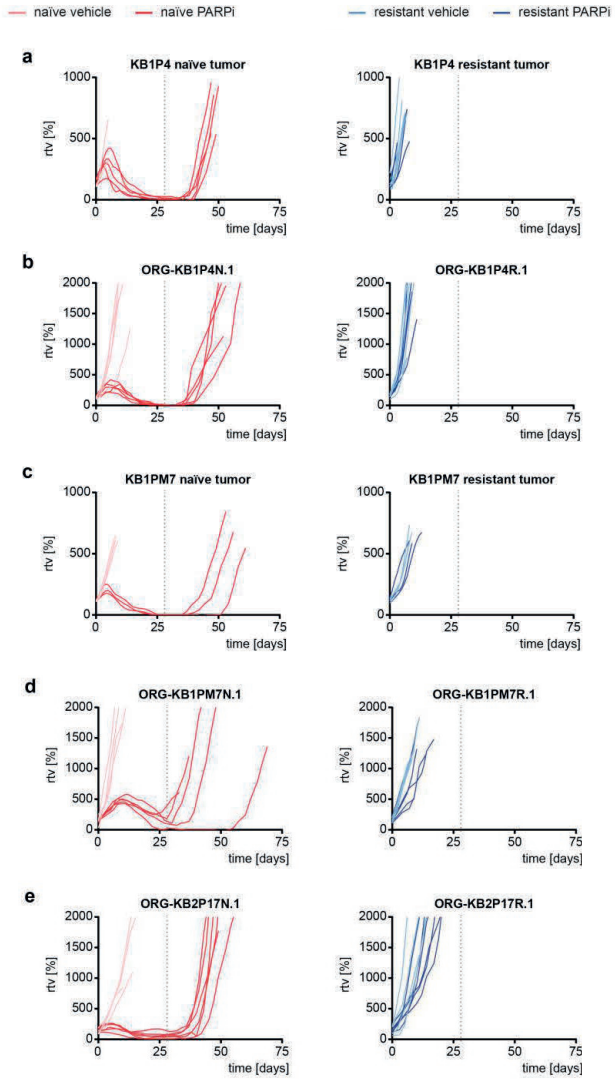

**SUPPLEMENTARY FIGURE 3 | Genetic characterization of mouse mammary tumor organoids by DNA copy number profiling.** *(A)* Unsupervised hierarchical clustering of a panel of 18 organoid lines and respective original GEMM tumors (extended version of Fig. 1C). *(B)* Unsupervised hierarchical clustering of original GEMM tumor (KB1P), two organoid lines (ORG-KB1P.1, ORG-KB1P.2) and two cell lines derived from the same tumor (independent clones, KB1P-B11 and KB1P-G3, previously described[8]; correlation distance, complete linkage).



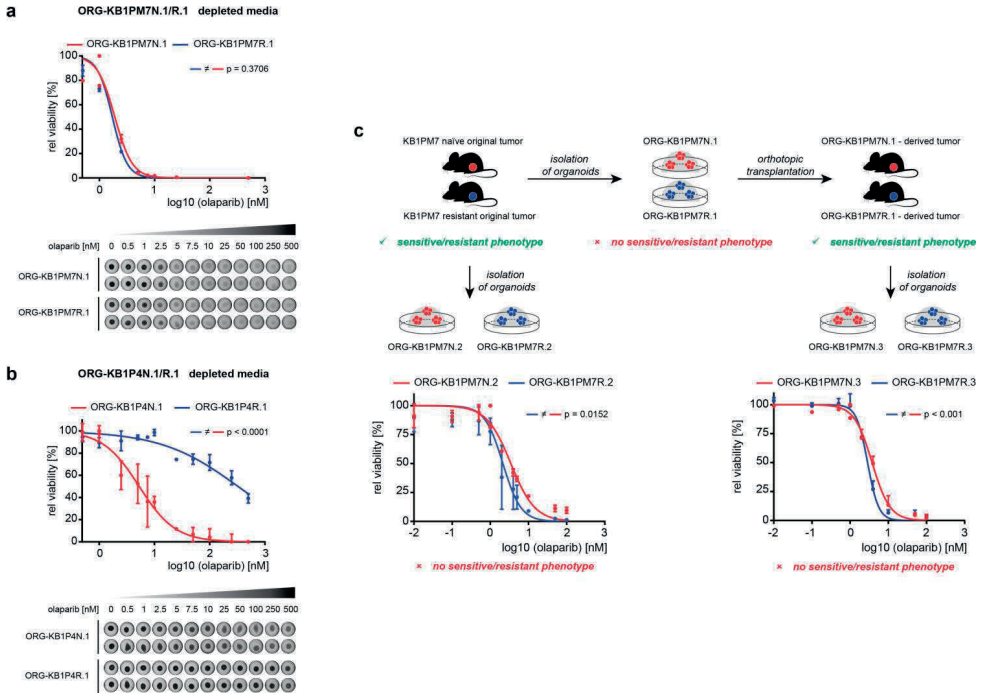

**SUPPLEMENTARY FIGURE 4 | Histological characterization of KB1P(M)/KB2P mammary tumor organoids.** *(A-C)* Representative images of hematoxylin & eosin (HE) stainings and immunohistochemical analyses of E-cadherin, Vimentin and Keratin-14 expression in KB1P4 *A*, KB1PM7 *B* and KB2P17 *C* GEMM tumors, tumor-derived organoids and organoid-derived tumors. Scale bar, 100 μm.



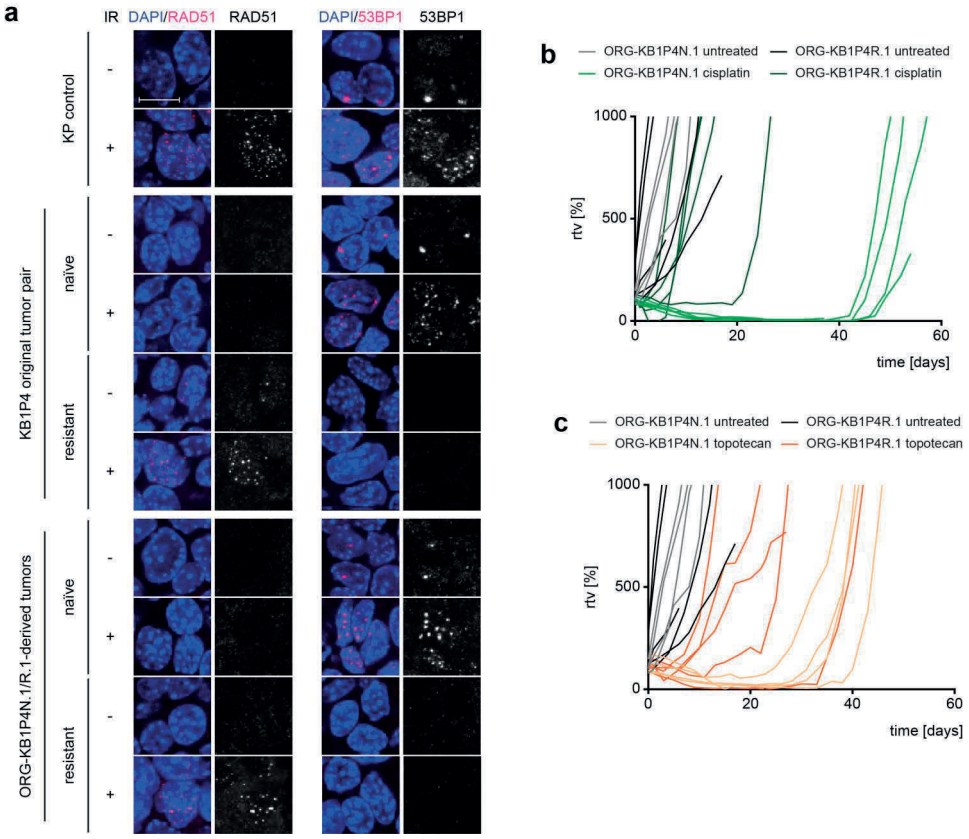

**SUPPLEMENTARY FIGURE 5 | Lentiviral transduction of KB1P mammary tumor organoids.** Green fluorescent protein (GFP) was introduced into ORG-KB1P4N.1 organoids by lentiviral transduction using pLenti6-GFP at the indicated theoretical multiplicities of infection (MOI). GFP expression was analyzed by flow cytometry 3 days after transduction.



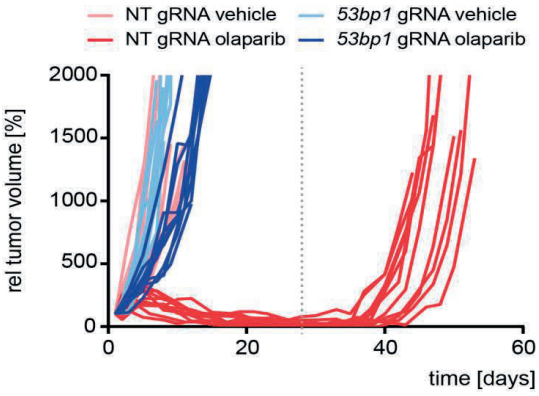

**SUPPLEMENTARY FIGURE 6 | Response of KB1P(M) and KB2P tumors to PARPi treatment.** (*A-E*) Mice orthotopically transplanted with olaparib-naïve or –resistant KB1P4 tumors (*n* = 2 naïve vehicle, *n* = 5 for other treatment groups) *A*, ORG-KB1P4N.1/R.1 organoids (*n* = 5) *B*, olaparib-naïve or –resistant KB1PM7 tumors (*n* = 4 resistant vehicle, *n* = 3 for other treatment groups) *C*, ORG-KB1PM7N.1/R.1 organoids (*n* = 5) *D* or AZD2461-naïve or –resistant ORG-KB2P17N.1/R.1 organoids (*n* = 4 for vehicle, *n* = 6 for AZD2461) *E* were treated with either vehicle *A-E*, olaparib *A-D* or AZD2461 *E* for 28 consecutive days. End of treatment is indicated by a dotted grid line. Graphs show relative tumor volume (ratio of tumor volume to initial size at start of treatment) as a function of time (see also Fig. 2).




**SUPPLEMENTARY FIGURE 7 | Comparison of *in vitro* PARPi response of GEMM tumor-derived organoids.** *(A-B) In vitro* response of ORG-KB1PM7N.1/R.1 *A* and ORG-KB1P4N.1/R.1 *B* organoids cultured in media depleted of R-spondin 1, Noggin and EGF as determined by a viability assay. Representative stainings of organoids are shown in duplicate. *P* values were determined by a non-linear regression model and extra sum-square F-test. *(C) In vitro* response of ORG-KB1PM7N.2/R.2 organoids, independently isolated from the original KB1PM7N/R tumors, and ORG-KB1PM7N.3/R.3 organoids, isolated from the vehicle-treated tumors that originated from transplantation of ORG-KB1PM7N.1/R.1 organoids. *P* values were determined as described for *A-B*. Data are presented as mean ± SD for at least 2 independent replicates.




**SUPPLEMENTARY FIGURE 8 | ORG-KB1P4R.1-derived tumors preserve PARPi resistance mechanism of the original tumor.** *(A)* RAD51 and 53BP1 ionizing radiation-induced foci (IRIF) formation in original KB1P4 olaparib-naïve and -resistant tumors and ORG-KB1P4N.1/R.1-derived tumors 2 hours after irradiation with 15 Gy (IR). A KP tumor was used as a positive control for RAD51 foci formation. Representative microscopic images are shown. Scale bar, 10 μm. See Fig. 3B-C for quantification. *(B-C) In vivo* response of tumors derived from ORG-KB1P4N.1/R.1 to cisplatin (*B*; *n* = 5 naïve vehicle, *n* = 3 resistant vehicle, *n* = 5 naïve/resistant cisplatin) and topotecan (*C*; *n* = 5 naïve vehicle, *n* = 3 resistant vehicle, *n* = 4 naïve topotecan, *n* = 5 resistant topotecan). Data presented as relative tumor volume over time.




**SUPPLEMENTARY FIGURE 9 | Response of genetically modified organoid-derived mammary tumors to olaparib treatment.** Mice bearing tumors derived from ORG-KB1PM7N.1 organoids modified *in vitro* by CRISPR/Cas9 using a gRNA targeting *Trp53bp1* (*Trp53bp1* gRNA) or a non-targeting gRNA (NT gRNA). Animals were treated with either vehicle or olaparib for 28 consecutive days ($n$ = 10 per treatment group). End of treatment is indicated by a dotted grid line. Graphs show relative tumor volume (ratio of tumor volume to initial size at start of treatment) as a function of time. See also Fig. 4.

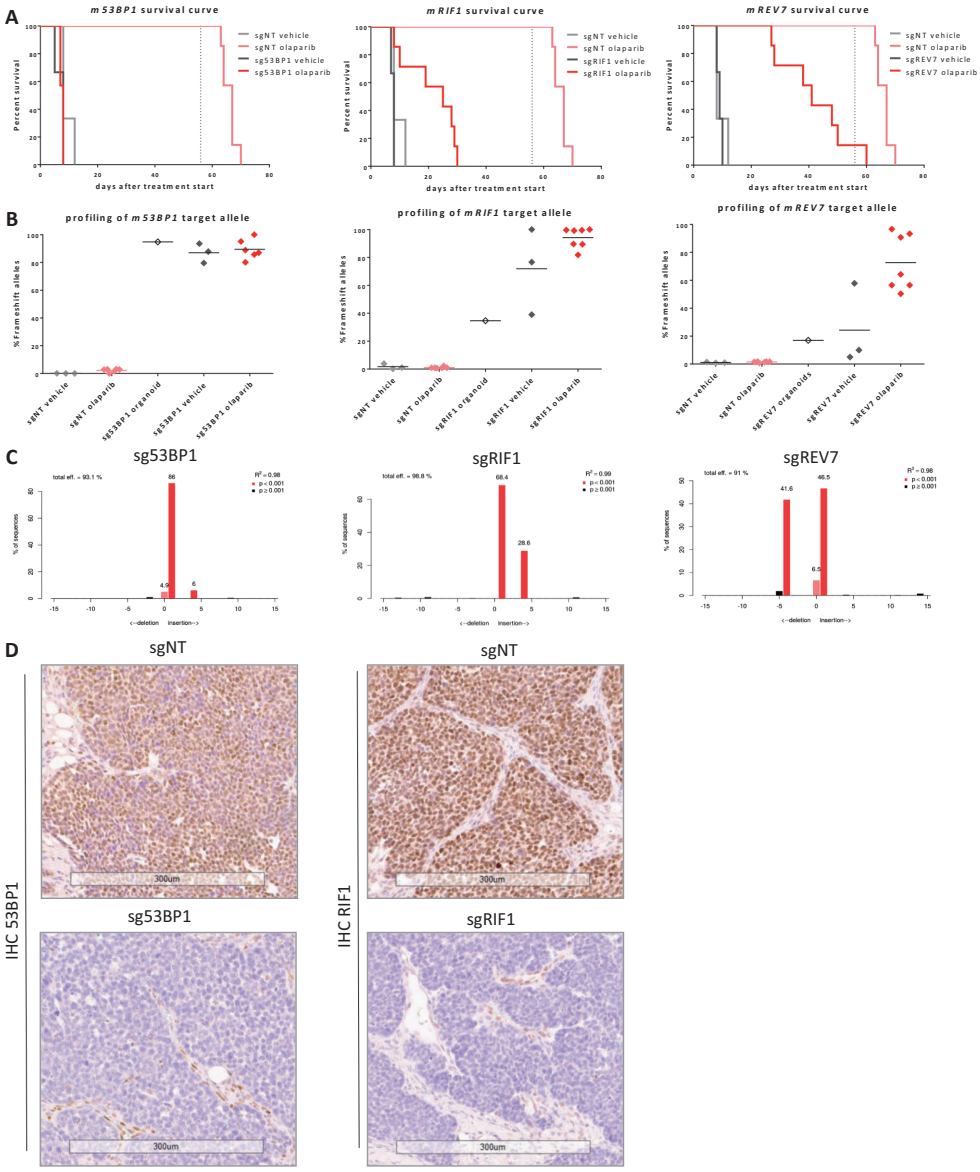


**SUPPLEMENTARY TABLE 1 | Overview of tumor outgrowth following transplantation of tumor (ORG-KB1P4N.1) and healthy tissue-derived (N-ORG) organoids at the indicated cell numbers** (see also Fig. 1b). Outgrowth rate: values in brackets indicate the number of tumors obtained *vs.* total number of mammary fat pads injected. Time until tumor volume = 75mm$^3$: mean ± SD. Tumor watch for N-ORG, 70 days.

| organoid line | number of cells transplanted | tumor outgrowth rate (flanks/tumors) [%] | time until tumor volume = 75mm³ [days] |
|---|---|---|---|
| ORG- KB-1P4N.1 | $10^6$ | 100 (4/4) | 10 ± 1 |
| | $10^5$ | 100 (7/7) | 16 ± 4 |
| | $10^4$ | 100 (7/7) | 25 ± 6 |
| | $10^3$ | 90 (9/10) | 39 ± 13 |
| | 102 | 20 (2/10) | n.d. |
| N-ORG | 105 | 0 (0/20) | n.d. |
| | 104 | 0 (0/14) | n.d. |

## Addendum

In this study, we present a proof-of-principle experiment to evaluate the effect of a known resistance factor, 53BP1, on PARPi-treatment response *in vivo.* Hereto, CRISPR/Cas9-mediated gene editing was combined with 3D organoid culture technology. We next used this versatile platform to evaluate two other known resistance factors in the 53BP1-pathway, RIF1 and REV7, side-by-side in an isogenic manner. Although the treatment duration has been prolonged to extend the evaluation window, this experiment confirmed that sgNT-targeted organoids remained responsive to continuous olaparib treatment for 56 consecutive days (median survival of 67 days) (Addendum Fig. 1A). In contrast, knock-out of 53BP1 or REV7 induced resistance to treatment with PARPi (median survival of 8 and 41 days, respectively; $P < 0.001$). Through this approach we also provide the first *in vivo* evidence for RIF1 as a driver of resistance to PARi (median survival of 25 days; $P < 0.001$). Profiling of the target allele in resistant tumors confirmed that resistant tumors were hallmarked by non-functional allelic variants (Addendum Fig. 1B-C). This tumor panel also provided sample material to establish an immunohistochemistry (IHC) protocol to stain endogenous mouse RIF1 protein on formalin-fixed and EAF-fixed material, allowing us to verify 53BP1 and RIF1 protein depletion in resistant tumors. Indeed, resistant sg53BP1- or sgRIF1-targeted tumors showed clear loss-of-53BP1- or RIF1 protein by IHC, respectively (Addendum Fig. 1D). An IHC protocol to stain for endogenous mouse REV7 protein could not be established. Subsequently, RIF1 IHC has been performed on a panel of KB1P(M) tumors with spontaneously acquired resistance to PARPi-treatment and observed that a subset of these tumors displayed loss-of-RIF1 expression (data not shown), suggesting that a subset of these tumors may have developed spontaneous PARPi resistance through inactivation of RIF1.




**ADDENDUM FIGURE 1 | isogenic *in vivo* evaluation of 53BP1-pathway factors on PARPi-response.** *(A)* Kaplan-Meier curves indicating the survival of mice bearing tumors targeted by the indicated sgRNA. Animals were treated with vehicle (n = 3) or olaparib (n = 7) for 56 consecutive days (indicated by the dashed line) and animals were sacrificed when tumors reached a size of ≥ 1500 $mm^3$. P-value was calculated using the log rank test (Mantel-Cox). *(B)* Frequency of frameshift indels in indicated tumors. *(C)* example of the allele distribution of a resistant tumor targeted by the indicated sgRNA. *(D)* Immunohistochemistry analysis of 53BP1 or RIF1 expression in resistant tumors targeted with the indicated sgRNA. Scale bar represents 300 µm.

## Abstract

53BP1 controls a specialized non-homologous end joining (NHEJ) pathway that is essential for adaptive immunity, yet oncogenic in BRCA1 mutant cancers. Intra-chromosomal DNA double-strand break (DSB) joining events during immunoglobulin class switch recombination (CSR) require 53BP1. However, in BRCA1 mutant cells, 53BP1 blocks homologous recombination (HR) and promotes toxic NHEJ, resulting in genomic instability. Here, we identify the protein dimerization hub-DYNLL1- as an organizer of multimeric 53BP1 complexes. DYNLL1 binding stimulates 53BP1 oligomerization, and promotes 53BP1's recruitment to, and interaction with, DSB-associated chromatin. Consequently, DYNLL1 regulates 53BP1-dependent NHEJ: CSR is compromised upon deletion of Dynll1 or its transcriptional regulator Asciz, or by mutation of DYNLL1 binding motifs in 53BP1; furthermore, Brca1 mutant cells and tumours are rendered resistant to poly-ADP ribose polymerase (PARP) inhibitor treatments upon deletion of Dynll1 or Asciz. Thus, our results reveal a mechanism that regulates 53BP1-dependent NHEJ and the therapeutic response of BRCA1-deficient cancers.

# Cancer Chess:

## The ASCIZ-DYNLL1 Axis

# Molecular Insights

## Promotes 53BP1 Dependent

# Into PARPi Resistance

## Non-Homologous End Joining

## And PARP Inhibitor Sensitivity

# Chapter 4

*Adapted from:*

*Jordan R Becker, Raquel Cuella-Martin*, **Marco Barazas***, Rui Liu*, Catarina Oliveira, et al.*

**Contributed equally*

*Nature Communications. 9(1):5406 (2018)*

## Introduction

To counteract the potentially carcinogenic effects of DNA damage and mutation, cells employ a complex network of DNA repair pathways [1]. DNA double-strand breaks (DSBs) are among the most toxic of genomic lesions. They arise from a variety of endogenous and exogenous sources, including ionizing radiation (IR) treatments, replication fork collapse, and as programmed intermediates of antigen receptor gene rearrangements during variable, diversity and joining (V(D)J) recombination and class-switch recombination (CSR) [2, 3]. DSBs are predominantly repaired by homologous recombination (HR) and non-homologous end joining (NHEJ) pathways. HR is an essential DNA repair pathway owing to its utility in the repair of DSBs encountered during the S/G2-phases of proliferating cell populations [4], and mutations affecting its fidelity are associated with tumourigenesis [1]. HR initiation involves the regulated nucleolytic resection of DSB termini in a 5'–3' direction, which is an important determinant of whether a given break is repaired by HR or NHEJ [5]. The resulting 3'-tailed ends are used to invade homologous sequences on the sister chromatid, which is used as a template for accurate repair. The availability of a sister chromatid in only replicated regions of the genome ensures that HR repair is largely restricted to S and G2 phase cells, while NHEJ predominates in G1 [2]. NHEJ instead involves the direct ligation of DSB ends, a mechanism utilized by developing and antigen-stimulated lymphocytes to generate programmed deletions during the diversification of antigen receptor genes. However, inappropriate activity of the NHEJ pathway is also known to promote genomic rearrangements and translocations associated with the onset of cancer. Activation of the appropriate pathway for a given DSB type, cellular context, or genomic locus is therefore crucial for the maintenance of genome stability and avoidance of deleterious errors or mutations [5].

TP53-binding protein 1 (53BP1) is a DSB responsive protein that mediates an important and specialised branch of the NHEJ pathway [6]. 53BP1 is rapidly recruited to DSB sites, where its interaction with modified nucleosomes in DSB-flanking chromatin functions to inhibit nucleolytic DNA end resection, favouring DNA joining by NHEJ. This involves binding to a combinatorial chromatin signature consisting of methylated histone H4 (H4K20me1/2) and ubiquitinated H2A (H2AK15Ub) within DSB-associated chromatin domains [7, 8] , and the recruitment of downstream effector proteins such as RIF1 (RAP1 interacting factor 1), whose binding to 53BP1 is required for efficient DNA end-protection and NHEJ [9-11]. RIF1-53BP1 complexes are essential for immunoglobulin (Ig) CSR, an NHEJ-driven deletional recombination reaction in activated B cells that mediates the replacement of excised default IgM-encoding constant (*C*) gene segments of the Ig heavy locus *(Igh)*, with downstream C segments of different class and function (e.g., IgG, IgE and IgA). Mice deficient in 53BP1 or RIF1 are immunodeficient owing to CSR failure [9, 12-14], defects that manifest as a result of the aberrant hyper-resection of *Igh* DSBs

that generate ssDNA intermediates non-amenable to NHEJ [9, 12, 15]. The 53BP1 pathway also plays an equivalent but pathological role in DNA end-joining at de-protected telomeres: telomeric DNA ends exposed upon disruption of the telomere capping complex Shelterin are predominantly repaired by 53BP1-dependent NHEJ, resulting in chromosome end fusions [16]. Accordingly, uncapped telomeric DNA ends are hyper-resected in *53bp1*- and *Rif1*-deficient cells, resulting in a near complete suppression of telomere end-joining [11, 17].

53BP1-dependent NHEJ is also problematic in *BRCA1*-deficient cancers, where it mediates chromosomal rearrangements that drive oncogenesis [18, 19]. In mice, germline *53bp1*-deletion suppresses the embryonic lethality and mammary tumourigenesis associated with homozygous *Brca1* loss-of-function mutations, a rescue explained by reactivation of HR [18]. Conversely, 53BP1 pathway-associated DSB repair activities underlie the synthetic lethal effect of poly-ADP ribose polymerase (PARP) inhibitor (PARPi) treatments in *BRCA1* mutation-associated cancers: genetic ablation of 53BP1 pathway components results in PARPi resistance in cellular and tumour models of *BRCA1*-deficiency [9, 20, 21].

Aside from DSB repair, distinct 53BP1 protein complexes regulate the activation of p53-dependent senescence programs triggered in response to p53-activating drug treatments and prolonged mitotic transit [22-25]. Here, 53BP1's C-terminal BRCT domains bridge p53's interaction with the deubiquitinating enzyme USP28, catalysing de-ubiquitination events that stimulate p53 binding to, and activation of, target gene promoters [22].

While mechanistically distinct, both NHEJ and p53-regulatory functions require 53BP1 multimerization [22, 26, 27] , a function thought to rely entirely on its oligomerization domain (OD; encoded within amino acid residues (a.a.) 1231–1277) [28]. NHEJ-deficits have been attributed to an inability to recruit 53BP1 to DSB-associated chromatin, as OD mutation/deletion blocks the retention of 53BP1 protein fragments at DNA damage sites, and also compromises their interaction with modified nucleosome core particles *in vitro* [28, 29]. Perhaps unexpectedly, we and others recently reported that the recruitment of a full-length 53BP1 protein into IR induced foci (IRIF) was only modestly impacted by OD- deletion or mutation [22, 27]. This prompted us to explore the molecular basis and function of OD-independent 53BP1 recruitment.

Here, we reveal that 53BP1 can interact with DNA damage sites independently of its OD, and this recruitment depends on interaction with the multifunctional homodimeric protein hub dynein light chain 1 (DYNLL1). We demonstrate that DYNLL1 binding promotes ordered 53BP1 oligomerization and is essential for efficient CSR and adaptive immunity in mice, while also contributing to 53BP1-dependent p53 regulation. In addition, we show DYNLL1-53BP1 interplay plays an essential role in mediating toxic NHEJ events in *Brca1* mutant cancer cells: deletion of *DYNLL1* or its transcriptional regulator ATM substrate Chk2-interacting $Zn^{2+}$ finger protein (ASCIZ; also known

asATMIN/ZNF822) is strongly selected for in *BRCA1*-deficient tumour cells, and results in PARPi resistance *in vitro* and *in vivo*. Thus, our findings identify an important mechanism in which DYNLL1 directly regulates the fidelity of 53BP1-dependent NHEJ.

## Results

*DYNLL1 is essential for OD-independent 53BP1 recruitment*

The minimal domain requirements for 53BP1 DSB localization were defined in the context of a 53BP1 fragment encompassing a.a. 1220–1711 [30, 31]. This fragment spans 53BP1's nuclear localization sequence (NLS), OD, tandem-tudor, and ubiquitin-dependent recruitment (UDR) domains, all of which were essential for its recruitment into IRIF [8, 28]. We were therefore surprised that complete deletion of its OD domain ($53BP1^{ODΔ}$) or Ala mutation of four key residues for OD activity ($53BP1^{ODm}$) only negligibly impacted on 53BP1 IRIF frequencies, despite completely blocking recruitment in the context of truncated $53BP1^{1220–1711}$ proteins (Fig. 1A). To map the sequences in 53BP1 that mediate OD-independent recruitment, IRIF localization patterns were examined across a panel of truncated $53BP1^{ODm}$ proteins in which 53BP1 sequences N- and C-terminal to a.a. 1220–1711 were restored (Fig. 1B and Supplementary Fig. 1A). We found that the addition of 113 residues N-terminal to $53BP1^{1220–1711}$ rescued $53BP1^{ODm}$ recruitment into IRIF (Fig. 1B), implicating a.a. 1107–1219 in OD-independent 53BP1 recruitment.

Interestingly, alanine substitutions at 28 N-terminal [Ser/Thr]-Gln consensus ATM/ATR phosphorylation site motifs in the full-length $53BP1^{ODm}$ protein recapitulated the effect of a.a. 1107–1219 deletion on IRIF recruitment (Fig. 1B), and suggested that some of these Ser-Gln or Thr-Gln motifs may be involved in the OD-independent 53BP1 recruitment to DSBs. We noted that Thr-1171, one of the three Ser-Gln/Thr-Gln motifs in the region critical for OD-independent IRIF formation (a.a. 1107–1219), also serves as a binding site (consensus Thr-Gln-Thr) for the dynein light chain protein DYNLL1 (LC8) [32]. As DYNLL1 is known to function as a ubiquitous sequence-specific dimerization hub for a plethora of diverse proteins [33, 34]w, we considered a role for DYNLL1 in the OD-independent 53BP1 recruitment mechanism. 53BP1 a.a. 1107–1219 also contains a second DYNLL1-binding site [32], and indeed, alanine substitution of the three anchor residues (GIQ and TQT, respectively) in each of the two DYNLL1-binding site motifs of 53BP1 ($53BP1^{LC8m}$) completely blocked OD-independent 53BP1 IRIF formation (Fig. 1C-D). Moreover, we found that DYNLL1 colocalized with 53BP1 in nuclear foci and that this interaction was abolished by the $53BP1^{LC8m}$ mutations (Supplementary Fig. 1B). However, the $53BP1^{LC8m}$ mutation did not interfere with OD-mediated oligomerization *in vitro* (Supplementary Fig. 2A), or downstream RIF1 recruitment (Supplementary Fig. 2B-C). Thus, collectively, these data indicate that direct binding of DYNLL1 to the LC8-binding motifs is critical for the OD-independent recruitment of 53BP1 to DSB sites.

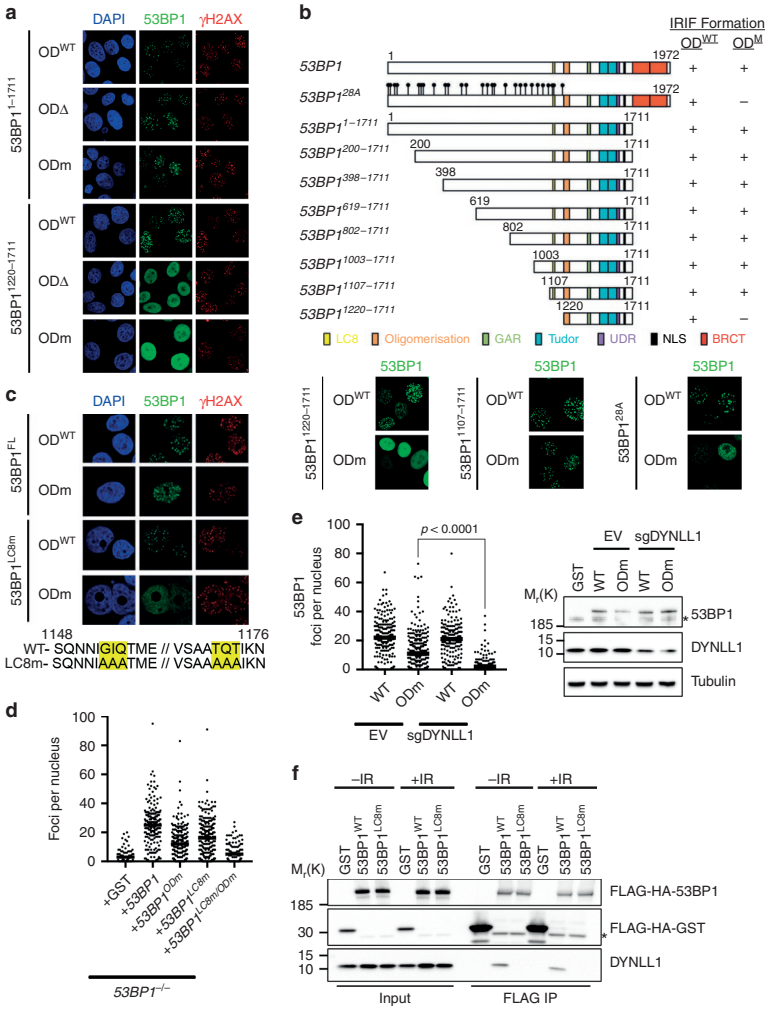



**FIGURE 1 | DYNLL1 promotes OD-independent 53BP1 recruitment to DSB sites.** *(A) 53BP1*$^{-/-}$ MCF-7 cells stably expressing the indicated 53BP1 transgenes were irradiated (5 Gy), fixed 4 h later, and immunostained with anti-HA (53BP1) and anti-γH2AX antibodies. Data, representative of $n = 3$ independent experiments. ODΔ indicates deletion of amino acids 1230–1270 and ODm indicates mutation of amino acids 1258–1261 to alanine. *(B)* IRIF forming capability of indicated 53BP1 constructs was determined in stable cell lines as in *A* 4 h following 5 Gy irradiation in a minimum of $n = 2$ independent experiments. *(C)* As in *A-B*, but with indicated WT and mutant 53BP1 constructs. Data, representative of $n = 2$ independent experiments. Amino acids 1142–1181 of 53BP1 are depicted including 6 amino acids mutated to alanine in the LC8m allele. *(D)* Automated 53BP1 IRIF quantification of data in C. Each point represents a single nucleus with $n \geq 65$ nuclei scored per condition. Median is indicated. Data, representative of $n = 2$ independent experiments. *(E)* Left, quantification of 53BP1 IRIF 4 h after irradiation (5 Gy). Significance determined by Mann–Whitney U Test. Right, immunoblot analysis of experimental cell lines. Each point represents a single nucleus with $n \geq 131$ nuclei scored per condition. Median is indicated. Data, representative of $n = 2$ independent experiments. *(F)* FLAG-HA-53BP1 immuno-complexes were isolated from whole cell extracts prepared from untreated and irradiated (10 Gy, 1 h) HEK 293 T cultures, 48 h following transfection with indicated control (GST) or 53BP1 expression plasmids. Representative data, $n = 2$ independent experiments

To further explore DYNLL1's role in modulating 53BP1 functions, we used CRISPR-Cas9 to mutagenize the *DYNLL1* gene in *53BP1*$^{-/-}$ MCF-7 cell populations stably complemented with wild type (WT) 53BP1 or 53BP1$^{ODm}$. DYNLL1-depletion in these populations (without selection for stable *DYNLL1* knockout clones) caused a near complete block in 53BP1$^{ODm}$ foci formation (Fig. 1E and Supplementary Fig. 2D, $p < 0.0001$), and residual 53BP1 IRIF frequencies in these experiments correlated to cells of increased DYNLL1 nuclear staining intensity (Supplementary Fig. 2E). In contrast, DYNLL1-depletion did not affect the frequencies of WT 53BP1 IRIF when the OD was intact (Fig. 1E; $p = 0.1363$). These experiments therefore suggested that DYNLL1-dependent binding to the LC8 motifs in 53BP1 promotes 53BP1 oligomerization, explaining the mechanism of OD-independent 53BP1 recruitment to IRIFs.

*DYNLL1-53BP1 interactions are DNA damage- and cell cycle-independent*

As indicated above, one of the two LC8 motifs (LC8 motif 2) in 53BP1 also comprises an ATM/ATR phosphorylation site (Thr-1171, consensus Thr-Gln) that is phosphorylated following IR-treatment [35], and a second putative ATM phosphorylation site (Ser-1148) is positioned only 5 a.a. residues upstream of LC8 motif 1. Thus, we considered that 53BP1-DYNLL1 interactions might be DNA damage regulated. To test this, Flag-HA tagged WT 53BP1 and 53BP1$^{LC8m}$ mutant protein complexes were immunoprecipitated from lysates prepared from irradiated and untreated stable cell lines and analyzed for the presence of DYNLL1. In confirmation of a role for the 53BP1 LC8 motifs in mediating DYNLL1 interactions, DYNLL1 co-precipitated with wild type, but not LC8-motif mutant 53BP1 complexes (Fig. 1F). Notably, DYNLL1-53BP1 interactions were not significantly altered upon IR-treatments (Fig. 1F), discounting a role for Thr-1171 phosphorylation in regulating DYNLL1-53BP1 interactions. In addition, mutation of Ser-1148, which would be expected to form the N-terminal residue of the fully extended ~8-residue beta-strand interacting with the DYNLL1-binding groove based on known structures for DYNLL1-target complexes [36], by itself had only a modest effect on DYNLL1 binding. Mutation of Thr-1171, however, reduced DYNLL1-binding to a greater extent, which was further reduced in concert with the Ser-1148-Ala mutation, albeit not to the same extent as the 53BP1$^{LC8m}$ interaction-blocking mutation in which the entire 3-residue anchor motifs are disabled (Supplementary Fig. 1C). Moreover, combined alanine substitutions at Thr-1171 and Ser-1148 resulted in the near total loss of OD-independent 53BP1 IRIF (Supplementary Fig. 1D). The most likely explanation for these results is that mutation of these two phosphorylation site motifs impacts the interaction with DYNLL1 by weakening its binding sites in 53BP1 rather than by impairing their phosphorylation state, reconciling the IRIF recruitment defect of the 53BP1$^{ODm,28A}$ mutant protein (Fig. 1B).

Next, we examined whether DYNLL1-53BP1 interactions might be regulated by cell cycle position. Cell synchronisation experiments confirmed DYNLL1 did not exhibit cell-cycle-dependent fluctuations in expression during interphase (Supplementary Fig. 3A),

or mitosis (Supplementary Fig. 3B). To determine whether 53BP1 might be regulated by cell-cycle dependent modification of DYNLL1, or otherwise, 53BP1 IRIF were quantified in G1, S and G2 cell-cycle stage classified populations in WT and mutant complemented *53BP1*$^{-/-}$ MCF-7 stable cell lines (Supplementary Fig. 3C). Here, the 53BP1$^{LC8m}$ mutation did not significantly impair foci formation at any cell cycle phase (Supplementary Fig. 3D). Likewise, 53BP1$^{ODm}$ IRIF frequencies, that rely entirely on DYNLL1-interactions (see Fig. 1C-F), were equally reduced at all cell cycle phases (Supplementary Fig. 3D). Collectively, these experiments indicate DYNLL1-53BP1 interactions are likely to be constitutive, and suggested that DYNLL1 might represent an integral component of 53BP1 complexes.

*53BP1-DYNLL1 interactions are required for class-switch recombination*

We next examined the function of DYNLL1 and DYNLL1-53BP1 interactions during CSR, which relies on 53BP1-mediated NHEJ [13, 14]. DYNLL1 is essential for normal B cell development, and its deletion in the early B cell lineage using *Mb1-Cre* leads to dramatic losses in circulating and mature splenic B cell populations (Supplementary Fig. 4A) [37]. We therefore used transgenic *Cd23-Cre* driver (*Cd23-Cre*$^{Tg}$) to delete *Dynll1* in mature B lymphocytes in *Dynll1*$^{F/F}$ mice, which supported the development of normal frequencies of mature splenic B cells in which DYNLL1 protein was efficiently depleted (Supplementary Fig. 4B-C)). Cultured *Dynll1*-deleted B splenocytes upon stimulation with IL-4 and LPS showed a reduction in class-switching to IgG1, and IgG1 switching frequencies in *Cd23-Cre*$^{Tg}$ *Dynll1*$^{F/F}$ cells were consistently reduced by >50% relative to *Cd23-Cre*$^{Tg}$ controls in all cell populations that had undergone equivalent numbers of cell divisions (Fig. 2A-B). This was independently confirmed by *Cd23-Cre*-mediated deletion of the *Asciz* gene in mouse mature B cells, which encodes DYNLL1's transcriptional regulator ASCIZ (ATMIN) [38, 39] and resulted in greatly reduced DYNLL1 expression and an equivalent reduction in class-switching efficiency (Supplementary Fig. 4D-E), consistent with previous results in B cells from *Cd19-Cre Asciz*-mutant mice [40]. The fact that CSR defects in *Dynll1*- and *Asciz*-deleted B cells could not be explained by the defective expression of *Igh* switch region germ-line transcripts (Supplementary Fig. 4F), nor the magnitude of proliferation defects in *Dynll1*-deleted B cells (Fig. 2B), was consistent with a role for DYNLL1 and its regulator ASCIZ in the end joining phase of CSR.

To exclude the possibility that indirect, 53BP1-independent, consequences of DYNLL1-deletion could account for CSR defects in *Dynll1*-deficient B cells, we next monitored the effect of LC8 binding site mutations on 53BP1-dependent CSR. LPS/IL-4-induced class-switching to IgG1 was analysed in stimulated *53bp1*$^{-/-}$ primary B splenocytes upon reconstitution with retroviruses that express wild type 53BP1, or the 53BP1$^{ODm}$, 53BP1$^{LC8m}$, and 53BP1$^{LC8m/ODm}$ mutant proteins, or as a negative control, the NHEJ-defective 53BP1$^{L1619A}$ UDR mutant [8] (Fig. 2C; note that to avoid the inefficient packaging of large *53BP1* inserts in retroviral particles, all rescue constructs express a truncated

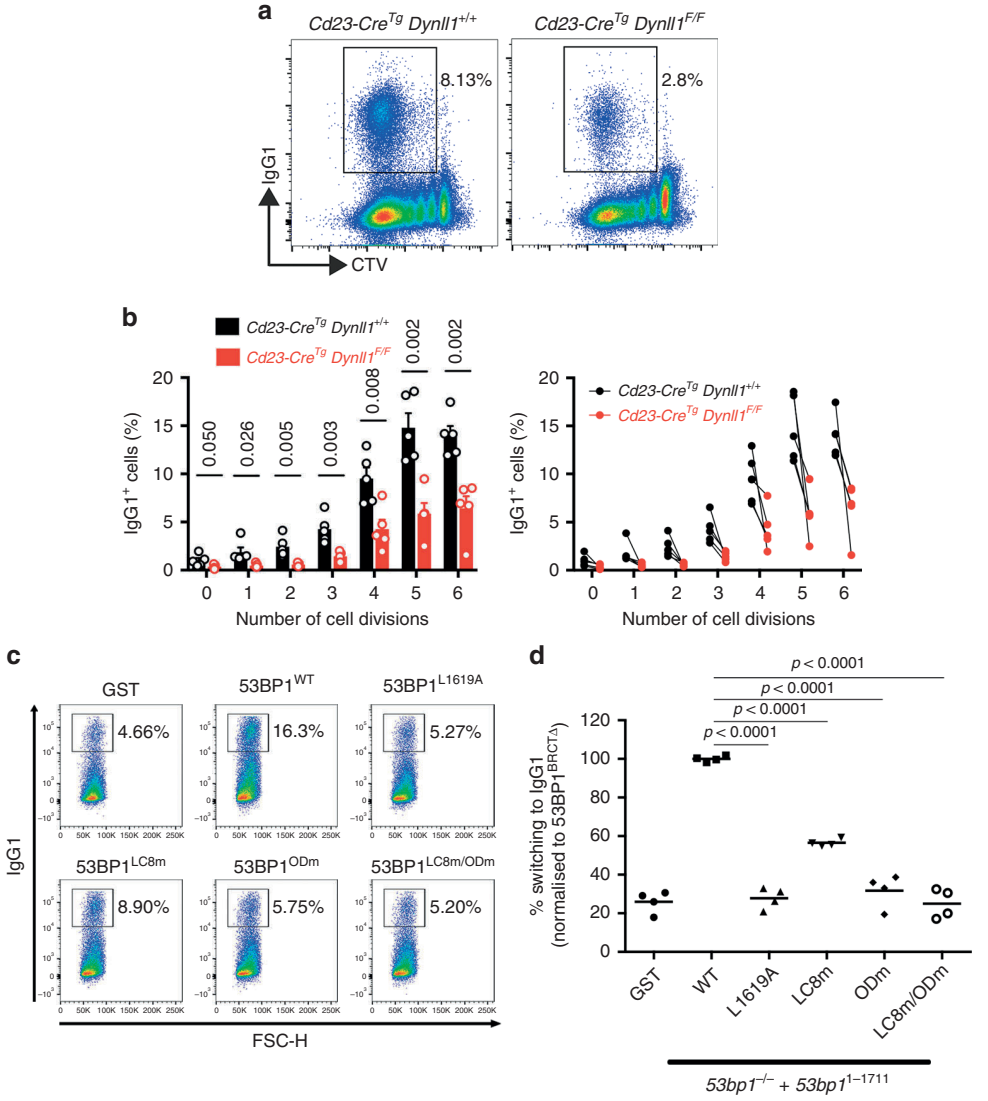



**FIGURE 2 | 53BP1-dependent class-switch recombination requires DYNLL1.** *(A) In vitro* CSR to IgG1 in *Dynll1*$^{F/F}$ *Cd23-Cre*$^{Tg}$ and control *Cd23-Cre*$^{Tg}$ mature B splenocytes, 96 h following stimulation with LPS and IL-4. Representative flow cytometric plots depict IgG1 positive fraction of cells, in cells co-stained with CellTrace Violet (CTV). *(B)* IgG1-positive (IgG1$^{+}$) B cells as a proportion of total B cells (%) for each cell generation as determined by CTV staining and proliferation-associated dye dilution. Significance was determined by unpaired two-tailed student's t-test with Holm-Sidak correction for multiple comparisons. Data, $n = 5$ mice, mean ± SEM. *(C) In vitro* CSR to IgG1 in mature B splenocytes from *53bp1*$^{-/-}$ mice, 96 h following stimulation with LPS and IL-4, and 72 h following retroviral complementation as indicated. Representative plots. *(D)* Quantification of C. Bars represent mean, $n = 4$ mice. Statistical analysis by unpaired two-tailed student's t-test

53BP1 protein (a.a. 1–1711) that supports WT CSR frequencies [26]). As expected, 53BP1$^{1–1711}$ expression rescued class switching in *53bp1*$^{-/-}$ B cell cultures, while the repair-deficient 53BP1$^{L1619A}$ mutant could not (Fig. 2C-D). In contrast, 53BP1$^{LC8m}$-reconstitution only restored CSR to ~50% of WT (Fig. 2C-D), a defect consistent in magnitude to *Dynll1*-deficient B cells, confirming DYNLL1 mediates CSR via its regulation of 53BP1 complexes and their NHEJ activities. As expected [26], *53bp1*$^{-/-}$ B cells complemented with a mutant OD-domain allele (53BP1$^{ODm}$) failed to restore CSR to any significant degree (Fig. 2C-D). Thus, while DYNLL1 can mediate OD-independent 53BP1 DSB recruitment, OD-independent recruitment alone is unable to support NHEJ during CSR, confirming a cooperation between OD- and DYNLL1-dependent oligomerization in the assembly of NHEJ-competent 53BP1 oligomers.



*DYNLL1 stimulates 53BP1 oligomerization to promote optimal chromatin interactions*

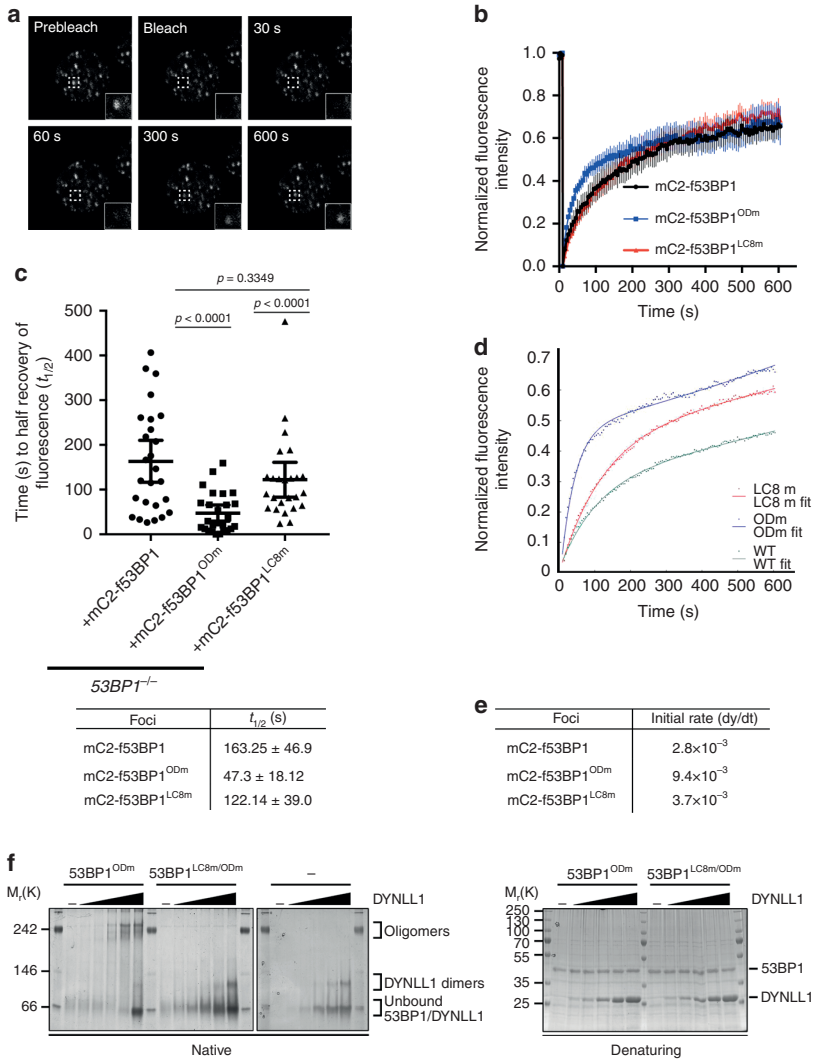
To ascertain why DYNLL1-mediated 53BP1 recruitment alone is insufficient for DNA repair, we investigated DYNLL1's contribution to 53BP1-chromatin interaction dynamics at DSB sites. Stable *53BP1*$^{-/-}$ MCF-7 cell lines were established that expressed equivalent levels of an mC2 (mClover2)-tagged 53BP1 a.a. 1107–1711 fragment, comprising WT (mC2-f53BP1) or mutated versions of the OD (mC2-f53BP1$^{ODm}$) or LC8 motifs (mC2-f53BP1$^{LC8m}$). The mobility of each protein in IRIF was then calculated in fluorescent recovery after photobleaching (FRAP) experiments (Fig. 3A). Fluorescence recovery of mC2-f53BP1$^{ODm}$ was >3-fold faster than that of WT mC2-f53BP1 protein, as calculated from the half-time for recovery to maximum fluorescence: $t_{1/2} = 47.3\,s \pm 18.12$ and $163.25\,s \pm 46.9$, for mC2-f53BP1$^{ODm}$ and mC2-f53BP1 proteins, respectively (Fig. 3B-C). Thus, DYNLL1-mediated 53BP1 oligomerization alone is insufficient for stable chromatin interaction at DSB sites. These results confirm canonical DYNLL1-independent oligomerization is primarily responsible for 53BP1 interactions with DSB-associated chromatin. To control for variation in fluorescence recovery endpoints between experimental repeats (Fig. 3D), we analyzed the rate of fluorescence recovery in a manner that, unlike $t_{1/2}$, was not related to the endpoint. Thus, we computationally modelled the fluorescence recovery data of three independent experiments (each comprising $n > 8$ cells per genotype) to calculate the initial rate of fluorescence recovery immediately after photobleaching (Fig. 3D). Initial rate calculations provide a concentration-independent measurement of fluorescence recovery that is independent of fluorescence recovery endpoint. Consistent with $t_{1/2}$ measurements, the initial recovery rates of each protein reproduced the trends seen in Fig. 3B-C, with large, and moderate increases in the recovery rates of mC2-f53BP1$^{ODm}$ and mC2-f53BP1$^{LC8m}$ mutant proteins, respectively, relative to WT mC2-f53BP1 (Fig. 3E). These data confirmed an important role for DYNLL1 in stabilizing OD-dependent 53BP1-chromatin interactions.

To determine the mechanism by which DYNLL1 contributes to 53BP1 function, we next probed DYNLL1's ability to promote 53BP1 oligomerization *in vitro*. Thus, purified

DYNLL1 was titrated into binding reactions that contained a recombinant monomeric 53BP1 protein fragment encoding the two LC8-binding motifs and a mutated OD domain (a.a. 1131–1292). Reactions were then resolved by native PAGE to ascertain DYNLL1's ability to stimulate OD-independent 53BP1 oligomerization. In these experiments, increasing DYNLL1 to levels equimolar and above that of the 53BP1 fragment, stimulated its robust oligomerization as determined by a marked increase in higher molecular weight protein complexes (Fig. 3F). In confirmation of a role for the 53BP1 LC8 binding motifs in mediating the assembly of DYNLL1-bridged 53BP1 oligomers, higher molecular weight complexes did not form when both LC8-binding motifs in the 53BP1 fragment were mutated, and these reactions were characterised by an increased presence of ligand-free DYNLL1 dimers (Fig. 3F). Taken together, our data indicate that optimal 53BP1 oligomerization is mediated via a cooperation between its OD-domain (Fig. 1A-B), and the binding of DYNLL1 to its upstream binding sites in 53BP1 (Fig. 3F). We therefore conclude that the intermolecular affinity afforded by DYNLL1-53BP1 interactions is sufficient to promote 53BP1 oligomerization, yet in isolation is insufficient to efficiently tether 53BP1 complexes to DSB-associated chromatin. We instead propose that DYNLL1 may provide order to large oligomeric 53BP1 complexes, a function required for optimal chromatin interactions and its associated DNA repair function.

*PARPi hypersensitivity in Brca1-deficient cells requires 53BP1-DYNLL1 cooperation*

The fact that DYNLL1-mediated regulation of 53BP1 oligomerization enhances 53BP1-dependent CSR next prompted us to test its importance more broadly in 53BP1-dependent NHEJ. The efficacy of PARPi in killing BRCA1-deficient cells is dependent on 53BP1, and its loss in BRCA1-deficient cell-lines and mice results in resistance to PARPi-induced cell death [9, 18, 20, 21]. We therefore theorized that reduced efficiency of 53BP1-dependent NHEJ upon DYNLL1 depletion might likewise confer PARPi resistance to BRCA1-deficient cells. Using CRISPR-Cas9, we mutagenized the *Dynll1* and *Asciz* genes in the KB1P-G3 *Brca1*$^{-/-}$ *p53*$^{-/-}$ murine mammary tumour cell line [20], and monitored locus-specific indels within cell populations by deconvolution of complex Sanger sequencing traces derived from Cas9 cleavage site-spanning PCR amplicons using the Tracking of Indels by Decomposition (TIDE) algorithm [41] (Supplementary Fig. 5A). To determine whether mutation of *Dynll1* or *Asciz* provided a selective advantage in KB1P-G3 cells due to PARPi resistance, the change in percentage of edited alleles between the starting population and the surviving fraction was compared, before, and after, outgrowth in the presence or absence of the PARPi olaparib (Fig. 4A and Supplementary Fig. 5A). In all experiments in which the initial indel frequency at the *Dynll1* and *Asciz* loci was below saturation (<85%) in treatment naive cells, olaparib treatments selected for striking increases in indel frequency (Fig. 4B and Supplementary Fig. 5B). These effects were coupled to reductions in DYNLL1 protein levels when compared to untreated controls (Supplementary Fig. 5C), collectively confirming that both proteins are




| Foci | $t_{1/2}$ (s) |
|---|---|
| mC2-f53BP1 | 163.25 ± 46.9 |
| mC2-f53BP1$^{ODm}$ | 47.3 ± 18.12 |
| mC2-f53BP1$^{LC8m}$ | 122.14 ± 39.0 |

| Foci | Initial rate (dy/dt) |
|---|---|
| mC2-f53BP1 | $2.8\times10^{-3}$ |
| mC2-f53BP1$^{ODm}$ | $9.4\times10^{-3}$ |
| mC2-f53BP1$^{LC8m}$ | $3.7\times10^{-3}$ |

**FIGURE 3 | Stable 53BP1-chromatin interactions require DYNLL1-dependent and -independent oligomerization modes.** *(A)* Representative FRAP series. Example shows recovery of WT mC2-f53BP1. Bottom right corner shows magnified region of bleached area. All FRAP experiments were performed in *53BP1*$^{-/-}$ MCF-7 cells stably expressing the indicated mC2-f53BP1 fragments. *(B)* Mean recovery from a single FRAP experiment in cells expressing mC2-f53BP1 ($n = 8$), mC2-f53BP1$^{LC8m}$ ($n = 9$), or mC2-f53BP1$^{ODm}$ ($n = 10$), mean ± SEM. Data, representative of $n = 3$ independent experiments. *(C)* Time for half-recovery of maximum final fluorescence for IRIF in individual cell expressing mClover2-WT ($n = 26$), mC2-f53BP1$^{LC8m}$ ($n = 26$), or mC2-f53BP1$^{ODm}$ ($n = 25$) proteins. Mean ± CI (95%). *P*-values, Mann–Whitney U test. *(D)* Curves of best fit for three aggregated experiments. Data points represent the mean of $n \leq 25$ determinations. *(E)* Calculated initial rates (dy/dt) for the curves generated in *D*. *(F)* Purified Smt3-His$_6$-tagged DYNLL1 was incubated with Smt3-His$_6$-tagged 53BP1$^{ODm}$ or 53BP1$^{LC8m/ODm}$ fragments (a.a. 1131–1292) as indicated. 1 µg of 53BP1 was added to each reaction with increasing concentrations of DYNLL1. Molar ratios of DYNLL1:53BP1 from left to right; 1:4, 1:2, 1:1, 2:1, 4:1. Samples were fractionated by native (8%) or denaturing (12%) PAGE and stained with Coomassie Brilliant Blue. Data, representative of $n = 2$ independent experiments

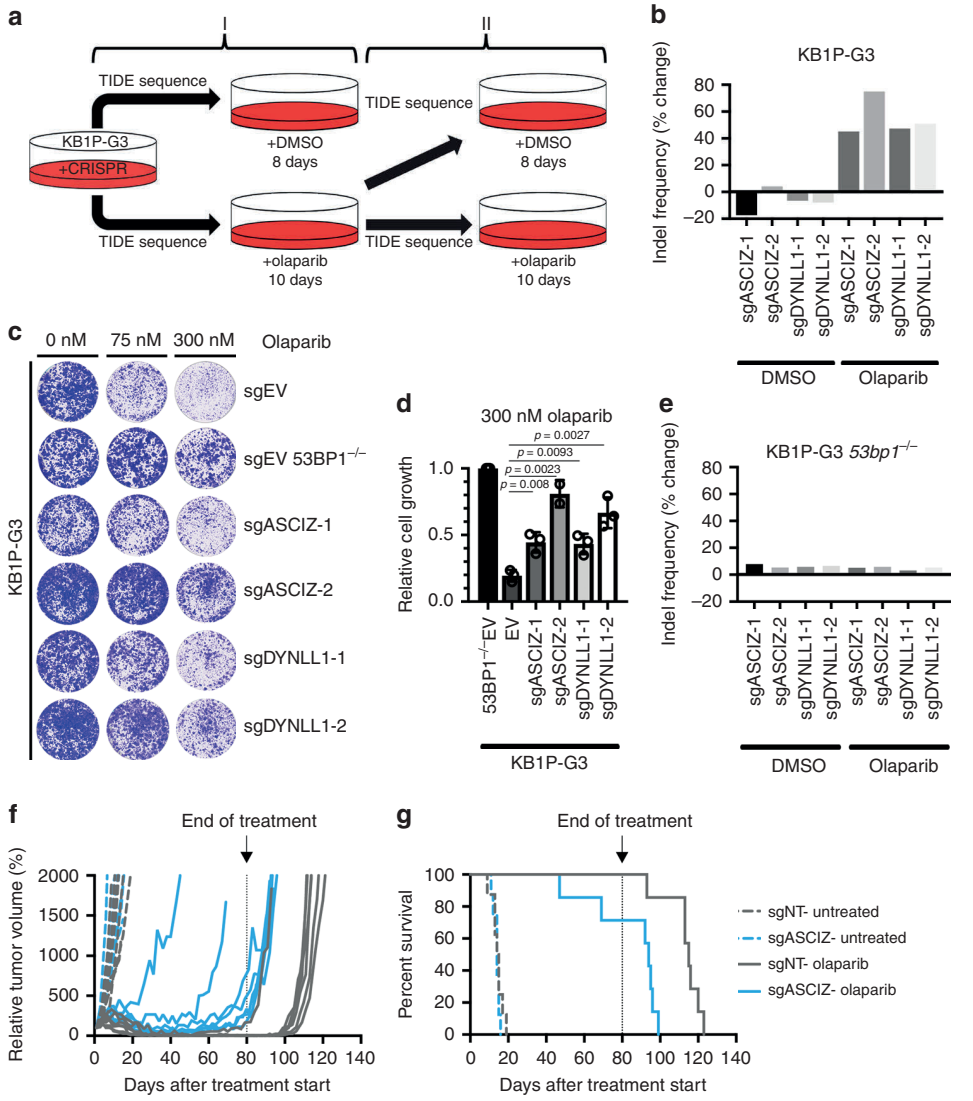



**FIGURE 4 | ASCIZ and DYNLL1 co-regulate 53BP1-dependent olaparib sensitivity in *Brca1*-deficient cells.** *(A)* Schematic of experiments to determine olaparib resistance. *(B)* Change in the percent of edited alleles for the indicated target genes in KB1P-G3 cells after growth in DMSO or olaparib (75 nM). Data, representative of $n = 3$ independent experiments. *(C)* Representative images from the second round of olaparib growth (II) in either DMSO or olaparib. *(D)* Quantification of growth in olaparib (300 nM) after transduction with indicated guide RNAs. Quantification of $n = 3$ independent experiments, each with three technical replicates. Mean ± SD. Significance determined by unpaired two-tailed t test. *(E)* Change in the percent of edited alleles in *53bp1*$^{-/-}$ *p53*$^{-/-}$ KB1P-G3 cells after growth in DMSO or olaparib (75 nM). Data, representative of $n = 2$ independent experiments. *(F)* Relative tumour volume of transplanted organoids after treatment with olaparib. $n > 7$ animals per condition. *(G)* Kaplan–Meier plot indicating survival of organoid-transplanted animals. Significance between sgNT — olaparib and sgASCIZ — olaparib was determined by Log-rank Mantel–Cox test ($p = 0.0018$). $n > 7$ animals per condition

required for the hypersensitivity of *Brca1*-deficient cells to PARPi. Cas9-dependent mutagenesis of either gene in KB1P-G3 cells also conferred olaparib resistance in clonogenic survival experiments (Fig. 4C-D). Importantly, the Olaparib resistance in *Asciz*-mutated KB1P-G3 cells could be completely reversed by transgene-mediated re-expression of exogenous DYNLL1 (Supplementary Fig. 6A-C), confirming the importance of ASCIZ-mediated DYNLL1 transcription in the response of BRCA1-deficient cells to PARPi. However, neither selection for CRISPR-Cas9-dependent *Dynll1* or *Asciz* locus editing, nor reduced DYNLL1 expression, was observed when equivalent experiments performed in *53bp1*$^{-/-}$ KB1P-G3 cells (Fig. 4E and Supplementary Fig. 5D-E), indicating that DYNLL1's role in mediating the PARPi sensitivity of *Brca1*-deficient cells occurs predominantly via its regulation of 53BP1 activities.

We next examined whether the ASCIZ-DYNLL1 axis was required for PARPi sensitivity *in vivo*. ASCIZ and DYNLL1 have previously been shown to have equivalent effects on the development and expansion of *Myc*-driven cancers [37, 42] , thus we monitored the growth of Cas9-expressing *Brca1*$^{-/-}$ *p53*$^{-/-}$ transplanted mouse cancer organoids [43] transduced with control or *Asciz*-targeting gRNA (Supplementary Fig. 5F-G). Olaparib treatment significantly delayed the onset of tumour growth in transplanted animals relative to an untreated cohort. However, PARPi-dependent inhibition of tumour growth was attenuated in *Asciz*-edited tumours (Fig. 4F), and resulted in decreased overall survival relative to control olaparib-treated cohorts (Fig. 4G). These data demonstrated that regulation of 53BP1 by the ASCIZ-DYNLL1 axis supports the efficacy of olaparib treatments in selectively killing *Brca1*-deficient cancer cells, confirming the importance of DYNLL1-53BP1 interactions in regulating 53BP1-dependent DNA repair.

*DYNLL1-binding sites contribute to 53BP1-dependent Nutlin-3 sensitivity*

In addition to its role in the DNA damage response, 53BP1 also contributes to p53-dependent transcriptional senescence programs and the corresponding cellular sensitivity to the treatments with MDM2 inhibitor Nutlin-3 [22, 44]. Interestingly, the 53BP1$^{LC8m}$ mutant, in contrast to wild type 53BP1 [22], was compromised in their ability to restore the sensitivity of *53BP1*$^{-/-}$ MCF-7 to Nutlin-3 (Fig. 5A-C). This agrees with a model in which DYNLL1 is likely to enforce optimal 53BP1 oligomerization, and is consistent with our published findings in which efficient 53BP1 oligomerization was similarly essential for 53BP1-dependent regulation of p53 [22].

## Discussion

Taken together, our findings reveal DYNLL1 to be an integral component of oligomeric 53BP1 complexes through which it plays an important role in 53BP1-dependent NHEJ. We speculate that DYNLL1-binding to 53BP1 may provide order to 53BP1 oligomers within chromatin-binding domains, enhancing productive chromatin interactions that enhance

effective resection inhibition and enable for efficient NHEJ. Deficiencies in either DYNLL1 or its binding sites in 53BP1, lead to substantial CSR defects. Given that 53BP1 is similarly important for resection inhibition and NHEJ during V(D)J recombination, a loss of which manifests in the defective development of B and T lymphocyte lineages [45-47], it is plausible that 53BP1-associated V(D)J recombination defects that accompany loss of DYNLL1-53BP1 interactions might contribute to the B cell lineage development defects recently reported in *Dynll1*-deficient mice [37]. We also found that DYNLL1 contributes to DNA damage-independent 53BP1 functions in the response to the MDM2 inhibitor Nutlin-3 (Fig. 5A-C). This agrees with a model in which DYNLL1 enforces optimal 53BP1 oligomerization, and is consistent with our published findings in which efficient 53BP1

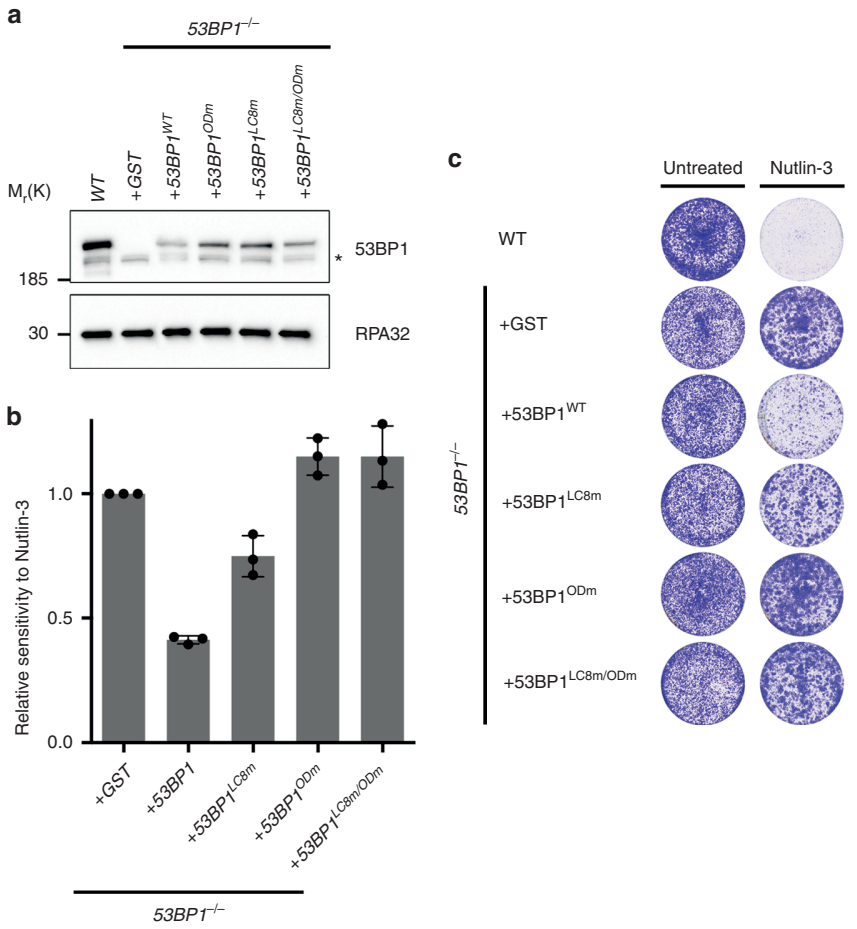



**FIGURE 5 | DYNLL1 is required for 53BP1-dependent p53 responses to Nutlin-3.** *(A)* Immunoblot analysis of the MCF-7 cell lines used in *A* with anti-53BP1 or anti-RPA32 antibodies prior to N3 treatment. *(B)* Quantification of $n = 3$ independent experiments represented in *A*, each performed in triplicate. Mean ± SD. *(C)* Indicated parental or stably complemented *53BP1*$^{-/-}$ MCF-7 cell lines were incubated in the presence (11 days) or absence (7 days) of Nutlin-3 (4 μM)

oligomerization was similarly essential for 53BP1-dependent regulation of p53 [22]. Our results therefore suggest bivalent oligomerization modes are necessary to coordinate the assembly of 53BP1 molecules into ordered, functionally competent multimeric complexes, insights that will be relevant for understanding other macromolecular complexes organized by DYNLL1 (Fig. 6). In identifying DYNLL1 and ASCIZ as essential mediators of 53BP1-dependent PARPi sensitivity in *Brca1*-deficient cancer cells, our findings provide a molecular explanation for the identification of both proteins as PARPi resistance factors in *BRCA1*-deficient cells in recently published genetic screens [48, 49], and reveal a previously unanticipated mechanism in which 53BP1 misregulation could lead to PARPi resistance in the clinic.



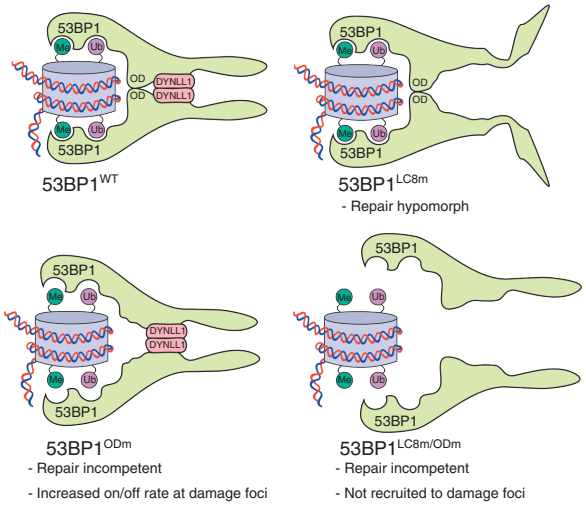



**FIGURE 6 | DYNLL1 and the OD mediate a bivalent mode of 53BP1 oligomerization.** 53BP1 localisation and function is dependent upon bivalent OD- and DYNLL1-mediated modes of oligomerization (top, left). OD-mediated oligomerization alone is sufficient for chromatin binding but results in severe DSB repair defects (top, right). DYNLL1-mediated oligomerization is also sufficient to support recruitment of 53BP1 to damage sites, but does not support DNA repair (bottom, left). Loss of both OD and DYNLL1-mediated modes of oligomerization eliminates 53BP1 recruitment to DNA damage sites and all associated repair functions (bottom, right)

## Materials and Methods

*Cell lines and culture conditions*

Cell lines used in this study are MCF-7 female human breast adenocarcinoma, RPE-1 female human retinal pigment epithelial, human female embryonic kidney (HEK) 293T cells (including the BOSC23 derivative cell line), and KB1P-G3 *Brca1*$^{-/-}$ *p53*$^{-/-}$ cells which were isolated from a female mouse mammary tumour. All cell lines were checked for mycoplasma contamination. KB1P-G3 and the KB1P-G3 *53bp1*$^{-/-}$ derivative were both kindly provided by Sven Rottenberg (NKI, Netherlands and University of Bern). All cell lines were cultured in DMEM—high glucose (D6546, Sigma-Aldrich) supplemented with 10% FBS, Pen-Strep, and 2 mM L-glutamine. Cultures were grown at 37°C with 5% $CO_2$. KB1-P3 (G3) and all derivative cells lines were additionally grown in 3% oxygen.

Primary B cells were isolated from red blood cell-lysed single-cell suspensions of *53bp1*$^{-/-}$ C57BL/6J mouse spleens and cultured in RPMI supplemented with 10% FCS, 100 U/ml penicillin, 100 ng/ml streptomycin, 2 mM L-glutamine, 1x MEM nonessential amino acids, 1 mM sodium pyruvate and 50 μM β-mercaptoethanol.

*Mouse models*

Mice harbouring conditional *Dynll1* or *Asciz* alleles (MGI ID: 5755433 and 5463697, respectively) were intercrossed with *Cd23-Cre* transgenic mice (MGI ID: 3803652) to generate *Cd23-Cre*$^{Tg}$ *Dynll1*$^{F/F}$ and *Cd23-Cre*$^{Tg}$ *Asciz*$^{F/F}$ experimental and *Cd23-Cre*$^{Tg}$ control animals. Mouse breeding and tissue collection was performed according to the Australian Code for the Care and Use of Animals for Scientific Purposes, 8th Edition (2013), and approved by the St. Vincent's Hospital Melbourne Animal Ethics Committee, approval number 002/17. *53bp1*$^{-/-}$ C57BL/6J mouse breeding and tissue collection was carried out according to the Animals (Scientific Procedures) Act (ASPA) under a Home Office project license to JRC.

*Gene editing and complementation*

CRISPR-Cas9 editing was carried out with gene-specific gRNAs integrated into a version of lentiCRISPR v2 (Addgene #52961) modified for blasticidin (lentiCRISPR-Bsr) resistance. Lentivirus was generated by co-transfection of lentiCRISPR-Bsr, pHDM-tat1b, pHDM-G, pRC/CMV-rev1b, and pHDM-Hgpm2 into HEK 293T cells using 1.29 μg polyethylenimine per 1 μg DNA in Opti-MEM (Thermo Fisher, 31985062). Viral supernatants were harvested at 48 and 72 h and passed through a 0.45-μm syringe filter. Two rounds of viral transduction were carried out on target cell populations in the presence of 4 μg/ml polybrene before selection in 10 μg/ml blasticidin. Once all cells in a non-transduced control population had died, the CRISPR population was removed from blasticidin selection. Stable transgene expression was similarly achieved by two rounds of lentiviral transduction with viral supernatants generated using the same procedure.

*Immunofluorescence*

For analysis of fixed samples, cells were seeded ($1.5 \times 10^5$) on glass coverslips (13 mm) in six-well plates 2 days before irradiation. IRIF formation was induced with γ-irradiation (5 Gy) and cells were fixed in 2% paraformaldehyde after 4 h recovery. Fixed cells were rinsed with PBS and then permeabilized in a 0.2% Triton X-100 PBS solution. After 15 min of blocking (3% BSA, 0.1% Triton X-100 in PBS) coverslips were incubated 1 h in a humidity chamber with primary antibodies diluted in blocking solution. The following primary antibodies were utilized at the indicated concentrations: mouse anti-HA (1:200, HA.11

Biolegend), rabbit anti-γ-H2AX (1:500, Epitomics), rabbit anti-Cyclin A (1:200, Santa Cruz sc-751), rabbit anti-DYNLL1 (1:250, AbCam Ab51603). The coverslips were rinsed three times with PBS containing 0.1% TX-100 and then incubated 1 h in a humidity chamber with secondary antibody. The following secondary antibodies were utilized at the indicated concentrations: goat anti-mouse Alexa Fluor 488 (1:500, Invitrogen A-11001), goat anti-rabbit Alexa Fluor 568 (1:500, Invitrogen A-11011). Coverslips were then washed three times in PBS containing 0.1% TX-100, once in PBS, and mounted on glass microscope slides using ProLong® Gold antifade reagent with DAPI (Life Technologies, P36935).

In experiments involving EdU incorporation, cultures were pulsed with 40 μM EdU for 10 min immediately preceding irradiation. After fixation, EdU was labelled using the Click-iT™ EdU Alexa Fluor 647 Imaging Kit (Thermo Fisher, C10340) according to the manufacturer's protocol. This was done immediately prior to antibody staining as described above.

Images for the initial mapping of the LC8 domain within the 53BP1 N-terminus (Fig. 1) were acquired on a Zeiss LSM510 META confocal imaging system (Fig. 1). RIF1 IRIF (Supplementary Fig. 2B-C) were analyzed on a Leica SP8 SMD X confocal microscope. All other fixed IRIF images were acquired on an Olympus Epi-fluorescence MMI CellEctor widefield microscope. Quantitative analysis of IRIF number and staining intensity was performed using Cell Profiler (Broad Institute). All image visualization and processing was done using Fiji.

*Olaparib sensitivity assays*

KB1P-G3 and KB1P-G3 *53bp1*$^{-/-}$ cells were subjected to two rounds of lentiviral transduction with viral supernatant generated using lentiCRISPR-Bsr. After selection in blasticidin (10 μg/ml), samples were collected to isolate genomic DNA (gDNA) immediately prior to seeding for olaparib sensitivity. Blasticidin-resistant populations were seeded in six-well plates at a density of $10^4$ cells per well ($5 \times 10^3$ for the KB1P-G3 *53bp1*$^{-/-}$ derivative) in the presence of olaparib or DMSO and grown at 37 °C (5% $CO_2$ and 3% $O_2$). Medium was refreshed at 4 days and 8 days. After 10 days outgrowth, cultures were expanded in fresh medium for 1 week in 6 cm dishes before harvesting gDNA. PCR fragments encompassing the CRISPR cut site were amplified from gDNA using Q5 polymerase (NEB, M0491), sequenced (GATC Biotech), and analyzed by Tracking of Indels by Decomposition (TIDE: https://tide.deskgen.com/). Surviving cells were collected and three replicates were plated in DMSO and three in olaparib for viability analysis. DMSO and olaparib-treated cells were stained with crystal violet (0.5% (w/v) crystal violet in 25% methanol) after 8 days and 10 days growth (37 °C, 5% $CO_2$ and 3% $O_2$), respectively. Crystal violet stained cells were dissolved in a 10% (v/v) acetic acid solution a minimum of 24 h after staining and the $OD_{595}$ was measured as a quantitative metric of relative growth.

*Nutlin-3 sensitivity assay*

Cells were seeded in triplicate at a density of $1.25 \times 10^4$ per well in a six-well plate in the presence (11 days growth) or absence (7 days growth) of Nutlin-3 (4 μM, Cayman Chemicals, added 16 h after seeding). Cells were stained with crystal violet and quantified as described for olaparib sensitivity assays. These experiments were performed in triplicate.

*Protein extraction and western blotting*

Protein extracts were prepared in ice cold benzonase cell lysis buffer (40 mM NaCl, 25 mM Tris pH 8.0, 0.05% SDS, 2 mM $MgCl_2$, 10 U/ml benzonase, and cOmplete™ protease inhibitor cocktail (Roche, 04693159001). Briefly, cells were harvested and washed once in ice cold PBS before resuspending in lysis buffer. After 10 min incubation on ice, protein concentration was calculated by Bradford (Bio-Rad, 500-0006) assay with reference to a standard curve generated with BSA. Extracts were mixed with 3X Laemmli buffer and heated at 95 °C for 5 min.

Extracts were fractionated on pre-cast NuPAGE™ 4–12% 1.0 mm Bis-Tris polyacrylamide gels (Life Technologies, NP0322) and transferred to nitrocellulose membranes. After blocking with 5% milk and washing in PBST, membranes were incubated overnight in primary antibody. Primary antibodies used in this study are: anti-53BP1 (Novus Biological, NB100-304, 1:2500), anti-DYNLL1 (Abcam, ab51603, 1:1000), anti-α-tubulin (Sigma-Aldrich, TAT-1, 1:10000), anti-Cyclin A (Santa Cruz, sc53227, 1:1000), anti-HA (BioLegend, 501901, 1:2000), and anti-RPA32 (Abcam, ab16855, 1:1000), anti-β-actin (Sigma-Aldrich, A1978, 1:2000). Membranes were then probed with HRP-conjugated goat anti-mouse (Thermo Fisher, 62-6520) or goat anti-rabbit (Thermo Fisher, 65-6120) secondary antibodies for 1 h (1:20000). The membranes were then developed using Clarity™ Western ECL Substrate (Bio-Rad, 170-5061) and visualized on a Gel Doc™ XR System (Bio-Rad).

*Class switch recombination*

B cells were purified from red blood cell-lysed single-cell suspensions of 8–16-week-old *53bp1*$^{-/-}$ C57BL/6 J mouse spleens by magnetic negative selection using a B Cell Isolation Kit (Miltenyi Biotec, 130-090-862). No controls were employed for gender and randomization methods were not used to allocate animals to control and experimental groups. B cells ($7.5 \times 10^5$ per well in a six-well plate) were cultured in RPMI supplemented with 10% FCS, 100 U/ml penicillin, 100 ng/ml streptomycin, 2 mM L-glutamine, 1x MEM nonessential amino acids, 1 mM sodium pyruvate and 50 μM β-mercaptoethanol. B cells were stimulated with 5 μg/ml LPS (Sigma, L7770-1MG) and 10 ng/ml mouse recombinant IL-4 (Peprotech, 214-14-20). Cultures were grown at 37 °C with 5% $CO_2$ under ambient oxygen conditions.

Retroviral supernatants were collected 48 h after co-transfection of BOSC23 cells with 7 µg pCL-Eco and 7 µg pMX-IRES-GFP-derived plasmids (both kindly provided by A. Nussenzweig) containing cloned transgene inserts in the presence of FuGENE 6 (Promega, E2691). Viral supernatants were passed through a 0.45 µm syringe filter. One round of viral transduction was carried out on B cells 24 h after stimulation in the presence of 2.5 µg/ml polybrene, 20 mM HEPES, 5 µg/ml LPS and 10 ng/ml mouse recombinant IL-4. B cells underwent spinoculation at 850×*g* for 90 min at 30 °C. After a rest period of 4 to 6 h, the viral supernatants were removed, and supplemented RPMI was added to the cells.

Three days after transduction, infected B cells were analysed for the percentage of GFP and IgG1 double-positive cells using a FACSCanto (Becton Dickinson); analysis was performed using FlowJo v10. Cells were resuspended in PBS with 2% BSA and 0.025% sodium azide, blocked with Mouse BD Fc Block™ (1:500, BD Pharmingen 553141), and immunostained with biotinylated rat anti-mouse IgG1 (1:100, BD Pharmingen 553441), and Streptavidin APC (1:500, eBioscience 17-4317-82). Live/dead cells were discriminated after staining with Zombie Aqua viability dye (1:200, BioLegend 423102).

For CSR analyses of *Cd23-Cre*$^{Tg}$ *Dynll1*$^{F/F}$ and *Cd23-Cre*$^{Tg}$ *Asciz*$^{F/F}$ mice, experiments were performed as above except that purified B cells were activated with 10 µg/ml LPS (Invivogen, tlrl-3pelps) and 1:100-diluted conditioned murine IL-4 supernatant (kind gift of Andreas Strasser, Walter and Eliza Hall Institute, Melbourne) for 4 days, and then stained with CellTrace Violet (Thermo Fisher Scientific, C34557) and rat anti-mouse IgG1-APC (BD Pharmingen, 550874).

To analyse the transcription of *Igh* germline transcripts, $3 \times 10^6$ MACS-purified B cells from *Cd23-Cre*$^{Tg}$, *Cd23-Cre*$^{Tg}$ *Asciz*$^{F/F}$, or *Cd23-Cre*$^{Tg}$ *Dynll1*$^{F/F}$ mice were cultured with LPS (15 µg/mL) and IL-4 (1/100) for 0 to 3 days. After treatment, cells were washed once with ice-cold PBS and cell pellets were snap frozen on dry ice and stored at –80 °C before RNA extraction. Total RNA was extracted by using ISOLATE II RNA Micro Kit (Bioline BIO-52075) following the manufacturer's protocol. 300 ng purified RNA was subjected to reverse transcription with oligo(dT) and random primers using the SuperScript® III First-Strand Synthesis System (Invitrogen™ 18080-051). qPCR reagents were mixed as follows: 4 µl cDNA (6 ng), 0.5 µl Primer mix (300 nM each), 5 µl SYBR™ Select Master Mix (Applied Biosystems™ 4472908), 0.5 µl RNAase/DNAase free water. qPCR conditions were set as follows: 1 cycle (10 min at 95 °C), 45 cycles (15 s at 95 °C), 60 s at 60 °C.

After each PCR run, a disassociation curve program was added to validate the primer specificity. The standard curve method of comparative quantification was employed to quantify the results [50]. Results for the *Iγ1-Cγ1* germline transcript were normalized to the *Cd79b* input control, and expressed as percentage of maximum expression. Primer sequences were the same as previously used [51]: Cd79b_forward (5'-TGTTGGAATCTGCAAATGGA-3'), Cd79b_reverse (5'-TAGGCTTTGGGTGATCCTTG-3'), Iγ1-Cγ1_forw (5'-TCGAGAAGCCTGAGGAATGTG-3'), Iγ1-Cγ1_rev (5'-GGATCCAGAGTTCCAGGTCACT-3').

*Immunoprecipitation*

One day before transfection, $4.5 \times 10^6$ HEK 293T cells were seeded in antibiotic-free DMEM in a 10 cm plate for each condition. 24 h after plating, cultures were transfected with 10 µg 53BP1 pLV-EF1α-FLAG-HA Puro or 53BP1$^{LC8m}$ pLV-EF1α-FLAG-HA Puro using polyethylenimine. 24 h after transfection, each culture was trypsinized and re-plated in 2 × 10 cm plates. After 24 h, one plate was X-ray irradiated (10 Gy) and both (irradiated and non-irradiated control) were harvested 1 h after irradiation. Cells were lysed in benzonase-containing lysis buffer (20 mM HEPES [pH 7.9], 40 mM KCl, 2 mM $MgCl_2$, 10% glycerol, 0.5% NP40, 0.05% [v/v] phosphatase inhibitor cocktails 2 and 3 (Sigma-Aldrich), 1X protease inhibitor (Roche), and benzonase [50 U/ml]) on ice for 10 min. KCl was adjusted to a final concentration of 450 mM and rotated at 4°C for 30 min before clarification. Clarified lysates were diluted to a final salt concentration of 150 mM KCl with No-salt equilibration buffer (20 mM HEPES [pH 7.9], 0.5 mM DTT, 0.05% [v/v] phosphatase inhibitor cocktails 2 and 3 (Sigma-Aldrich), 1X protease inhibitor (Roche)) and 2 mg of protein was incubated with anti-FLAG M2 magnetic beads for 2 h. Bead-substrate complexes were washed five times in wash buffer (20 mM HEPES [pH 7.9], 100 mM KCl, 0.5 mM DTT, 1X protease inhibitor (Roche)) at 4°C before elution with 3x FLAG peptide (150 mM NaCl, 0.05% Tween, 150 ng/µl FLAG peptide (Sigma-Aldrich)). Eluates were boiled with Laemmli buffer and fractionated by SDS-PAGE.

*FRAP*

*53BP1*$^{-/-}$ MCF-7 cells were stably transduced with an mClover2-tagged fragment of 53BP1 encompassing amino acids 1107–1711 of the wild type protein. Two days before FRAP, $2.5 \times 10^5$ cells were seeded on a 35 mm glass-bottom plate. Cells were irradiated (5 Gy) with an X-ray source to induce IRIF formation 2 h before imaging. Individual foci were selected and 10 prebleach images were acquired prior to a single bleach pulse with an Argon laser at a laser transmission of 100%. Immediately after bleaching, 120 images were acquired in 5 s intervals at 0.5% laser intensity. All acquisition files were processed in ImageJ with the Stackreg plugin to account for nuclear migration in the recovery period. Regions of interest encompassing the bleached area, the entire nuclei and a section of background were selected and mean intensity values were quantified for each in ImageJ. These values were then normalized and fitted using the easyFRAP software [52]. All acquisitions were performed on a Leica SP8 SMD X confocal microscope.

Initial rate values were calculated based on curve of best fit generated in MATLAB according to the following equation.

F(X)=A*EXP(B*X)+C*EXP(D*X)

Curves of best fit were generated with the following coefficient values (with 95% confidence bounds), mC2-f53BP1: $a = 0.3191$ (0.3083, 0.33), $b = 0.0006296$ (0.0005654, 0.0006938), $c = -0.3105$ (−0.32, −0.301), $d = -0.009148$ (−0.009856, −0.00844), goodness of fit, SSE = 0.00501, R-square = 0.9964, adjusted R-square = 0.9963, RMSE = 0.006572; mC2-f53BP1$^{ODm}$: $a = 0.4695$ (0.463, 0.4759), $b = 0.000618$ (0.0005858, 0.0006501), $c = -0.5312$ (−0.5555, −0.5069), $d = -0.02533$ (−0.02711, −0.02355), goodness of fit, SSE = 0.01578, R-square = 0.9909, adjusted R-square = 0.9906, RMSE = 0.01167; mC2-f53BP1$^{LC8m}$: $a = 0.4598$ (0.4451, 0.4745), $b = 0.0004644$ (0.0004064, 0.0005225), $c = -0.4654$ (−0.4778, −0.4531), $d = -0.008194$ (−0.008687, −0.007701), SSE = 0.00528, R-square = 0.9979, adjusted R-square = 0.9979, RMSE = 0.006747. Rates for x = 10 s are presented in Fig. 3E.

*Expression and purification of 53BP1*

Smt3-$His_6$-tagged fragments (amino acids 1131–1292) of wild type (LC8-OD), OD-mutated (ODm-LC8), LC8-mutated (OD-LC8m), double mutant (LC8m-ODm) 53BP1, and DYNLL1 were expressed from pET-17b in *E. coli* BL21(DE3). Cells were lysed by sonication in 20 mM HEPES pH 7.5, 250 mM NaCl, and 0.25 mM TCEP. Lysates were clarified by centrifugation and the supernatant was applied to a TALON IMAC column (Supplementary Fig. 2A) or Ni-NTA agarose beads (Fig. 3F). Bound complexes were washed with 20 mM HEPES pH 7.5, 250 mM NaCl, 0.25 mM TCEP, supplemented with 10 mM imidazole and then eluted by increasing the imidazole concentration to 250 mM. Equal concentrations of eluate were then fractionated over a Superdex S200 column (Supplementary Fig. 2A).

*In vivo tumourigenesis studies*

All animal experiments were approved by the Animal Ethics Committee of The Netherlands Cancer Institute (Amsterdam, the Netherlands) and performed in accordance with the Dutch Act on Animal Experimentation (November 2014). KB1P4 tumour organoids were established previously and cultured in AdDMEM/F12 supplemented with 1 M HEPES (Sigma), GlutaMAX (Invitrogen), penicillin/streptomycin (Gibco), B27 (Gibco), 125 µM N-acetyl-L-cysteine (Sigma), 50 ng/mL murine epidermal growth factor (Invitrogen) (Duarte et al. [43]). Tumour organoid transduction was performed by spinoculation with pLentiCRISPRv2 lentiviral constructs in which either no gRNA or a gRNA targeting ASCIZ was cloned. Following puromycin selection, modified organoids were collected, incubated with TripLE at 37°C for 5', dissociated into single cells, washed in PBS, resuspended in tumour organoid medium and mixed in a 1:1 ratio of tumour organoid suspension and BME in a cell concentration of $10^4$ cells per 40 µl. Subsequently, $10^4$ cells were transplanted in the fourth right mammary fat pad of 6–9-week-old female NMRI nude mice. Mammary tumour size was measured

by caliper measurements and tumour volume was calculated ($0.5 \times \text{length} \times \text{width}^2$). Treatment of tumour bearing mice was initiated when tumours reached a size of 50–100 $mm^3$, at which point mice were stratified into the untreated ($n = 8$) or olaparib treatment group ($n = 8$). Olaparib was administered at 100 mg/kg intraperitoneally for 80 consecutive days. Animals were sacrificed with $CO_2$ when the tumour reached a volume of 1500 $mm^3$. Sample sizes were not pre-determined and no blinding or randomization was employed during analysis.

*Quantification and statistical analysis*

Prism 6 (GraphPad Software Inc.) was used for statistical analysis and production of all graphs and dot plots. The relevant statistical methods and measures of significance for each experiment are detailed in the figure legends. Cell Profiler (Broad Institute) was used for automated quantitation of immunofluorescence data. Normalization of FRAP recovery curves was performed using the easyFRAP software and curves of best fit were generated in MATLAB.

*Data availability*

The source data underlying Figs. 1D-F, 2B and D, 3B-D and F, 4D,F-G, 5A-B, and Supplementary Figures 1C-D, 2B-E, 3A-D, 4B-F, 5C and E, and 6A and C are provided as a Source Data file. All other original data and code that supports the findings of this study are available from the corresponding author upon reasonable request.

## Acknowledgements

This study was funded by Cancer Research UK Career Development Fellowship (CRUK CDF; C52690/A19270) awarded to J.R.C., that provides salary support for C.O. and J.R.B.; a Nuffield Department of Medicine Prize DPhil studentship to R.C.M.; CRUK CDF funding to ANB (C29215/A20772); CRUK grant (C302/A24386) to AWO; grants from Worldwide Cancer Research (WCR 16-0156) and the National Health and Medical Research Council of Australia (NHMRC 1139099) to JH; financial support also came from the Dutch Cancer Society (KWF 2014-6532 to S.R. and J.J.), the Netherlands Organization for Scientific Research (VICI 91814643, NGI 93512009, Cancer Genomics Netherlands and a National Roadmap grant for Large-Scale Research Facilities to J.J.), the Swiss National Science Foundation (310030_156869 to S.R.), the Swiss Cancer League (KLS-4282-08-2017 to S.R.), and the European Union (ERC StG 311565 to J.J.L.J., ERC CoG-681572 to S.R.). The Wellcome Centre for Human Genetics is supported by Wellcome core award 090532/Z/09/Z. St. Vincent's Institute of Medical Research is supported by NHMRC Independent Research Institutes Infrastructure Support and Victorian State Government Operational Infrastructure

Support grants. The authors thank A. Nussenzweig and E. Callen-Moreau for advice/reagents, S. Snellenberg for cell-cycle lysates, and all laboratory members for discussions and critique. We also thank C. Green (Chromosome Dynamics core) for expertise and assistance with FRAP experiments. We thank D. Durocher and D. Chowdhury for discussing unpublished results, and credit D. Durocher and S. Noordermeer for sharing DYNLL1-targeting CRISPR reagents and for initiating the mouse tumour studies with S.R. and J.J.

## Author contributions

J.R.B. co-wrote the manuscript, prepared the figures and designed, performed and analysed the majority of experiments, with assistance from R.C.M., C.O., A.W.O., K.B. and A.N.B. *In vivo* tumour models were performed by M.B. under the supervision of J.J. and SR. CSR experiments involving *Dynll1* and *Asciz*-mutant mice were performed by R.L. under the supervision of J.H. A.B.H. provided computational analysis. J.R.C. conceived and supervised the study and co-wrote the manuscript.



## Disclosure of Potential Conflicts of Interest

The authors declare no competing interests.

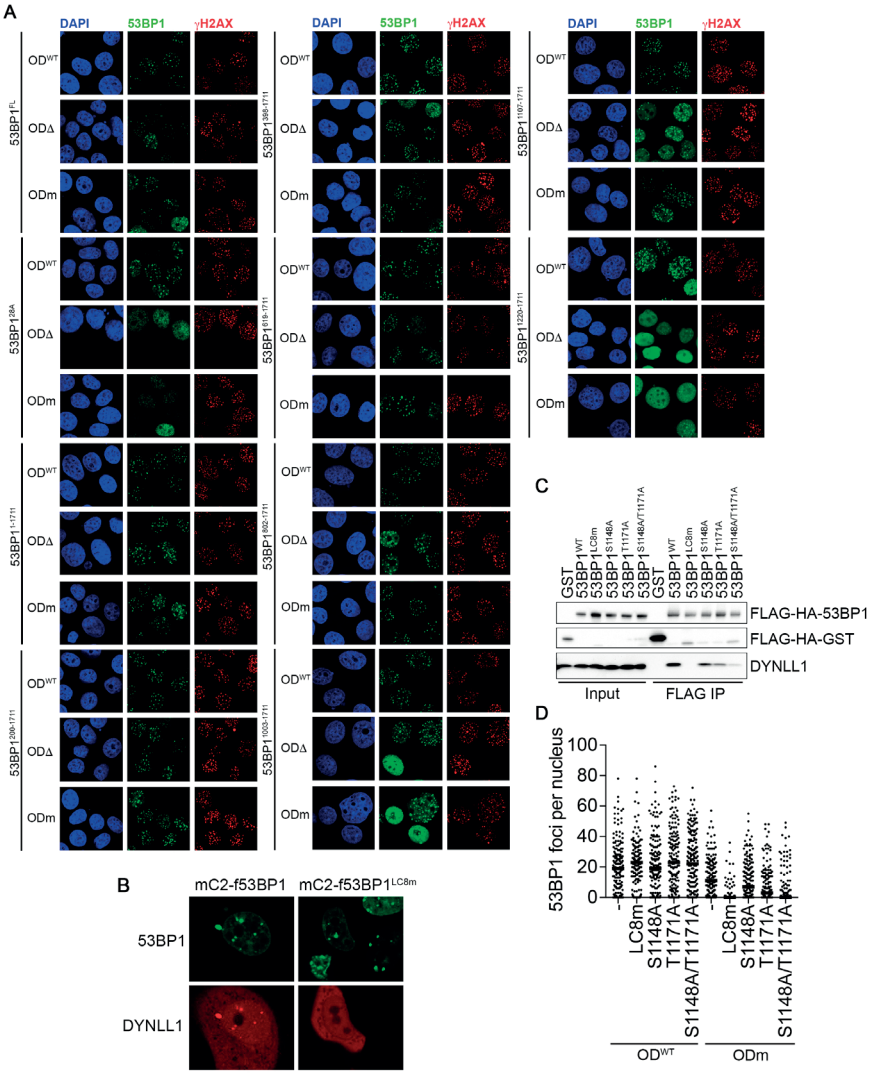
## References

1. Jackson SP, Bartek J. The DNA-damage response in human biology and disease. Nature. 2009; 461: 1071-8.
2. Ciccia A, Elledge SJ. The DNA damage response: making it safe to play with knives. Mol Cell. 2010; 40: 179-204.
3. Dudley DD, Chaudhuri J, Bassing CH, Alt FW. Mechanism and control of V(D)J recombination versus class switch recombination: similarities and differences. Adv Immunol. 2005; 86: 43-112.
4. Hustedt N, Durocher D. The control of DNA repair by the cell cycle. Nat Cell Biol. 2016; 19: 1-9.
5. Chapman JR, Taylor MR, Boulton SJ. Playing the end game: DNA double-strand break repair pathway choice. Mol Cell. 2012; 47: 497-510.
6. Panier S, Boulton SJ. Double-strand break repair: 53BP1 comes into focus. Nat Rev Mol Cell Biol. 2014; 15: 7-18.
7. Botuyan MV, Lee J, Ward IM, Kim JE, Thompson JR, Chen J, et al. Structural basis for the methylation state-specific recognition of histone H4-K20 by 53BP1 and Crb2 in DNA repair. Cell. 2006; 127: 1361-73.
8. Fradet-Turcotte A, Canny MD, Escribano-Díaz C, Orthwein A, Leung CC, Huang H, et al. 53BP1 is a reader of the DNA-damage-induced H2A Lys 15 ubiquitin mark. Nature. 2013; 499: 50-4.
9. Chapman JR, Barral P, Vannier JB, Borel V, Steger M, Tomas-Loba A, et al. RIF1 is essential for 53BP1-dependent nonhomologous end joining and suppression of DNA double-strand break resection. Mol Cell. 2013; 49: 858-71.
10. Escribano-Díaz C, Orthwein A, Fradet-Turcotte A, Xing M, Young JT, Tkáč J, et al. A cell cycle-dependent regulatory circuit composed of 53BP1-RIF1 and BRCA1-CtIP controls DNA repair pathway choice. Mol Cell. 2013; 49: 872-83.
11. Zimmermann M, Lottersberger F, Buonomo SB, Sfeir A, de Lange T. 53BP1 regulates DSB repair using Rif1 to control 5' end resection. Science. 2013; 339: 700-4.
12. Di Virgilio M, Callen E, Yamane A, Zhang W, Jankovic M, Gitlin AD, et al. Rif1 prevents resection of DNA breaks and promotes immunoglobulin class switching. Science. 2013; 339: 711-5.

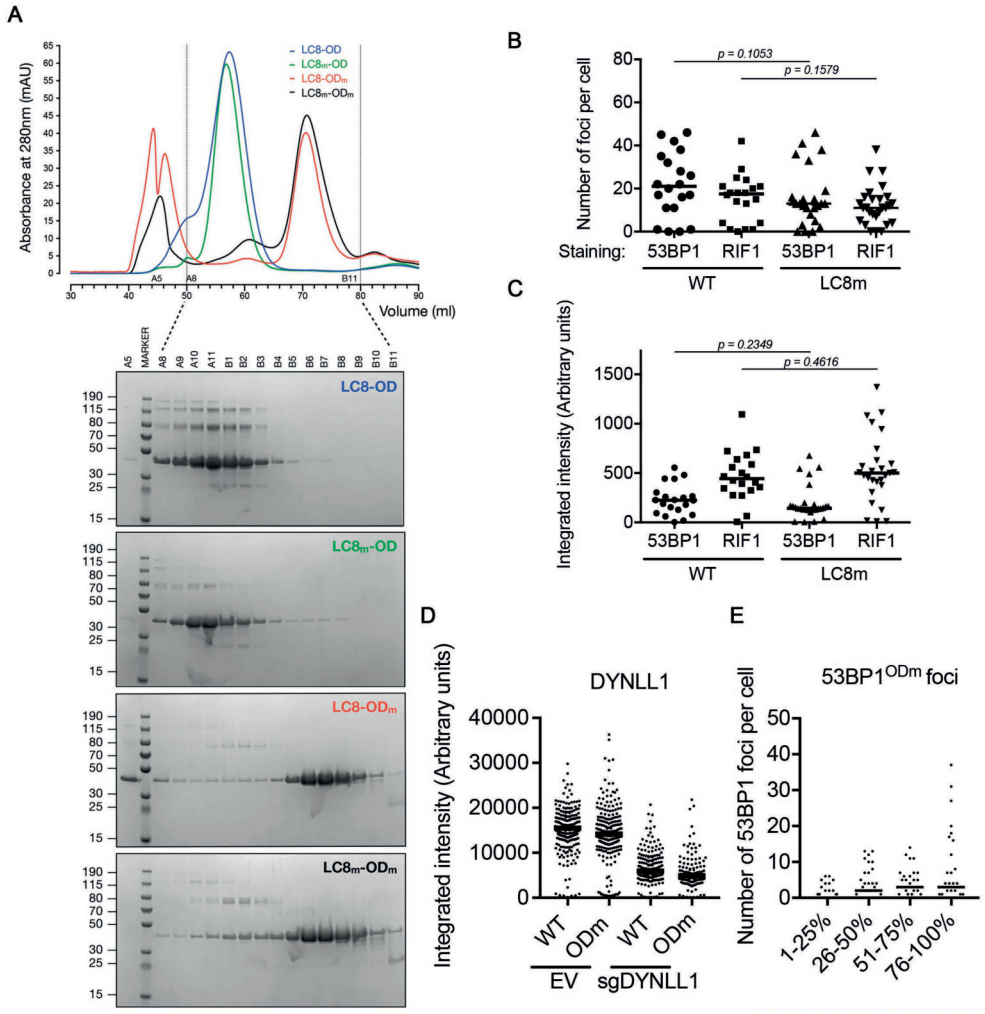
13. Manis JP, Morales JC, Xia Z, Kutok JL, Alt FW, Carpenter PB. 53BP1 links DNA damage-response pathways to immunoglobulin heavy chain class-switch recombination. Nat Immunol. 2004; 5: 481-7.
14. Ward IM, Reina-San-Martin B, Olaru A, Minn K, Tamada K, Lau JS, et al. 53BP1 is required for class switch recombination. J Cell Biol. 2004; 165: 459-64.
15. Hakim O, Resch W, Yamane A, Klein I, Kieffer-Kwon KR, Jankovic M, et al. DNA damage defines sites of recurrent chromosomal translocations in B lymphocytes. Nature. 2012; 484: 69-74.
16. Dimitrova N, Chen YC, Spector DL, de Lange T. 53BP1 promotes non-homologous end joining of telomeres by increasing chromatin mobility. Nature. 2008; 456: 524-8.
17. Sfeir A, de Lange T. Removal of shelterin reveals the telomere end-protection problem. Science. 2012; 336: 593-7.
18. Bunting SF, Callén E, Wong N, Chen HT, Polato F, Gunn A, et al. 53BP1 inhibits homologous recombination in Brca1-deficient cells by blocking resection of DNA breaks. Cell. 2010; 141: 243-54.
19. Cao L, Xu X, Bunting SF, Liu J, Wang RH, Cao LL, et al. A selective requirement for 53BP1 in the biological response to genomic instability induced by Brca1 deficiency. Mol Cell. 2009; 35: 534-41.
20. Jaspers JE, Kersbergen A, Boon U, Sol W, van Deemter L, Zander SA, et al. Loss of 53BP1 causes PARP inhibitor resistance in Brca1-mutated mouse mammary tumors. Cancer Discov. 2013; 3: 68-81.
21. Xu G, Chapman JR, Brandsma I, Yuan J, Mistrik M, Bouwman P, et al. REV7 counteracts DNA double-strand break resection and affects PARP inhibition. Nature. 2015; 521: 541-4.
22. Cuella-Martin R, Oliveira C, Lockstone HE, Snellenberg S, Grolmusova N, Chapman JR. 53BP1 Integrates DNA Repair and p53-Dependent Cell Fate Decisions via Distinct Mechanisms. Mol Cell. 2016; 64: 51-64.
23. Fong CS, Mazo G, Das T, Goodman J, Kim M, O'Rourke BP, et al. 53BP1 and USP28 mediate p53-dependent cell cycle arrest in response to centrosome loss and prolonged mitosis. Elife. 2016; 5.
24. Lambrus BG, Daggubati V, Uetake Y, Scott PM, Clutario KM, Sluder G, et al. A USP28-53BP1-p53-p21 signaling axis arrests growth after centrosome loss or prolonged mitosis. J Cell Biol. 2016; 214: 143-53.
25. Meitinger F, Anzola JV, Kaulich M, Richardson A, Stender JD, Benner C, et al. 53BP1 and USP28 mediate p53 activation and G1 arrest after centrosome loss or extended mitotic duration. J Cell Biol. 2016; 214: 155-66.
26. Bothmer A, Robbiani DF, Di Virgilio M, Bunting SF, Klein IA, Feldhahn N, et al. Regulation of DNA end joining, resection, and immunoglobulin class switch recombination by 53BP1. Mol Cell. 2011; 42: 319-29.
27. Lottersberger F, Bothmer A, Robbiani DF, Nussenzweig MC, de Lange T. Role of 53BP1 oligomerization in regulating double-strand break repair. Proc Natl Acad Sci U S A. 2013; 110: 2146-51.
28. Zgheib O, Pataky K, Brugger J, Halazonetis TD. An oligomerized 53BP1 tudor domain suffices for recognition of DNA double-strand breaks. Mol Cell Biol. 2009; 29: 1050-8.
29. Wilson MD, Benlekbir S, Fradet-Turcotte A, Sherker A, Julien JP, McEwan A, et al. The structural basis of modified nucleosome recognition by 53BP1. Nature. 2016; 536: 100-3.
30. Huyen Y, Zgheib O, Ditullio RA, Jr., Gorgoulis VG, Zacharatos P, Petty TJ, et al. Methylated lysine 79 of histone H3 targets 53BP1 to DNA double-strand breaks. Nature. 2004; 432: 406-11.
31. Iwabuchi K, Basu BP, Kysela B, Kurihara T, Shibata M, Guan D, et al. Potential role for 53BP1 in DNA end-joining repair through direct interaction with DNA. J Biol Chem. 2003; 278: 36487-95.
32. Lo KW, Kan HM, Chan LN, Xu WG, Wang KP, Wu Z, et al. The 8-kDa dynein light chain binds to p53-binding protein 1 and mediates DNA damage-induced p53 nuclear accumulation. J Biol Chem. 2005; 280: 8172-9.
33. Barbar E. Dynein light chain LC8 is a dimerization hub essential in diverse protein networks. Biochemistry. 2008; 47: 503-8.
34. King SM. Dynein-independent functions of DYNLL1/LC8: redox state sensing and transcriptional control. Sci Signal. 2008; 1: pe51.
35. Matsuoka S, Ballif BA, Smogorzewska A, McDonald ER, 3rd, Hurov KE, Luo J, et al. ATM and ATR substrate analysis reveals extensive protein networks responsive to DNA damage. Science. 2007; 316: 1160-6.
36. Clark S, Myers JB, King A, Fiala R, Novacek J, Pearce G, et al. Multivalency regulates activity in an intrinsically disordered transcription factor. Elife. 2018; 7.
37. King A, Li L, Wong DM, Liu R, Bamford R, Strasser A, et al. Dynein light chain regulates adaptive and innate B cell development by distinctive genetic mechanisms. PLoS Genet. 2017; 13: e1007010.
38. Jurado S, Conlan LA, Baker EK, Ng JL, Tenis N, Hoch NC, et al. ATM substrate Chk2-interacting Zn2+ finger (ASCIZ) Is a bi-functional transcriptional activator and feedback sensor in the regulation of dynein light chain (DYNLL1) expression. J Biol Chem. 2012; 287: 3156-64.

39. Jurado S, Gleeson K, O'Donnell K, Izon DJ, Walkley CR, Strasser A, et al. The Zinc-finger protein ASCIZ regulates B cell development via DYNLL1 and Bim. J Exp Med. 2012; 209: 1629-39.
40. Loizou JI, Sancho R, Kanu N, Bolland DJ, Yang F, Rada C, et al. ATMIN is required for maintenance of genomic stability and suppression of B cell lymphoma. Cancer cell. 2011; 19: 587-600.
41. Brinkman EK, Chen T, Amendola M, van Steensel B. Easy quantitative assessment of genome editing by sequence trace decomposition. Nucleic Acids Res. 2014; 42: e168.
42. Wong DM, Li L, Jurado S, King A, Bamford R, Wall M, et al. The Transcription Factor ASCIZ and Its Target DYNLL1 Are Essential for the Development and Expansion of MYC-Driven B Cell Lymphoma. Cell Rep. 2016; 14: 1488-99.
43. Duarte AA, Gogola E, Sachs N, Barazas M, Annunziato S, J RdR, et al. BRCA-deficient mouse mammary tumor organoids to study cancer-drug resistance. Nat Methods. 2018; 15: 134-40.
44. Brummelkamp TR, Fabius AW, Mullenders J, Madiredjo M, Velds A, Kerkhoven RM, et al. An shRNA barcode screen provides insight into cancer cell vulnerability to MDM2 inhibitors. Nat Chem Biol. 2006; 2: 202-6.
45. Difilippantonio S, Gapud E, Wong N, Huang CY, Mahowald G, Chen HT, et al. 53BP1 facilitates long-range DNA end-joining during V(D)J recombination. Nature. 2008; 456: 529-33.
46. Ghezraoui H, Oliveira C, Becker JR, Bilham K, Moralli D, Anzilotti C, et al. 53BP1 cooperation with the REV7-shieldin complex underpins DNA structure-specific NHEJ. Nature. 2018; 560: 122-7.
47. Ward IM, Minn K, van Deursen J, Chen J. p53 Binding protein 53BP1 is required for DNA damage responses and tumor suppression in mice. Mol Cell Biol. 2003; 23: 2556-63.
48. Dev H, Chiang TW, Lescale C, de Krijger I, Martin AG, Pilger D, et al. Shieldin complex promotes DNA end-joining and counters homologous recombination in BRCA1-null cells. Nat Cell Biol. 2018; 20: 954-65.
49. Noordermeer SM, Adam S, Setiaputra D, Barazas M, Pettitt SJ, Ling AK, et al. The shieldin complex mediates 53BP1-dependent DNA repair. Nature. 2018; 560: 117-21.
50. Pfaffl MW. A new mathematical model for relative quantification in real-time RT-PCR. Nucleic Acids Res. 2001; 29: e45.
51. Pone EJ, Zhang J, Mai T, White CA, Li G, Sakakura JK, et al. BCR-signalling synergizes with TLR-signalling for induction of AID and immunoglobulin class-switching through the non-canonical NF-κB pathway. Nat Commun. 2012; 3: 767.
52. Rapsomaniki MA, Kotsantis P, Symeonidou IE, Giakoumakis NN, Taraviras S, Lygerou Z. easyFRAP: an interactive, easy-to-use tool for qualitative and quantitative analysis of FRAP data. Bioinformatics. 2012; 28: 1800-1.

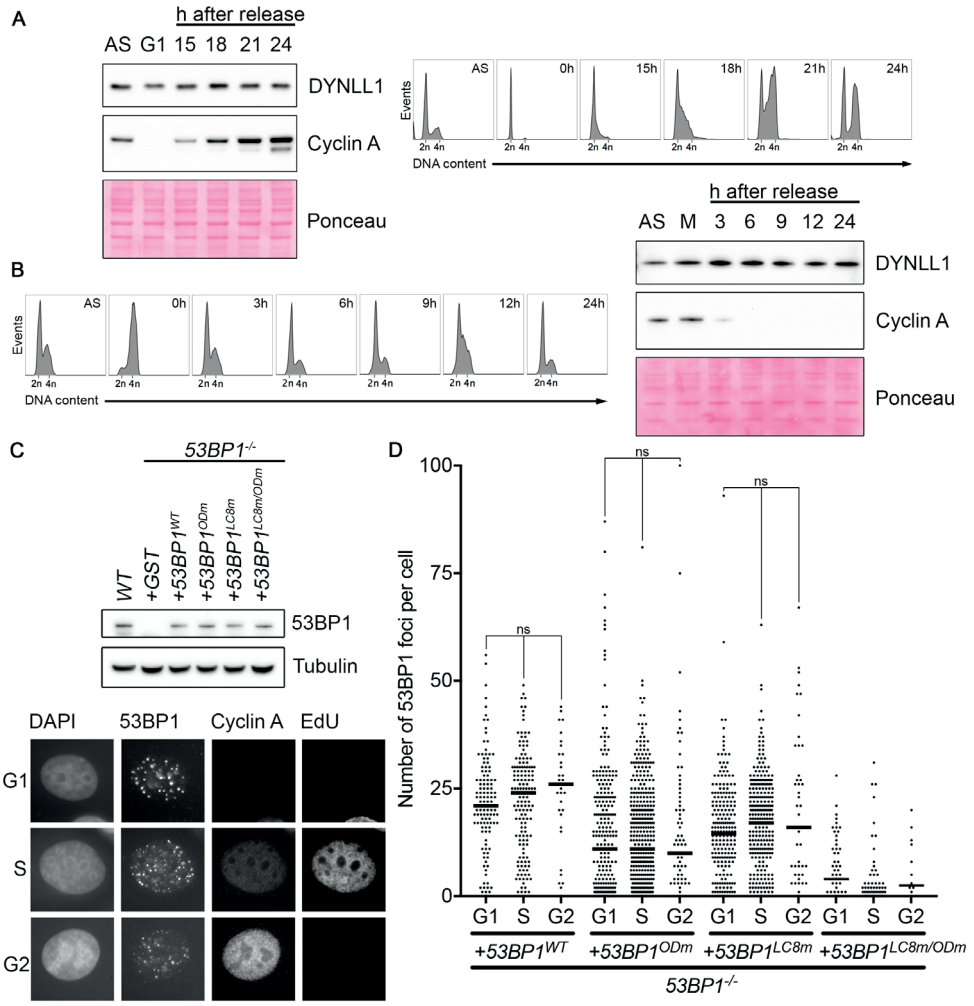
# Supplementary Figures



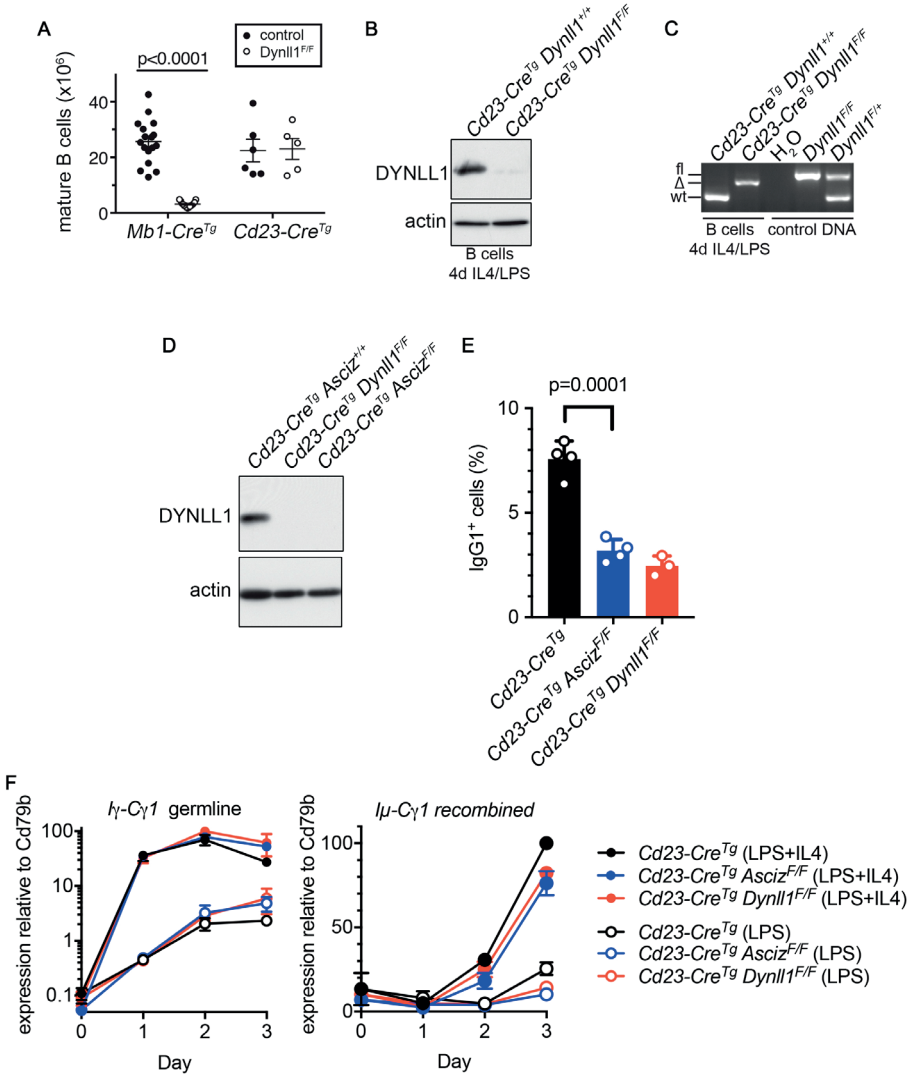

**SUPPLEMENTARY FIGURE 1 (RELATED TO FIGURE 1) | Screen of N-terminal 53BP1 truncations for IRIF formation.** *(A) 53BP1*$^{-/-}$ MCF-7 cells were transduced with lentivirus encoding the indicated FLAG-HA- 53BP1 alleles. The resulting cells were seeded on glass coverslips 48h before irradiation (5 Gy). Cells were fixed 4h after irradiation and stained with anti-HA and anti-H2AX antibodies. Images were acquired on a Zeiss LSM510 META confocal imaging system. *(B) 53BP1*$^{-/-}$ MCF-7 cells were stably transduced with mC2-f53BP1 (wild type) or mC2-f53BP1$^{LC8m}$. Cells were then transiently transfected with DsRed-DYNLL1 24 h before live imaging. Data, representative of *n=2* independent experiments. *(C)* FLAG-HA-53BP1 immuno-complexes were isolated from whole cell extracts prepared from HEK 293T cultures, 48 h following transfection with indicated control (GST) or 53BP1 expression plasmids. Representative data, *n=3* independent experiments. *(D)* Quantification of 53BP1 foci number in MCF7 *53bp1*$^{-/-}$ cells complemented with the indicated transgenes 4 h after 5 Gy irradiation. >139 nuclei were scored per condition. Black bar represents median value.



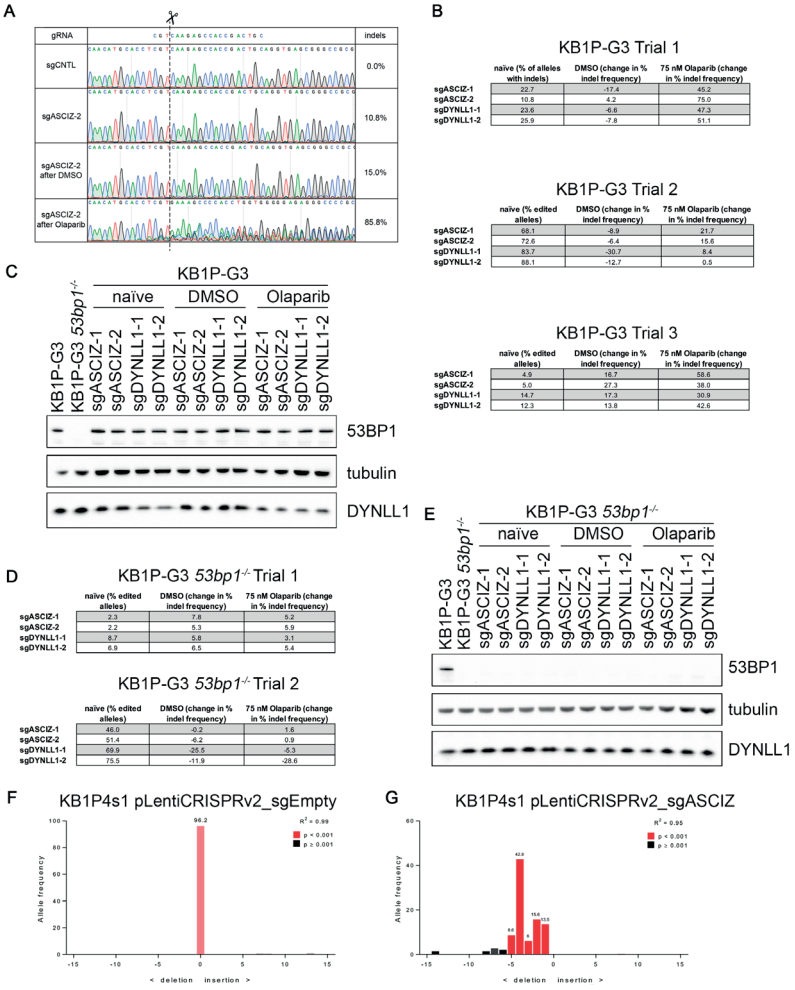

**SUPPLEMENTARY FIGURE 2 (RELATED TO FIGURE 1) | LC8 motif mutation does not intrinsically impair 53BP1 oligomerization or RIF1 foci formation.** *(A)* 53BP1 fragments encompassing the LC8 motifs and OD (a.a. 1131-1292) with C-terminal Smt3-$His_6$ tags were expressed in *E. coli* and purified using a TALON IMAC column. Wild type (LC8-OD), OD-mutated (ODm-LC8), LC8-mutated (OD-LC8m), or double mutant (LC8m- ODm) fragments were prepared in this manner and fractionated over a Superdex S200 column. *(B)* MCF-7 cells expressing either wild type 53BP1 or $53BP1^{LC8m}$ were irradiated (5 Gy) 4h prior to fixation and staining. Number of RIF1 and 53BP1 foci per cell in MCF-7 cells expressing either wild type 53BP1 or $53BP1^{LC8m}$ as indicated. Significance was determined by Mann-Whitney U Test. *(C)* Relative intensity of RIF1 and 53BP1 foci (arbitrary units). Foci number and intensity were quantified using Cell Profiler. Significance was determined by Mann-Whitney U Test. *(D)* Per nucleus integrated intensity of DYNLL1 signal. Related to Figure 1E. Black bars represent median values. *(E)* MCF-7 cells expressing FLAG-HA-$53BP1^{ODm}$ transduced with a CRISPR/Cas9 lentivirus co-expressing *DYNLL1*-specific sgRNA. Cultures were irradiated (5 Gy) 72h after infection and fixed 4h after irradiation. Fixed cells were probed with anti-HA and anti-DYNLL1 antibodies. Foci number and intensity were measured using CellProfiler. DYNLL1 signal intensity is binned into quartiles and sorted from lowest to highest intensity. Positive correlation between foci number and intensity was determined by ordinary 1-way ANOVA test for trend ($p < 0.0001$).



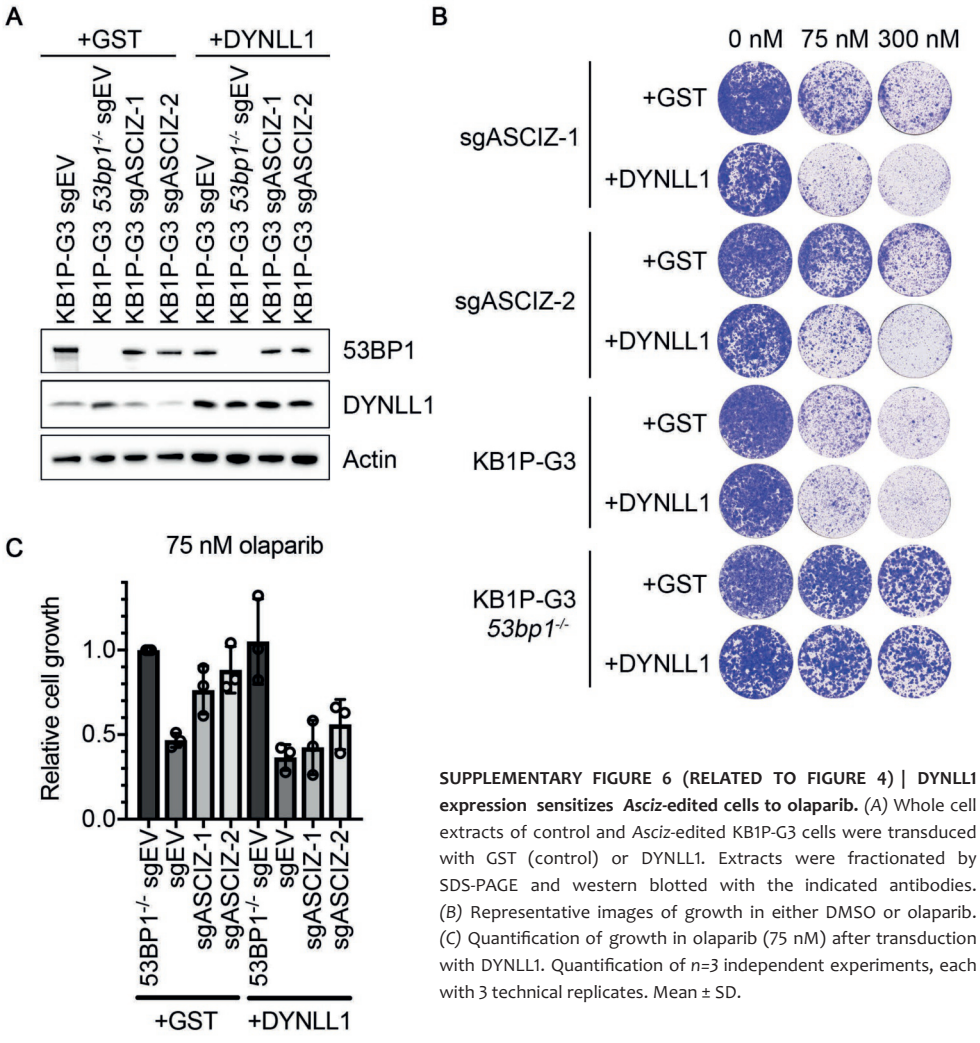

**SUPPLEMENTARY FIGURE 3 (RELATED TO FIGURE 1) | DYNLL1 regulation of 53BP1 is cell cycle-independent**. *(A)* RPE1 cells were released into serum containing medium from a G0 serum-arrest block (>95% G0 purity). Samples taken at the indicated time points were immunoblotted with indicated antibodies. DNA content was measured by propidium iodide staining and flow cytometry (right). *(B)* RPE1 cells synchronized in G2/M with nocodazole and mitotic shake-off, were released into mitosis, and protein samples collected at the indicated time points following nocodozole removal. DNA content was measured by propidium iodide staining and flow cytometry (left). *(C)* Western blot analysis of the cell lines utilized in *D*. Representative images of G1, S and G2 cells as discriminated by Cyclin A and EdU staining (below). *(D)* Quantification of 53BP1 foci number 4 h after 5 Gy irradiation. Significance was determined by Mann-Whitney U Test (*ns*, $p>0.05$).




**SUPPLEMENTARY FIGURE 4 (RELATED TO FIGURE 2) | DYNLL1 protein is undetectable in Δ*Dynll1* B cells.** *(A)* Quantification of mature B cell numbers in *Mb1-Cre*$^{Tg}$, *Mb1-Cre*$^{Tg}$ Dynll1$^{F/F}$, *Cd23-Cre*$^{Tg}$, and *Cd23-Cre*$^{Tg}$ *Dynll1*$^{F/F}$. Significance was determined by Mann-Whitney U Test. *(B)* Lysates prepared from *Cd23-Cre*$^{Tg}$ *Dynll1*$^{+/+}$ control and *Cd23-Cre*$^{Tg}$ *Dynll1*$^{F/F}$-deleted B cells were fractionated by SDS-PAGE and probed with anti-actin and anti-DYNLL1 antibodies as indicated. *(C)* PCR validation of complete *Dynll1*$^{F/F}$ recombination in mature *Cd23-Cre*$^{Tg}$ *Dynll1*$^{F/F}$ B splenocytes. *(D)* Lysates prepared from *Cd23-Cre*$^{Tg}$ *Asciz*$^{+/+}$ control, *Cd23-Cre*$^{Tg}$ *Asciz*$^{F/F}$*-deleted*, and *Cd23-Cre*$^{Tg}$ *Dynll1*$^{F/F}$*-deleted* B cells were fractionated by SDS-PAGE and probed with anti- actin and anti-DYNLL1 antibodies as indicated. *(E) In vitro* CSR to IgG1 in *Cd23-Cre*$^{Tg}$ *Asciz*$^{F/F}$, *Cd23-Cre*$^{Tg}$ *Dynll1*$^{F/F}$ and control *Cd23-Cre*$^{Tg}$ mature B splenocytes, 96 h following stimulation with LPS and IL-4. Data, *n*=4 mice. Significance was determined by unpaired two-tailed t test. *(F)* Relative expression of germline (left) and recombined (right) transcripts in purified B cells from *Cd23-Cre*$^{Tg}$, *Cd23-Cre*$^{Tg}$ *Asciz*$^{F/F}$, or *Cd23-Cre*$^{Tg}$ *Dynll1*$^{F/F}$ mice cultured with LPS (15 μg/mL) and IL-4 (1/100) for 0 to 3 days. Normalised to Cd79b loading control and expressed as a percentage of maximum signal. Data, *n*=2 mice per condition, mean ± range.




**SUPPLEMENTARY FIGURE 5 (RELATED TO FIGURE 4) | *DYNLL1* and *ASCIZ* gene-editing provides a growth advantage in olaparib treated *Brca1-/- p53-/-* tumour cells.** *(A)* Representative Sanger sequencing chromatograms generated from cell populations transduced with sgCNTL or sgASCIZ encoding virus and after outgrowth in DMSO or olaparib as indicated. *(B)* Additional independent trials of the experiment presented in Figure 4B. Percentage of edited alleles after transduction with the indicated gRNAs and antibiotic selection (naïve), after 8 days outgrowth in DMSO (negative control), or after 10 days outgrowth in the presence of olaparib (75 nM). *(C)* Whole cell extracts were isolated from KB1P-G3 cells after transduction with the indicated gRNAs and antibiotic selection (naïve), after 8 days outgrowth in DMSO (negative control), or after 10 days outgrowth in the presence of olaparib (75 nM). Extracts were fractionated by SDS-PAGE and probed with antibodies specific to the indicated antigens. *(D)* Additional independent trials of the experiment presented in Figure 4E. Percentage of edited alleles after transduction with the indicated gRNAs and antibiotic selection (naïve), after 8 days outgrowth in DMSO (negative control), or after 10 days outgrowth in the presence of olaparib (75 nM) is presented for 2 independent experiments (trials 2 and 3). *(E)* Whole cell extracts were isolated from KB1P-G3 *53bp1-/-* cells after transduction with the indicated gRNAs and antibiotic selection (naïve), after 8 days outgrowth in DMSO (negative control), or after 10 days outgrowth in the presence of olaparib (75 nM). Extracts were fractionated by SDS-PAGE and probed with antibodies specific to the indicated antigens. *(F)* and *(G)* TIDE analysis histograms of control *C* and ASCIZ-edited *D* organoids used for transplantation in Figure 4F-G.




**SUPPLEMENTARY FIGURE 6 (RELATED TO FIGURE 4) | DYNLL1 expression sensitizes *Asciz*-edited cells to olaparib.** *(A)* Whole cell extracts of control and *Asciz*-edited KB1P-G3 cells were transduced with GST (control) or DYNLL1. Extracts were fractionated by SDS-PAGE and western blotted with the indicated antibodies. *(B)* Representative images of growth in either DMSO or olaparib. *(C)* Quantification of growth in olaparib (75 nM) after transduction with DYNLL1. Quantification of *n=3* independent experiments, each with 3 technical replicates. Mean ± SD.

## Abstract

53BP1 is a chromatin-binding protein that regulates the repair of DNA double-strand breaks by suppressing the nucleolytic resection of DNA termini. This function of 53BP1 requires interactions with PTIP and RIF1, the latter of which recruits REV7 (also known as MAD2L2) to break sites. How 53BP1-pathway proteins shield DNA ends is currently unknown, but there are two models that provide the best potential explanation of their action. In one model the 53BP1 complex strengthens the nucleosomal barrier to end-resection nucleases, and in the other 53BP1 recruits effector proteins with end-protection activity. Here we identify a 53BP1 effector complex, shieldin, that includes C20orf196 (also known as SHLD1), FAM35A (SHLD2), CTC-534A2.2 (SHLD3) and REV7. Shieldin localizes to double-strand-break sites in a 53BP1- and RIF1-dependent manner, and its SHLD2 subunit binds to single-stranded DNA via OB-fold domains that are analogous to those of RPA1 and POT1. Loss of shieldin impairs non-homologous end-joining, leads to defective immunoglobulin class switching and causes hyper-resection. Mutations in genes that encode shieldin subunits also cause resistance to poly(ADP-ribose) polymerase inhibition in BRCA1-deficient cells and tumours, owing to restoration of homologous recombination. Finally, we show that binding of single-stranded DNA by SHLD2 is critical for shieldin function, consistent with a model in which shieldin protects DNA ends to mediate 53BP1-dependent DNA repair.

# Cancer Chess:

## The Shieldin Complex Mediates

# Molecular Insights

## 53BP1-Dependent DNA Repair

# Into PARPi Resistance

# Chapter 5

*Adapted from:*

*Sylvie M Noordermeer*, Salomé Adam*, Dheva Setiaputra*,* ***Marco Barazas****, Stephen J Pettitt, et al.*

**Contributed equally*

*Nature. 560(7716):117-121 (2018)*

## Main Text

53BP1 is a chromatin-binding protein that regulates DNA double-strand break (DSB) repair by suppressing the nucleolytic resection of DNA termini [1, 2]. This function of 53BP1 requires interactions with PTIP [3] and RIF1 [4-9], the latter also recruiting REV7/MAD2L2 to break sites [10, 11]. How 53BP1-pathway proteins shield DNA ends is unknown but two models best explain their action: in one model, the 53BP1 complex strengthens the nucleosomal barrier to end-resection nucleases [12, 13] , whereas in a second model, 53BP1 recruits effector proteins with end-protection activity. Here we describe the identification of such a 53BP1 effector complex, Shieldin, which includes C20orf196 (SHLD1), FAM35A (SHLD2), CTC-534A2.2 (SHLD3) and REV7. Shieldin localizes to DSB sites in a 53BP1- and RIF1-dependent manner and its SHLD2 subunit binds to ssDNA via OB-fold domains analogous to those of RPA1 and POT1. Loss of Shieldin impairs non-homologous end-joining (NHEJ), leads to defective immunoglobulin class switching and causes hyper-resection. Mutations in Shieldin subunit genes also cause resistance to poly(ADP-ribose) polymerase (PARP) inhibition in BRCA1-deficient cells and tumours due to restoration of homologous recombination (HR). Finally, we show that ssDNA binding by SHLD2 is critical for Shieldin function, consistent with a model where Shieldin protects DNA ends to mediate 53BP1-dependent DNA repair.

To discover proteins acting in the 53BP1 pathway, we searched for genes whose mutation restores HR in BRCA1-deficient cells leading to PARP inhibition resistance, a hallmark of 53BP1 deficiency [14-16]. We undertook three independent CRISPR/Cas9 screens that entailed the transduction of BRCA1-deficient cells with lentiviral libraries of single-guide (sg) RNAs (Supplementary Fig. S1A). The resulting pools of edited cells were exposed to near-lethal doses of two clinically used PARP inhibitors (PARPi), either olaparib or talazoparib [17]. We screened both an engineered human RPE1-hTERT *TP53*$^{-/-}$ *BRCA1*$^{-/-}$ cell line (hereafter referred to as RPE1 *BRCA1-KO*) and SUM149PT cells carrying a hemizygous *BRCA1* frameshift mutation. The gene-based results of the screens are found in Supplementary Table 1.

The genes coding for 53BP1 and for the uncharacterized protein C20orf196 were hits in all three screens (Fig. 1A). We also identified *SCAF1* and *ATMIN*, which encode an SR-family protein and a transcription factor, respectively (Fig. 1A). *PARP1* was a hit in the talazoparib-resistance screen, as expected [18], whereas genes coding for proteins acting upstream (H2AX, MDC1, RNF8 and RNF168) or downstream (RIF1) of 53BP1, were hits in the RPE1 *BRCA1-KO* screen (Supplementary Table 1). The presence of 53BP1 and 53BP1-pathway proteins suggested that these screens could reveal hitherto uncharacterized 53BP1 effectors.

In competitive growth assays (Fig. 1B), sgRNAs targeting *53BP1* led to outgrowth of *BRCA1-KO* cells in the presence of olaparib (Fig. 1C; genotyping information in Supplementary Table 2). Similarly, sgRNAs targeting *C20orf196*, *ATMIN* and *SCAF1* led

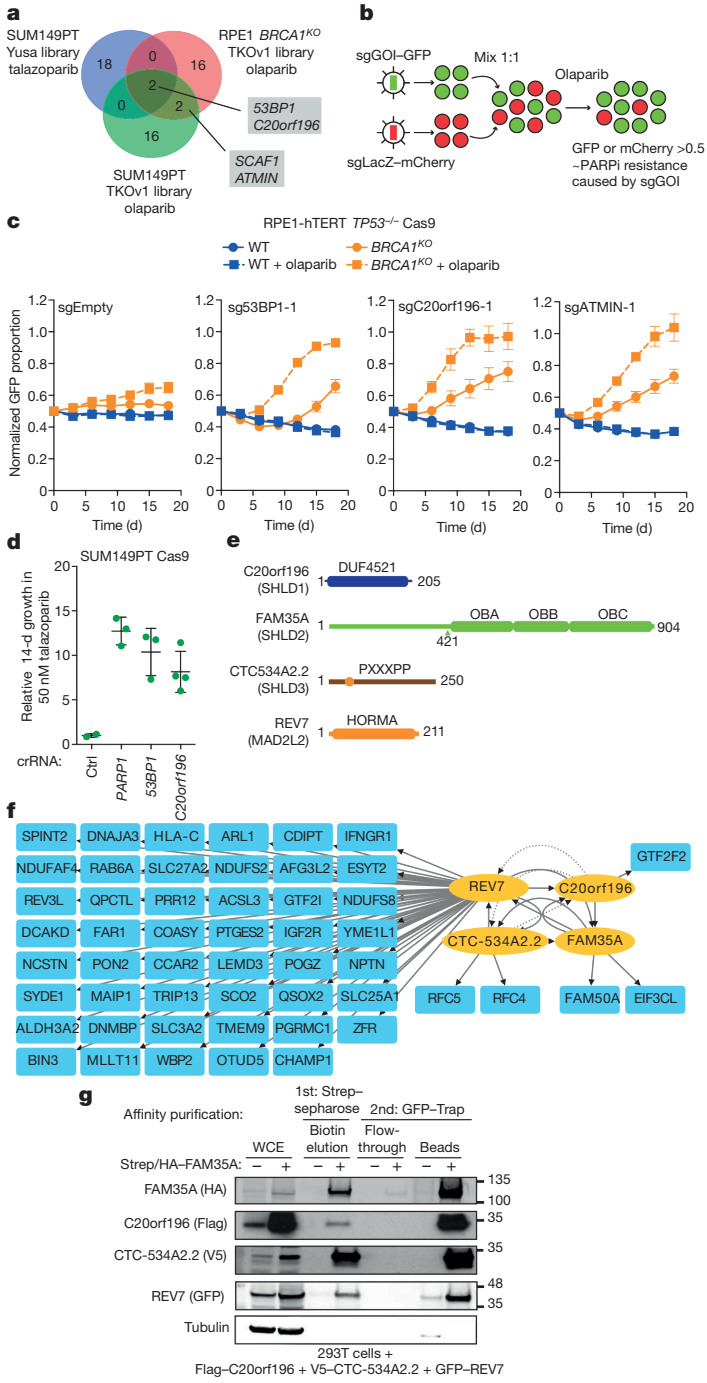



**FIGURE 1 | Identification of Shieldin.** *(A)* Venn diagram of the top 20 hits in each screen. *(B)* Schematic of the competitive growth assays. *(C)* Competitive growth assays ± olaparib (16 nM) in RPE1 *BRCA1-KO* cells. Data represents mean fraction of GFP positive cells ± SEM, normalized to day 0 (n = 3, independent transductions). *(D)* PARPi resistance caused by mutation of *C20orf196*. SUM149PT cells transfected with indicated crRNAs were treated with 50 nM talazoparib for 14 d. Relative growth was normalized to a non-targeting crRNA (CTRL). Bars represent mean ± SD of multiple crRNAs per gene (shown is a representative plot of 2 biologically independent experiments). *(E)* Domain architecture of Shieldin subunits. SHLD3 contains a REV7-binding PXXXPP motif [19]. *(F)* Protein interaction network surrounding REV7, C20orf196, FAM35A and CTC-534A2.2. Solid and dashed arrows represent interactions at an FDR of ≤1% and ≤5%, respectively. *(G)* Sequential affinity purifications from 293T cell lysates expressing the indicated proteins. Bound proteins were immunoblotted with the indicated antibodies (n = 2 independent experiments).

to PARPi resistance (Fig. 1C and Supplementary Fig. S1B). In parallel studies, transfection of tracrRNA and crRNAs targeting *C20orf196*, *53BP1* or *PARP1* caused talazoparib resistance in SUM149PT cells (Fig. 1D and Supplementary Fig. S1C). Since C20orf196 was identified as a hit in all three screens and validated in independent assays, we sought to determine its role in DNA repair.

C20orf196 is an uncharacterized protein of 205 amino acid residues (Fig. 1E) previously identified as a candidate REV7-interacting protein [20]. We used immunoprecipitation coupled to mass spectrometry (IP-MS) to expand the interaction network surrounding these proteins (Fig. 1F and Supplementary Table 3). One protein, FAM35A, was enriched in both C20orf196 and REV7 IP samples (Fig. 1F). FAM35A was striking due to the presence of three predicted OB-fold domains (OBA, OBB and OBC; Fig. 1E), reminiscent of those in the single-stranded (ss) DNA binding proteins RPA1 [21] and POT1 [22]. FAM35A IP-MS experiments recovered CTC-534A2.2, also identified in the REV7 IP-MS (Fig. 1F and Supplementary Table 3). CTC-534A2.2 is a protein encoded by an alternative mRNA emanating from the *TRAPPC13* locus (Fig. 1E and Supplementary Fig. S1D). sgRNAs against *CTC-534A2.2* were not present in either of our first-generation sgRNA libraries. IP-MS with CTC-534A2.2 recovered C20orf196, FAM35A and REV7 (Fig. 1F and Supplementary Table 3), suggesting that these proteins form a single protein complex, which was confirmed by sequential affinity purification of epitope-tagged C20orf196, CTC-534A2.2, FAM35A and REV7 (Fig. 1G).

*FAM35A*, *C20orf196* and *CTC-534A2.2* were identified in a fourth CRISPR/Cas9 screen employing a second-generation sgRNA library, TKOv2. This screen sought to identify genes promoting resistance to ionizing radiation (IR) in RPE1 cells (Supplementary Fig. S1E). 75 genes scored at a false discovery rate (FDR) <1% and this gene set was highly enriched in genes encoding NHEJ factors by gene ontology enrichment ($p= 1.11 \times 10^{-11}$, Fisher's exact test with multiple correction; Fig. 2A and Supplementary Table 4). *RIF1*, *FAM35A*, *C20orf196*, *CTC-534A2.2*, *53BP1* and *REV7* were all hits at FDR <1% (Fig. 2A). These data suggest that the complex formed by C20orf196, FAM35A, REV7 and CTC-534A2.2 promotes DSB repair by NHEJ. For reasons that will become apparent below, we named this complex Shieldin with C20orf196, FAM35A and CTC-534A2.2 renamed SHLD1, SHLD2 and SHLD3, respectively.

Independent sgRNAs targeting *SHLD2* or *SHLD3* caused sensitivity to the clastogen etoposide in competitive growth assays (Supplementary Fig. S1F) and caused resistance to olaparib in RPE1 *BRCA1-KO* cells, consistent with SHLD2/3 acting with REV7 and SHLD1 (Fig. 2B and Supplementary Fig. S1G). Clonal knockouts of *SHLD1* or *SHLD2* led to olaparib resistance in *BRCA1-KO* cells, with the *SHLD2-KO* resulting in a phenotype that approached that of 53BP1 loss (Fig. 2C). Similar results were obtained with 11 independent clonal knockouts of *SHLD1* in SUM149PT cells exposed to talazoparib (Supplementary Fig. S1H). Furthermore, expressing GFP-SHLD2 in *BRCA1-KO SHLD2-KO* cells restored olaparib sensitivity (Supplementary Fig. S1I). Resistance to PARPi in *BRCA1-KO* cells was likely due to restoration of HR, as measured both by RAD51 IR-induced focus

formation and by a reporter for gene conversion, the traffic light reporter assay [23] (Fig. 2D-E and Supplementary Fig. S2A-D).

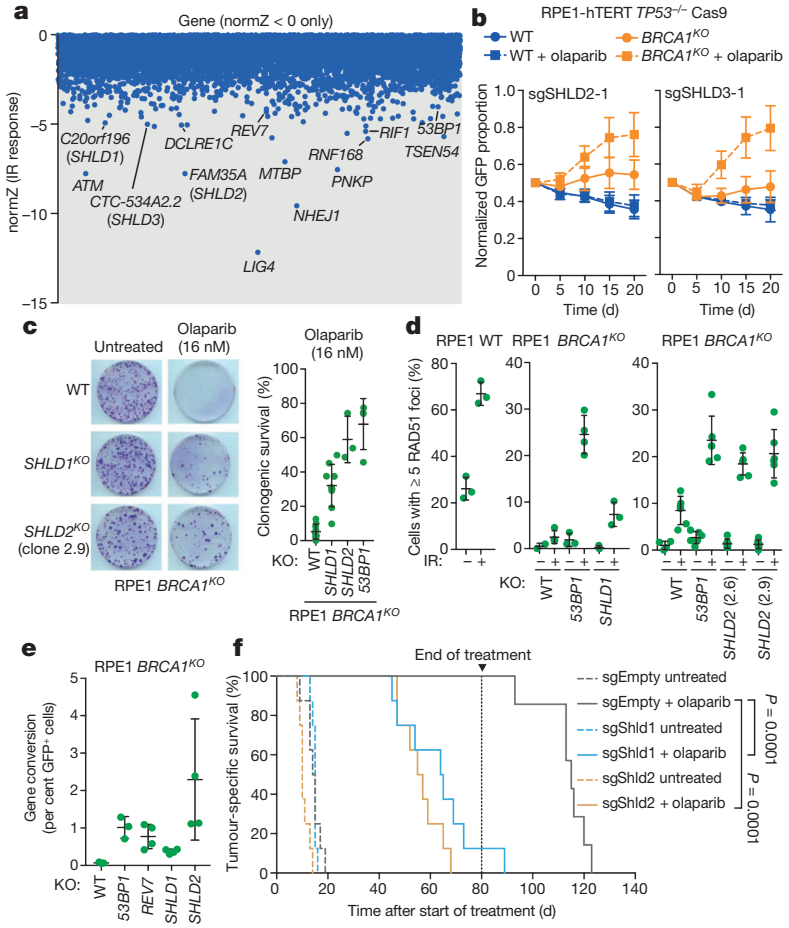



**FIGURE 2 | Shieldin loss promotes PARPi resistance in cell and tumor models of *BRCA1*-deficiency.** *(A)* CRISPR dropout screen results in RPE1 WT cells exposed to IR. Shown are gene-level normZ scores <0. *(B)* Competitive growth assays using olaparib (16 nM) in RPE1 *BRCA1-KO* cells. Data is presented as mean ± SD, normalized to day 0 (n = 3, independent transductions). *(C)* Clonogenic survival in response to 16 nM olaparib. Representative images are shown (left) and quantified (right). Bars represent mean ± SD (n=9: RPE1 WT and *BRCA1-KO SHLD1-KO*; n=3: *BRCA1-KO SHLD2-KO*, n=4: *BRCA1-KO 53BP1-KO*; biologically independent experiments). *(D)* Quantitation of cells with ≥5 RAD51 foci ± 10 Gy IR (6 h recovery). Biologically independent experiments are shown and the bar represents the mean ± SD. From left to right, the number of replicates was n=3 and n=3 (left panel); n=3, n=4, n=3, n=4, n=3 and n=3 (middle panel); and n=4, n=6, n=6, n=6, n=6, n=6, n= 6 and n=6 (right panel). *(E)* Assessment of gene conversion by traffic light reporter assay. Biologically independent experiments are shown and the bar represents the mean ± SD (n=3 for WT and *53BP1-KO*; n=4 for *SHLD1-KO, SHLD2-KO,* and *REV7-KO*). *(F)* Kaplan-Meier curve showing tumor-specific survival of mice transplanted with KB1P4 tumor organoids ± olaparib treatment for 80 d (n = 8 per treatment; editing efficiencies found in Supplementary Table 2). P-values were calculated using a log-rank test (Mantel-Cox).

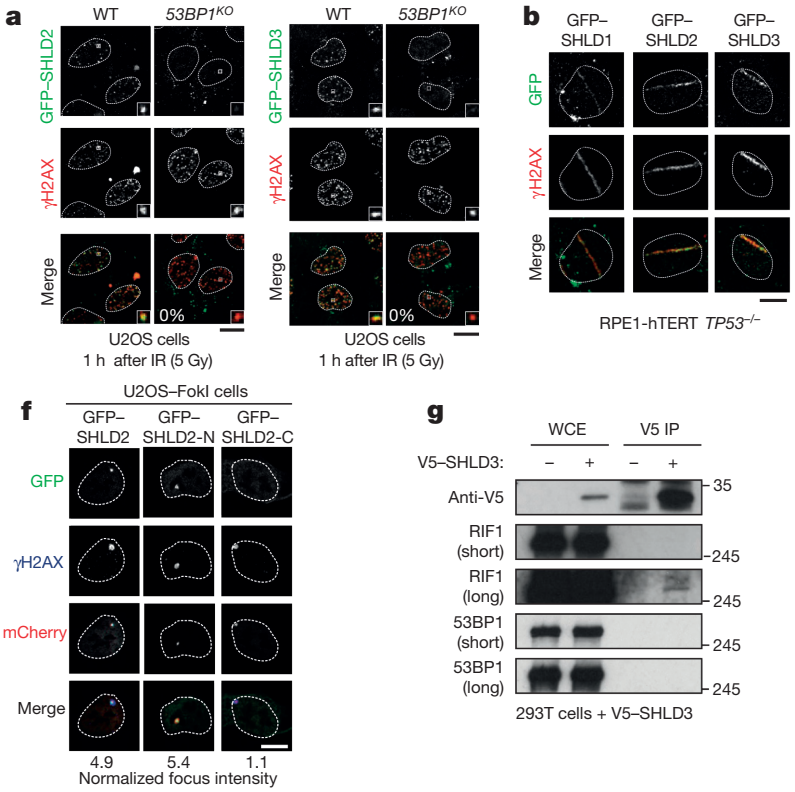
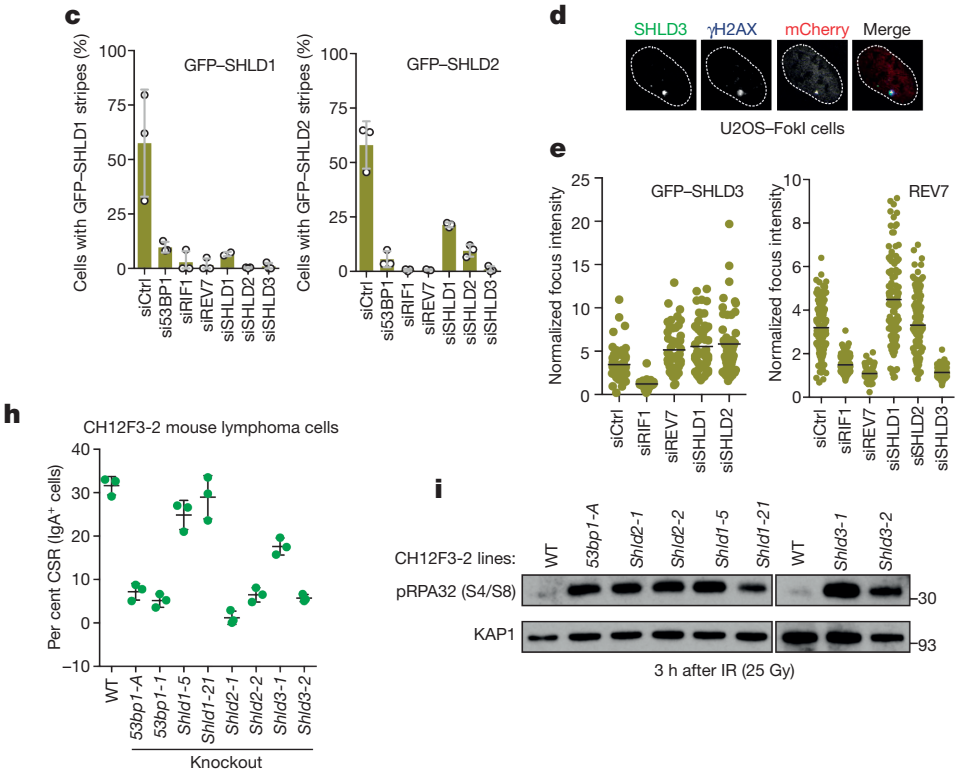



**FIGURE 3 | Shieldin accumulates at DSB sites downstream of 53BP1-RIF1 and promotes class switch recombination.** *(A-B)* Representative micrographs of Shieldin subunit accumulation into IR-induced foci in U2OS cells *A* or at laser-microirradiation sites in RPE1 cells *B* (n=3 biologically independent experiments. *(C)* Quantitation of *B*. Points represent individual experiments counting ≥100 cells. Bar represents mean ± SD. *(D)* Colocalization of GFP-tagged Shieldin subunits with mCherry foci in U2OS-FokI cells upon mCherry-LacR-FokI expression. *(E)* Quantitation of GFP-SHLD3 or endogenous REV7 focus intensity. Each point represents a cell. Line represents the mean. Data is the aggregate of two biological replicates with a total of 50 and 120 (GFP-SHLD3 and REV7, respectively), 45 and 122, 48 and 112, 54 and 116, 49 and 111, and 117 cells counted for siCTRL, siRIF1, siREV7, siSHLD1, siSHLD2 and siSHLD3, respectively. *(F)* mCherry-LacR-FokI colocalization with GFP-SHLD2, SHLD2N, and SHLD2C. Mean normalized focus intensity is shown with a total of 52 (SHLD2 and SHLD2N) or 53 (SHLD2C) cells counted (n=2, biologically independent experiments). *(G)* RIF1 co-immunoprecipitation with V5-SHLD3 (representative of two independent experiments). *(H)* CSR analysis of CH12F3-2 cells following stimulation. Data is represented as the mean ± SD (n=3 biologically independent replicates). *(I)* Irradiated (25 Gy) CH12F3-2 clones were immunoblotted for RPA2 phosphorylation (representative of three biological replicates).

Next, we tested whether loss of Shieldin causes PARPi resistance in the KB1P mouse mammary tumor model deficient in *Brca1* and *Trp53* (p53) [24]. sgRNAs targeting *Shld1* and *Shld2* led to PARPi resistance in clonogenic survival assays in KB1P-G3 mammary tumor cells and in *Brca1*$^{-/-}$; *Trp53*$^{-/-}$ mouse embryonic stem (mES) cells (Supplementary Fig. S3A-C). This resistance was also associated with restoration of HR (Supplementary Fig. S3B). Furthermore, transduction of *Shld1*- and




*Shld2*-targeting sgRNAs suppressed the cell lethality associated with *Brca1* loss in p53-proficient mES cells (Supplementary Fig. S3D). We transduced the same sgRNAs into KB1P4 mammary tumor organoids (Supplementary Table 2) and implanted them into the fat pads of mice. Olaparib treatment was initiated when tumors reached 50-100 $mm^3$ and was continued for 80 days. While all untreated mice succumbed to excessive tumour burden within 20 days, the control group responded to olaparib for the duration of the treatment (Fig. 2F). However, mice implanted with *Shld1*- and *Shld2*-mutated tumours exhibited a partial response to olaparib, with mice succumbing by day 60 (Fig. 2F). We conclude that Shieldin loss causes PARPi resistance in both human and mouse BRCA1-deficient tumour cells by reactivating HR.

As expected of a complex with a direct role in DSB repair, Shieldin accumulates at DSB sites in a 53BP1/RIF1-dependent manner (Fig. 3A-F and Supplementary Fig. S4A-D). Loss of Shieldin components did not impair formation of 53BP1 or RIF1 IR-induced foci, indicating that Shieldin acts downstream of 53BP1-RIF1 (Supplementary Fig. S4E-F). Consistent with this possibility, we observed genetic epistasis between *53BP1* and the Shieldin genes using the RAD51 focus formation assay in RPE1 *BRCA1-KO cells* (Supplementary Fig. S5A). We also observed

that *SHLD1* and *53BP1* were epistatic in terms of modulating talazoparib resistance in SUM149PT cells (Supplementary Fig. S5B).

Analyses of the dependencies within the Shieldin complex indicate that SHLD3 is the most apical component followed by REV7, SHLD2, and then SHLD1 (Fig. 3C-E, Supplementary Fig. S4A-D, Supplementary Fig. S6, Supplementary Fig. S7C-E and Supplementary Document 1 for mapping details). Indeed, SHLD3 interacts with RIF1, suggesting that it recruits Shieldin to chromatin-bound 53BP1-RIF1 (Fig. 3G and Supplementary Fig. S7F). Further mapping studies suggest that Shieldin consists of a DSB-recruitment module composed of SHLD3-REV7 that binds to the N-terminus of SHLD2 (residues 1-50; Supplementary Fig. S6, Supplementary Fig. S7A-C), and a presumptive DNA-binding module (SHLD2-SHLD1) featuring the OB-fold domains at the SHLD2 C-terminus (SHLD2C residues 421-904; Supplementary Fig. S7A).

To assess the role of Shieldin in NHEJ, we first analyzed class switch recombination (CSR) in CH12F3-2 cells [25]. Mutation of each of the Shieldin subunits compromised CSR, with *Shld1*-edited cells having a reproducibly milder phenotype (Fig. 3H and Supplementary Fig. S8A-C). *Shld2-KO* was epistatic with both *53bp1-KO* and *Shld1-KO* mutations, consistent with them acting in the same genetic pathway (Supplementary Fig. S8B-C). The expression of AID, which initiates CSR, was not altered in Shieldin mutants, consistent with NHEJ deficiency (Supplementary Fig. S8D). Supporting this possibility, *SHLD1* and *SHLD2* mutations impaired random plasmid integration, which occurs largely through NHEJ [26], to an extent similar to that of 53BP1-deficient cells (Supplementary Fig. S8E-F).

The loss of each Shieldin subunit led to IR-induced RPA2 Ser4/Ser8 phosphorylation, a surrogate marker of end-resection [21], suggesting that Shieldin protects DNA ends (Fig. 3I and Supplementary Fig. S8G). Supporting this hypothesis, restoration of HR in Shieldin-defective KB1P-G3 cells was dependent on ATM activity (Supplementary Fig. S3A-B), which promotes DNA end-resection in the absence of 53BP1 [15] or REV7 [11]. In an accompanying paper, Mirman *et al*. [27] show that *Shld2*-mutated cells have increased end-resection at dysfunctional telomeres. Shieldin therefore antagonizes end-resection.

We surmised that if Shieldin is a downstream effector of 53BP1, artificially targeting Shieldin to DSB sites should rescue phenotypes associated with 53BP1 loss. To do this, we fused SHLD2 to the RNF8 FHA domain, which is recruited to damaged chromatin independently of 53BP1 (Fig. 4A). We found that the FHA-dependent targeting of SHLD2 to DSB sites suppressed RAD51 IR-induced focus formation in *BRCA1-KO 53BP1-KO* cells (Fig. 4B and Supplementary Fig. S9A). These results suggest that SHLD2 mediates 53BP1-dependent DNA repair.

We observed that the FHA-SHLD2C protein, which contains the OB-fold domains, potently suppressed RAD51 recruitment to DSB sites in *BRCA1-KO 53BP1-KO* cells (Fig. 4B and Supplementary Fig. S9A). This result suggested that DNA binding might underpin the effector function of the SHLD2 C-terminus. To test for DNA

binding activity, we affinity-purified SHLD2C in the presence or absence of SHLD1 (Supplementary Fig. S9B). We observed SHLD2C binding to a radiolabeled ssDNA probe by electrophoretic mobility shift assays (EMSA), and competition with unlabeled oligonucleotides revealed that SHLD2C preferentially binds to ssDNA over dsDNA (Fig. 4C). While SHLD1 is not essential for SHLD2C DNA-binding, its presence increased the amount of SHLD2C purified, and the retarded complex displayed a difference in mobility consistent with the SHLD2C-SHLD1 complex binding to ssDNA (Fig. 4D, lanes 2 vs 5). We estimate the binding affinity of the SHLD2C-ssDNA interaction to be ~10 nM (Fig. 4E and Supplementary Fig. S9C). We conclude that SHLD2 possesses ssDNA-binding activity.

To explore whether ssDNA-binding is involved in Shieldin function, we generated four mutant versions (m1-m4) of the SHLD2 OB-folds by modeling the SHLD2 C-terminus on an RPA1 structure (PDB 4GNX; Supplementary Fig. S9D) [28]. We also employed a splice variant of SHLD2 that disrupts OBB, which we refer to as SHLD2S. We found that

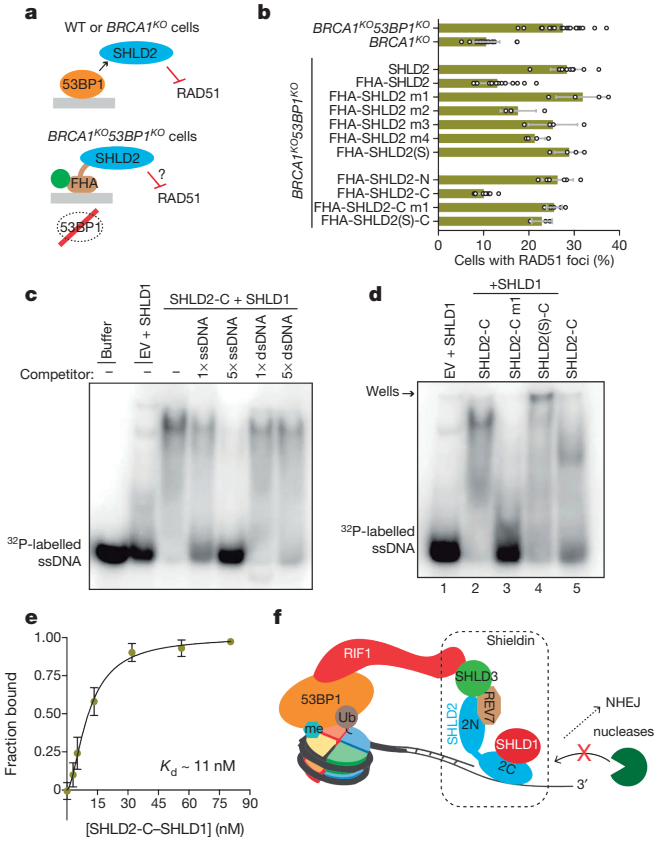



**FIGURE 4 | Shieldin is an effector of 53BP1 by binding ssDNA.** *(A)* Schematic for artificially targeting Shieldin to DSB sites. *(B)* RAD51 IRIF formation 3 h following 10 Gy irradiation in *BRCA1-KO 53BP1-KO* cells expressing the indicated fusion proteins. The bar represents the mean ± SD. From top to bottom the number of biologically independent experiments was n=20, n=22, n=12, n=12, n=16, n=4, n=4, n=4, n=4, n=6, n=6 and n=3. *(C)* EMSA of the SHLD2C-SHLD1 complex isolated from 293T cells (see Supplementary Fig. S9B) incubated with radiolabeled ssDNA ± unlabelled oligonucleotides (n=2 independent experiments). EV refers to empty vector. *(D)* EMSA of SHLD2C WT and variants (n=4 independent experiments). *(E)* Determination of SHLD2C-SHLD1 ssDNA binding dissociation constant ($K_d$). Mean values are presented ± SD (n=3 independent experiments). Representative EMSA shown in Supplementary Fig. S9C. *(F)* Model of Shieldin function. We speculate that the SHLD2 OB-fold domains bind to ssDNA at DSB sites to suppress resection and favour NHEJ.

the m1 and SHLD2S mutants, either in the context of full-length or SHLD2C proteins, were unable to suppress RAD51 focus formation in *BRCA1-KO 53BP1-KO* cells when fused to the RNF8 FHA domain (Fig. 4B and Supplementary Fig. S9A). Expression of full-length SHLD2-m1 and SHLD2S in *BRCA1-KO SHLD2-KO* cells also failed to suppress RAD51 IR-induced focus formation, unlike wild-type SHLD2 (Supplementary Fig. S10A-B). Importantly, both mutants localized to DSB sites (Supplementary Fig. S10C-D) and interacted with the other members of the Shieldin complex (Supplementary Fig. S10E). Therefore, the SHLD2-m1 and SHLD2S mutants are defective in suppressing HR.

Strikingly, the SHLD2C-m1 mutant was completely defective in ssDNA binding (Fig. 4D, lane 3) whereas the SHLD2C-S mutant displayed reduced and aberrant ssDNA-binding behaviour (Fig. 4D, lane 4). Since the m1 mutation produces a protein defective both in ssDNA-binding and suppression of HR, but which is proficient in both complex assembly and DSB recruitment, we conclude that ssDNA binding by Shieldin is critical for 53BP1-dependent DSB repair.

In conclusion, the identification of Shieldin forces us to re-evaluate how DNA end stability is regulated in vertebrates. Indeed, our results are consistent with a model in which Shieldin is the ultimate mediator of 53BP1-dependent DNA repair by binding ssDNA and occluding access to resection nucleases (Fig. 4F). Our discovery of Shieldin also has implications for the management of *BRCA1*-mutated malignancies, as alterations in Shieldin-coding genes may cause clinical resistance to PARP inhibitors.

## Materials and Methods

*Plasmids*

DNA corresponding to sgRNAs were cloned into pX330 (Addgene: 42230, Cambridge, MA, USA), LentiGuide-Puro (Addgene: 52963), LentiCRISPRv2 (Addgene: 52961), or a modified form in which Cas9 was replaced by NLS-tagged GFP or mCherry using *Age*I and *Bam*HI (designated as LentiGuide-NLS-GFP or –mCherry), as described [19, 29, 30]. Sequences of the sgRNAs used in this study are included in Supplementary Table 5. Coding sequences of C20orf196 and the short isoform of FAM35A were obtained from the ORFeome collection (horfdb.dfci.harvard.edu/), archived in the Lunenfeld-Tanenbaum Research Institute's OpenFreezer [31]. The complete coding sequence of the long isoform of FAM35A was generated by combining a synthesized fragment (GeneArt, Regensburg, Germany) corresponding to the long isoform C-terminus using an internal KpnI restriction site. The coding sequence of CTC534A2.2 was generated by gene synthesis (GeneArt). The coding sequences were PCR amplified using AscI and ApaI flanking primers and cloned into pcDNA5-FRT/TO-eGFP and pcDNA5-FRT/TO-Flag to obtain N-terminally tagged FAM35A, C20orf196 and CTC534A2.2. pGLUE-HA-Strep-FAM35A was generated by PCR amplification of the long isoform of FAM35A and cloning into pGLUE (Addgene: 15100) using *Asc*I and *Not*I. To generate FAM35A

fragments and mutants, standard protocols for primer-directed mutagenesis or self-ligation of truncated PCR-products were used. To generate pcDNA5-FRT/TO-V5-CTC534A2.2, eGFP was replaced by a V5 tag in the cloning vector pcDNA5-FRT/TO-eGFP using *Kpn*I and *Asc*I restriction enzymes after which the coding sequence for CTC534A2.2 was PCR-amplified and inserted into pcDNA5-FRT/TO-V5-MCS using *Asc*I and *Xho*I restriction enzymes.

To generate RNF8-FHA fusions, the N-terminus of RNF8 (aa 1-160) was PCR amplified from pcDNA3-RNF8-FHA(1-160)-RNF168 with flanking AscI sites and inserted into pcDNA5-FRT/TO-eGFP-FAM35A. eGFP-(FHA-) fusions of FAM35A were introduced into pCW57.1 (Addgene: 41393) by Gateway cloning using the pDONR221 donor vector. FAM35A amino acid substitution mutations and deletions were introduced by site directed mutagenesis and deletion PCR, respectively.

The REV7 coding sequence was obtained from the ORFeome collection and was cloned into the pDEST-FRT/TO-eGFP vector using Gateway cloning and into the pcDNA5-FRT/TO-Flag vector by PCR amplification. The N-terminal 967 residues of RIF1 were amplified by PCR and cloned into the pDONR221 vector using Gateway technology. The fragment was then integrated into the pDEST-mCherry-LacR vector by Gateway cloning. Plasmids for the traffic light reporter system were obtained from Addgene (pCVL-TrafficLightReporter-Ef1a-Puro lentivirus: #31482; pCVL-SFFV-d14GFP-Ef1a-HA-NLS-Sce(opt)-T2A-TagBFP: #32627).

*Cell lines and gene editing*

293T and RPE1 hTERT cell lines were obtained from ATCC (Manassas, VA, USA), 293 Flp-In cells were obtained from Invitrogen (Carlsbad, CA, USA) and SUM149PT [32] cells were obtained from Asterand Bioscience (Detroit, MI, USA). U2OS ER-mCherry-LacIFokI-DD cells (U2OS-265, referred to in the text as U2OS-FokI) were a kind gift of R. Greenberg (University of Pennsylvania, Philadelphia, PA, USA). All cell lines are routinely authenticated by STR-analysis and tested negative for mycoplasma. 293T, 293 Flp-In, U2OS and RPE1 cells were cultured in high glucose- and GlutaMAX-supplemented DMEM (Gibco, Thermo Fisher Scientific, Waltham, MA, USA) + 1% Penicillin / Streptomycin (Thermo Fisher Scientific) and 10% heat inactivated fetal calf serum (Wisent, St-Bruno, Canada) at 37°C, 5% $CO_2$. SUM149PT cells were cultured in Ham's F12 medium (Gibco) supplemented with 5% FCS, 10 mM HEPES, 1 µg/mL hydrocortisone (Sigma-Aldrich, St. Louis, MI, USA), and 5 µg/mL insulin (Sigma-Aldrich) at 37°C, 5% $CO_2$. Except for RPE1 clonogenic survival assays, which were performed at 3% $O_2$, cells were kept under normoxia conditions. Transient transfections of DNA and siRNA were performed using Lipofectamine 2000 (Thermo Fisher Scientific), PEI (Sigma-Aldrich) or calcium phosphate and Lipofectamine RNAiMAX, respectively (Thermo Fisher Scientific). siRNA efficiency was analysed by qPCR and immunoblotting. Stable integration of Flag-C20orf196/FAM35A/REV7 with the Flp-In system was achieved by co-transfection of the pcDNA5-

FRT/TO plasmid with the recombinase vector pOG44 (Thermo Fisher Scientific) and hygromycin selection for integration. Lentiviral particles were produced in 293T cells by co-transfection of the targeting vector with vectors expressing VSV-G, RRE and REV using calcium phosphate or PEI (Sigma-Aldrich). Viral transductions were performed in the presence of 4-8 μg/μL polybrene (Sigma-Aldrich) at an MOI <1, unless stated otherwise. Transduced RPE1 cells were selected by culturing in the presence of 15 μg/mL puromycin. For the BRCA1-deficient mouse cell experiments, all experiments were performed using virus produced with the LentiCRISPRv2 backbone (see Supplementary Table 5) and cells were infected using polybrene (8 μg/mL). The medium was refreshed after 12 h and transduced cells were selected with puromycin.

The generation of RPE1 hTERT *TP53*$^{-/-}$ *BRCA1-KO* Cas9 cells has been described elsewhere [33]. *REV7*, *53BP1*, *FAM35A* and *C20orf196* gene knockouts were generated by electroporation of LentiGuide or LentiCRISPRv2 vectors using a Lonza Amaxa II Nucleofector (Basel, Switzerland) (for sgRNA sequences employed see Supplementary Table 5; REV7 - sgRNA1, FAM35A - sgRNA2 and C20orf196 - sgRNA1 were used for clonal knockout generation). 24 h following transfection, cells were selected for 24-48 h with 15 μg/mL puromycin, followed by single clone isolation. Triple knockout cell lines of *TP53*, *BRCA1* and *53BP1* were created by mutating *BRCA1* from the *TP53*$^{-/-}$ *53BP1-KO* double knockout cell line. Triple knockout cell lines of *TP53*, *BRCA1* and *REV7*, *FAM35A* or *C20orf196* were created by mutating *REV7*, *FAM35A* or *C20orf196* in the *TP53*$^{-/-}$ *BRCA1-KO* cells. Loss of protein(s) was verified by immunoblotting when antibodies were available. Gene mutations were further confirmed by PCR amplification and TIDE analysis [34] (for primers used for genomic PCR, see Supplementary Table 6, for genomic editing information, see Supplementary Table 2).

To generate SUM149PT *53BP1*, *PARP1* or *C20orf196* knockout populations of cells, SUM149PT-doxCAS9 cells were treated with doxycycline for 24 h at 1 μg/ml prior to transfection with EditR crRNA (Dharmacon, Lafayette, CO, USA). Transfection of guides 53BP1_5_1, 53BP1_5_3, PARP1_5_2, PARP1_5_4, C20orf196_5-1, C20orf196_5-2, C20orf196_5-3 and C20orf196_5-5 (see Supplementary Table 5) was performed at a concentration of 20 nM (crRNA:tracrRNA) in the presence of doxycycline (1 μg/ml) using Lipofectamine RNAiMAX in 48-well plates (35,000 cells per well). The following day cells were split 1:3, fed 24 h later with media supplemented with 50 nM talazoparib (without doxycycline) and kept in batch culture or further split to generate single cell colonies. Drug-containing media was replenished every 3-4 d until PARP inhibitor resistant pools or clones were established. Clones were subsequently picked, expanded and validated by genomic PCR and sequence analysis (for primers used, see Supplementary Table 6, for genomic editing information, see Supplementary Table 2). Four SUM149PT *C20orf196-KO* clones with mutations were chosen for further experimentation: clone A (C20orf196 5-1-C1), clone B (C20orf196 5-1-C2), clone C (C20orf196 5-3-C5) and clone D (C20orf196 5-5-C4).

To generate *53BP1-KO* double mutant clones, SUM149PT *C20orf196* clones A and D were infected with a lentivirus expressing an sgRNA targeting *TP53BP1* or a non-targeting control sgRNA (for sequences, see Supplementary Table 5) in media containing 1 µg/ml doxycycline. 48 h after infection, puromycin (1 µg/ml) was added to the media. Selection was maintained for 3 d, until the uninfected control cells were killed. Pools of selection-resistant cells were seeded into 384-well plates for short term survival assays (see below) or subcloned to generate clonal lines.

Mouse ES cells with a selectable conditional *Brca1* deletion (*Rosa26*$^{CreERT2/wt}$;*Brca1*$^{SCo/\Delta}$) [35] were cultured on gelatin-coated plates in 60% buffalo red liver (BRL) cell-conditioned medium supplied with 10% fetal calf serum, 0.1 mM β-mercaptoethanol (Merck, Kenilworth, NJ, USA) and $10^3$ U/ml ESGRO LIF (Millipore, Burlington, MA, USA) under normal oxygen conditions (21% $O_2$, 5% $CO_2$, 37 °C).

The KB1P-G3 2D cell line was previously established from a *Brca1*$^{-/-}$ *p53*$^{-/-}$ mouse mammary tumor and cultured as described [16]. Briefly, cells were cultured in DMEM/F-12 medium (Life Technologies, Carlsbad, CA, USA) in the presence of 10% FCS, penicillin/streptomycin (Gibco), 5 µg/mL insulin (Sigma-Aldrich), 5 ng/mL epidermal growth factor (Life Technologies) and 5 ng/mL cholera toxin (Gentaur, Kampenhout, Belgium) under low oxygen conditions (3% $O_2$, 5% $CO^2$ at 37 °C).

The KB1P4 3D tumor organoid line was previously established from a *Brca1*$^{-/-}$ *p53*$^{-/-}$ mouse mammary tumor and cultured as described [36]. Cells were seeded in Basement Membrane Extract Type 2 (BME, Trevigen, Gaithersburg, MD, USA) on 24-well suspension plates (Greiner Bio-One, Kremsmünster, Austria) and cultured in AdDMEM/F12 supplemented with 10 mM HEPES (Sigma-Aldrich), GlutaMAX (Invitrogen), penicillin/streptomycin (Gibco), B27 (Gibco), 125 µM N-acetyl-L-cysteine (Sigma-Aldrich), and 50 ng/mL murine epidermal growth factor (Invitrogen).

CH12F3-2 mutant clones were edited either through transient transfection with pX330 plasmid constructs expressing sgRNAs against *Trp53bp1* (sgRNA: *Trp53bp1*_e6_834, see Supplementary Table 5), *Fam35a*, and *Ctc534a2.2* or by lentiviral lentiCRISPR v2 transduction for *C20orf196*. Double knock-out cell lines of *Fam35a* and *Trp53bp1* or *C20orf196* were generated by transient transfection of a pX330 plasmid expressing an sgRNA against *Trp53bp1* or by lentiviral transduction with lentiCRISPRv2 with an sgRNA targeting *C20orf196*.

*Antibodies, siRNAs and drugs.*

An overview of all the antibodies used in this study, including dilution factors, can be found in Supplementary Table 7. The following siRNAs from Dharmacon were used in this study (final siRNA concentration: 10 or 20nM): 53BP1: siRNA #2 (D-003548-02-0020); RIF1: siGENOME RIF1 siRNA (D-027983-02-0050); REV7: siGENOME MAD2L2 siRNA (M-003272-03-0010); C20orf196: SMARTpool: siGENOME C20orf196 siRNA (M-018767-00-0005); FAM35A: SMARTpool: siGENOME FAM35A siRNA (M-013761-01-0005);

CTC534A2.2 (custom order): siRNA#1: 5'-GGACAAAACUCAAUCAAAU-3', siRNA#2: 5'-CAGUAGAUCUAUUGGAGUU-3', siRNA#3: 5'-CUGGAAGACAUUUGGACAA-3', siRNA#4: 5'-GCAAGAUAGUUUAAAGGCA-3' (used as a pool).

The following drugs were used in the course of this study: olaparib (SelleckChem, Houston, TX, USA, or Astra Zeneca, Cambridge, UK), talazoparib (SelleckChem), cisplatin (Sigma-Aldrich), the ATM-inhibitor KU60019 (Sigma-Aldrich), and etoposide (Sigma-Aldrich). Concentration and duration of treatment are indicated in the corresponding figure legends.

*Olaparib resistance screens*

Viral particles of the TKOv1 sgRNA library were produced as previously described [37]. This library contains 91,320 sgRNA sequences, with a modal number of six sgRNAs per gene. Cas9-expressing cells were infected with an MOI < 0.3 and the coverage of sgRNA representation was maintained at > 100x (SUM149PT) or > 200x (RPE1) (per replicate, if applicable). 24 h following transduction, transduced cells were selected for 120 h with 10 µg/mL puromycin (RPE1) or 48 h with 3 µg/mL puromycin, followed by 72 h with 0.5 µg/mL puromycin (SUM149PT). Three days after transduction, the transduced cells were split into three technical replicates. Cells were passaged once every three days until nine days after infection, at which time olaparib (16 nM for RPE1 *TP53*$^{-/-}$ *BRCA1-KO*, 2 µM for SUM149PT) was added to the cells. Olaparib-containing medium was refreshed every 4 d. Cells were harvested at 3, 9, 18 and 23 d post-infection (RPE1) or at 3, 9, 19 and 26 d post-infection (SUM149PT) for downstream processing as described [37]. In short, total genomic DNA was isolated from 2 x $10^7$ (t3 sample) or 1 x $10^7$ (later time points) cells using the QIAamp DNA Blood Maxi Kit (Qiagen, Germantown, MD, USA). DNA was precipitated with ethanol and sodium chloride and reconstituted in EB buffer (10 mM Tris-HCl pH 7.5). sgRNA sequences were PCR-amplified using primers harbouring Illumina TruSeq adapters with i5 and i7 barcodes, and the resulting libraries were sequenced on a Illumina NextSeq500 (San Diego, CA, USA) using parameters previously described [37]. Analysis was performed using Model-based Analysis of Genome-wide CRISPR-Cas9 Knockout (MAGeCK) version 0.5.3 [38], in conjunction with Python v3.5.1 on a Mac OS X El Capitan operating system. Non-treated samples collected at day 9 after transduction were compared to treated samples collected at day 23 (RPE1) or day 26 (SUM149PT). The positive score for each gene was calculated by using the 'run' function with the following arguments:

```
MAGECK RUN -L /PATH/TO/TKOV1_LIBRARY/ -N 08-02-2017_141703 --SAMPLE-LABEL
TEST,CTRL -T 1 -C 0 --FASTQ /PATH/TO/FASTQ1 /PATH/TO/FASTQ2.
```

*SUM149PT talazoparib resistance screen*

A derivative of SUM149PT with an integrated tetracycline-inducible Cas9 expression allele was lentivirally infected with a genome-wide guide RNA library ("Yusa" library of 90,709 sgRNAs) designed to target 18,010 genes [39], using a multiplicity of infection of 0.3 and infecting >1000 cells per sgRNA. After puromycin selection (3 µg/ml) to remove non-tranduced cells, a sample was removed (t0); remaining cells were cultured in the presence or absence of doxycycline plus 100 nM talazoparib, a concentration which normally results in complete inhibition of the cell population. No cells survived in the absence of doxycycline. After two weeks of selection, gDNA from the remaining cells in the doxycycline-treated sample was recovered. The sgRNA sequences from this gDNA were PCR-amplified using barcoded and tailed primers and deep sequenced to identify sgRNAs in the talazoparib-resistant population. sgRNA read data was analysed using a gene-level method (MaGeCK version 0.5.5) as well as using a normalised read frequency method to identify individual sgRNAs associated with resistance, by comparing sgRNA abundances in the resistant and starting populations.



Command used for read count generation:

```
MAGECK COUNT --OUTPUT-PREFIX PREFIX --LIST-SEQ
HUMAN_GENOME_LIBRARY_GUIDES_FOR_MAGECK.CSV --FASTQ T1.FASTQ T0.FASTQ --
SAMPLE-LABEL T1,T0 --TRIM-5 0
```

Command used for MLE analysis:

```
MAGECK MLE --NORM-METHOD NONE --OUTPUT-PREFIX PREFIX --SGRNA-EFF-NAME-
COLUMN 3 --SGRNA-EFF-SCORE-COLUMN 4 --SGRNA-EFFICIENCY
ANNOTATION/SGRNAS.BED --COUNT-TABLE PPTM.COUNTS.TXT --DESIGN-MATRIX
DESIGNMATRIX.TXT
```

*IR dropout screen and TKOv2 library*

The TKOv2 lentiviral CRISPR library was used for whole-genome CRISPR knockout screening. To design TKOv2, all possible 20mer sequences upstream of NGG PAM sites were collected where the SpCas9 double-strand break would occur within a coding exon (defined by hg19/Gencode v19 "appris_principal," "appris_candidate_longest," or "appris_candidate" transcript). Guides with 40-75% GC content were retained and further filtered to exclude homopolymers of length ≥4, SNPs (dbSNP138), and relevant restriction sites, including *Bsm*I (GAATCG) and *Bsm*BI (CGTCTC). Candidate gRNA+PAM sequences were mapped to hg19 and sequences with predicted off-target sites in exons or introns, or sequences with more than two predicted off-target sites (with up to two mismatches) in any location, were discarded. Remaining guides were scored using a "sequence score table" described previously [40]. Four guides per gene were

selected, with a bias toward high sequence scores and maximal coverage across exons (i.e. moderate-scoring guides targeting different exons were preferred to high-scoring guides targeting the same exon). The final library contains 70,555 gRNA targeting 17,942 protein-coding genes, as well as 142 sequences targeting LacZ, luciferase, and eGFP. Oligo sequences were ordered from CustomArray (Bothell, WA), PCR-amplified, and cloned into the pLCKO vector as previously described [37].

hTERT RPE1 *TP53*$^{-/-}$ Cas9-expressing cells were transduced with the lentiviral TKOv2 library (see below) at a low MOI (~0.35) and puromycin-containing media was added the next day to select for transductants. Selection was continued until 72 h post-transduction, which was considered the initial time point, t0. To identify IR sensitizers, the negative-selection screen was performed by subculturing at days 3 and 6 (t3 and t6), at which point the cultures were split into two populations. One was left untreated while the second was treated with 3 Gy of IR using a Faxitron X-ray cabinet (Faxitron, Tucson, AZ, USA) every 3 d after day 6. Cell pellets were frozen at day 18 for gDNA isolation. Screens were performed in technical duplicates and library coverage of ≥375 cells/sgRNA was maintained at every step. gDNA from cell pellets was isolated using the QIAamp Blood Maxi Kit (Qiagen) and genome-integrated sgRNA sequences were amplified by PCR using the KAPA HiFi HotStart ReadyMix (Kapa Biosystems, Wilmington, MA, USA). i5 and i7 multiplexing barcodes were added in a second round of PCR and final gel-purified products were sequenced on Illumina NextSeq500 systems to determine sgRNA representation in each sample. DrugZ [41] was used to identify gene knockouts which were depleted from IR-treated t18 populations but not depleted from untreated cells.

*Two-color competitive growth assay*

20,000 cells were infected at an MOI of ~ 1.2 to ensure 100% transduction efficiency with either virus particles of NLS-mCherry LacZ-sgRNA or NLS-GFP GOI-sgRNA. 96 h following transduction, mCherry- and GFP-expressing cells were mixed 1:1 (2,500 cells + 2,500 cells) and plated with or without olaparib (16 nM) or etoposide (100 nM) in 12-well format. During the course of the experiment, cells were subcultured when near-confluency was reached. Olaparib- or etoposide-containing medium was replaced every three days. Cells were imaged for GFP- and mCherry signal the day of initial plating (t=0) and on days 3, 6, 9, 12, 15 and 18 (olaparib), or, in a separate set of experiments, on days 5, 10, 15 and 20 (etoposide). Cells were imaged using the automatic InCell Analyzer (GE Healthcare Life Sciences, Marlborough, MA, USA) with a 4x objective. Segmentation and counting of the number of GFP-positive and mCherry-positive cells was performed using an Acapella script (PerkinElmer, Waltham, MA, USA). Efficiency of indel formation was analysed by performing PCR amplification of the region surrounding the sgRNA sequence and TIDE analysis on DNA isolated from GFP-expressing cells 9 d post-transduction.

*Mass spectrometry*

Following 24 h of doxycycline-induction of stably integrated 293 FLP-IN cells (expressing Flag, Flag-FAM35A, Flag-REV7, Flag-C20orf196, Flag-CTC-534A2.2), cell pellets from two 150 mm plates were lysed in 50 mM HEPES-KOH (pH8.0), 100 mM KCl, 2 mM EDTA, 0.1% NP-40, 10% glycerol and affinity-purified using Flag-M2 magnetic beads (Sigma-Aldrich). Subsequently, digestion with trypsin (Worthington, Columbus, OH, USA) was performed on-beads. All immunoprecipitations were performed in biological replicates (three for CTC-534A2.2, five for C20orf196 and six for FAM35A and REV7).

For LC-MS/MS analysis, peptides were reconstituted in 5% formic acid and loaded onto a 12-15cm fused silica column with pulled tip packed with C18 reversed-phase material (Reprosil-Pur 120 C18-AQ, 3 µm, Dr. Maisch, Ammerbuch-Entringen, Germany). Peptides were analysed using an LTQ-Orbitrap Velos (Thermo Scientific) or a 6600 Triple TOF (AB SCIEX, Framingham, MA, USA) coupled to an Eksigent NanoLC-Ultra HPLC system and a nano-electrospray ion source (Proxeon Biosystems, Thermo Fisher Scientific). Peptides were eluted from the column using a 90-100 min gradient of acetonitrile in 0.1% formic acid. Tandem MS spectra were acquired in a data-dependent mode for the top 10 most abundant ions using collision-induced dissociation. After each run, the column was washed extensively to prevent carry-over.

Mass spectrometry data extraction and interaction scoring was performed essentially as described previously [42]. In short, raw mass spectrometry files were converted to mzXML and analyzed using the iProphet pipeline [43], implemented within ProHits [44]. The data were searched against the human and adenovirus complements of the Uniprot (forward and reverse) database (Version 2017_09; reviewed Swiss-Prot entries only), to which common epitope tags were added as well as common contaminants (common contaminants are from the Max Planck Institute, http://141.61.102.106:8080/share.cgi?ssid=0f2gfuB, and the Global Proteome Machine, http://www.thegpm.org/crap/index.html; 85393 entries were searched). Mascot and Comet search engines were used with trypsin specificity (2 missed cleavages allowed) and deamidation (NQ) and methylation (M) as variable modifications. Charges +2, +3 and +4 were allowed with a parental mass tolerance of maximum 12 ppm and a fragment bin tolerance of 0.6 Da selected for Orbitrap instruments, while 35 ppm and 0.15 Da were allowed for the TripleTOF 6600. For subsequent SAINT analysis (see below), only proteins with an iProphet protein probability ≥ 0.95 were considered, corresponding to an estimated protein false discovery rate (FDR) of ~0.5%.

Interactions were analysed with SAINTexpress (v3.6.1) [45, 46]. SAINT probability scores were computed independently for each replicate against eight biological replicate analyses of the negative control (FLAG alone; controls were "compressed" to six virtual controls to increase robustness as described [47]) and the average probability (AvgP) of the best three out of three (CTC534A2.2), five out of five (C20orf196) or six (FAM35A, REV7) biological replicates for each bait was reported as the final SAINT

score. Preys with an estimated FDR ≤1% were considered true interactors (AvgP ≥0.91). The entire dataset, including the peptide identification and complete SAINTexpress output was deposited as a complete submission in ProteomeXchange through the partner MassIVE housed at the Center for Computational Mass Spectrometry at University of California, San Diego (UCSD; http://massive.ucsd.edu). Data are available at MassIVE (ftp://massive.ucsd.edu/MSV000082207). Unique accession numbers are MSV000082207 and PXD009313, respectively. Data can also been viewed at the prohits website (prohits-web.lunenfeld.ca) under data set 29: Durocher lab. Data in Fig. 1F is represented using Cytoscape, using analyses with an FDR ≤ 1 or 5 %.

*Immunoprecipitation*

1 x $10^7$ 293T cells were transfected with pcDNA5.1-FRT/TO -FLAG-c20orf196 (10 µg), -GFP-REV7 (2 µg), -V5-CTC534A2.2 (14 µg) and pGLUE-HA-Strep-FAM35A (14 µg) or empty vectors using a standard calcium phosphate or PEI protocol. After 48 h, cells were washed with PBS, scraped, and lysed in 1 ml of lysis buffer (50 mM Tris-HCl pH 8.0, 100 mM NaCl, 2 mM EDTA, 0.5% NP-40, 10mM NaF, 10 mM $MgCl_2$ and 10 U/ml Benzonase (Sigma-Aldrich)) on ice for 30 min. Lysates were centrifuged at 15,000g for 5 min at 4 °C, and supernatants were incubated with 100 µl of Streptavidin Sepharose High Performance beads (GE Healthcare) or Dynabeads M-280 Streptavidin magnetic beads (Invitrogen) for 1 h at 4 °C. Beads were washed 5 times with lysis buffer and eluted with 10 mM D-biotin (Invitrogen) in lysis buffer for 2 h at 4 °C. When applicable, the eluate was incubated with 20 µl of GFP-Trap_M resin (Chromotek, Planegg-Martinsried, Germany) for 1 h at 4 °C, washed 5 times with lysis buffer and eluted by boiling in sample buffer. Pull-downs and whole cell extracts were loaded onto SDS-PAGE gels, followed by immunoblotting and probing with indicated antibodies. For GFP-CTC534A2.2 immunoprecipitations, an identical GFP-Trap pulldown procedure as above was used. For V5-CTC534A2.2 immunoprecipitations, lysates from one confluent 10-cm dish of 293T cells transfected with 10 µg pcDNA5.1-FRT/TO-V5-CTC534A2.2 vector was incubated with 10 µg/ml anti-V5 antibody (Invitrogen) for 2 hours at 4 °C. Subsequently 50 µl of protein G Dynabeads (Invitrogen) was added to the lysates and incubated for an additional 1 h at 4 °C. Beads were washed 4 times with lysis buffer and boiled in 50 µl 2xSDS buffer.

*Clonogenic survival assays*

RPE1-hTERT *TP53*$^{-/-}$ cells were seeded in 10-cm dishes (WT: 250 cells: *BRCA1-KO 53BP1-KO*, 500 cells; *BRCA1-KO* or *BRCA1-KO C20orf196-KO*: 1,500 cells; *BRCA1-KO FAM35A-KO*: 750 cells) in the presence of 800 nM cisplatin or 16 nM olaparib or left untreated. Cisplatin dosing lasted 24 h, after which cells were grown in drug-free medium. Olaparib-containing medium was refreshed after 7 d. After 14 d, colonies were stained with crystal

violet solution (0.4 % (w/v) crystal violet, 20% methanol) and manually counted. Relative survival was calculated for the drug treatments by setting the number of colonies in non-treated controls at 100%.

For *Rosa26*$^{CreERT2/wt}$ *Brca1*$^{SCo/\Delta}$ cells, Cre-mediated inactivation of the endogenous mouse *Brca1SCo* allele was achieved by overnight incubation of cells with 0.5 μM 4-hydroxytamoxifen (Sigma-Aldrich). Four days after switching, cells were seeded in triplicate at 10,000 cells per well in 6-well plates for clonogenic survival assays. For experiments with *Rosa26*$^{CreERT2/wt}$ *Brca1*$^{SCo/\Delta}$ p53-null cells, cells were plated in the presence of 15 nM olaparib. Cells were stained with 0.1% crystal violet one week later. Clonogenic survival assays with PARPi (olaparib) and ATMi (KU60019) combination treatment were performed as described previously with minor adjustments [42].

5 x $10^3$ KB1P-G3 cells were seeded per well into 6-well plates on day 0, and then PARPi, ATMi, both or neither were added. The medium was refreshed every 3 d. On day 6, the ATMi alone and untreated groups were stopped and stained with 0.1% crystal violet, the other groups were stopped and stained on day 9. Plates were scanned with a GelCount (Oxford Optronics, Abingdon, UK). Quantifications were performed by solubilizing the retained crystal violet using 10% acetic acid and measuring the absorbance at 562 nm using a Tecan plate reader (Tecan, Männedorf, Switzerland).



*Short term survival assays*

10,000 RPE1-hTERT Cas9 *TP53*$^{-/-}$ parental cells and additional mutants (*BRCA1-KO* and/or *FAM35A-KO*) with or without stable integration of indicated eGFP-fusions by viral transduction were seeded in 12-well format with or without 200 nM olaparib (and 1 μg/mL doxycycline if applicable). Medium with olaparib (and doxycycline) was replaced after 4 d, and cells were trypsinized and counted after seven days using an automated Z2 Coulter Counter analyzer (Beckman Coulter, Indianapolis, IN, USA).

SUM149PT cells were plated at 500 cells per well in 384-well plates and varying amounts of talazoparib in DMSO were added the following day using an Echo 550 liquid handler (Labcyte, San Jose, CA, USA). After 5 d of growth, cell survival was assayed using CellTiter-Glo according to the manufacturer's protocol (Promega, Madison, WI, USA).

*Immunofluorescence*

For 53BP1 immunofluorescence (IF), cells were cultured on coverslips and treated with 5 or 10 Gy X-irradiation and fixed with 2-4% paraformaldehyde (PFA) 1 h after irradiation. Cells were permeabilized with 0.3% Triton X-100, followed by blocking in 10% goat serum, 0.5% saponin, 0.5% NP-40 in PBS (blocking buffer A). Cells were co-stained using 53BP1 and γH2AX primary antibodies (see Supplementary Table 7) in blocking buffer A for 1.5 h at room temperature, followed by 4 washes in PBS, incubation with appropriate secondary

antibodies in blocking buffer A plus 0.8 µg/mL DAPI for 1.5 h at room temperature, and finally four washes in PBS.

For RAD51 IF, cells with or without stable integration of eGFP-tagged proteins or sgRNAs via viral transduction were grown on glass coverslips and treated with 10 Gy X-irradiation and recovered for 3 to 6 h (as indicated). Cells were fixated and extracted using 1% PFA, 0.5% Triton X-100 in PBS for 20 min at room temperature, followed by a second extraction/fixation using 1% PFA, 0.3% Triton X-100, 0.5% methanol in PBS for 20 min at room temperature. Blocking, primary and secondary antibody incubations (1.5 h at room temperature followed by 4 PBS washes) were performed in BTG buffer (10 mg/mL BSA, 0.5% Triton X-100, 3% goat serum, 1 mM EDTA in PBS) or $PBS^{+}$ (0.5% BSA, 0.15% glycine in PBS).

For REV7 and RIF1 IF, cells were grown on glass coverslips, treated with 5 or 10 Gy X-irradiation and fixed with 2-4% PFA 1-2 h after irradiation. Cells were permeabilized with 0.3% Triton X-100. For REV7 blocking, primary and secondary antibody incubations (1.5 h at room temperature followed by 4 washes in PBS) were performed in blocking buffer A. For RIF1 blocking, primary and secondary antibody incubations (1.5 h at room temperature followed by 4 washes) were performed in PBG buffer (0.2% cold water fish gelatin (Sigma Aldrich), 0.5% BSA in PBS).

For GFP-Shieldin focus and laser stripe analysis, U2OS or RPE1 cells were grown on glass coverslips and either transiently transfected with 1 µg vector expressing GFP-FAM35A or –CTC534A2.2, or virally transduced with GFP-FAM35A-expressing vector. 48 h post transfection, or 24 h post 0.5 µg/mL doxycyclin induction, cells were treated with 5 Gy X-irradiation or micro-irradiated, pre-extracted 10 min on ice with NuEx buffer (20 mM HEPES, pH 7.4, 20 mM NaCl, 5 mM $MgCl_2$, 0.5% NP-40, 1 mM DTT and protease inhibitors) followed by 10 min 2% PFA fixation 1 h post-IR/micro-irradiation. Antibody staining and blocking were performed as described above except in PBS + 0.1% Tween-20 + 5% BSA using GFP and γH2AX antibodies. 0.8 µg/mL DAPI was included in all experiments to stain nuclear DNA. Coverslips were mounted using Prolong Gold mounting reagent (Invitrogen) or Aqua PolyMount (Polyscience, Warrington, PA, USA). Images were acquired using a Zeiss LSM780 laser-scanning microscope (Oberkochen, Germany), a Leica SP8 confocal microscope (Wetzlar, Germany) or a Zeiss AxioImager D2 widefield fluorescence microscope. Foci were manually counted.

RAD51 immunofluorescence in KB1P-G3 cells was performed as described previously, with minor modifications [11]. Cells were grown on 8-well chamber slides (Millipore). Ionizing-radiation induced foci were induced by γ-irradiation (10 Gy) 4 h prior to sample preparation. Cells were then washed in PBS++ (2% BSA, 0.15% glycine, 0.1% Triton X-100) and fixed with 2% PFA/PBS++ for 20 min on ice. Fixed cells were washed with PBS++ and were permeabilized for 20 min in 0.2% Triton X-100/PBS++. All subsequent steps were performed in PBS++. Cells were washed three times and blocked for 30 min at room temperature, incubated with the primary antibody for 2 h at RT, washed thrice and incubated with the secondary antibody for 1 h at room temperature. Lastly, cells were

mounted and counterstained using Vectashield mounting medium with DAPI (H1500, Vector Laboratories, Burlingame, CA, USA).

Scale bars indicated in the figure panels represent 10 µm, unless stated otherwise.

*LacR-RIF1-N-terminus and FokI-induced focus formation*

For monitoring recruitment of GFP-tagged Shieldin subunits to mCherry-LacR-Rif1(1-967) foci, 150,000 U2OS-FokI cells (known also as U2OS-DSB) [48] were seeded on 6-well plates containing glass coverslips without any induction of FokI. 24 h after seeding, cells were transfected using 1µg of pDEST-mCherry-LacR or pDEST-mCherry-LacR-Rif1(1-967), if applicable, and 0.5-1 µg of GFP fusion expression vectors. Cells were fixed with 4% PFA 24-48 h after transfection. For monitoring the localization of the FAM35A N-terminus to Rif1(1-967) foci with siRNA knockdown of other Shieldin subunits, an essentially identical protocol was used with the following adjustments: 350,000 U2OS-FokI cells were reverse-transfected with Lipofectamine RNAiMAX-siRNA (10 nM) complex. 24 h after siRNA transfection, the mCherry-LacR and GFP fusion plasmids were transfected. Cells were fixed with 4% PFA 48 h after DNA transfection. For monitoring recruitment of GFP-tagged Shieldin subunits to DSBs at the LacO array, FokI stabilization and nuclear translocation was induced by treating cells with 0.1 µM Shield1 (Clontech, Mountain View, CA, USA) and 10 µg/mL hydroxytamoxifen for 4 h.

ImageJ (https://imagej.nih.gov/ij/) was used to quantify foci in the U2OS-FokI system. An mCherry focus and DAPI nuclear signal were used to generate masks. The average GFP fluorescence or immunofluorescence intensity in the mCherry focus mask was divided by the corresponding average nuclear intensity, and the ratio is reported. Cells displaying a ratio of focus/nuclear average intensity >3 are defined as containing a focus.

*Microirradiation*

For laser microirradiation, virally transduced RPE1 cells expressing the indicated eGFP-tagged proteins were grown on glass coverslips and transfected with siRNAs. 48 h post-transfection, protein expression was induced using 0.5 µg/mL doxycycline, and 24 h later cells were presensitized with 1 µg/mL Hoechst for 15 min at 37 °C. DNA damage was introduced with a 355 nm laser (Coherent, Santa Clara, CA, USA, 40mW) focused through a Plan-Apochromat 40x oil objective to yield a spot size of 0.5-1 mm using a LSM780 confocal microscope (Zeiss) and the following laser settings: 100% power, 1 iteration, frame size 128 x 128, line step 7, pixel dwell: 25.21 µs.

*Traffic light reporter assay*

Cells were infected with pCVL.TrafficLightReporter.Ef1a.Puro lentivirus at a low MOI (0.3-0.5) and selected with puromycin (15 µg/µl). 7 x $10^5$ cells were nucleofected with

5 µg of pCVL.SFFV.d14GFP.Ef1a.HA.NLS.Sce(opt).T2A.TagBFP plasmid DNA in 100 µL of electroporation buffer (25 mM $Na_2HPO_4$ pH 7.75, 2.5 mM KCl, 11 mM $MgCl_2$), using program T23 on a Nucleofector 2b (Lonza). After 72 h, GFP and mCherry fluorescence was assessed in BFP-positive cells using a Fortessa X-20 (BD Biosciences, San Jose, CA, USA) flow cytometer.

*Phospho-RPA immunoblotting*

For phospho-RPA staining, CH12 cells were left untreated, or were treated with 25 Gy of ionizing radiation using a Faxitron X-ray cabinet, and were then collected by centrifugation 3 h later. Pellets were lysed on ice for 10 min in high salt lysis buffer (50 mM Tris-HCl pH 7.6, 300 mM NaCl, 1 mM EDTA, 1% Triton X-100, 1 mM DTT, 1x EDTA-free protease inhibitor cocktail (Roche, Basel, Switerzerland)), cleared by centrifugation at 20,000 x *g* for 10 min at 4 °C, and quantified by bicinchoninic acid assay (BCA; Pierce, Thermo Fisher Scientific). Equal amounts of whole-cell extracts were separated by SDS-PAGE on 4-12% Bis-Tris gradient gels (Invitrogen), transferred to nitrocellulose and immunoblotted for pRPA32 (S4/S8).

*Mouse mammary tumour models*

All animal experiments were approved by the Animal Ethics Committee of The Netherlands Cancer Institute (Amsterdam, the Netherlands) and performed in accordance with the Dutch Act on Animal Experimentation (November 2014). KB1P4 tumor organoids were transduced using spinoculation as described previously [49]. NMRI-nude female mice were purchased from Janvier Laboratories and used for transplantation studies at the age of 6-9 weeks. A power analysis was performed to calculate that a minimum of 8 mice per group were needed to achieve a power of 0.8 (two-sided test, alpha=0.05). Tumor organoids were allografted in mice as described previously with minor adjustments [35]. Briefly, tumor organoids were collected, incubated with TripLE at 37 °C for 5 min, dissociated into single cells, washed and embedded in a 1:1 mixture of tumor organoid culture medium and Basement Membrane Extract (Trevigen) in a cell concentration of $10^4$ cells per 40 µL. Subsequently, $10^4$ cells were injected in the fourth right mammary fat pad of NMRI nude mice. Mammary tumor size was determined by caliper measurements and tumor volume was calculated (0.5 x length x $width^2$). Treatment of tumor-bearing mice was initiated when tumors reached a size of 50-100 $mm^3$. Mice were randomly allocated into the untreated (n = 8) or olaparib treatment group (n = 8). Olaparib was administered in a blinded fashion at 100 mg/kg intraperitoneally for 80 consecutive days. Animals were sacrificed with $CO_2$ when the tumor reached a volume of 1,500 $mm^3$. The tumor was collected, fixed in formalin for histology and several tumor pieces were harvested for DNA analysis.

*Class switch recombination assays*

To induce switching in CH12F3-2 murine B cell lymphoma cells, $2x10^5$ cells were cultured in CH12 media supplemented with a mixture of IL4 (10 ng/mL, R&D Systems #404-ML-050, Minneapolis, MN, USA), TGFβ (1 ng/mL, R&D Systems #7666-MB-005) and anti-CD40 antibody (1 µg/mL, #16-0401-86, eBioscience, Thermo Fisher) for 48 h. Cells were then stained with anti-IgA-PE and fluorescence signal was acquired on an LSR II or Fortessa X-20 flow cytometer (BD Biosciences). To probe AID levels in the stimulated cells, immunoblotting was performed on total cell lysates using anti-AID and anti-β-actin antibodies (Supplementary Table 7). Band quantification was analysed by ImageJ.

*Plasmid integration assay*

200,000 RPE1 cells were seeded into 6-well plates and 24 h later transfected with 2 µg of *Bam*HI/*Eco*RI-linearized peGFP-c1 using PEI. 72 h post-transfection, cells were seeded for colony formation into 10 cm dishes in the presence (50,000 cells per dish) or absence (500 cells per dish) of 600 µg/mL G418. At this point, transfection efficiency was analysed by measuring GFP-positivity using flow cytometry. Medium with G418 was refreshed every 3 d. 14 d after seeding, colonies were stained with crystal violet solution and manually counted. NHEJ efficiency was calculated according to the following formula:

%SURVIVING COLONIES ON SELECTION /
(%OF SURVIVING COLONIES WITHOUT SELECTION) * (%OF TRANSFECTED CELLS)

The data shown for the different KO clones in Supplementary Fig. S8E is representing NHEJ efficiency as calculated with the above formula, followed by normalisation to WT cells (for which NHEJ efficiency is set to 100%).

*DNA binding assays*

Shieldin proteins were isolated using the immunoprecipitation protocol described above with the following modifications. 293T cells were transfected with pGLUE-FAM35A(421-904), the indicated mutants of this construct, or the empty pGLUE Strep/HA-tagging vector and pcDNA5.1-FRT/TO -FLAG-C20orf196 in a 2:1 ratio for a total of 10 µg per 10 cm dish. Complexes were immunoprecipitated as described, except using a reduced NP-40 detergent concentration (0.1%) for the last two washes and elution buffer. Eluted proteins were concentrated using Amicon Ultra 0.5 ml 10K centrifugal filter units (Millipore). Concentrations of isolated proteins were estimated by SDS-PAGE and Coomassie staining, followed by comparison to a standard curve of known bovine serum albumin (BSA) concentrations measured by fluorescence in the 700 nM channel of the Odyssey imager (LI-COR). A radiolabeled ssDNA probe was

prepared by T4 polynucleotide kinase (New England Biolabs, Ipswich, MA, US) phosphorylation of HPLC-purified 59-nt DNA oligo (BioBasic, Markham, ON, CA; TACGTTAGTATGCGTTCTTCCTTCCAGAGGTTTTTTTTTTTTTTTTTTTTTTTTTTTT) using [γ-32P]-ATP (3000 Ci/mmol, 10 mCi/ml; Perkin-Elmer, Woodbridge, ON, CA). Unlabeled competitors were prepared using the same oligo sequence alone or hybridized to the complementary sequence (AAAAAAAAAAAAAAAAAAAAAAAAAAAAAACCTCTGGAAGGAAGAACGCATACTAACGTA) by heating at 80 °C for 10 mins and gradual cooling to room temperature overnight.

For electrophoretic mobility shift assays, 20 nM of labeled ssDNA probe was incubated with purified proteins for 20 min in the elution buffer with the addition of 1 mM DTT and 1 mg/ml BSA at room temperature. Glycerol was then added to a final concentration of 8.3% and resolved on 6% acrylamide-TAE gels. Gels were adhered onto blotting paper (VWR) and enclosed in plastic wrap. Gels were exposed to a storage phosphor screen (GE Healthcare) and visualized using a Typhoon FLA 9500 biomolecular imager (GE Healthcare). Dissociation constant ($K_D$) was determined in GraphPad Prism from nonlinear regression analysis assuming single-site specific binding of saturation titration experiments, defining all signal above the free probe band to be bound probe, as measured in ImageQuant TL(GE Healthcare). The fraction of probe bound is defined as:

SIGNAL OF BOUND PROBE/(SIGNAL OF BOUND PROBE+SIGNAL OF FREE PROBE)

and the concentration of unbound FAM35AC-C20orf196 (referred in the text as SHLD2C-SHLD1) complex is calculated by multiplying the fraction of probe bound by the initial concentration of ssDNA probe, and subtracting this from the initial concentration of SHLD2-C–SHLD1, given the assumption of 1:1 binding.

*Statistical analysis*

All data is represented as individual replicates and replicate number, mean and error bars are explained in the figure legends. Used statistical tests (all common tests) and resulting p-values are indicated in the figure legends and/or figure panels and have been generated using GraphPad Prism software.

*Data availability statement*

All source data represented in the graphs displayed in this article are available online (Supplementary Data files 1-12). Uncropped Western blots can be found online as Supplementary Figure 1. Data of the CRISPR Cas9 screens are included as Supplementary Table 1 (PARPi positive selection screens) or Supplementary Table 4 (IR sensitivity dropout screen). IP-MS data (Supplementary Table 3) are available at MassIVE (ftp://

massive.ucsd.edu/MSV000082207, with unique accession numbers MSV000082207 and PXD009313). IP-MS data can also been viewed at the prohits website (prohits-web.lunenfeld.ca) under data set 29: Durocher lab.

## Acknowledgements

We thank J. Young (Repare Therapeutics), M. Bashkurov (NBCC, LTRI), L. Kesselman (LTRI), S. Rossi (LTRI) and M. Rother (LUMC). We thank R. Greenberg (U Penn) for the U2OS-FokI cells. The authors acknowledge that J. Lukas first proposed the name Shieldin. SN is funded by a research fellowship from the Dutch Cancer Society (KWF). SAd is a Banting Post-Doctoral Fellow. DS is funded by a post-doctoral research fellowship from CIHR. HvA is funded by the European Research Council (CoG-50364). TH is supported by MD Anderson Cancer Center Support Grant P30 CA016672 and the Cancer Prevention Research Institute of Texas (CPRIT/RR160032). Work in the AM lab is funded through CIHR grant PJT153307. ACG is funded by CIHR grant FDN143301. Work in the CJL lab is funded by Programme Grants from Cancer Research UK (CRUK/A14276) and Breast Cancer Now (CTR-Q4-Y2). Work in the SR and JJ labs is funded by the Dutch Cancer Society (KWF 2014-6532), the Netherlands Organization for Scientific Research (VICI 91814643 and a National Roadmap grant for Large-Scale Research Facilities to JJ), the Swiss National Science Foundation (310030_156869 to SR), the European Research Council (CoG-681572 to SR and SyG-319661 to JJ). DD and ACG are Canada Research Chairs (Tier I). DD is funded by CIHR grant FDN143343, Canadian Cancer Society (CCS grant #705644) and OICR grant OICR-OC-TRI.

## Author Contributions

SMN initiated the project in the DD lab, performed the RPE1 *BRCA1-KO* screen, validated hits and performed functional follow up. SAd performed validation and localization studies. DS carried out structure-function analyses and DNA binding studies. MB performed murine tumor model studies. SJP analyzed the SUM149PT talazoparib screen and validated hits. AL generated knockouts in CH12F3-2 cells, carried out CSR assays and analyzed AID levels. MO performed the IR screen and validation. AAQ carried out immunopurifications and helped with IF quantitation. NM performed CSR, TLR and pRPA assays. MZ carried out the SUM149PT olaparib screen and generated the RPE1 *BRCA1-KO* cells. SAn examined *Shld1* and *Shld2* mutations in mES cells. DK, IB, FS, JF and RB performed the SUM149PT talazoparib screen and validation. IB and FS developed SUM149PT knockout cells. FS carried out SUM149PT epistasis experiments. AS performed the REV7 IP-MS. SL initiated work on REV7. RKS generated vectors and edited the manuscript. MMM generated IP-MS cell lines. AMc carried out screen analysis, cloning and TIDE. TGR performed Shieldin qPCR. ZYL carried out IP-MS for SHLD1-3 under supervision of ACG. TH analyzed screen data and built the TKOv2 library with JM. AMa

supervised AL. JJ and SR supervised MB and SAn. DD and HvA supervised SMN. CJL supervised SJP, DK, FS, IB, JF and RB. SMN and DD wrote the manuscript with input from the other authors.

## Disclosure of Potential Conflicts of Interest

DD and TH are advisors to Repare Therapeutics. CJL is a named inventor on patents describing the use of PARP inhibitors (DK3044221 (T3), ES2611504 (T3), US2014378525 (A1), WO2008020180 (A2), WO2009027650 (A1)) and stands to gain from their use as part of the ICR "Rewards to Inventors" scheme.

## References

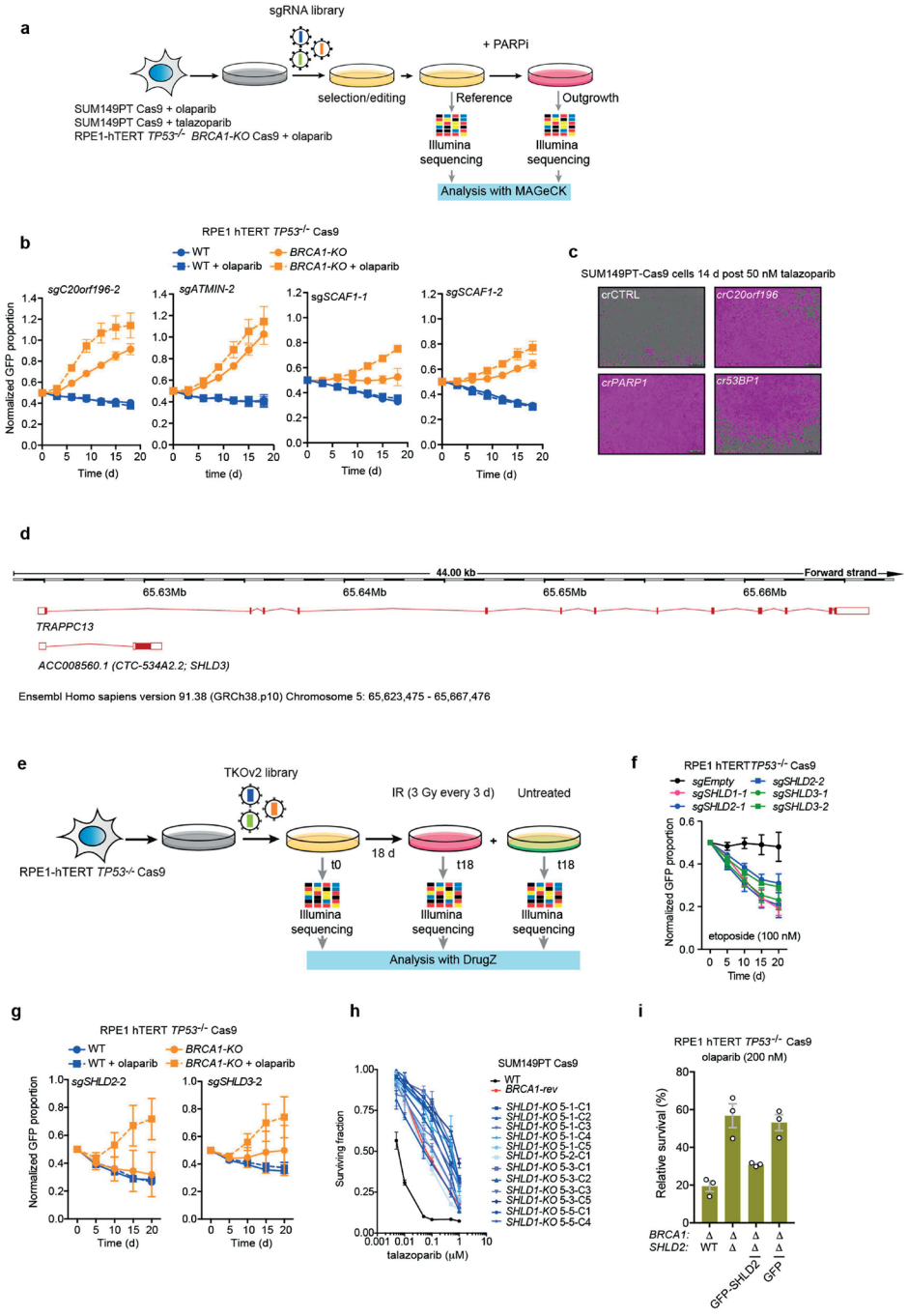
1. Hustedt N, Durocher D. The control of DNA repair by the cell cycle. Nature Cell Biology. 2017; 19: 1-9.
2. Panier S, Boulton SJ. Double-strand break repair: 53BP1 comes into focus. Nat Rev Mol Cell Biol. 2014; 15: 7-18.
3. Munoz IM, Jowsey PA, Toth R, Rouse J. Phospho-epitope binding by the BRCT domains of hPTIP controls multiple aspects of the cellular response to DNA damage. Nucleic Acids Res. 2007; 35: 5312-22.
4. Callen E, Di Virgilio M, Kruhlak MJ, Nieto-Soler M, Wong N, Chen HT, et al. 53BP1 mediates productive and mutagenic DNA repair through distinct phosphoprotein interactions. Cell. 2013; 153: 1266-80.
5. Chapman JR, Barral P, Vannier JB, Borel V, Steger M, Tomas-Loba A, et al. RIF1 is essential for 53BP1-dependent nonhomologous end joining and suppression of DNA double-strand break resection. Mol Cell. 2013; 49: 858-71.
6. Di Virgilio M, Callen E, Yamane A, Zhang W, Jankovic M, Gitlin AD, et al. Rif1 prevents resection of DNA breaks and promotes immunoglobulin class switching. Science. 2013; 339: 711-5.
7. Escribano-Díaz C, Orthwein A, Fradet-Turcotte A, Xing M, Young JT, Tkáč J, et al. A cell cycle-dependent regulatory circuit composed of 53BP1-RIF1 and BRCA1-CtIP controls DNA repair pathway choice. Mol Cell. 2013; 49: 872-83.
8. Feng L, Li N, Li Y, Wang J, Gao M, Wang W, et al. Cell cycle-dependent inhibition of 53BP1 signaling by BRCA1. Cell Discov. 2015; 1: 15019.
9. Zimmermann M, Lottersberger F, Buonomo SB, Sfeir A, de Lange T. 53BP1 regulates DSB repair using Rif1 to control 5' end resection. Science. 2013; 339: 700-4.
10. Boersma V, Moatti N, Segura-Bayona S, Peuscher MH, van der Torre J, Wevers BA, et al. MAD2L2 controls DNA repair at telomeres and DNA breaks by inhibiting 5' end resection. Nature. 2015; 521: 537-40.
11. Xu G, Chapman JR, Brandsma I, Yuan J, Mistrik M, Bouwman P, et al. REV7 counteracts DNA double-strand break resection and affects PARP inhibition. Nature. 2015; 521: 541-4.
12. Adkins NL, Niu H, Sung P, Peterson CL. Nucleosome dynamics regulates DNA processing. Nat Struct Mol Biol. 2013; 20: 836-42.
13. Fradet-Turcotte A, Canny MD, Escribano-Díaz C, Orthwein A, Leung CC, Huang H, et al. 53BP1 is a reader of the DNA-damage-induced H2A Lys 15 ubiquitin mark. Nature. 2013; 499: 50-4.
14. Bouwman P, Aly A, Escandell JM, Pieterse M, Bartkova J, van der Gulden H, et al. 53BP1 loss rescues BRCA1 deficiency and is associated with triple-negative and BRCA-mutated breast cancers. Nat Struct Mol Biol. 2010; 17: 688-95.
15. Bunting SF, Callén E, Wong N, Chen HT, Polato F, Gunn A, et al. 53BP1 inhibits homologous recombination in Brca1-deficient cells by blocking resection of DNA breaks. Cell. 2010; 141: 243-54.
16. Jaspers JE, Kersbergen A, Boon U, Sol W, van Deemter L, Zander SA, et al. Loss of 53BP1 causes PARP inhibitor resistance in Brca1-mutated mouse mammary tumors. Cancer Discov. 2013; 3: 68-81.
17. Lord CJ, Ashworth A. PARP inhibitors: Synthetic lethality in the clinic. Science. 2017; 355: 1152-8.

18. Pettitt SJ, Krastev DB, Brandsma I, Dréan A, Song F, Aleksandrov R, et al. Genome-wide and high-density CRISPR-Cas9 screens identify point mutations in PARP1 causing PARP inhibitor resistance. Nat Commun. 2018; 9: 1849.
19. Hanafusa T, Habu T, Tomida J, Ohashi E, Murakumo Y, Ohmori H. Overlapping in short motif sequences for binding to human REV7 and MAD2 proteins. Genes Cells. 2010; 15: 281-96.
20. Hutchins JR, Toyoda Y, Hegemann B, Poser I, Hériché JK, Sykora MM, et al. Systematic analysis of human protein complexes identifies chromosome segregation proteins. Science. 2010; 328: 593-9.
21. Maréchal A, Zou L. RPA-coated single-stranded DNA as a platform for post-translational modifications in the DNA damage response. Cell Res. 2015; 25: 9-23.
22. Baumann P, Price C. Pot1 and telomere maintenance. FEBS Lett. 2010; 584: 3779-84.
23. Kuhar R, Gwiazda KS, Humbert O, Mandt T, Pangallo J, Brault M, et al. Novel fluorescent genome editing reporters for monitoring DNA repair pathway utilization at endonuclease-induced breaks. Nucleic Acids Res. 2014; 42: e4.
24. Liu X, Holstege H, van der Gulden H, Treur-Mulder M, Zevenhoven J, Velds A, et al. Somatic loss of BRCA1 and p53 in mice induces mammary tumors with features of human BRCA1-mutated basal-like breast cancer. Proc Natl Acad Sci U S A. 2007; 104: 12111-6.
25. Nakamura M, Kondo S, Sugai M, Nazarea M, Imamura S, Honjo T. High frequency class switching of an IgM+ B lymphoma clone CH12F3 to IgA+ cells. Int Immunol. 1996; 8: 193-201.
26. Luijsterburg MS, de Krijger I, Wiegant WW, Shah RG, Smeenk G, de Groot AJL, et al. PARP1 Links CHD2-Mediated Chromatin Expansion and H3.3 Deposition to DNA Repair by Non-homologous End-Joining. Mol Cell. 2016; 61: 547-62.
27. Mirman Z, Lottersberger F, Takai H, Kibe T, Gong Y, Takai K, et al. 53BP1–RIF1–shieldin counteracts DSB resection through CST- and Polα-dependent fill-in. Nature. 2018; 560: 112-6.
28. Fan J, Pavletich NP. Structure and conformational change of a replication protein A heterotrimer bound to ssDNA. Genes Dev. 2012; 26: 2337-47.
29. Sanjana NE, Shalem O, Zhang F. Improved vectors and genome-wide libraries for CRISPR screening. Nat Methods. 2014; 11: 783-4.
30. Shalem O, Sanjana NE, Hartenian E, Shi X, Scott DA, Mikkelson T, et al. Genome-scale CRISPR-Cas9 knockout screening in human cells. Science. 2014; 343: 84-7.
31. Olhovsky M, Williton K, Dai AY, Pasculescu A, Lee JP, Goudreault M, et al. OpenFreezer: a reagent information management software system. Nat Methods. 2011; 8: 612-3.
32. Elstrodt F, Hollestelle A, Nagel JH, Gorin M, Wasielewski M, van den Ouweland A, et al. BRCA1 mutation analysis of 41 human breast cancer cell lines reveals three new deleterious mutants. Cancer research. 2006; 66: 41-5.
33. Zimmermann M, Murina O, Reijns MAM, Agathanggelou A, Challis R, Tarnauskaitė Ž, et al. CRISPR screens identify genomic ribonucleotides as a source of PARP-trapping lesions. Nature. 2018; 559: 285-9.
34. Brinkman EK, Chen T, Amendola M, van Steensel B. Easy quantitative assessment of genome editing by sequence trace decomposition. Nucleic Acids Res. 2014; 42: e168.
35. Bouwman P, van der Gulden H, van der Heijden I, Drost R, Klijn CN, Prasetyanti P, et al. A high-throughput functional complementation assay for classification of BRCA1 missense variants. Cancer Discov. 2013; 3: 1142-55.
36. Duarte AA, Gogola E, Sachs N, Barazas M, Annunziato S, J RdR, et al. BRCA-deficient mouse mammary tumor organoids to study cancer-drug resistance. Nat Methods. 2018; 15: 134-40.
37. Hart T, Chandrashekhar M, Aregger M, Steinhart Z, Brown KR, MacLeod G, et al. High-Resolution CRISPR Screens Reveal Fitness Genes and Genotype-Specific Cancer Liabilities. Cell. 2015; 163: 1515-26.
38. Li W, Xu H, Xiao T, Cong L, Love MI, Zhang F, et al. MAGeCK enables robust identification of essential genes from genome-scale CRISPR/Cas9 knockout screens. Genome Biol. 2014; 15: 554.
39. Tzelepis K, Koike-Yusa H, De Braekeleer E, Li Y, Metzakopian E, Dovey OM, et al. A CRISPR Dropout Screen Identifies Genetic Vulnerabilities and Therapeutic Targets in Acute Myeloid Leukemia. Cell Rep. 2016; 17: 1193-205.
40. Hart T, Tong AHY, Chan K, Van Leeuwen J, Seetharaman A, Aregger M, et al. Evaluation and Design of Genome-Wide CRISPR/SpCas9 Knockout Screens. G3 (Bethesda). 2017; 7: 2719-27.
41. Wang G, Zimmermann M, Mascall K, Lenoir WF, Moffat J, Angers S, et al. Identifying drug-gene interactions from CRISPR knockout screens with drugZ. bioRxiv. 2017: 232736.

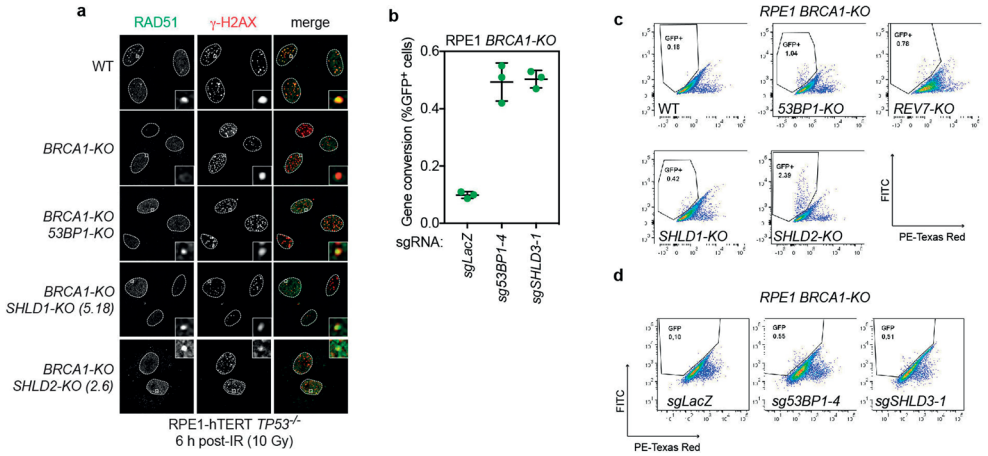
42. Tkáč J, Xu G, Adhikary H, Young JTF, Gallo D, Escribano-Díaz C, et al. HELB Is a Feedback Inhibitor of DNA End Resection. Mol Cell. 2016; 61: 405-18.
43. Shteynberg D, Deutsch EW, Lam H, Eng JK, Sun Z, Tasman N, et al. iProphet: multi-level integrative analysis of shotgun proteomic data improves peptide and protein identification rates and error estimates. Mol Cell Proteomics. 2011; 10: M111.007690.
44. Liu G, Zhang J, Larsen B, Stark C, Breitkreutz A, Lin ZY, et al. ProHits: integrated software for mass spectrometry-based interaction proteomics. Nat Biotechnol. 2010; 28: 1015-7.
45. Choi H, Larsen B, Lin ZY, Breitkreutz A, Mellacheruvu D, Fermin D, et al. SAINT: probabilistic scoring of affinity purification-mass spectrometry data. Nat Methods. 2011; 8: 70-3.
46. Teo G, Liu G, Zhang J, Nesvizhskii AI, Gingras AC, Choi H. SAINTexpress: improvements and additional features in Significance Analysis of INTeractome software. J Proteomics. 2014; 100: 37-43.
47. Mellacheruvu D, Wright Z, Couzens AL, Lambert JP, St-Denis NA, Li T, et al. The CRAPome: a contaminant repository for affinity purification-mass spectrometry data. Nat Methods. 2013; 10: 730-6.
48. Tang J, Cho NW, Cui G, Manion EM, Shanbhag NM, Botuyan MV, et al. Acetylation limits 53BP1 association with damaged chromatin to promote homologous recombination. Nat Struct Mol Biol. 2013; 20: 317-25.
49. Koo BK, Stange DE, Sato T, Karthaus W, Farin HF, Huch M, et al. Controlled gene expression in primary Lgr5 organoid cultures. Nat Methods. 2011; 9: 81-3.
50. Dréan A, Williamson CT, Brough R, Brandsma I, Menon M, Konde A, et al. Modeling Therapy Resistance in BRCA1/2-Mutant Cancers. Molecular cancer therapeutics. 2017; 16: 2022-34.

## Supplementary Figures and Tables

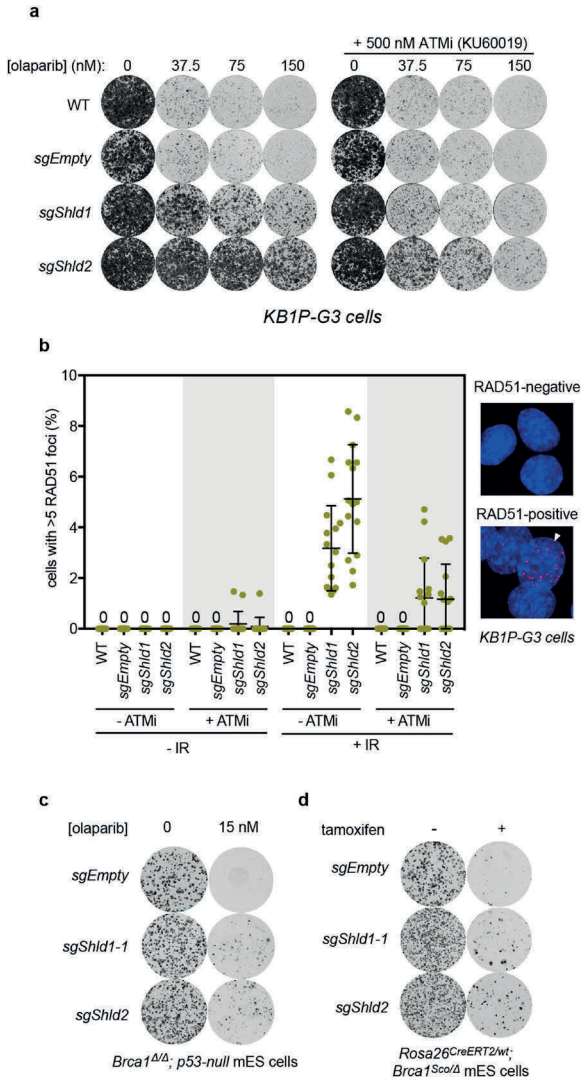
**SUPPLEMENTARY FIGURE S1 | Supporting data for the identification of the Shieldin complex and its role in the response to genotoxic treatments.** *(A)* Schematic of the PARPi resistance screens. *(B)* Competitive growth assays determining the capacity of the indicated sgRNAs to cause resistance to PARP inhibitors in RPE1 *BRCA1-KO* cells. Data is presented as the mean fraction of GFP-positive cells ± SEM, normalized to day 0 (n = 3, independent viral transductions). Gene editing efficiencies of the sgRNAs can be found in Supplementary Table 2. Note that we have not been able to obtain TIDE data for the *ATMIN*-targeting sgRNAs. *(C)* Representative images of SUM149PT-Cas9 cells transfected with indicated crRNAs (see Methods) and exposed to 50 nM talazoparib for 14 d. Purple coloration indicates cells detected by Incucyte live-cell imaging. Scale bar represents 100 µm. The data is a representative set of images from two biologically independent experiments. *(D)* Screenshot of the genomic locus surrounding human CTC-534A2.2 taken from ENSEMBL. *(E)* Schematic of the screen performed in RPE1-hTERT *TP53*$^{-/-}$ cells stably expressing Cas9 to study genes mediating IR-sensitivity. *(F-G)* Competitive growth assays measuring the capacity of the indicated sgRNAs to cause resistance to etoposide (100 nM) in RPE1 WT cells *(F)* or PARP inhibitors (16 nM) in RPE1 *BRCA1-KO* cells *(G)*. Data is presented as the mean fraction of GFP-positive cells ± SD, normalized to day 0 (n = 3, independent viral transductions). Gene editing efficiencies of the sgRNAs can be found in Supplementary Table 2. *(H)* Talazoparib sensitivity in 11 *SHLD1-KO* SUM149PT clones obtained after co-transfection of tracrRNA and one of four distinct *SHLD1* crRNAs (5-1, 5-2, 5-3 or 5-5). Each clone was exposed to talazoparib in a 384-well plate format for five days. As a comparison, talazoparib sensitivity in parental SUM149PT cells with WT SHLD1 (WT) is shown, as is talazoparib resistance in a *BRCA1* revertant subclone (*BRCA1-rev)* of SUM149PT [50]. Bars represent the mean ± SD (n=4 biologically independent experiments). ANOVA was performed for each *SHLD1*-KO clone vs. WT using Dunnett correction for multiple comparisons, $p<10^{-15}$. Gene editing efficiencies can be found in Supplementary Table 2. *(I) BRCA1-KO* and *BRCA1-KO*/*SHLD2-KO* cells were virally transduced with expression vectors for GFP alone or GFP-SHLD2. Sensitivity to olaparib (200 nM) was determined by a short-term survival assay in the presence of 1 µg/mL doxycycline to induce protein expression. Data is represented as dots for every individual experiment with the bar representing the mean ± SD (n=3).


a
sgRNA library
+ PARPi
selection/editing
Reference
Outgrowth
SUM149PT Cas9 + olaparib
SUM149PT Cas9 + talazoparib
RPE1-hTERT TP53-/- BRCA1-KO Cas9 + olaparib
Illumina sequencing
Illumina sequencing
Analysis with MAGeCK
b
RPE1 hTERT TP53-/- Cas9
WT
WT + olaparib
BRCA1-KO
BRCA1-KO + olaparib
sgC20orf196-2
sgATMIN-2
sgSCAF1-1
sgSCAF1-2
Normalized GFP proportion
Time (d)
time (d)
c
SUM149PT-Cas9 cells 14 d post 50 nM talazoparib
crCTRL
crC20orf196
crPARP1
crS3BP1
d
44.00 kb
Forward strand
65.63Mb
65.64Mb
65.65Mb
65.66Mb
TRAPPC13
ACC008560.1 (CTC-534A2.2; SHLD3)
Ensembl Homo sapiens version 91.38 (GRCh38.p10) Chromosome 5: 65,623,475 - 65,667,476
e
TKOv2 library
IR (3 Gy every 3 d)
Untreated
RPE1-hTERT TP53-/- Cas9
18 d
t0
t18
t18
Illumina sequencing
Illumina sequencing
Illumina sequencing
Analysis with DrugZ
f
RPE1 hTERT TP53-/- Cas9
sgEmpty
sgSHLD1-1
sgSHLD2-1
sgSHLD2-2
sgSHLD3-1
sgSHLD3-2
Normalized GFP proportion
etoposide (100 nM)
Time (d)
g
RPE1 hTERT TP53-/- Cas9
WT
WT + olaparib
BRCA1-KO
BRCA1-KO + olaparib
sgSHLD2-2
sgSHLD3-2
Normalized GFP proportion
Time (d)
Time (d)
h
SUM149PT Cas9
WT
BRCA1-rev
SHLD1-KO 5-1-C1
SHLD1-KO 5-1-C2
SHLD1-KO 5-1-C3
SHLD1-KO 5-1-C4
SHLD1-KO 5-1-C5
SHLD1-KO 5-2-C1
SHLD1-KO 5-3-C1
SHLD1-KO 5-3-C2
SHLD1-KO 5-3-C3
SHLD1-KO 5-3-C5
SHLD1-KO 5-5-C1
SHLD1-KO 5-5-C4
Surviving fraction
talazoparib (μM)
i
RPE1 hTERT TP53-/- Cas9
olaparib (200 nM)
Relative survival (%)
BRCA1:
SHLD2:
WT
GFP-SHLD2
GFP

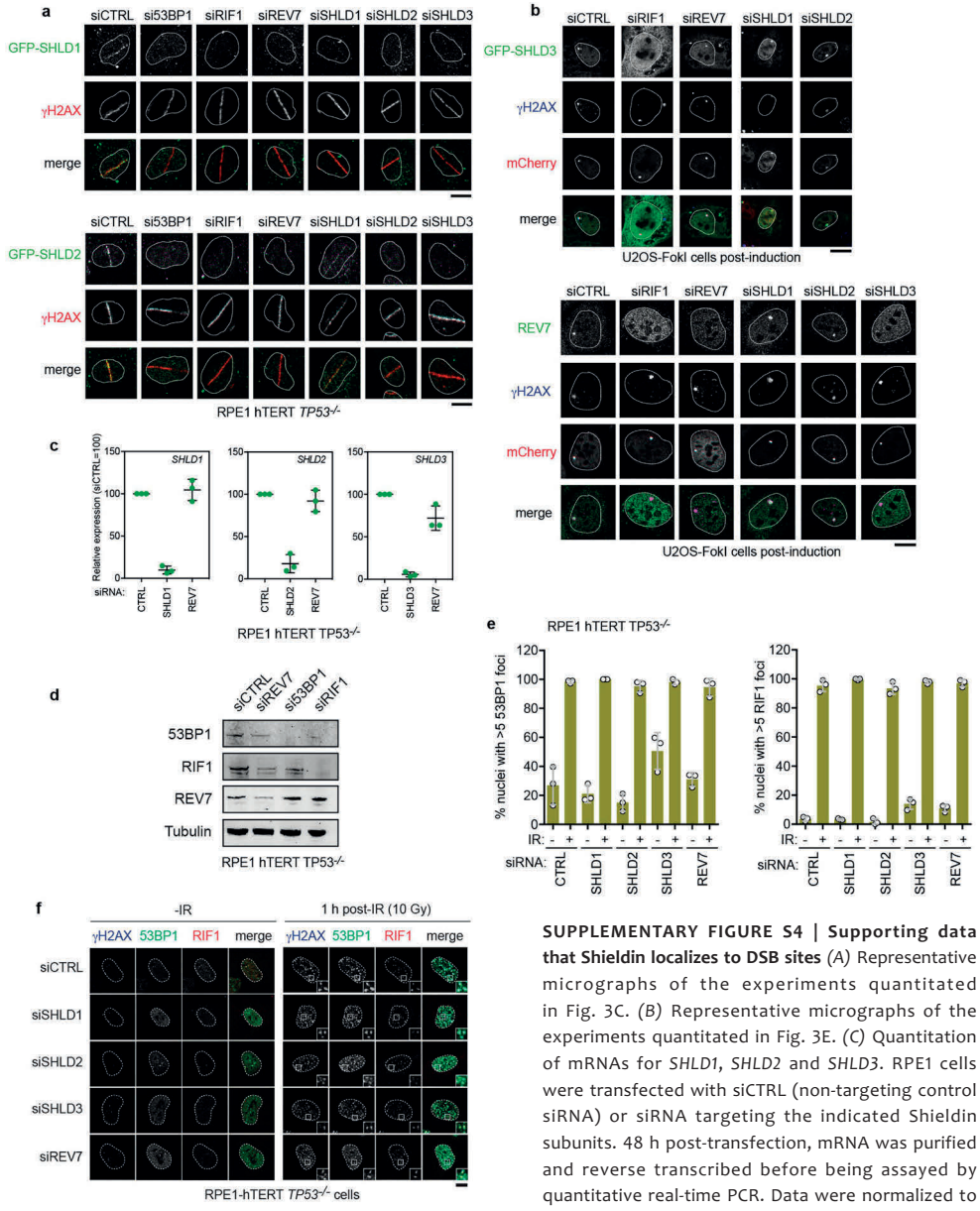
5



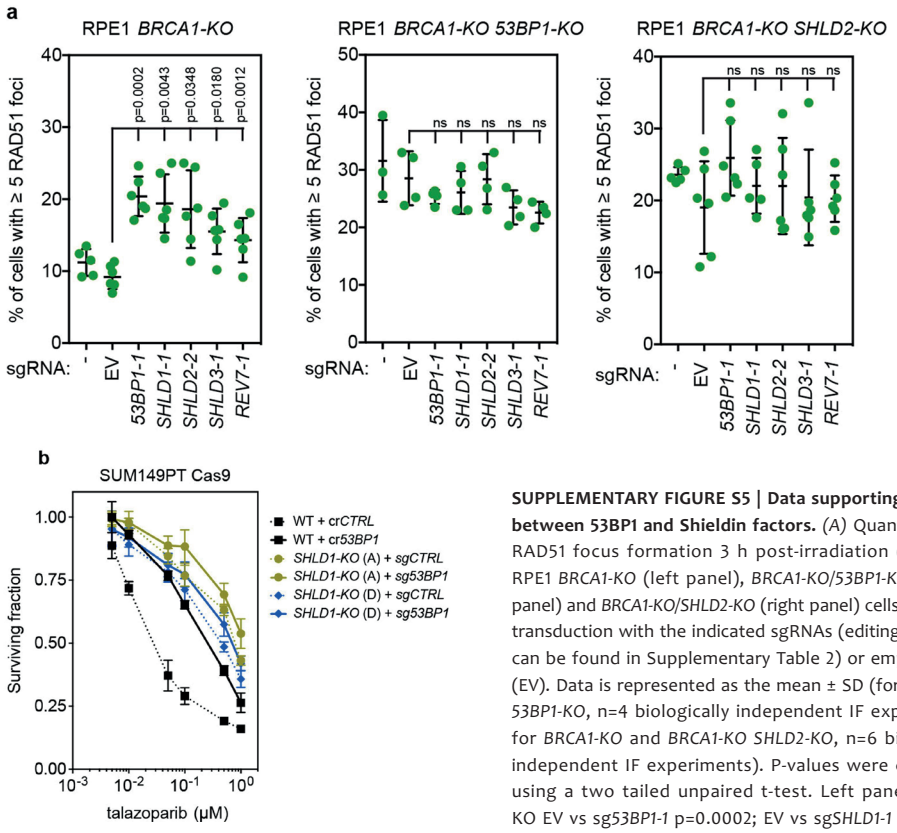

**SUPPLEMENTARY FIGURE S2 | Supporting data that Shieldin inhibits HR.** *(A)* Representative micrographs of RAD51 focus formation in the indicated RPE1 cell lines (data quantitated in Fig. 2D, n ≥ 3). *(B)* Traffic light reporter (TLR) assay testing RPE1 *BRCA-KO* cells virally transduced with sgRNAs targeting *53BP1* or *SHLD3*. Data is represented as dots for individual experiments with the bar representing the mean ± SD (n=3). Gene editing efficiencies of the sgRNAs can be found in Supplementary Table 2). *(C)* Representative flow cytometry plots of cells analysed with the TLR assay (data quantitated in Fig. 2E, n ≥ 3). *(D)* Representative flow cytometry plots of cells analysed with the TLR assay (data quantitated in Supplementary Fig. S2B).




**SUPPLEMENTARY FIGURE S3 | Supporting data that mouse Shieldin promotes resistance to PARP inhibition in *Brca1*-mutated cells and tumours.** *(A)* Clonogenic survival assays of transduced KB1P-G3 cells treated with indicated olaparib doses ± ATM inhibitor (ATMi) KU60019 (500 nM). On day 6, the ATMi alone and untreated groups were stopped and stained with 0.1% crystal violet; the other groups were stopped and stained on day 9. Data shown is a representative set from 3 biologically independent experiments (with 3 technical replicates each). *(B)* Left, quantitation of Rad51 focus formation in parental KB1P-G3 (*Brca1*$^{-/-}$; *Trp53*$^{-/-}$) cells or KB1P-G3 cells that were transduced with the indicated lentiviral sgRNA vectors. Cells were fixed without treatment or 4 h after irradiation (10 Gy dose). Each data point represents a microscopy field containing a minimum of 50 cells; the bar represents the mean ± SD (n=15). Right, representative micrographs of Rad51-negative and -positive cells (the latter is indicated by an arrowhead). DNA was stained with DAPI. *(C)* Clonogenic survival assay of *Rosa26*$^{CreERT2/wt}$; *Brca1*$^{Δ/Δ}$; *p53-null* mES-cells virally transduced with the indicated sgRNA and treated without or with 15 nM olaparib for 7 d. Gene editing efficiencies of the sgRNAs can be found in Supplementary Table 2. Data shown is a representative set from 3 biologically independent experiments (with ≥ 2 technical replicates each). *(D)* Clonogenic survival assay of *Rosa26*$^{CreERT2/wt}$;*Brca1*$^{Sco/Δ}$ mES-cells virally transduced with the indicated sgRNA and treated without or with 0.5 μM tamoxifen to induce BRCA1 depletion. Gene editing efficiencies of the sgRNAs can be found in Supplementary Table 2. Data shown is a representative set from 2 biologically independent experiments (with 3 technical replicates each).

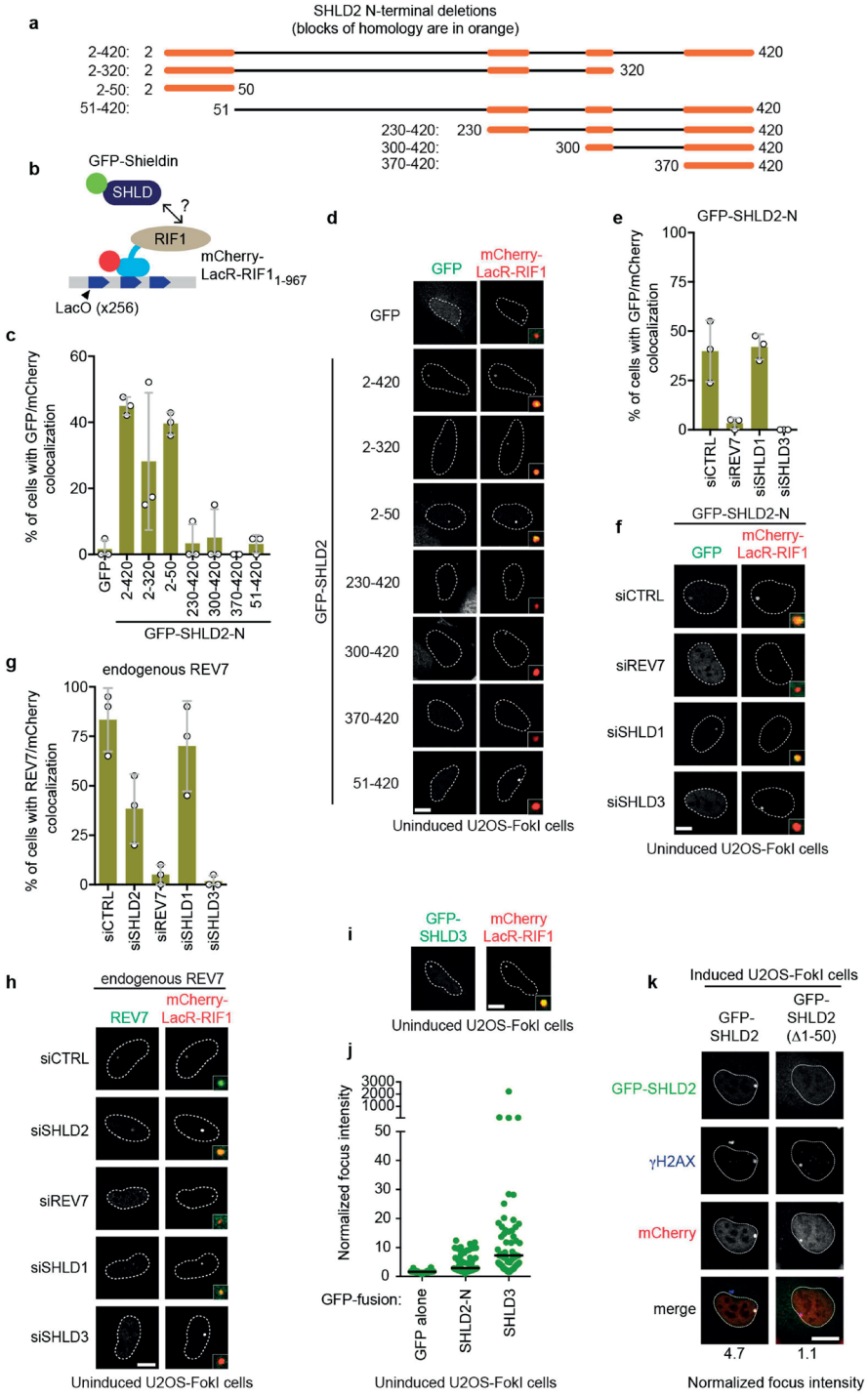


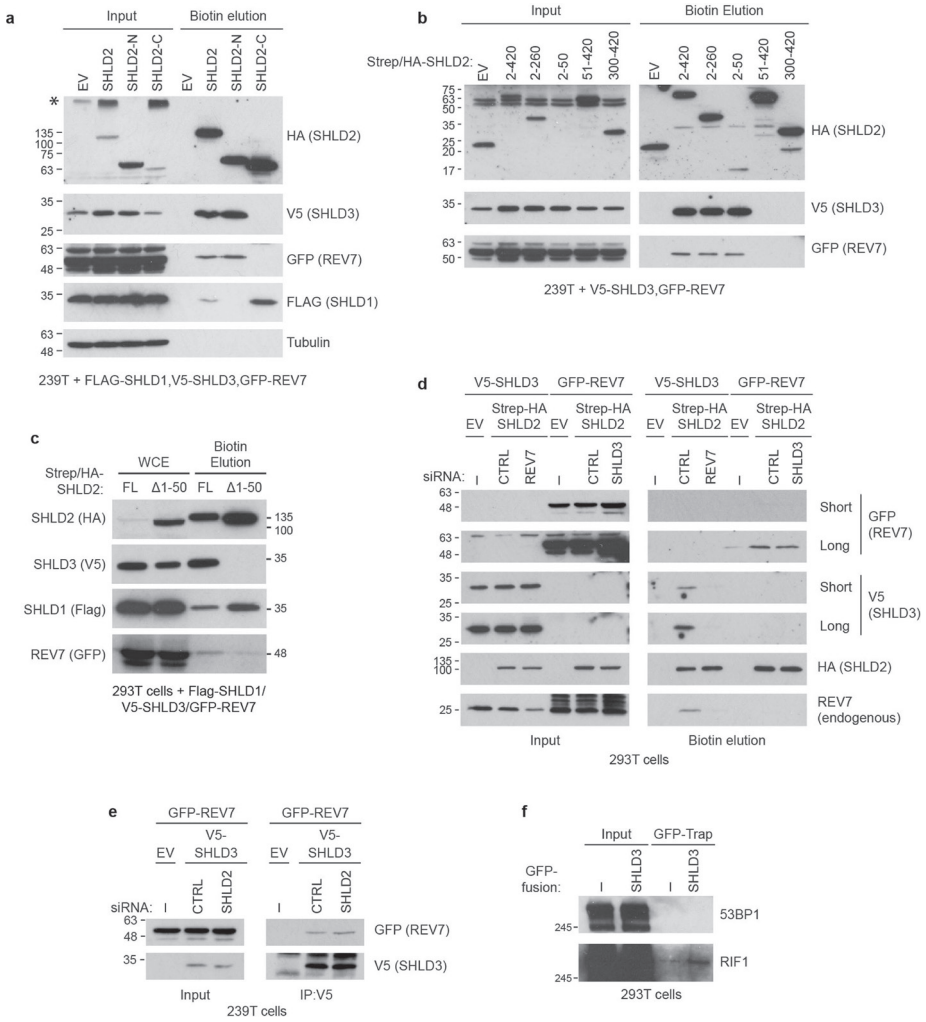

**SUPPLEMENTARY FIGURE S4 | Supporting data that Shieldin localizes to DSB sites** *(A)* Representative micrographs of the experiments quantitated in Fig. 3C. *(B)* Representative micrographs of the experiments quantitated in Fig. 3E. *(C)* Quantitation of mRNAs for *SHLD1*, *SHLD2* and *SHLD3*. RPE1 cells were transfected with siCTRL (non-targeting control siRNA) or siRNA targeting the indicated Shieldin subunits. 48 h post-transfection, mRNA was purified and reverse transcribed before being assayed by quantitative real-time PCR. Data were normalized to the amount of *GAPDH* mRNA and expressed relative to the corresponding value for cells transfected with siCTRL. Data is presented as the mean ± SD (n=3, independent siRNA transfections). *(D)* Whole cell extracts from RPE1 WT cells transfected with the indicated siRNAs were processed for immunoblotting with the indicated antibodies. Tubulin is used as a loading control (n=1 experiment; siRNA efficiency is also monitored by immunofluorescence). *(E)* Quantitation of 53BP1 and RIF1 recruitment to IR-induced DSBs (1 h post-irradiation with 10 Gy) following depletion of the indicated Shieldin components. Data is represented as the mean ± SD (n=3, independent siRNA transfections). *(F)* Representative micrographs of the experiments quantitated in Supplementary Fig. S4E.




**SUPPLEMENTARY FIGURE S5 | Data supporting epistasis between 53BP1 and Shieldin factors.** *(A)* Quantitation of RAD51 focus formation 3 h post-irradiation (10 Gy) in RPE1 *BRCA1-KO* (left panel), *BRCA1-KO*/*53BP1-KO* (middle panel) and *BRCA1-KO*/*SHLD2-KO* (right panel) cells after viral transduction with the indicated sgRNAs (editing efficiency can be found in Supplementary Table 2) or empty vector (EV). Data is represented as the mean ± SD (for *BRCA1-KO 53BP1-KO*, n=4 biologically independent IF experiments; for *BRCA1-KO* and *BRCA1-KO SHLD2-KO*, n=6 biologically independent IF experiments). P-values were calculated using a two tailed unpaired t-test. Left panel: BRCA1-KO EV vs sg*53BP1-1* p=0.0002; EV vs sg*SHLD1-1* p=0.0043; EV vs sg*SHLD2-2* p=0.0348; EV vs sg*SHLD3-1* p=0.0180; EV vs sg*REV7-1* p=0.0012). Middle and right panel: all comparisons to the EV condition were non-significant (ns). Values for *BRCA1-KO 53BP1-KO* EV vs sg*53BP1-1* p=0.2332; EV vs sg*SHLD1-1* p=0.4451; EV vs sg*SHLD2-2* p=0.9632; EV vs sg*SHLD3-1* p=0.1187; EV vs sg*REV7-1* p=0.0568. Values for *BRCA1-KO SHLD2-KO*: EV vs sg*53BP1-1* p=0.0550; EV vs sg*SHLD1-1* p=0.1864; EV vs sg*SHLD2-2* p=0.3568; EV vs sg*SHLD3-1* p=0.4641; EV vs sg*REV7-1* p=0.2888. *(B)* Talazoparib sensitivity of WT or two independent *SHLD1-KO* SUM149PT-dox-Cas9 clones (A and D) virally transduced with an sgRNA targeting *53BP1* (*sg53BP1*) or a control non-targeting sgRNA (*sgCTRL*), following induction of Cas9. Data is presented as the mean ± SD (n=3 biologically independent experiments).

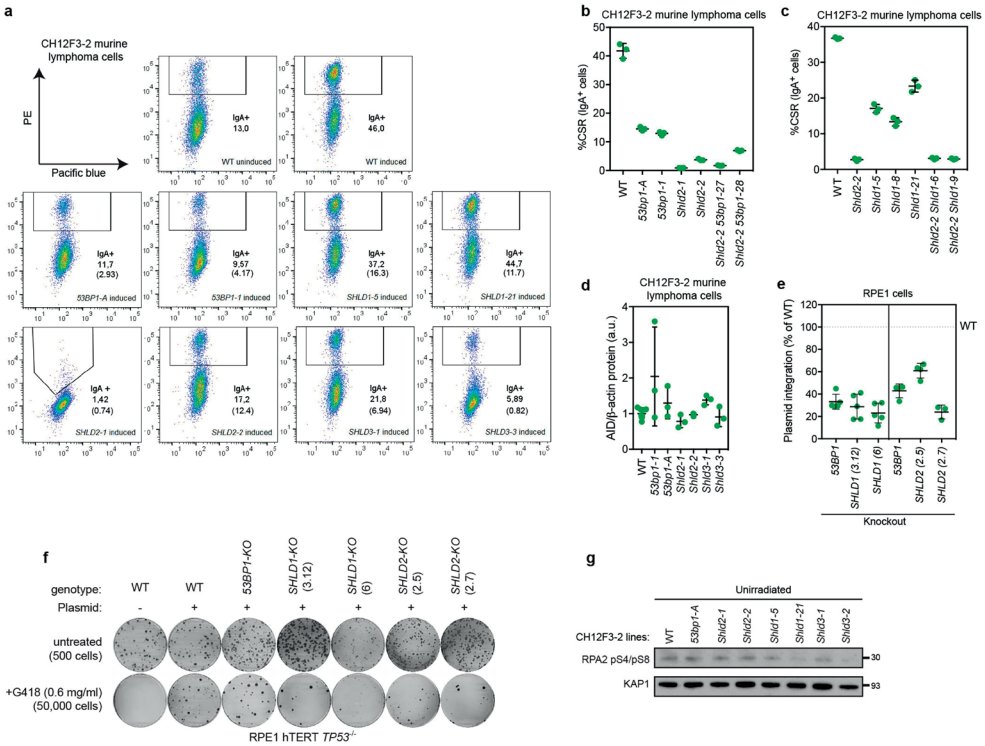
**SUPPLEMENTARY FIGURE S6 | Data supporting the co-localization of Shieldin with RIF1 on chromatin.** *(A)* Representation of the deletion mutants of SHLD2N used in Supplementary Fig. S6C-D. The orange shading indicates blocks of homology. *(B)* Schematic of the LacR-RIF1 chromatin recruitment assay. *(C)* Quantitation of the experiment shown in Supplementary Fig. S6D. Colocalization was considered positive when the average GFP intensity at the mCherry focus was 3-fold over background nuclear intensity. A minimum of 20 cells were imaged per biological replicate (circles); the bar represents the mean ± SD (n=3). *(D)* Representative images of the data quantitated in Supplementary Fig. S6C. The main focus is shown in inset and the scale bar = 10 μm. *(E-H)*, Quantitation *(E,G)* and representative micrographs *(F,H)* of overexpressed GFP-SHLD2N and mCherry-LacR-RIF1(1-967) co-transfected into uninduced U2OS-FokI cells along with siRNA against Shieldin complex subunits after processing for mCherry and GFP *(E,F)* or mCherry and REV7 *(G,H)* immunofluorescence. Colocalization was considered positive when the average GFP or REV7 intensity at the mCherry focus was 3-fold over background nuclear intensity. A minimum of 20 cells were imaged per condition (circles); the bar represents the mean ± SD (n=3 biologically independent experiments). *(I)* Representative images of the data quantitated in Supplementary Fig. S6J. The main focus is shown in inset and the scale bar = 10 μm. *(J)* Quantitation of GFP intensity at the mCherry-LacR-RIF1(1-967) focus, normalized to nuclear background. Each data point represents a cell transfected with the vector coding for the indicated GFP fusion. The line is at the median. The data is an aggregate of three independent experiments with a minimum of 20 cells counted (total cells counted: 62, 60, and 61 for GFP, GFP-SHLD2C, and GFP-SHLD3, respectively). *(K)* mCherry-LacR-FokI colocalization with full length or N-terminally truncated (Δ1-50) GFP-SHLD2. Mean normalized focus intensity is shown from a total of 59 (SHLD2 full length) or 56 (SHLD2 Δ1-50) cells counted (n=2 biologically independent experiments).


a
SHLD2 N-terminal deletions
(blocks of homology are in orange)
2-420: 2 420
2-320: 2 320
2-50: 2 50
51-420: 51 420
230-420: 230 420
300-420: 300 420
370-420: 370 420
b
GFP-Shieldin
SHLD
RIF1
?
mCherry-
LacR-RIF1 1-967
LacO (x256)
c
% of cells with GFP/mCherry colocalization
GFP
2-420
2-320
2-50
230-420
300-420
370-420
51-420
GFP-SHLD2-N
d
GFP
mCherry-LacR-RIF1
GFP-SHLD2
Uninduced U2OS-FokI cells
e
GFP-SHLD2-N
% of cells with GFP/mCherry colocalization
siCTRL
siREV7
siSHLD1
siSHLD3
f
GFP-SHLD2-N
GFP
mCherry-LacR-RIF1
siCTRL
siREV7
siSHLD1
siSHLD3
Uninduced U2OS-FokI cells
g
endogenous REV7
% of cells with REV7/mCherry colocalization
siCTRL
siSHLD2
siREV7
siSHLD1
siSHLD3
h
endogenous REV7
REV7
mCherry-LacR-RIF1
siCTRL
siSHLD2
siREV7
siSHLD1
siSHLD3
Uninduced U2OS-FokI cells
i
GFP-SHLD3
mCherry LacR-RIF1
Uninduced U2OS-FokI cells
j
Normalized focus intensity
GFP-fusion:
GFP alone
SHLD2-N
SHLD3
Uninduced U2OS-FokI cells
k
Induced U2OS-FokI cells
GFP-SHLD2
GFP-SHLD2 (Δ1-50)
GFP-SHLD2
γH2AX
mCherry
merge
4.7
1.1
Normalized focus intensity

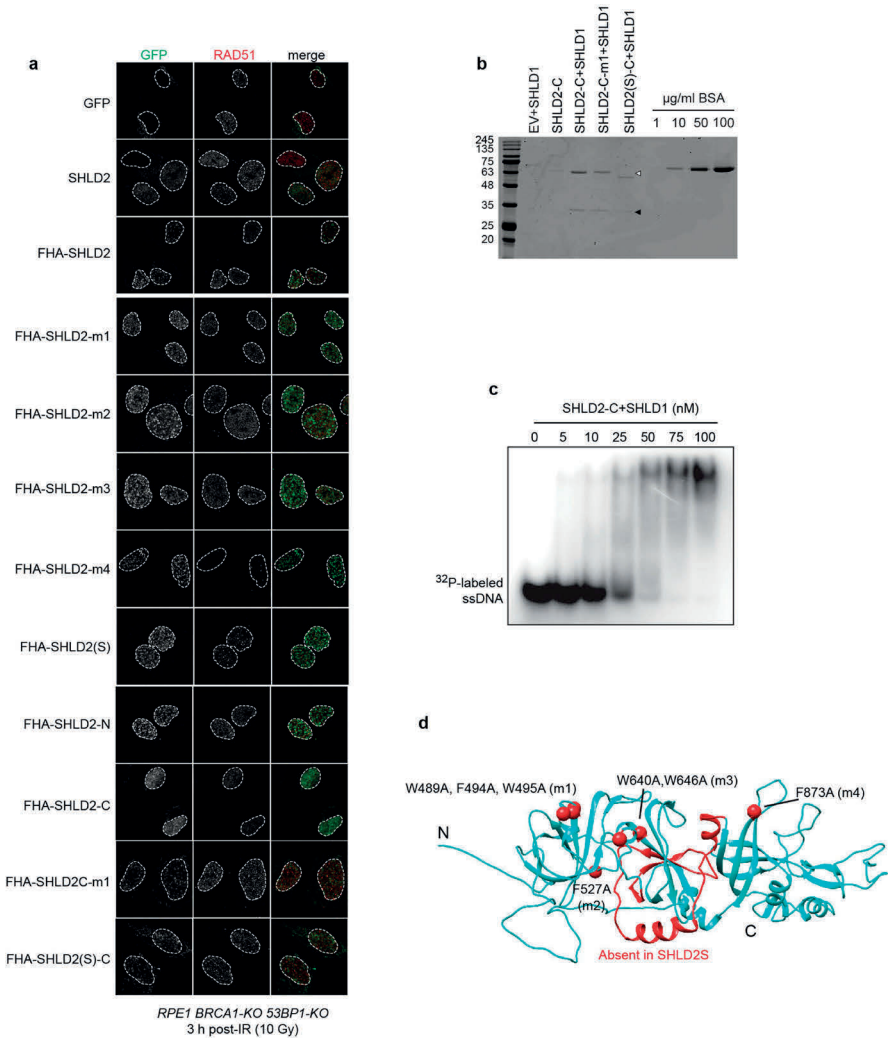



**SUPPLEMENTARY FIGURE S7 | Mapping the architecture of the Shieldin complex.** *(A)* Streptavidin pulldown analysis determining which region of SHLD2 associates with the other Shieldin subunits. Whole cell extracts (WCEs) of 293T cells transfected with an expression vector for FLAG-SHLD1, V5-SHLD3, GFP-REV7 and Strep/HA-tagged SHLD2, SHLD2N (residues 2-420), SHLD2C (residues 421-904), or empty Strep/HA vector (EV) were incubated with streptavidin resin and bound proteins were eluted with biotin. WCEs and elutions were analysed by SDS-PAGE and immunoblotting with the indicated antibodies. Tubulin was used as a loading control. Results are representative set of immunoblots from 2 independent experiments. *denotes a non-specific band. *(B)* Mapping the SHLD3 and REV7 binding sites on the SHLD2 N-terminus through streptavidin pulldowns with different SHLD2 constructs (detailed in Supplementary Fig. S6A) and immunoblotting. Results are a representative of a set of immunoblots from 3 independent experiments. *(C)* Affinity purification of Shieldin complex components using N-terminally truncated SHLD2(Δ1-50) analyzed by immunoblotting (representative of three independent experiments). *(D)* Streptavidin pulldown analysis of SHLD2 association with REV7 and SHLD3. 293T cells were transfected with siRNAs and expression vectors for epitope-tagged Shieldin components as indicated (EV, empty Strep/HA vector). WCEs were incubated with streptavidin resin and bound proteins were eluted with biotin. WCEs and elutions were analysed by SDS-PAGE and immunoblotted with the indicated antibodies. Short and long exposures are shown for GFP and V5 immunoblots (n=1). *Figure legend continues on next page.*

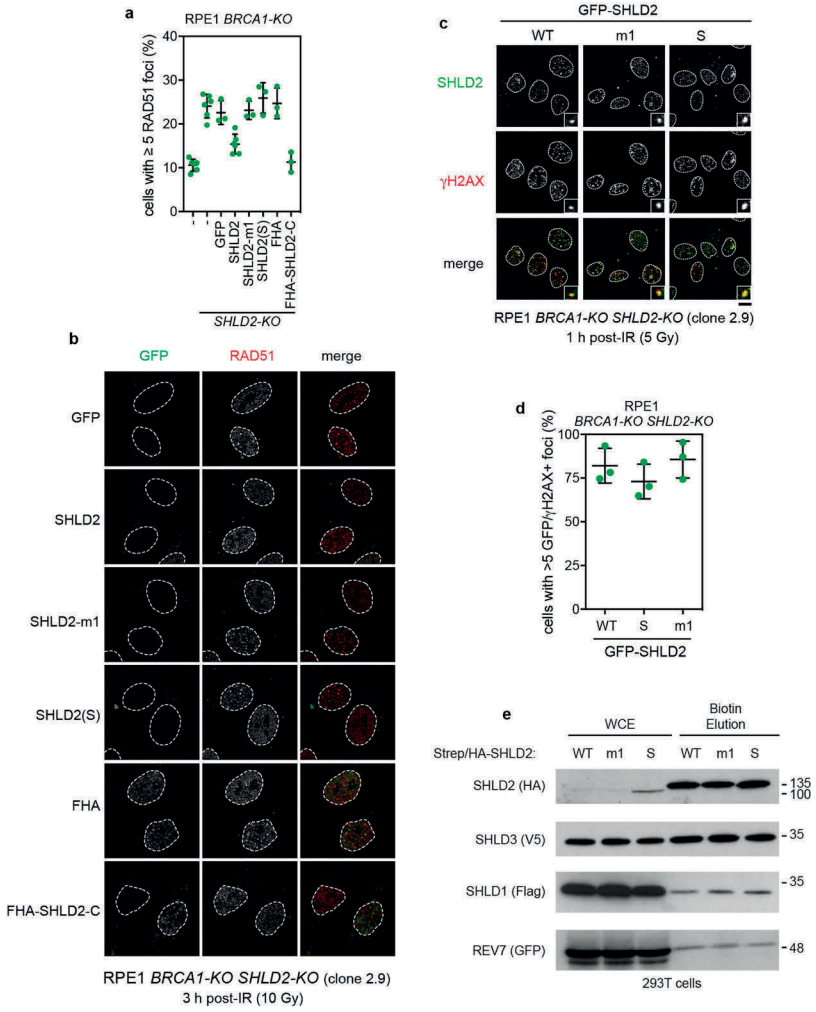
*(E)* Dependency of V5-SHLD3 co-immunoprecipitation with GFP-REV7. 293T cells were transfected with siRNAs and expression vectors for epitope-tagged REV7 and SHLD3 as indicated (EV, empty V5 vector). WCEs were incubated with anti-V5 antibody and protein G resin. Bound proteins were boiled in SDS sample buffer and analysed by immunoblotting with GFP and V5 antibodies (n=1). *(F)* Association between SHLD3 and RIF1. WCEs of 293T cells transfected with an expression vector for unfused GFP (-) or GFP-SHLD3 (SHLD3) were incubated with GFP-Trap resin. Bound proteins were boiled in SDS sample buffer and analysed by SDS-PAGE and immunoblotting against 53BP1 and RIF1. Results are representative of 2 SHLD3 IPs, utilizing SHLD3 fused to GFP (shown here) and V5 (show in Fig. 3G) affinity tags.




**SUPPLEMENTARY FIGURE S8 | Controls supporting the role of Shieldin in promoting physiological NHEJ.** *(A)* Representative dot plots of the flow cytometry data obtained (of n=3 biologically independent experiments) to assess class switching in Fig. 3H. CSR was determined as the percentage of IgA$^+$ cells following stimulation after subtracting the baseline percentage of IgA$^+$ cells in the indicated clones (values in brackets). *(B-C)* Epistasis analysis of Shieldin and 53BP1 in CSR. Shown is the percentage of class switching in CH12F3-2 wild type, single knockout, or double knockout cells (as indicated) following stimulation. Each data point represents a biological replicate; the line represents the mean ± SD (n=3). Genomic editing efficiencies of the sgRNAs can be found in Supplementary Table 2. *(D)* Whole cell extracts of the indicated CH12F2-3 clones were probed for AID and β-actin (loading control) by immunoblotting and were quantitated by densitometry. Each data point represents a biological replicate; the line represents the mean ± SD (n=9 for WT, n=3 for other samples). *(E)* Random plasmid integration of linearized pcGFP-c1 conferring G418 resistance. Resistant colonies were quantified after 14 d. Bar represents the mean ± SD with WT cells set at 100% (left panel: n=5, right panel n=4 except SHLD2-KO (2.7) n=3 biologically independent experiments). *(F)* Representative images of the plasmid integration assays quantitated in Supplementary Fig. S3E. *(G)* Unirradiated CH12F3-2 clones (25 Gy) were immunoblotted for RPA2 phosphorylation (a representative set from n=3 biological replicates; data relates to Fig. 3I).




**SUPPLEMENTARY FIGURE S9 | Data supporting the role of DSB-targeted SHLD2 in the suppression of HR and the mapping of the SHLD2C-SHLD1 complex binding to ssDNA.** *(A)* Representative micrographs of RPE1 *BRCA1-KO/53BP1-KO* cells transduced with the indicated GFP-fusion proteins, pre-extracted, fixed and stained for RAD51 and GFP 3 h post-IR (10 Gy). Protein expression was induced for 24 h before IR using 1 µg/mL doxycycline. Data relates to Fig. 4B. Note that due to the pre-extraction required for visualization of RAD51 foci, the visualization of non-FHA tagged SHLD2 is lost. *(B)* SDS-PAGE analysis of purified SHLD2C-SHLD1 complexes. Strep/HA-SHLD2(421-904)–Flag-SHLD1 complexes were purified from transiently transfected 293T cells. Concentrations of purified proteins were estimated by Coomassie staining and comparison to a standard curve of known BSA concentrations visualized by fluorescence at 700 nm. SHLD2C-m1 and SHLD2CS denote SHLD2C constructs carrying the OB fold m1 mutation and the internal deletion (Δ655-723) corresponding to the naturally occurring splice variant of SHLD2, respectively. Open and filled arrowheads mark the bands corresponding to SHLD2C and SHLD1, respectively. EV refers to empty Strep/HA vector. Shown is a representative stained gel from 2 independent experiments. *(C)* Representative image of the [$^{32}$P]-labeled ssDNA EMSA with SHLD2C-SHLD1 for $K_D$ determination shown in Fig. 4E. *(D)* Model of the SHLD2-OB fold domains and the engineered mutations (red spheres, point mutations; red ribbons, splice variant deletion). Model relates to Fig. 4B-D.




**SUPPLEMENTARY FIGURE S10 | SHLD2 OB-folds are required for suppression of RAD51 IR-induced focus formation.** *(A)* Quantitation of RAD51 foci 3 h following 10 Gy irradiation in RPE1 *BRCA1-KO*/*SHLD2-KO* cells complemented with the indicated GFP-tagged SHLD2 constructs via viral transduction. Protein expression was induced with 1 µg/mL doxycycline for 24 h prior to IR. Each data point is a biological replicate; the bar represents the mean ± SD (n=6 for *BRCA1-KO* untransduced cells, *BRCA1-KO* / *SHLD2-KO* untransduced and GFP-SHLD2 cells, n=3 for remaining cell lines, biologically independent experiments). *(B)* Representative micrographs of the data shown in Supplementary Fig. S10A. Note that due to the pre-extraction required for visualization of RAD51 foci, the visualization of non-FHA tagged SHLD2 foci is lost. *(C)* Representative micrographs of RPE1 *BRCA1-KO*/*SHLD2-KO* cells virally transduced with vectors expressing GFP-tagged SHLD2 WT or its OB-fold m1 mutant (m1), or short splice variant (S), 1 h post 5 Gy IR. Scale bar = 10 µm. *(D)* Quantitation of the data shown in Supplementary Fig. S10C. Each data point represents an independent biological replicate counting ≥100 cells. Data is represented as mean ± SD (n=3). *(E)* Whole cell extracts (WCE) of 293T cells co-transfected with Strep/HA-SHLD2 WT, -SHLD2-m1, or -SHLD2-S mutants, and other Shieldin subunits (Flag-SHLD1, V5-SHLD3, and GFP-REV7) were incubated with streptavidin resin and bound proteins were eluted with biotin. WCEs and eluted proteins were visualized by SDS-PAGE and immunoblotting with the indicated antibodies. Results shown are a representative set from 2 independent experiments.

**SUPPLEMENTARY TABLE 1 | can be accessed via the online version of this article.**

**SUPPLEMENTARY TABLE 2 |**

| cell lines | additional genotype cells (clone) | KO (clone) | sgRNA used for editing | mutation* |
|---|---|---|---|---|
| RPE1 hTERT +flag-Cas9 | | *TP53 (1.1)* | CAGAATGCAAGAAGCCCAGA | 322delT |
| RPE1 hTERT +flag-Cas9 *TP53*$^{-/-}$ (1.1) | | *BRCA1 (3.6)* | AAGGGTAGCTGTTAGAAGGC | 4277delTC |
| | | *53BP1* | TCCAATCCTGAACAAACAGC | 218delCA |
| | *BRCA1-KO (3.6)* | *53BP1 (3.3)* | TCCAATCCTGAACAAACAGC | 218delCA |
| | | *SHLD1 (3.12)* | TCTGACTGGCCTTTCACAGC | complex (no WT sequence detected) |
| | | *SHLD1 (6)* | TCTGACTGGCCTTTCACAGC | 246insG; 246insCA |
| | *BRCA1-KO (3.6)* | *SHLD1 (5.18)* | TCTGACTGGCCTTTCACAGC | 246insG |
| | | *SHLD2 (2.3)* | GCCTCGGAGGAAGATCTCTG | 1708insT; 1707delG |
| | | *SHLD2 (2.5)* | GCCTCGGAGGAAGATCTCTG | 1706insA |
| | | *SHLD2 (2.7)* | GCCTCGGAGGAAGATCTCTG | 1706insA |
| | *BRCA1-KO (3.6)* | *SHLD2 (2.6)* | GCCTCGGAGGAAGATCTCTG | 1706insT |
| | *BRCA1-KO (3.6)* | *SHLD2 (2.9)* | GCCTCGGAGGAAGATCTCTG | 1704delAG |
| | *BRCA1-KO (3.6)* | *REV7* | GAGGTCTTGTCGTGTGAGCG | KO confirmed by WB (data not shown) |
| SUM149PT | | *SHLD1 (5-1-C1)* | ATAAGAGATTACGTCCTGC | 85del5 + 92insT |
| | | *SHLD1 (5-1-C2)* | ATAAGAGATTACGTCCTGC | 92insCAGCT |
| | | *SHLD1 (5-1-C3)* | ATAAGAGATTACGTCCTGC | 92insCAGCT |
| | | *SHLD1 (5-1-C4)* | ATAAGAGATTACGTCCTGC | 92insCAGCT |
| | | *SHLD1 (5-1-C5)* | ATAAGAGATTACGTCCTGC | 92insCAGCT |
| | | *SHLD1 (5-2-C1)* | TGACTGGCCTTTCACAGCA | 247insT |
| | | *SHLD1 (5-3-C2)* | GATGGCCTTCGGAAATCCC | 293delC; 286del7 |
| | | *SHLD1 (5-3-C3)* | GATGGCCTTCGGAAATCCC | 286del7 |
| | | *SHLD1 (5-3-C5)* | GATGGCCTTCGGAAATCCC | 286del11; 286del7; 288del5 |
| | | *SHLD1 (5-5-C1)* | GGCCATTTGAAAACTGCGG | 371del62 |
| | | *SHLD1 (5-5-C4)* | GGCCATTTGAAAACTGCGG | 371del62 |
| CH12F3-2 | | *53bp1 (A)* | TTCTAGCCCGCTATCTGATG | KO confirmed by WB (data not shown) |
| | | *53bp1 (1)* | CAGTTGGTGACCACTAACTC | KO confirmed by WB (data not shown) |
| | | *Shld1 (5)* | ACACACCGCGGGTAGATCCA | 55insA |
| | | *Shld1 (8)* | ACACACCGCGGGTAGATCCA | 57delT |
| | | *Shld1 (21)* | ACACACCGCGGGTAGATCCA | 57delT + CtoG58; 46del10 |
| | | *Shld2 (1)* | AACCTGAGTGATATGACTAG | 341insC; 338del8 |
| | | *Shld2 (2)* | ACGTTTTGACGACTTCTGTG | 249insT; 250del5 |
| | | *Shld3 (1)* | AGTGAAGGAGCAGACCAATG | 350del4; 349del7 |
| | | *Shld3 (2)* | GGAAGTTTGGACTCATCGTA | 149delA;147delC |
| | *Shld2-KO (2)* | *Shld1 (6)* | ACACACCGCGGGTAGATCCA | 48del11; 45del16 |
| | *Shld2-KO (2)* | *Shld1 (9)* | ACACACCGCGGGTAGATCCA | 51del7; 48del11 |
| | *Shld2-KO (2)* | *53BP1 (27)* | CAGTTGGTGACCACTAACTC | KO confirmed by WB (data not shown) |
| | *Shld2-KO (2)* | *53BP1 (28)* | CAGTTGGTGACCACTAACTC | KO confirmed by WB (data not shown) |
| | | | | alleles are separated by ';' |

| | cell lines | additional genotype cells* | pooled sgRNA transduction/ transfection | editing efficiency | |
|---|---|---|---|---|---|
| **PARPi two-colour competitive growth assay** | | | | | |
| related to Fig. 1c and ED Fig. 1b | RPE1 hTERT +flag-Cas9 *TP53*$^{-/-}$ | *BRCA1-KO* (3.6) | sgRNA1 *53BP1* | 80.5% | |
| | | *BRCA1-KO* (3.6) | sgRNA1 *RNF8* | 92.7% | |
| | | *BRCA1-KO* (3.6) | sgRNA1 *C20orf196* | 74.1% | |
| | | *BRCA1-KO* (3.6) | sgRNA2 *C20orf196* | 66.5% | |
| | | *BRCA1-KO* (3.6) | sgRNA1 *SCAF1* | 23.2% | |
| | | *BRCA1-KO* (3.6) | sgRNA2 *SCAF1* | 15.4% | |
| | | *BRCA1-KO* (3.6) | sgRNA1 *ATMIN* | ND | |
| | | *BRCA1-KO* (3.6) | sgRNA2 *ATMIN* | ND | |
| **Etoposide two-colour competitive growth assay** | | | | | |
| related to ED Fig. 1f | RPE1 hTERT +flag-Cas9 *TP53*$^{-/-}$ | | sgRNA1 *SHLD2* | 91.7% | |
| | | | sgRNA2 *SHLD2* | 90.7% | |
| | | | sgRNA1 *SHLD3* | 58.2% | |
| | | | sgRNA2 *SHLD3* | 63.5% | |
| **Traffic light reporter assay** | | | | | |
| related to ED Fig. 2b | RPE1 hTERT +flag-Cas9 *TP53*$^{-/-}$ | *BRCA1-KO* (3.6) | sgRNA4 *53BP1* | 77.4 | |
| | | *BRCA1-KO* (3.6) | sgRNA1 *SHLD3* | 16.5% | |
| **Epistasis experiments** | | | | | |
| related to ED Fig. 5a | RPE1 hTERT +flag-Cas9 *TP53*$^{-/-}$ | *BRCA1-KO* (3.6) | sgRNA1 53BP1 | 52.9% | |
| | | *BRCA1-KO* (3.6) | sgRNA1 SHLD1 | 51,20% | |
| | | *BRCA1-KO* (3.6) | sgRNA2 SHLD2 | 88,90% | |
| | | *BRCA1-KO* (3.6) | sgRNA1 SHLD3 | 77,40% | |
| | | *BRCA1-KO* (3.6) | sgRNA1 REV7 | ND | (reduced expression of REV7 confirmed by WB (data not shown)) |
| | | *BRCA1-KO 53BP1-KO* (3.3) | sgRNA1 53BP1 | 100% | (mutation already present in KO clone) |
| | | *BRCA1-KO 53BP1-KO* (3.3) | sgRNA1 SHLD1 | 59,80% | |
| | | *BRCA1-KO 53BP1-KO* (3.3) | sgRNA2 SHLD2 | 92,30% | |
| | | *BRCA1-KO 53BP1-KO* (3.3) | sgRNA1 SHLD3 | 56% | |
| | | *BRCA1-KO 53BP1-KO* (3.3) | sgRNA1 REV7 | ND | (reduced expression of REV7 confirmed by WB (data not shown)) |
| | | *BRCA1-KO SHLD2-KO* (2.9) | sgRNA1 53BP1 | 74,40% | |
| | | *BRCA1-KO SHLD2-KO* (2.9) | sgRNA1 SHLD1 | 55% | |
| | | *BRCA1-KO SHLD2-KO* (2.9) | sgRNA2 SHLD2 | 100% | (mutation already present in KO clone) |
| | | *BRCA1-KO SHLD2-KO* (2.9) | sgRNA1 SHLD3 | 83,50% | |
| | | *BRCA1-KO SHLD2-KO* (2.9) | sgRNA1 REV7 | ND | (reduced expression of REV7 confirmed by WB (data not shown)) |
| **mouse BRCA1 tumour model** | | | | | |
| related to ED Fig. 3 | KB1P-G3 | | sgRNA Shld1 | 80.8% | |
| | | | sgRNA Shld2 | 94.5% | |
| | *Rosa26*$^{CreERT2/wt}$; *Brca1*$^{Δ/Δ}$; *p53-null* mES cells | | sgRNA1 Shld1 | 83.9% | |
| | | | sgRNA Shld2 | 89.8% | |
| | *Rosa26*$^{CreERT2/wt}$; *Brca1*$^{Sco/Δ}$; *p53-null* mES cells | | sgRNA1 Shld1 | 92.4% | |
| | | | sgRNA Shld2 | 96% | |
| | KB1P4s.1 | | sgRNA Shld1 | 97.2% | |
| | | | sgRNA Shld2 | 95.9% | |

**SUPPLEMENTARY TABLE 3 |**

| BAIT | PREY UNIPROT | PREY | AvgSpec | BFDR |
|---|---|---|---|---|
| C20orf196 | Q86V20-2 | FAM35A | 10,2 | 0 |
| C20orf196 | P13984 | GTF2F2 | 4,8 | 0 |
| CTC-534A2.2 | P40937-2 | RFC5 | 4,33 | 0 |
| CTC-534A2.2 | Q6ZNX1 | CTC-534A2.2 | 45,67 | 0 |
| CTC-534A2.2 | Q9UI95 | MAD2L2 | 30,33 | 0 |
| CTC-534A2.2 | P35249 | RFC4 | 5,33 | 0 |
| CTC-534A2.2 | Q86V20-2 | FAM35A | 13 | 0 |
| FAM35A | B5ME19 | EIF3CL | 10,67 | 0 |
| FAM35A | Q6ZNX1 | CTC-534A2.2 | 2,83 | 0,01 |
| FAM35A | Q9UI95 | MAD2L2 | 5,67 | 0 |
| FAM35A | Q14320 | FAM50A | 5,33 | 0,01 |
| FAM35A | Q8IYI0 | C20orf196 | 3 | 0,02 |
| MAD2L2 | NP_000407.1 | IFNGR1 | 4,17 | 0 |
| MAD2L2 | P11717 | IGF2R | 3 | 0,01 |
| MAD2L2 | P08195-2 | SLC3A2 | 14,17 | 0 |
| MAD2L2 | NP_001122103.1 | DCAKD | 8,67 | 0 |
| MAD2L2 | NP_001128582.1 | DNAJA3 | 8,83 | 0 |
| MAD2L2 | NP_001153101.1 | SLC27A2 | 5 | 0 |
| MAD2L2 | NP_001157616.1 | CHAMP1 | 97,83 | 0 |
| MAD2L2 | O75306-2 | NDUFS2 | 5,83 | 0 |
| MAD2L2 | NP_001161086.1 | LEMD3 | 6,33 | 0 |
| MAD2L2 | O43819 | SCO2 | 6,67 | 0 |
| MAD2L2 | P40616-2 | ARL1 | 7,33 | 0,02 |
| MAD2L2 | NP_001181866.1 | POGZ | 5,33 | 0 |
| MAD2L2 | NP_001240795.1 | YME1L1 | 10,17 | 0 |
| MAD2L2 | P53007 | SLC25A1 | 3 | 0,01 |
| MAD2L2 | O00217 | NDUFS8 | 4,33 | 0 |
| MAD2L2 | NP_002903.3 | REV3L | 3,5 | 0,01 |
| MAD2L2 | O14735-3 | CDIPT | 3,83 | 0 |
| MAD2L2 | O00264 | PGRMC1 | 19,33 | 0 |
| MAD2L2 | Q13015 | MLLT11 | 11,67 | 0 |
| MAD2L2 | NP_036610.2 | WBP2 | 5,17 | 0 |
| MAD2L2 | Q9P032 | NDUFAF4 | 8,5 | 0 |
| MAD2L2 | NP_056036.1 | DNMBP | 33 | 0 |
| MAD2L2 | NP_056146.1 | NCSTN | 2,67 | 0,01 |
| MAD2L2 | NP_057191.2 | ZFR | 3,17 | 0 |
| MAD2L2 | NP_057540.1 | TMEM9 | 2,83 | 0,01 |
| MAD2L2 | NP_061158.1 | BIN3 | 11,83 | 0 |
| MAD2L2 | Q86V20-2 | FAM35A | 14,67 | 0 |
| MAD2L2 | NP_065770.1 | PRR12 | 7,33 | 0 |
| MAD2L2 | Q8N163-2 | CCAR2 | 18,17 | 0 |
| MAD2L2 | Q8WWC4 | MAIP1 | 5,17 | 0 |
| MAD2L2 | NP_115604.1 | FAR1 | 4,5 | 0 |
| MAD2L2 | NP_149014.3 | SYDE1 | 4,67 | 0 |
| MAD2L2 | P51648-2 | ALDH3A2 | 11 | 0 |
| MAD2L2 | NP_001035997.2 | COASY | 17,33 | 0 |
| MAD2L2 | NP_001129629.1 | OTUD5 | 15 | 0 |
| MAD2L2 | P78347-2 | GTF2I | 207,83 | 0 |
| MAD2L2 | P10321 | HLA-C | 4,67 | 0 |
| MAD2L2 | O95573 | ACSL3 | 7,67 | 0,02 |
| MAD2L2 | Q9Y4W6 | AFG3L2 | 15,33 | 0 |
| MAD2L2 | NP_036560.1 | NPTN | 7 | 0 |
| MAD2L2 | NP_001230648.1 | RAB6A | 3,33 | 0,01 |
| MAD2L2 | NP_079348.1 | PTGES2 | 4,5 | 0 |
| MAD2L2 | Q9NXS2-3 | QPCTL | 3 | 0,01 |
| MAD2L2 | Q6ZNX1 | CTC-534A2.2 | 3,5 | 0,01 |
| MAD2L2 | NP_001159575.1 | SPINT2 | 4 | 0 |
| MAD2L2 | NP_859052.3 | QSOX2 | 4 | 0 |
| MAD2L2 | NP_000296.2 | PON2 | 2,33 | 0,02 |
| MAD2L2 | Q8IYI0 | C20orf196 | 2,67 | 0,02 |
| MAD2L2 | A0FGR8-2 | ESYT2 | 2,5 | 0,02 |
| MAD2L2 | NP_004228.1 | TRIP13 | 3,5 | 0 |
| CTC-534A2.2 | Q8IYI0 | C20orf196 | 2 | 0,17 |
| C20orf196 | Q9UI95 | MAD2L2 | 0,8 | 0,41 |
| C20orf196 | Q6ZNX1 | CTC-534A2.2 | 0,2 | 0,93 |

**SUPPLEMENTARY TABLE 4 | CAN BE ACCESSED VIA THE ONLINE VERSION OF THIS ARTICLE.**

**SUPPLEMENTARY TABLE 5 |**

| targeting gene | sgRNA sequence | Usage RPE1 cells | SUM149PT cells |
|---|---|---|---|
| LacZ control | CCCGAATCTCTATCGTGCGG | √ | |
| *TP53* | CAGAATGCAAGAAGCCCAGA | √ | |
| *BRCA1* | AAGGGTAGCTGTTAGAAGGC | √ | |
| *53BP1* gRNA1 | TCCAATCCTGAACAAACAGC | √ | |
| *53BP1* gRNA4 | CACCGACCTTCTCAATAAAGTTGAT | √ | |
| *53BP1* gRNA5_1 | TCTAGTGTGTTAGATCAGG | | √ |
| *53BP1* gRNA5_3 | GACTGCTAGGAACGATAAA | | √ |
| *53BP1* gRNA_A10 | GCACAAGAACTTATGGAAAG | | √ (used for epistasis experiment (Supplementary Figure S5B)) |
| *C20orf196* gRNA1 | TCTGACTGGCCTTTCACAGC | √ | |
| *C20orf196* gRNA2 | ATCTATCCAGGGATTTCCGA | √ | |
| *C20orf196* gRNA5_1 | ATAAGAGATTACGTCCTGC | | √ |
| *C20orf196* gRNA5_2 | TGACTGGCCTTTCACAGCA | | √ |
| *C20orf196* gRNA5_3 | GATGGCCTTCGGAAATCCC | | √ |
| *C20orf196* gRNA5_4 | ATTTCATAGAATCTATCCA | | √ |
| *C20orf196* gRNA5_5 | GGCCATTTGAAAACTGCGG | | √ |
| *FAM35A* gRNA1 | CAAGGTCTGAAGCAGCAGTT | √ | |
| *FAM35A* gRNA2 | GCCTCGGAGGAAGATCTCTG | √ | |
| *CTC534A2.2* gRNA1 | TGTGAGAGTGATCCCACACA | √ | |
| *CTC534A2.2* gRNA2 | AACCTGGTCACACACACTGA | √ | |
| *RNF8* gRNA1 | AAGGGGTCCTGTGGAGCGGA | √ | |
| *RNF8* gRNA2 | CCCAGAGTCTAAATGGTGTT | √ | |
| *SCAF1* gRNA1 | CCACGGACAGCTTCCTCGCA | √ | |
| *SCAF1* gRNA2 | CAACCTGGCGAGCCGAGCGA | √ | |
| *REV7* gRNA1 | GAGGTCTTGTCGTGTGAGCG | √ | |
| *REV7* gRNA2 | GTGCGCGAGGTCTACCCCGT | √ | |
| *PTIP* gRNA1 | GGAGGTCAAGTATTACGCGG | √ | |
| *PTIP* gRNA2 | GTGTGAGGCTAGTGCATTGT | √ | |
| *ATMIN* gRNA1 | GATGTTGGTCCGCACGGCCC | √ | |
| *ATMIN* gRNA2 | GGATGTTGGTCCGCACGGCC | √ | |
| *PARP1* gRNA5_2 | GACCCGAGCATTCCTCGCA | | √ |
| *PARP1* gRNA5_4 | GCTAGGCATGATTGACCGC | | √ |
| Control [Targets a mouse olfactory receptor] | CAACAGTCGCATCGCCAAGA | | √ (used for epistasis experiment (Supplementary Figure S) |
| Nontargeting | AAAACACGATGACGTCTCT | | √ (for crRNA experiments) |

| targeting gene | sgRNA sequence | Usage mES | KB1P-G3, KB1P4s | CH12F3-2 |
|---|---|---|---|---|
| *Trp53bp1_e6_834* | CAGTTGGTGACCACTAACTC | | | √ |
| *Trp53bp1_e6_857* | TTCTAGCCCCGCTATCTGATG | | | √ |
| *Shld1* gRNA1 | GATCAGTAGTCGAAGAAGAA | √ | | |
| *Shld1* gRNA2 | ACACACCGCGGGTAGATCCA | | √ | √ |
| *Shld1* gRNA2_2 | GGCCCCGGTGCCACCGGCCC | | | √ |
| *Shld2* gRNA1 | ATCAGTCAGATCCCTGCGTT | √ | √ | |
| *Shld2_e4_772* | ACGTTTTGACGACTTCTGTG | | | √ |
| *Shld2_e4_864* | AACCTGAGTGATATGACTAG | | | √ |
| *Shld3_e2_686* | GACTCATCGTATGGAAACCA | | | √ |
| *Shld3_e2_695* | GGAAGTTTGGACTCATCGTA | | | √ |
| *Shld3_e2_905* | AGTGAAGGAGCAGACCAATG | | | √ |
| non targeting gRNA | TGATTGGGGGTCGTTCGCCA | √ | | |

**SUPPLEMENTARY TABLE 6 |**

| targeting gene | genomic locus | forward primer | reverse primer | for sequencing |
|---|---|---|---|---|
| *BRCA1* | gRNA 1 | TCTCAAAGTATTTCATTTTCTTGGTGCC | TGAGCAAGGATCATAAAATGTTGG | |
| *53BP1* | gRNA 1 | CCAGCACCAACAAGAGC | GGATGCCTGGTACTGTTTGG | |
| *53BP1* | gRNA 4 | CCTTTTATCCTTGGGATGAGGCA | CTGAAAGCCAGGTTCTAGAGGATGA | |
| *C20orf196* | gRNA1+2 | GGCTAAGAATCCTTGGTCCACA | GGCTCTCCTGGCCTCTTAGTT | |
| *C20orf196* | gRNA 5_1 | ACAAAATAACTCCTGGACCGC | CCTGGGTTTGGCTTTTCATCA | |
| *C20orf196* | gRNA 5_2 to 5 | AGGATCCTGCTATGTGGTGC | ATCACACACCCGTATTGCTG | |
| *FAM35A* | gRNA 1 | CCAGAATCTATTGGTTCTCCAGA | GAGTTTATGTGAATGCGGCT | |
| *FAM35A* | gRNA 2 | GGAACCAATTGGCTGTTACA | CCATAATACAAGCGCATAATGT | |
| *CTC534A2.2* | gRNA 1+2 | CATTGTCCTCAATTTAAGTTTGCCTC | GTGTTCTATTGTCCATCTTGCTC | TTCCTTTTCTCCCTGCCTGTTG |
| *RNF8* | gRNA 1 | TGAGAAGAGGTTCCAGTCTGG | ACAGACACTTCGCTCCTCTTC | |
| *RNF8* | gRNA 2 | AGCAGCAGGAGAGAGATTCC | CCCTGAAGACCACTCTTGC | |
| *RNF168* | gRNA 1+2 | GGACAAAATCTTGCCCTTGAC | GAGCAGCCAGGCTCCTCC | |
| *SCAF1* | gRNA 1 | GGAGAGTCTGGGGGCCTGATC | GATCACCGCTACCATCACTACC | |
| *SCAF1* | gRNA 2 | CACTCCTGCCACTGTCTCATC | CTTTCTGTGGCTGAGGATCTG | GGTATGGGCTGTTCTCTCATT |
| *REV7* | gRNA 1+2 | TGTCACCCAGGCTGGAATGC | GGGAACTGGGGAAGGACCT | |
| *PTIP* | gRNA 1 | TTGTAATCCCAGCTACTCAGG | CATCTGTCTTGAGGACAGACC | |
| *PTIP* | gRNA 2 | TAGGGGCCGAGGTACAGAGC | GAGCGGACCCCGATTCGC | |
| *ATMIN* | gRNA 1+2 | ACGACAGGAGCCGCCGCC | TTCGAGAGCCGCCTCCGGCC | |

| targeting gene | genomic locus | forward primer | reverse primer |
|---|---|---|---|
| *C20orf196* | gRNA1 and 2 | ATTTGTCATTATGTCTGGCTCC | TTGGCCAATTCAAACTGTGC |
| *C20orf196* | gRNA2_2 | ATTTGTCATTATGTCTGGCTCC | TTGGCCAATTCAAACTGTGC |
| *Trp53bp1* | e6 | GCTACCACACCCAGTCTGAT | CAGCACTCACAACAATGGCT |
| *Fam35a* | gRNA1 | TCTGCTCAGGTGGATGAGGA | CCTGTTGGTTCTGCCTCCAT |
| *Fam35a* | e4 | ATATGTGGTAGTGTGGGCCG | ACCGTGTGTCAGAGAAGCTC |
| *Shld3* | e2 | AGCTCTGAAGAATTCAGCTAAGAAA | TCCATATTCATTTCATTCAGAATTC |
| *HPRT* | qPCR primers | CCCAGCGTCGTGATTAGC | GGAATAAACACTTTTTCCAAAT |
| μ germline transcript | qPCR primers | CTCTGGCCCTGCTTATTGTTG | CTGACTCTGGGTGGCAGAAG |
| α germline transcript | qPCR primers | CCTGGCTGTTCCCCTATGAA | GAGCTGGTGGGAGTGTCAGTG |

**SUPPLEMENTARY TABLE 7 |**

| Primary antibodies | Company | WB dilution | IF dilution |
|---|---|---|---|
| Rb anti RAD51 | Santa Cruz, sc-8349 | | 1:150 |
| Rb anti RAD51 | Bio Academia, #70-001 | | 1:2,000 |
| Rb anti REV7 | Abcam, ab180579 | 1:1,000 | 1:500 |
| Rb anti 53BP1 | Santa Cruz, sc-22760 | | 1:5,000 |
| M anti 53BP1 | Becton Dickinson, #612523 | 1:1,000-3,000 | |
| G anti RIF1 | Santa Cruz, sc-55979 | 1:1,000 | 1:200 |
| R anti RIF1 | Bethyl A300-569A | 1:7,500 | |
| M anti γH2AX | Millipore, #05-636 | | 1:5,000 |
| Rb anti BRCA1 | homemade | 1:1,000 | |
| Rb anti pRPA32 (S4/S8) | Bethyl, A300-245A | 1:1,000 | |
| Rb anti KAP1 | Bethyl, A300-274A | 1:2,000 | |
| M anti Tubulin | Calbiochem, CP06 | 1:2,000 | |
| M anti Tubulin | Sigma, T6199 | 1:5,000 | |
| Rb anti Flag | Cell Signalling Technologies, #2368S | 1:2,000 | |
| M anti Flag-HRP | Sigma, A8592 | 1:1,000 | |
| G anti GFP | Homemade by Pelletier lab, Lunenfeld-Tanenbaum Research Institute | 1:5,000 | |
| Rb anti GFP | Abcam, ab290 | 1:1,000-5,000 | 1:2,000 |
| M anti GFP | Roche, #11814460001 | | 1:2,000 |
| M anti V5 | Invitrogen, #46-0705 | 1:1,000 | |
| M anti HA | Biolegend, #901502 | 1:1,000 | |
| G anti mouse IgA-PE | Southern Biotech #1040-09 | | FACS: 1:100-150 |
| M anti-AID | Cell Signaling Technologies, #4975 | 1:1,000 | |
| Anti-β-actin | Sigma | 1:2,000 | |

| Secondary antibodies | Company | WB dilution | IF dilution |
|---|---|---|---|
| HRP-tagged Rabbit anti Mouse | DakoCytomation, P0260 | 1:5,000 | |
| HRP-tagged Goat anti Rabbit | Jackson Laboratories, #111-035-144 | 1:5,000 | |
| HRP-tagged bovine-anti-goat | Jackson Laboratories, #805-035-180 | 1:5,000 | |
| IRDye-conjgated Goat anti Mouse | Li-cor, #926-32210 | 1;10,000 | |
| IRDye-conjgated Goat anti Rabbit | Li-cor, #926-68071 | 1;10,000 | |
| AlexaFluor-488 Goat anti Mouse | Invitrogen, A-11029 | | 1:1,000 |
| AlexaFluor-488 Goat anti Rabbit | Invitrogen, A-11034 | | 1:1,000 |
| AlexaFluor-488 Donkey anti Goat | Invitrogen, A-11055 | | 1:1,000 |
| AlexaFluor-555 Goat anti Mouse | Invitrogen, A-21424 | | 1:1,000 |
| AlexaFluor-555 Goat anti Rabbit | Invitrogen, A-21429 | | 1:1,000 |
| AlexaFluor-647 Goat anti Mouse | Invitrogen, A-21236 | | 1:1,000 |
| AlexaFluor-647 Goat anti Rabbit | Invitrogen, A-21245 | | 1:1,000 |
| Alexa fluor 568 $F(ab')_2$ Fragment goat anti-rabbit | Invitrogen, A-21069 | | 1:1,000 |

## Abstract

Selective elimination of BRCA1-deficient cells by inhibitors of poly(ADP-ribose) polymerase (PARP) is a prime example of the concept of synthetic lethality in cancer therapy. This interaction is counteracted by the restoration of BRCA1-independent homologous recombination through loss of factors such as 53BP1, RIF1, and REV7/MAD2L2, which inhibit end resection of DNA double-strand breaks (DSBs). To identify additional factors involved in this process, we performed CRISPR/SpCas9-based loss-of-function screens and selected for factors that confer PARP inhibitor (PARPi) resistance in BRCA1-deficient cells. Loss of members of the CTC1-STN1-TEN1 (CST) complex were found to cause PARPi resistance in BRCA1-deficient cells *in vitro* and *in vivo*. We show that CTC1 depletion results in the restoration of end resection and that the CST complex may act downstream of 53BP1/RIF1. These data suggest that, in addition to its role in protecting telomeres, the CST complex also contributes to protecting DSBs from end resection.

# Cancer Chess: Molecular Insights Into PARPi Resistance

## The CST Complex Mediates End Protection at Double-Strand Breaks and Promotes PARP Inhibitor Sensitivity in BRCA1-Deficient Cells

# Chapter 6

*Adapted from:*
***Marco Barazas**, Stefano Annunziato, Stephen J Pettitt, Inge de Krijger, Hind Ghezraoui , et al.*
*Cell Reports. 2018; 23(7): 2107-2118.*

## Introduction

The synthetic lethal interaction between BRCA1 deficiency and poly(ADP-ribose) polymerase (PARP) inhibition is a well-established therapeutic paradigm with encouraging response rates in the clinic [1]. This has resulted in the recent regulatory approval of three PARP inhibitors (PARPis) for the treatment of serous ovarian cancers and one PARPi, olaparib, for the treatment of *BRCA*-mutated, HER2-negative breast cancers. Moreover, the BRCA-PARP paradigm might be extended beyond breast and ovarian cancer because recent clinical studies indicate that a subset of prostate cancers harbor a homologous recombination (HR) defect and, hence, might benefit from olaparib treatment [2, 3].

Despite this success, long-lasting clinical response rates in patients with advanced disease are limited by the development of resistance, the mechanisms of which have not been fully elucidated. A major class of resistance mechanisms centers on re-expression of functional BRCA1 or BRCA2 protein, either through promoter demethylation, genetic reversion, or gene fusions [4-6]. However, our previous work also identified the existence of additional BRCA1-independent resistance mechanisms in the *K14cre;Brca1*$^{F/F}$*; p53*$^{F/F}$ (KB1P) genetically engineered mouse model of hereditary breast cancer [7]. In this model, re-expression of functional BRCA1 is excluded because of the large, engineered, intragenic *Brca1* deletion, which spans multiple exons. Despite the absence of functional BRCA1 restoration, KB1P tumors acquired resistance to PARPi treatment. In addition to activation of the P-glycoprotein drug efflux transporter [8], the BRCA1-independent resistance mechanisms in KB1P tumors predominantly involved the partial restoration of HR activity through re-wiring of the DNA damage response (DDR); for example, by loss of 53BP1 [9-11]. These seminal findings have spurred a number of studies in which additional downstream antagonists of end resection were identified, including RIF1 [12-15] and REV7/MAD2L2 [16, 17]. However, the currently known resistance factors cannot explain all PARPi-resistant cases, suggesting that additional proteins functioning in this pathway remain to be identified. Moreover, although the loss of resection antagonists partially restores end resection of DNA double-strand breaks (DSBs), none of these factors have direct functions in DNA metabolism, raising the question of how DNA metabolism at DSBs might be altered to stimulate end resection.

The function of the 53BP1 pathway is not exclusive to canonical DSB repair, but it also acts on telomeres [18]. Because telomere ends resemble DSBs located at chromosomal termini, cells have evolved several mechanisms to protect telomeres from DSB end processing and chromosome end-to-end fusions [19]. Mammalian telomeres consist of TTTAGG repeats ending with a single-strand G-rich overhang. The single-stranded DNA (ssDNA) overhang is crucial in telomere maintenance because it is required for the formation of the T-loop structure [20, 21]. Notably, excessive resection of telomere ends is inhibited by the action of the shelterin complex and by the 53BP1 pathway [19, 22].

Besides the mechanisms that have evolved to protect telomeric overhangs from excessive processing, it has recently been shown that the RPA-like CTC1-STN1-TEN1 (CST) complex is able to localize to telomeric ssDNA and mediate a fill-in reaction executed by polymerase-alpha (POLA) to buffer resection activity [23-25]. Notably, it was demonstrated that the binding of the CST complex to ssDNA is not particularly sequence-specific, although a partial preference for G-rich regions has been described [24, 26]. Additionally, CST components do not localize exclusively to telomeres [24]. This might argue that the CST complex also has non-telomeric functions.

In this study, three independent forward genetic CRISPR/SpCas9-based loss-of-function screening approaches were employed to identify factors that induce PARPi resistance in BRCA1-deficient cells. Together, these screens identified that defects in *Ctc1*, or its CST complex members *Stn1* or *Ten1*, suppress the synthetic lethal interaction between BRCA1 and PARP inhibition. Inactivation of CTC1 is sufficient to drive PARPi resistance *in vivo*. Depletion of CTC1 increased end resection activity and subsequently restored RAD51 focus formation upon ionizing radiation (IR)-induced DNA damage, providing a mechanistic basis for these observations. Moreover, the CST complex facilitates canonical non-homologous end joining (c-NHEJ)-driven repair. Together, these data demonstrate that the CST complex plays a more global role in DNA repair beyond the protection of telomeres.



## Results

*Forward Genetic CRISPR/SpCas9 Screens Identify Selective Enrichment for Loss of CTC1 during PARPi Treatment in BRCA1-Deficient Cells*

To identify factors that modulate the synthetic lethal interaction between BRCA1 and PARP, we carried out three independent forward genetic loss-of-function CRISPR/SpCas9 screens (Fig. 1). All screens were analyzed by harvesting cells before and after PARPi treatment, after which single guide RNA (sgRNA) sequences were amplified from genomic DNA by PCR and analyzed by next-generation sequencing. The screening data were processed by the model-based analysis of genome-wide CRISPR-Cas9 knockout (MAGeCK) or the drugZ algorithm [27, 28], and the results were sorted on positive selected gene ranks to allow comparison across screens. Additional experimental details are provided in the Supplementary Materials and Methods.

The first PARPi resistance screen was performed in SpCas9-expressing KB1P-G3 mouse mammary tumor cells [11] using a custom-made lentiviral sgRNA library targeting 1,752 DDR-related genes (Table S1) cloned into the doxycycline-inducible pLenti-sgRNA-tetR-T2A-PuroR vector [29]. The screen was performed at 100× coverage, and cells were selected with two different PARPis, olaparib and AZD2461 [30], at the approximate inhibitory concentration 90 (IC90) for 14 days (Fig. 1A). Although sgRNAs targeting *Tp53bp1* were deliberately removed from the library to avoid the possibility

that this potent PARPi resistance factor might obscure the effects of other genes, its upstream regulatory factor *Rnf8* scored among the top genes (Fig. 1B).

The second PARPi resistance screen was performed in SpCas9-expressing *Brca1*$^{-/-}$*;Trp53*$^{-/-}$ mouse embryonic stem cells (mESCs) infected with a genome-wide lentiviral sgRNA library targeting 19,150 genes [31]. The screen was performed at 75× coverage in two independent transductions, and cells were selected with olaparib at a concentration of 15 nM for 10 days. As expected, *Tp53bp1* and *Rnf8* scored among the top genes and ranked #1 and #15, respectively (Fig. 1C).

A third PARPi resistance screen was performed in *BRCA1*$^{2288delT}$ mutant SUM149PT human breast cancer cells [32]. SUM149PT cells expressing doxycycline-inducible SpCas9 were lentivirally infected with a genome-wide sgRNA library targeting 18,010 genes [33]. This screen was performed at 1,000× coverage, and cells were selected in the presence of doxycycline plus 100 nM talazoparib for 2 weeks. The screen was dominated by sgRNAs targeting *PARP1*, the drug target of talazoparib. Although PARP1 loss is expected to be lethal in BRCA1-deficient cells, the selection for PARP1 loss in SUM149PT cells might be attributed to residual BRCA1 activity, which might enable cell survival in the absence of PARP [34, 35]. Moreover, *TP53BP1* scored among the top enriched genes and ranked #7 (Fig. 1D).

The results from these three independent screens were collated to identify consistent outliers. The top 20 genes were selected from the DDR-focused library screen in KB1P-G3 cells. Because the genome-wide libraries contain about 10-fold more genes than the DDR-focused library, the top 200 genes were selected from the mESC and SUM149PT screens, and these were plotted in a Venn diagram (Fig. 1E). Notably, *Ctc1* was the only gene that consistently scored in all three screens (ranked #10, #39, and #39 in the KB1P-G3, mESC, and SUM149PT screens, respectively). Moreover, *Stn1* (also known as *Obfc1*) scored in two of three screens. These results caught our attention because both CTC1 and STN1 are members of the CST complex. Although the CST complex has known functions in telomere metabolism, these PARPi resistance screens might point toward non-telomeric functions of the CST complex. Because *Ctc1* was a top hit in all three independent screens in both mouse and human cells, we prioritized this gene for further validation.

*Depletion of CTC1 Suppresses the Synthetic Lethal Interaction between BRCA1 Deficiency and PARP Inhibition*

To validate the effect of CTC1 on PARPi sensitivity in BRCA1-deficient cells, we transfected KB1P-G3 cells with pX330 vectors containing three sgRNAs targeting a putative oligonucleotide-binding (OB) fold domain of *Ctc1* (Fig. 2A). The polyclonal targeted populations were efficiently modified for the target site (Fig. 2B–D), as shown by TIDE (tracking of insertions or deletions [indels] by decomposition) analysis [36]. These populations were subsequently treated with olaparib (75 nM) or AZD2461

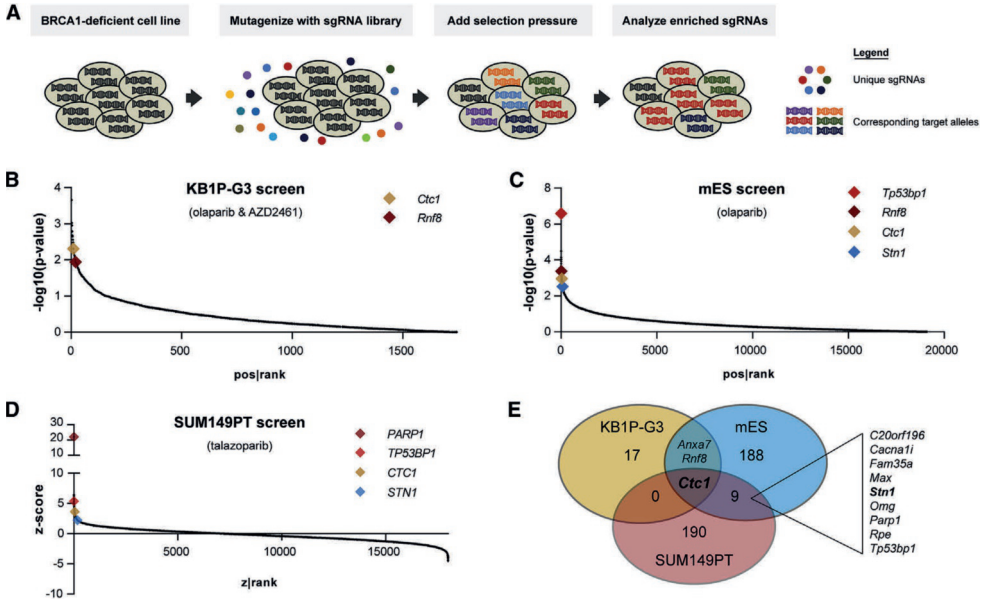



**FIGURE 1 | Multiple Independent CRISPR/SpCas9 Loss-of-Function Screens Identify CTC1 as a Driver of PARPi Resistance in BRCA1-Deficient Cells.** *(A)* Schematic overview of the screening approach utilized across the different screens. Each screen was performed on a different cell line and screened with a different library, which is indicated per screen. *(B)* SpCas9-expressing KB1P-G3 cells were screened with a DNA damage response (DDR)-focused library at 100× coverage. Cells were plated for clonogenic growth in the presence of olaparib (75 nM) or AZD2461 (250 nM) for 14 days, and sgRNA abundance in treated populations was compared with the starting population using MAGeCK software. Gene-based p values were log-transformed and plotted based on the positive rank (enrichment). Each dot represents a unique gene. *(C)* *Brca1*$^{-/-}$;*Trp53*$^{-/-}$ mouse embryonic stem cells (mESCs) were screened with a genome-wide library in two independent transductions at 75× coverage. After 10 days of culture in the presence of olaparib (15 nM), treated populations were compared with the untreated population using MAGeCK software. Gene based p values were log-transformed and plotted based on the positive rank (enrichment). Each dot represents a unique gene. *(D)* A derivative of the *BRCA1* mutant SUM149PT human triple-negative breast tumor cell line carrying a doxycycline-inducible SpCas9 expression construct was lentivirally infected with a genome-wide guide RNA library at more than 1,000× coverage. Cells were cultured in the presence of doxycycline plus 100 nM talazoparib for 2 weeks. The sgRNA abundance in treated populations was compared with the starting population using drugZ. Gene-based *Z* scores were log-transformed and plotted based on the positive z-rank (enrichment). Each dot represents an individual gene.

(250 nM), the same concentrations as used for the screen. As expected, parental KB1P-G3 cells or KB1P-G3 cells targeted by a non-targeting sgRNA (sgNT) showed high sensitivity to PARPi treatment. In contrast, *Ctc1*-targeted cells showed resistance to treatment, indicating that depletion of CTC1 suppresses the synthetic lethal interaction between BRCA1 deficiency and PARP inhibition (Fig. 2E-F). This could not be attributed to an effect on cell proliferation because we observed no difference in the doubling time upon depletion of CTC1 (Fig. 2G).

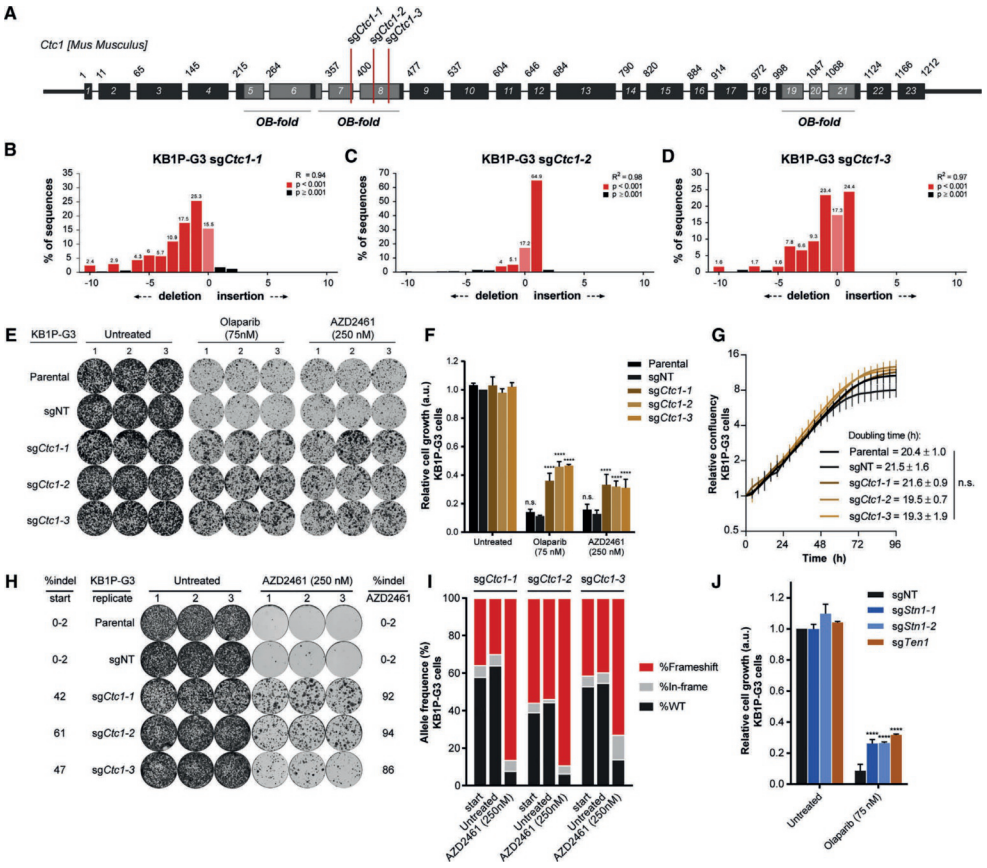



**FIGURE 2 | Depletion of CTC1 Suppresses the Synthetic Lethal Interaction between BRCA1 Deficiency and PARP Inhibition.** *(A)* Schematic overview of the *Ctc1* gene, in which putative OB fold domains and sgRNA target locations are indicated (adapted from [24]). *(B–D)* KB1P-G3 cells were transfected with pX330puro vectors containing the indicated sgRNAs, and the target region was PCR-amplified to verify allele modification using TIDE software. *(E)* The indicated *Ctc1*-mutated KB1P-G3 cell lines were plated for clonogenic growth upon olaparib (75 nM) or AZD2461 (250 nM) treatment. Three independent experiments were performed, and each condition was plated in triplicate. One representative well per condition is shown for each independent experiment. *(F)* Quantification of crystal violet staining in (E). Data were plotted relative to the growth of untreated sgNT cells and are presented as mean ± SD (n = 3 independent experiments). Significance was calculated by two-way ANOVA with Dunnett's multiple comparisons test (**** adjusted p = 0.0001). *(G)* Relative cell proliferation was determined by IncuCyte Zoom Live – Cell Analysis System measurements. Each data point represents the average of three independent experiments, and in each experiment, six replicate wells were measured and averaged. Data represent mean ± SD (n = 3). Doubling times (exponential growth equation) were calculated using GraphPad software, and significance was calculated by one-way ANOVA with Dunnett's multiple comparisons test. *(H-I)* SpCas9-expressing KB1P-G3 cells were transduced with doxycycline-inducible pLenti-sgRNA-tetR-T2A-PuroR vectors containing the indicated sgRNAs. Polyclonal populations were plated for clonogenic growth with or without AZD2461 (250 nM) *(H)*. Cells were passaged every 10 days for a total of three times. At the endpoint, wells were fixed and stained with crystal violet, and allele distributions were determined from each condition using TIDE software *(I)*. *(J)* KB1P-G3 cells were transfected with pX330puro vectors containing sgRNAs targeting *Stn1* and *Ten1* and cultured in the presence or absence of 75 nM olaparib as in *(E)*. Data were analyzed as in *(F)* and reflect at least two independent experiments.

We next investigated whether *Ctc1*-mutated cells would be specifically selected out from a mixed population by prolonged PARPi treatment. A competition assay was performed in which the evolution of polyclonal populations was monitored by the TIDE algorithm to quantify changes in allele distributions. sgRNAs were cloned in the pLenti-sgRNA-tetR-T2A-Puro vector and introduced in SpCas9-expressing KB1P-G3 cells by lentiviral transduction. The population was mutagenized by doxycycline-induced expression of the sgRNA for 5 days, after which cells were plated without doxycycline for clonogenic growth. After 10 days of culture in the presence or absence of AZD2461, the cells were harvested and re-plated at equal amounts every 10 days for an additional two rounds, resulting in a total treatment duration of 30 days. Although non-transduced cells or cells transduced with a non-targeting sgRNA were effectively killed by this prolonged treatment, *Ctc1*-targeted cells survived (Fig. 2H). This coincided with an enrichment of *Ctc1* frameshift mutations compared with untreated populations, which were kept in culture for the same duration (Fig. 2I).

To study whether this effect is CTC1-specific or a feature of the CST complex, we genetically inactivated the other two CST complex members *Stn1* and *Ten1*, and treated these cells with olaparib under the same conditions as used for *Ctc1*. CRISPR/SpCas9-mediated disruption of *Stn1* or *Ten1* also induced PARPi resistance, recapitulating the effect of *Ctc1* (Fig. 2J). This is consistent with the identification of STN1 in the PARPi resistance screens (Fig. 1E) and shows that PARPi sensitivity is modulated by all CST complex members rather than CTC1 alone.

These data were corroborated in *Brca1*$^{-/-}$*;Trp53*$^{-/-}$ mESCs in which CRISPR/SpCas9-assisted inactivation of *Ctc1* increased survival upon olaparib treatment, which was accompanied by a selection for frameshifting alleles (Supplementary Fig. S1A-B). Furthermore, we targeted the CST complex members in *R26*$^{CreERT2}$*;Brca1*$^{Sco/\Delta}$ mESCs, which harbor a selectable conditional Brca1$^{Sco}$ allele that can be inactivated by CreERT2 through the addition of 4-hydroxytamoxifen (4-OHT) [9]. Although 4-OHT-induced inactivation of BRCA1 caused lethality in untransduced *R26*$^{CreERT2}$*;Brca1*$^{Sco/\Delta}$ mESCs, clonal outgrowth was observed for cells depleted of CTC1, STN1, or TEN1 (Fig. 3A). Complete switching of the conditional *Brca1*$^{Sco}$ allele in the surviving population was confirmed by PCR, ruling out that clonal outgrowth was due to a non-recombined *Brca1*$^{Sco}$ allele (Fig. 3B). Finally, depletion of CTC1 in SUM149PT cells enhanced cell survival in the presence of talazoparib, as did depletion of 53BP1 (Fig. 3C), confirming that this effect was not restricted to mouse cells.

In summary, we confirmed that the CST complex promotes PARPi-induced cell lethality in BRCA1-deficient cells. We therefore looked at the role of the CST complex in preventing global DNA damage, focusing on CTC1.

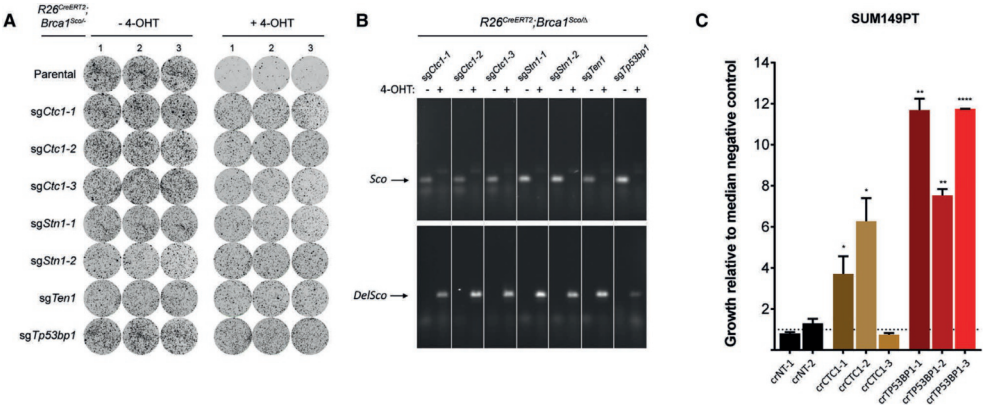



**FIGURE 3 | Loss of CST Complex Members Induces PARPi Resistance in BRCA1-Deficient mESCs and SUM149PT Breast Cancer Cells.** *(A) Ctc1*, *Stn1*, and *Ten1* were targeted in *R26*$^{CreERT2}$;*Brca1*$^{Sco/\Delta}$ mESCs using pLentiCRISPRv2 vectors. Following transduction and selection, the *Brca1-Sco* allele was recombined by activation of CreERT2 via addition of 4-OHT, after which cells were plated out for clonogenic growth. Cells were fixed and stained with crystal violet. *(B) Brca1* alleles from surviving populations were PCR-amplified using specific primers to detect *Brca1*$^{Sco}$ (*Sco*) and recombined *Brca1*$^{\Delta Sco}$ (*DelSco*) alleles. *(C) BRCA1*-mutant SUM149PT cells were transfected with the EditR CRISPR system, and the indicated CRISPR RNA (crRNA) and then continuously cultured in the presence of 50 nM talazoparib over a 14-day period, at which point cell viability was estimated by use of CellTiter-GLo reagent. Median effects from three independent experiments are shown. Error bars represent SEM. $^{*}p = 0.0415$ and 0.0201, respectively; $^{**}p = 0.0013$ and 0.0011, respectively; $^{****}p = < 0.0001$; unpaired two-tailed Student's t test.

### *CTC1 Antagonizes End Resection at Non-Telomeric DSBs*

During the repair of DSBs, a critical decision is made between initiating repair via NHEJ or via HR, which both require distinct end processing. This decision is tightly balanced by end protection factors, such as 53BP1 or RIF1, which antagonize resection to direct repair via NHEJ, and BRCA1, which promotes end resection to direct repair via HR [12, 14, 18, 23, 37]. It was previously shown that the end resection defect in BRCA1-deficient cells can be rescued via loss of 53BP1, and this also rescued cell lethality induced by BRCA1 loss [9, 38]. Hence, the finding that loss of the CST complex (Fig. 3A) rescued BRCA1 lethality points toward a potential inhibitory role in DSB end resection. Moreover, depletion of CTC1 did not induce PARPi resistance in BRCA2-deficient cells (Supplementary Fig. S2A-B), which is in line with a possible role of the CST complex upstream of BRCA2.

DSB end resection produces ssDNA overhangs, which are protected from nucleolytic degradation and the formation of secondary structures by the coating of RPA. Therefore, we visualized RPA loading in response to α-particle-induced DNA damage by immunofluorescence as a readout for end resection [39]. In line with previous studies [25, 40], KB1P-G3 tumor cells showed a clear resection defect that was partially restored in *Ctc1*-mutated KB1P-G3 cells but not in sgNT-transfected control cells (Fig. 4A-B).

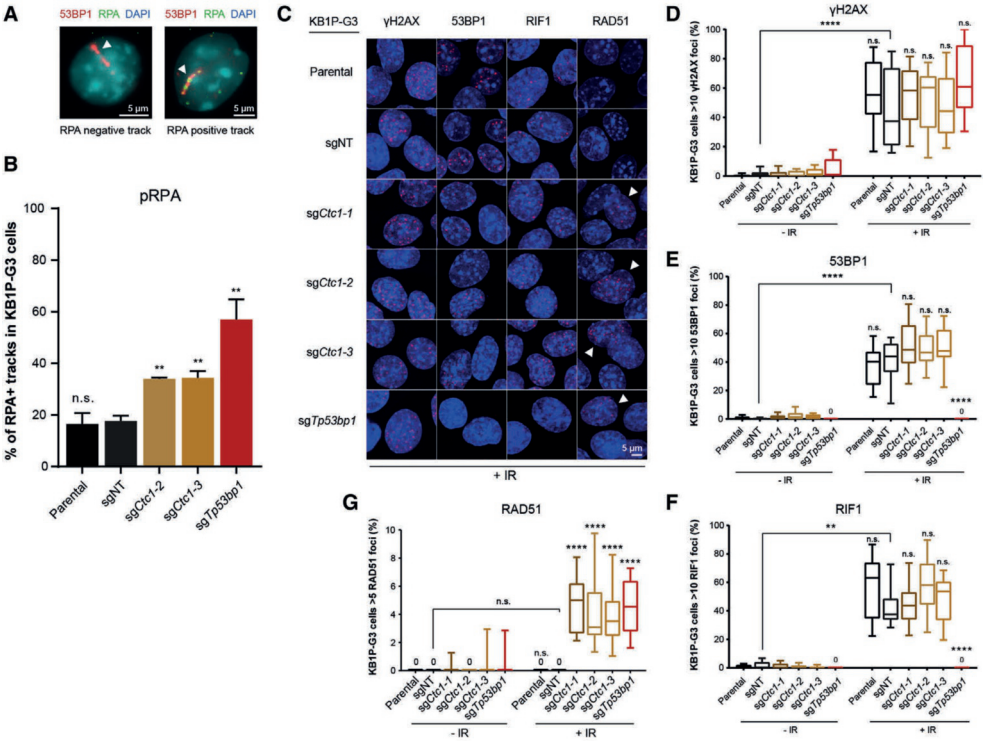



**FIGURE 4 | CTC1 Functions as a Resection Antagonist on Non-telomeric DSBs.** *(A-B)* CTC1 depletion induces RPA-coated ssDNA overhangs at sites of DNA damage in BRCA1-defient KB1P cells. *(A)* Representative images of RPA-negative and RPA-positive 53BP1-labeled alpha tracks in the indicated CRISPR/SpCas9-targeted KB1P-G3 cells (highlighted by the white arrowheads). Scale bars represent 5 µm. *(B)* RPA co-localization was quantified 1 hr after irradiation with an Americium-241 ($^{241}$Am) point source. The experiment was performed three times, and in each independent experiment, a minimum of 100 tracks were analyzed. Data are plotted as mean ± SEM. Significance was calculated by unpaired two-tailed Student's t test (**p < 0.01). *(C-G)* CTC1 depletion restores formation of DNA damage-induced RAD51 foci in BRCA1-deficient cells. *(C)* Representative confocal images of CRISPR/SpCas9-expressing KB1P-G3 cells targeted with the indicated sgRNAs. Cells were stained 3 hr after 10 Gy of ionizing radiation (IR) for the indicated proteins. RAD51-positive cells are highlighted by the white arrowheads. The scale bar represents 5 µm. *(D–G)* Quantification of confocal images, plotted as a box and whiskers plot. The box represents the 25$^{th}$ to 75$^{th}$ percentiles, and the whiskers show the minimum to maximum values. The experiment was performed at least twice, and data are plotted as a percentage of yH2AX- (D), 53BP1- (E), or RIF1-positive cells (> 10 foci) (F) or RAD51-positive cells (> 5 foci) (G) per field. Statistics were performed by Kruskal-Wallis non-parametric test followed by Dunn's multiple comparisons test. The indicated cell lines were compared with sgNT-treated cells (**** p < 0.0001). Also see Supplementary Fig. S3.

We next investigated whether CTC1 loss affects the recruitment of DDR factors to sites of irradiation-induced DNA damage. CRISPR/SpCas9-targeted KB1P-G3 cells were either left untreated or treated with 10 Gy of IR, which potently induced yH2AX foci (Fig. 4C-D; Supplementary Fig. S3A-B). Although depletion of 53BP1 in KB1P-G3 cells abolished the formation of IR-induced 53BP1 and RIF1 foci, these effects were not

observed in CTC1-depleted cells (Fig. 4E-F and S3C-D). Despite the capacity to form 53BP1 and RIF1 foci, KB1P-G3 cells that were depleted of CTC1 restored IR-induced RAD51 focus formation, whereas sgNT-transfected control cells were deficient for this activity (Fig. 4G-E). Similar conclusions were obtained when DNA damage was induced by treatment with 500 nM olaparib for 24 hr (Supplementary Fig. S3A,F–M). As expected, PARPi treatment resulted in more heterogeneous DNA damage induction compared with IR because PARP inhibition primarily exerts its cytotoxic effects during replication.

We then tested whether CTC1 loss resulted in productive HR events in conditional BRCA1-deficient $R26^{CreERT2}$;$Brca1^{SCo/\Delta}$;$Pim1^{DR\text{-}GFP/wt}$ mESC cells carrying a stably integrated DR-GFP reporter [41]. These cells were transfected to transiently express mCherry and I-SceI, and the percentage of mCherry/GFP double-positive cells was quantified by fluorescence-activated cell sorting (FACS) 24 hr later. Switching of the conditional $Brca1^{SCo}$ allele impaired HR activity, which was partially rescued upon depletion of the CST complex (Supplementary Fig. S3N-O).

Together, these data support a role for CTC1 as a resection antagonist acting on non-telomeric DSBs and as a mediator of the HR defect in BRCA1-deficient cells.

*CTC1 Facilitates c-NHEJ-Mediated Repair at Telomeric and Non-Telomeric DSBs*

It was previously shown that 53BP1, RIF1, and REV7/MAD2L2 antagonize resection and promote c-NHEJ [9, 10, 12-17]. However, this is not a universal phenotype for resection antagonists because it is not shared by HELB [40]. We therefore sought to determine whether CTC1 affects NHEJ activity. First, we used $Terf2^{-/-}$;$Trp53^{-/-}$ mouse embryonic fibroblasts (MEFs) that express a temperature-sensitive $TRF2^{Ile468Ala}$ mutant (TRF2ts) [31]. TRF2ts is functional and maintains intact TRF2-protected telomeres at 32°C, but it dissociates from telomeres at 37°C–39°C, inducing a DDR response and end-to-end chromosome fusions [31]. It was previously demonstrated that these fusions are driven by c-NHEJ and can be rescued by depletion of RNF8, LIG4, or REV7/MAD2L2 [16, 42-44].

We depleted CTC1 in TRF2ts MEFs grown under permissive conditions (Fig. 5A), which did not affect cell cycle distribution (Supplementary Fig. S4A-B). Cells were then grown at the non-permissive temperature (39°C) for 24 h to uncap telomeres and induce a DDR response prior to harvesting metaphase spreads for telomere fluorescence *in situ* hybridization (FISH). Although chromosome fusions were readily observed in control cells upon temperature-induced TRF2 inactivation, this was significantly reduced in *Ctc1*-mutated cells (Fig. 5B-C; Supplementary Fig. S4C–E). In line with this finding and with NHEJ being inhibited by long ssDNA overhangs, it was previously shown that depletion of CTC1 increased ssG overhang length [45, 46].

We next assessed whether CTC1 depletion in mouse CH12 B cells affects the ability to undergo class switch recombination (CSR) as a measure for non-telomeric c-NHEJ capacity [47]. CH12 cells were transfected with *Ctc1*-targeting CRISPR/SpCas9 constructs

and subcloned to obtain *Ctc1*-mutated CH12 cell clones. Notably, only 2 of 96 tested clones showed heterozygous *Ctc1* allele disruption, and no homozygous knockouts were obtained (Supplementary Fig. S4F-G), raising the possibility that complete loss of CTC1 is lethal in CH12 cells. Wild-type and heterozygous *Ctc1* knockout clones were subsequently stimulated with CD40Ab, interleukin-4 (IL-4), and transforming growth factor β-1 (TGF-β-1, CD40Ab, IL-4, and TGFβ-1 [CIT]) to induce CSR from immunoglobulin M (IgM) to IgA, which was monitored by flow cytometry. Interestingly, heterozygous knockout of *Ctc1* significantly diminished CSR in both

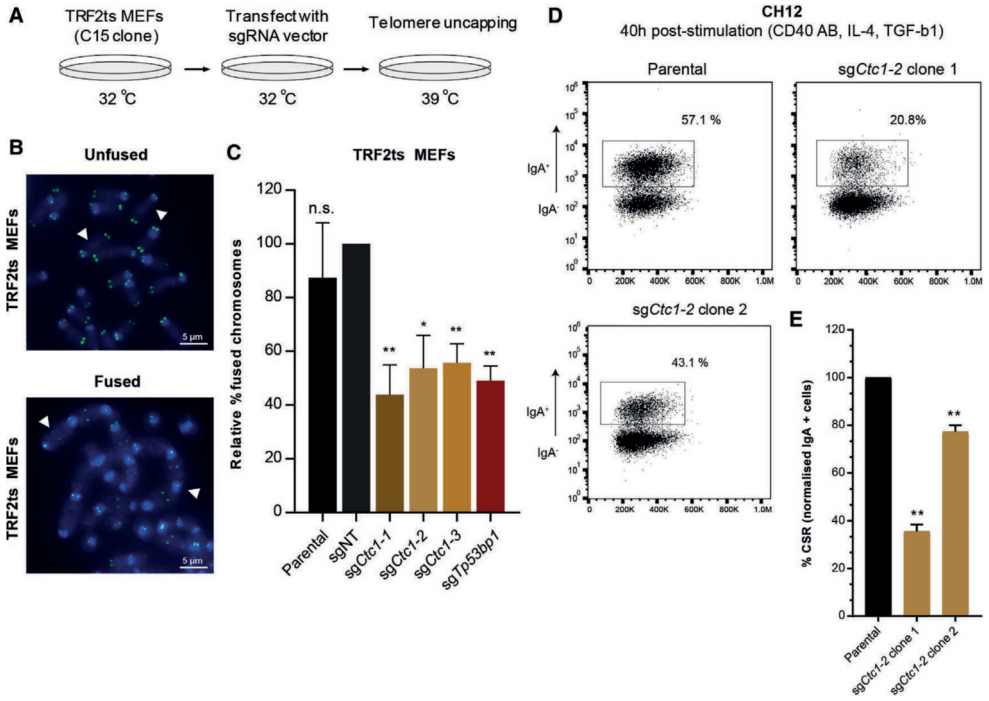



**FIGURE 5 | CTC1 Facilitates c-NHEJ at Telomeric and Non-telomeric DSBs.** *(A–C)* CTC1 depletion suppresses end-to-end fusions of uncapped telomeres. *(A)* Schematic overview of the telomere fusion assay. TRF2ts mouse embryonic fibroblasts (MEFs) of the indicated genotypes were cultured at the non-permissive temperature (39°C) for 24 hr before harvesting. *(B)* Representative images of metaphase spreads showing chromosomes unfused or fused at their telomeres (examples highlighted by white arrowheads). Chromosomes were stained with DAPI and a telomere-specific FISH probe (green). *(C)* Metaphases were detected and imaged automatically by Metafer. At least two independent experiments were performed, in each independent experiment, more than 2,000 chromosomes were counted manually. Genotypes were blinded during counting. Data are plotted as mean ± SEM. Significance was determined by unpaired two-tailed Student's t test ($^{*}p \leq 0.05$; $^{**}p \leq 0.01$). *(D-E)* Heterozygous inactivation of *Ctc1* impairs IgM-to-IgA class switch recombination (CSR) in CH12 B cells. *(D)* FACS analysis of CH12 clones of the indicated genotype 40 hr after induction of CSR by incubation with CD40Ab, IL-4, and TGF-β-1 (CIT). *(E)* Quantification of FACS data, representing mean ± SD of two independent experiments. Significance was calculated by unpaired Student's t test ($^{**}$ p value ≤ 0.01).

clones (Fig. 5D and 5E). We therefore conclude that CTC1 facilitates DSB repair via c-NHEJ at both telomeric and non-telomeric regions.

*Depletion of CTC1 Mediates PARPi Resistance in the KB1P Mouse Model*

Last, we explored the *in vivo* effects of CTC1 on the treatment response of BRCA1-deficient tumors to PARP inhibition. We analyzed whether *Ctc1* mRNA expression levels were altered in our previously generated collection of BRCA1- and p53-deficient KB1P and KB1PM mouse mammary tumors with acquired resistance to PARP inhibition [11]. In total, this collection comprises 60 treatment-naive tumors and 85 matched PARPi-resistant tumors derived from 23 unique donors. To examine the expression levels of *Ctc1* in treatment-naive and PARPi-resistant tumors, we produced RNA sequencing (RNA-seq) data for all tumors [48] and obtained the normalized expression values using edgeR [49]. We observed that the expression of *Ctc1* is significantly downregulated in PARPi-resistant tumors compared with naive tumors ($p = 6.34 \times 10^{-4}$) (Fig. 6A). Moreover, in tumors for which copy number variation by sequencing (CNVseq) data were available, CTC1 mRNA downregulation correlated with CNV loss (Supplementary Fig. S5A,D). Although a similar correlation was observed for STN1 and TEN1, these factors were not significantly downregulated in resistant tumors (Supplementary Fig. S5B-C,E-F).

Finally, we used mammary tumor organoid technology [50] to perform an *in vivo* intervention study with the PARPi olaparib in mice carrying tumors derived from isogenic KB1P organoids with or without disruption of *Ctc1*. For this purpose, KB1P4 organoids, derived from a KB1P mammary tumor, were cultured *ex vivo* and co-transduced with lentiviruses produced from pCMV-SpCas9 and pLenti-sg*Ctc1*-tetR-T2A-Puro vectors. Control organoids were generated by co-transduction with pCMV-SpCas9 and pLenti-sgNT-tetR-T2A-Puro lentivirus encoding a non-targeting sgRNA (Fig. 6B). The transduced KB1P4 tumor organoids were orthotopically transplanted in mice that were left untreated or treated daily with the PARPi olaparib for 56 consecutive days when tumors reached a size of 50–100 $mm^3$. As expected, the *Ctc1* target site was efficiently disrupted in tumors derived from KB1P4 organoids transduced with pCMV-SpCas9 and pLenti-sg*Ctc1*-tetR-T2A-Puro (Fig. 6C-D). Although KB1P4 control tumors only relapsed after treatment was stopped, CTC1-depleted tumors relapsed during treatment, resulting in accelerated mammary tumor-related death (median latencies: 39 days for sg*Ctc1_2* and 42 days for sg*Ctc1_3* cohorts compared with 73 days for control animals; log rank test, $p = 0.0019$ and $p = 0.0086$, respectively; Fig. 6E). These data confirmed that depletion of CTC1 confers PARPi resistance in BRCA1-deficient tumors *in vivo*.

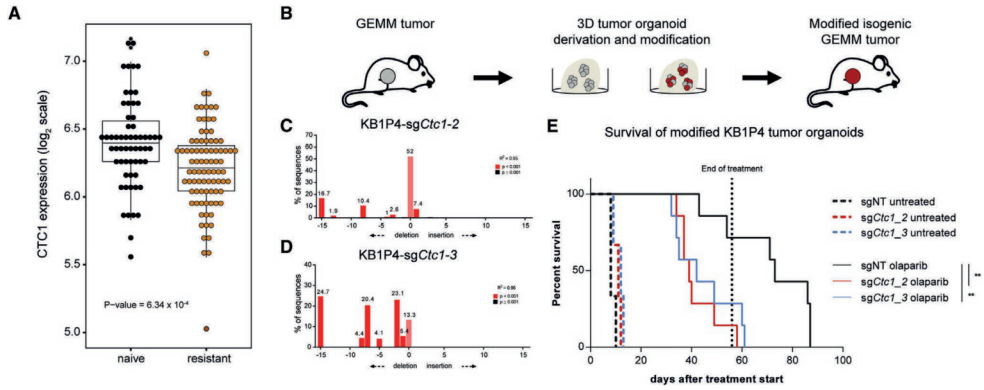



**FIGURE 6 | Depletion of CTC1 Induces PARP Inhibitor Resistance *In Vivo*.** *(A)* mRNA expression levels of Ctc1 in matched treatment-naive and PARPi-resistant BRCA1-deficient mouse mammary tumors. The y axis indicates the log2 (counts per million) value. *(B)* Schematic overview of the generation of isogenic Ctc1-mutated and control tumors via *ex vivo* manipulation of tumor organoids. *(C-D)* Example TIDE plots of untreated mammary tumors derived from Ctc1-mutated KB1P4 tumor organoids of the indicated genotype. *(E)* Survival of mice orthotopically transplanted with modified KB1P4 tumor organoids. Mice were stratified into untreated (n = 3) or olaparib-treated (100 mg/kg intraperitoneally daily for 56 consecutive days, n = 7) groups when tumors reached a size of 50–100 mm3. Significance was calculated by log rank (Mantel-Cox) test (**p < 0.01).



## Discussion

In this study, we show that loss of the CST complex members CTC1, STN1, and TEN1 induces PARPi resistance in tumors with irreversible loss of function of BRCA1. Our data highlight the CST complex as a pathway for tumor cells to escape the synthetic lethal effects of PARPi by restoring HR independently of BRCA1. In particular, we demonstrate that the underlying mechanism is a restoration of end resection of DSBs. Together, our findings demonstrate that the CST complex contributes to the regulation of DNA end stability not only at telomeres but also at non-telomeric DSBs.

We and others have recently shown that the 53BP1-RIF1-REV7/MAD2L2 pathway is crucial for blocking end resection of DSBs [9, 10, 12-17]. However, it has remained elusive how DNA end stability is regulated by 53BP1-RIF1-REV7/MAD2L2 because none of these factors have been shown to contain direct DNA binding capacity and do not contain DNA processing activities. Our finding that the CST complex functions as a resection antagonist at DSBs sheds light on this puzzle. The CST complex is an RPA-like complex that can directly bind ssDNA via multiple OB folds [24]. In collaboration with the laboratory of Dan Durocher, we recently identified another RPA-like complex, the Shieldin (SHLD) complex, which is composed of SHLD1 (C20ORF196), SHLD2 (FAM35A), SHLD3 (FLJ26957/CTC-534A2.2), and REV7/MAD2L2, as a downstream effector of 53BP1 in DSB repair [51]. Hence, in addition to RPA and the SHLD complex, the CST complex is another trimeric complex that contains direct DNA binding capacity and affects DSB end stability. How these three complexes are recruited to DSBs in

time and space remains to be elucidated. Possibly, RPA, SHLD, and CST compete for ssDNA at resected DSBs or collapsed forks to either promote or antagonize HR. Not mutually exclusive with this model, it is conceivable that these complexes might contain specialized functions dependent on the ssDNA substrate since the CST complex has been reported to preferentially bind to and promote melting of G-rich regions and G4-quadruplexes [52, 53].

Future work is also required to elucidate whether these complexes form the final step in the regulation of DSB end stability (for instance, through steric hindrance) or whether additional downstream factors are involved. Intriguingly, the CST complex has been described to buffer resection at telomeres via POLA-dependent fill-in DNA synthesis, which is required to prevent excessive telomere erosion [22]. Our finding that the CST complex antagonizes resection at non-telomeric DSBs raises the question of whether this is dependent on POLA activity. Resection can possibly be antagonized not only by shielding the ends of DSBs from end-processing activities but also by directly counteracting ongoing resection via fill-in DNA synthesis. This buffering activity might fine-tune the length of ssDNA around the DSB, which is vulnerable for nucleolytic degradation, and it might provide a rescue mechanism in case HR cannot be completed.

The identification of the CST complex as a mediator of PARPi response in BRCA1-deficient tumors might also have clinical implications because loss-of-function mutations in the CST-encoding genes are predicted to cause clinical PARPi resistance. Moreover, we expect that these alterations provide therapeutic vulnerabilities because we recently found that depletion of the 53BP1-dependent DNA repair pathway enhances sensitivity to IR [54].

## Materials and Methods

*Cell Culture and Gene Editing*

The KB1P-G3 cell line was previously established from a *K14cre;Brca1$^{F/F}$;Trp53$^{F/F}$* (KB1P) mouse mammary tumor and cultured as described by Jaspers et al. [11]. The KB2P-3.4 cell line was previously established from a *K14cre;Brca2$^{F/F}$;Trp53$^{F/F}$* (KB2P) mouse mammary tumor and cultured as described by Evers et al [55]. The KB1P4 3D tumor organoid line was previously established from a *Brca1$^{-/-}$;p53$^{-/-}$* mouse mammary tumor and cultured as described by Duarte et al [50] . Further *in vitro* culture details and gene editing details are provided in the Supplementary Materials and Methods.

*Plasmids*

Plasmids and cloning methods are provided in the Supplementary Materials and Methods.

*PARPis*

Olaparib (CAS 763113-22-0) and AZD2461 (CAS 1174043-16-3) were synthesized by and purchased from Syncom (Groningen, the Netherlands). Talazoparib was purchased from Selleckchem (catalog no.S7048).

*Genomic DNA Isolation, PCR Amplification, and TIDE Analysis*

Allele modification frequencies were quantified from genomic DNA isolated from tumor and cell line samples using Gentra Puregene (QIAGEN) according to the manufacturer's protocol. Target loci were amplified by PCR and submitted for Sanger sequencing to confirm target modification using the TIDE algorithm [36]. Parental cells were used as a reference sequence. PCR primer sequences are provided in Table S3. Further details are provided in the Supplementary Materials and Methods.

*CRISPR Library Screens*

Screening details are provided in the Supplementary Materials and Methods.



*Alpha Track Assay*

Experiments were performed as described previously [17] with minor modifications. Details are provided in the Supplementary Materials and Methods.

*Focus Formation Experiments*

RAD51 immunofluorescence in CRISPR/SpCas9-transfected KB1P-G3 cells was performed as described previously with minor modifications [17]. Details are provided in the Supplementary Materials and Methods.

*DR-GFP*

The DR-GFP was performed as described previously [41] Genes were targeted using the pLentiCRISPRv2 system containing the indicated sgRNAs.

*Assessment of Telomere NHEJ*

*Trf2*$^{-/-}$;*Trp53*$^{-/-}$;TRF2ts (TRF2ts) MEFs were described before [43], and metaphase chromosome analysis was done as described before [16]. Details are provided in the Supplementary Materials and Methods.

*CSR Assay*

Immunoglobulin CSR was performed as described previously [17]. Details are provided in the Supplementary Materials and Methods.

*Generation of RNA-Seq Data*

To determine the effects of Ctc1, Ten1, and Stn1 on PARPi treatment *in vivo*, we used RNA-seq dataset generated from a cohort of PARPi-naive and -resistant KB1P(M) tumors [11, 48]. Further details are provided in the Supplementary Materials and Methods.
*Generation of CNV Sequencing Data*

Genomic DNA was isolated from a subset of matched naive-and resistant KB1P-derived fresh-frozen tumor material using standard phenol:chloroform extraction [11, 48]. Further details are provided in the Supplementary Materials and Methods.

*In Vivo Studies*

All animal experiments were approved by the Animal Ethics Committee of the Netherlands Cancer Institute (Amsterdam, the Netherlands) and performed in accordance with the Dutch Act on Animal Experimentation (November 2014). Tumor organoids were allografted in 6- to 9-week-old female mice as described previously [50] with minor modifications. Further details are provided in the Supplementary Materials and Methods.

*Quantification and Statistical Analysis*

Statistical differences were calculated in GraphPad Prism using Student's t tests. Statistical significance in Fig. 2F was calculated by two-way ANOVA and *post hoc* Dunnett's correction for multiple comparisons and in Fig. 2G by one-way ANOVA and *post hoc* Dunnett's correction for multiple comparisons. Statistical differences in Fig. 4D–4G and Supplementary Fig. S3F–S3M were calculated by Kruskal-Wallis non-parametric test and *post hoc* Dunnett's correction for multiple comparisons. Statistical differences in Fig. 6E were calculated by log rank Mantel-Cox test. Significance is as follows: $p > 0.05$, not significant (n.s.); $^{*}p \leq 0.05$; $^{**}p \leq 0.01$; $^{***}p \leq 0.001$; $^{****}p \leq 0.0001$ unless otherwise stated in the figure legends. Original data files used to prepare the figures in this manuscript have been deposited in Mendeley Data and are available at https://doi.org/10.17632/6wyzgw8z8k.1.

*Contact for Reagent and Resource Sharing*

Further information and requests for resources and reagents should be directed to and will be fulfilled by S.R. (sven.rottenberg@vetsuisse.unibe.ch).

*Data and Software Availability*

The accession number for the raw data of RNA-seq and CNV sequencing reported in this paper is European Nucleotide Archive (ENA): PRJEB25803.

## Acknowledgements

We wish to thank Piet Borst for critical reading of the manuscript, the members of the Preclinical Intervention Unit of the Mouse Clinic for Cancer and Aging (MCCA) at the Netherlands Cancer Institute (NKI) for their technical support with the animal experiments, and Julian R. de Ruiter for assistance with bioinformatic analysis. We are grateful to the NKI animal facility, digital microscopy facility, flow cytometry facility, and genomics core facility for their excellent service. Financial support came from the Dutch Cancer Society (KWF 2011-5220 and 2014-6532 to S.R. and J.J.), the Netherlands Organization for Scientific Research (VICI 91814643, NGI 93512009, Cancer Genomics Netherlands, and a National Roadmap Grant for Large-Scale Research Facilities to J.J. and STW 13577 to D.C.v.G.), the Swiss National Science Foundation (310030_156869 to S.R.), the Swiss Cancer League (KLS-4282-08-2017 to S.R.), the European Union (ERC StG 311565 to J.J.L.J., ERC CoG-681572 to S.R., and ERC Synergy Grant 319661 to J.J.), Cancer Research UK (CRUK/A14276 to C.J.L.), and a Breast Cancer Now Program Grant (CTR-Q4-Y2 to C.J.L.). R.C. and H.G. are supported by Cancer Research UK (C52690/A19270) and MRC (MR/M009971/1) grants, respectively, and a Wellcome core award (090532/Z/09/Z).

## Author Contributions

*Conceptualization*, M.B., J.J., and S.R.; *Methodology*, M.B., S.A., S.J.P., B.E., and J.B.; *Software and Formal Analysis*, M.B., J.B., J.J., and S.R.; *Investigation*, M.B., S.A., S.J.P., I.d.K., H.G., S.J.R., C.L., J.F., F.F.S., and R.B.; *Resources,* B.E. and E.G.; *Writing*, M.B., J.J., and S.R.; *Supervision*, M.v.d.V., D.C.v.G., J.J.L.J., R.C., C.J.L., J.J., and S.R.; *Funding Acquisition*, D.C.v.G., J.J.L.J., R.C., C.J.L., J.J., and S.R.

## Disclosure of Potential Conflicts of Interest

C.J.L. is a named inventor on patents describing the use of PARPis and stands to gain as part of the ICR's "Rewards to Investors" scheme.

## References


1. Lord CJ, Ashworth A. PARP inhibitors: Synthetic lethality in the clinic. Science. 2017; 355: 1152-8.
2. Mateo J, Carreira S, Sandhu S, Miranda S, Mossop H, Perez-Lopez R, et al. DNA-Repair Defects and Olaparib in Metastatic Prostate Cancer. N Engl J Med. 2015; 373: 1697-708.
3. Pritchard CC, Mateo J, Walsh MF, De Sarkar N, Abida W, Beltran H, et al. Inherited DNA-Repair Gene Mutations in Men with Metastatic Prostate Cancer. N Engl J Med. 2016; 375: 443-53.
4. Patch AM, Christie EL, Etemadmoghadam D, Garsed DW, George J, Fereday S, et al. Whole-genome characterization of chemoresistant ovarian cancer. Nature. 2015; 521: 489-94.
5. Swisher EM, Sakai W, Karlan BY, Wurz K, Urban N, Taniguchi T. Secondary BRCA1 mutations in BRCA1-mutated ovarian carcinomas with platinum resistance. Cancer research. 2008; 68: 2581-6.
6. Ter Brugge P, Kristel P, van der Burg E, Boon U, de Maaker M, Lips E, et al. Mechanisms of Therapy Resistance in Patient-Derived Xenograft Models of BRCA1-Deficient Breast Cancer. J Natl Cancer Inst. 2016; 108.
7. Liu X, Holstege H, van der Gulden H, Treur-Mulder M, Zevenhoven J, Velds A, et al. Somatic loss of BRCA1 and p53 in mice induces mammary tumors with features of human BRCA1-mutated basal-like breast cancer. Proc Natl Acad Sci U S A. 2007; 104: 12111-6.
8. Rottenberg S, Jaspers JE, Kersbergen A, van der Burg E, Nygren AO, Zander SA, et al. High sensitivity of BRCA1-deficient mammary tumors to the PARP inhibitor AZD2281 alone and in combination with platinum drugs. Proc Natl Acad Sci U S A. 2008; 105: 17079-84.
9. Bouwman P, Aly A, Escandell JM, Pieterse M, Bartkova J, van der Gulden H, et al. 53BP1 loss rescues BRCA1 deficiency and is associated with triple-negative and BRCA-mutated breast cancers. Nat Struct Mol Biol. 2010; 17: 688-95.
10. Bunting SF, Callén E, Wong N, Chen HT, Polato F, Gunn A, et al. 53BP1 inhibits homologous recombination in Brca1-deficient cells by blocking resection of DNA breaks. Cell. 2010; 141: 243-54.
11. Jaspers JE, Kersbergen A, Boon U, Sol W, van Deemter L, Zander SA, et al. Loss of 53BP1 causes PARP inhibitor resistance in Brca1-mutated mouse mammary tumors. Cancer Discov. 2013; 3: 68-81.
12. Chapman JR, Barral P, Vannier JB, Borel V, Steger M, Tomas-Loba A, et al. RIF1 is essential for 53BP1-dependent nonhomologous end joining and suppression of DNA double-strand break resection. Mol Cell. 2013; 49: 858-71.
13. Di Virgilio M, Callen E, Yamane A, Zhang W, Jankovic M, Gitlin AD, et al. Rif1 prevents resection of DNA breaks and promotes immunoglobulin class switching. Science. 2013; 339: 711-5.
14. Escribano-Díaz C, Orthwein A, Fradet-Turcotte A, Xing M, Young JT, Tkáč J, et al. A cell cycle-dependent regulatory circuit composed of 53BP1-RIF1 and BRCA1-CtIP controls DNA repair pathway choice. Mol Cell. 2013; 49: 872-83.
15. Zimmermann M, Lottersberger F, Buonomo SB, Sfeir A, de Lange T. 53BP1 regulates DSB repair using Rif1 to control 5' end resection. Science. 2013; 339: 700-4.
16. Boersma V, Moatti N, Segura-Bayona S, Peuscher MH, van der Torre J, Wevers BA, et al. MAD2L2 controls DNA repair at telomeres and DNA breaks by inhibiting 5' end resection. Nature. 2015; 521: 537-40.
17. Xu G, Chapman JR, Brandsma I, Yuan J, Mistrik M, Bouwman P, et al. REV7 counteracts DNA double-strand break resection and affects PARP inhibition. Nature. 2015; 521: 541-4.
18. Panier S, Boulton SJ. Double-strand break repair: 53BP1 comes into focus. Nat Rev Mol Cell Biol. 2014; 15: 7-18.
19. Sfeir A, de Lange T. Removal of shelterin reveals the telomere end-protection problem. Science. 2012; 336: 593-7.
20. Makarov VL, Hirose Y, Langmore JP. Long G tails at both ends of human chromosomes suggest a C strand degradation mechanism for telomere shortening. Cell. 1997; 88: 657-66.
21. McElligott R, Wellinger RJ. The terminal DNA structure of mammalian chromosomes. Embo j. 1997; 16: 3705-14.
22. Lazzerini-Denchi E, Sfeir A. Stop pulling my strings - what telomeres taught us about the DNA damage response. Nat Rev Mol Cell Biol. 2016; 17: 364-78.
23. Feng X, Hsu SJ, Kasbek C, Chaiken M, Price CM. CTC1-mediated C-strand fill-in is an essential step in telomere length maintenance. Nucleic Acids Res. 2017; 45: 4281-93.

24. Miyake Y, Nakamura M, Nabetani A, Shimamura S, Tamura M, Yonehara S, et al. RPA-like mammalian Ctc1-Stn1-Ten1 complex binds to single-stranded DNA and protects telomeres independently of the Pot1 pathway. Mol Cell. 2009; 36: 193-206.
25. Wu P, Takai H, de Lange T. Telomeric 3' overhangs derive from resection by Exo1 and Apollo and fill-in by POT1b-associated CST. Cell. 2012; 150: 39-52.
26. Hom RA, Wuttke DS. Human CST Prefers G-Rich but Not Necessarily Telomeric Sequences. Biochemistry. 2017; 56: 4210-8.
27. Li W, Xu H, Xiao T, Cong L, Love MI, Zhang F, et al. MAGeCK enables robust identification of essential genes from genome-scale CRISPR/Cas9 knockout screens. Genome Biol. 2014; 15: 554.
28. Wang G, Zimmermann M, Mascall K, Lenoir WF, Moffat J, Angers S, et al. Identifying drug-gene interactions from CRISPR knockout screens with drugZ. bioRxiv. 2017: 232736.
29. Prahallad A, Heynen GJ, Germano G, Willems SM, Evers B, Vecchione L, et al. PTPN11 Is a Central Node in Intrinsic and Acquired Resistance to Targeted Cancer Drugs. Cell Rep. 2015; 12: 1978-85.
30. Oplustil O'Connor L, Rulten SL, Cranston AN, Odedra R, Brown H, Jaspers JE, et al. The PARP Inhibitor AZD2461 Provides Insights into the Role of PARP3 Inhibition for Both Synthetic Lethality and Tolerability with Chemotherapy in Preclinical Models. Cancer research. 2016; 76: 6084-94.
31. Koike-Yusa H, Li Y, Tan EP, Velasco-Herrera Mdel C, Yusa K. Genome-wide recessive genetic screening in mammalian cells with a lentiviral CRISPR-guide RNA library. Nat Biotechnol. 2014; 32: 267-73.
32. Elstrodt F, Hollestelle A, Nagel JH, Gorin M, Wasielewski M, van den Ouweland A, et al. BRCA1 mutation analysis of 41 human breast cancer cell lines reveals three new deleterious mutants. Cancer research. 2006; 66: 41-5.
33. Tzelepis K, Koike-Yusa H, De Braekeleer E, Li Y, Metzakopian E, Dovey OM, et al. A CRISPR Dropout Screen Identifies Genetic Vulnerabilities and Therapeutic Targets in Acute Myeloid Leukemia. Cell Rep. 2016; 17: 1193-205.
34. Pettitt SJ, Krastev DB, Brandsma I, Dréan A, Song F, Aleksandrov R, et al. Genome-wide and high-density CRISPR-Cas9 screens identify point mutations in PARP1 causing PARP inhibitor resistance. Nat Commun. 2018; 9: 1849.
35. Wang Y, Bernhardy AJ, Cruz C, Krais JJ, Nacson J, Nicolas E, et al. The BRCA1-Δ11q Alternative Splice Isoform Bypasses Germline Mutations and Promotes Therapeutic Resistance to PARP Inhibition and Cisplatin. Cancer research. 2016; 76: 2778-90.
36. Brinkman EK, Chen T, Amendola M, van Steensel B. Easy quantitative assessment of genome editing by sequence trace decomposition. Nucleic Acids Res. 2014; 42: e168.
37. Daley JM, Sung P. 53BP1, BRCA1, and the choice between recombination and end joining at DNA double-strand breaks. Mol Cell Biol. 2014; 34: 1380-8.
38. Bunting SF, Callén E, Kozak ML, Kim JM, Wong N, López-Contreras AJ, et al. BRCA1 functions independently of homologous recombination in DNA interstrand crosslink repair. Mol Cell. 2012; 46: 125-35.
39. Stap J, Krawczyk PM, Van Oven CH, Barendsen GW, Essers J, Kanaar R, et al. Induction of linear tracks of DNA double-strand breaks by alpha-particle irradiation of cells. Nat Methods. 2008; 5: 261-6.
40. Tkáč J, Xu G, Adhikary H, Young JTF, Gallo D, Escribano-Díaz C, et al. HELB Is a Feedback Inhibitor of DNA End Resection. Mol Cell. 2016; 61: 405-18.
41. Bouwman P, van der Gulden H, van der Heijden I, Drost R, Klijn CN, Prasetyanti P, et al. A high-throughput functional complementation assay for classification of BRCA1 missense variants. Cancer Discov. 2013; 3: 1142-55.
42. Celli GB, de Lange T. DNA processing is not required for ATM-mediated telomere damage response after TRF2 deletion. Nat Cell Biol. 2005; 7: 712-8.
43. Peuscher MH, Jacobs JJ. DNA-damage response and repair activities at uncapped telomeres depend on RNF8. Nat Cell Biol. 2011; 13: 1139-45.
44. Smogorzewska A, Karlseder J, Holtgreve-Grez H, Jauch A, de Lange T. DNA ligase IV-dependent NHEJ of deprotected mammalian telomeres in G1 and G2. Curr Biol. 2002; 12: 1635-44.
45. Chen LY, Redon S, Lingner J. The human CST complex is a terminator of telomerase activity. Nature. 2012; 488: 540-4.
46. Gu P, Min JN, Wang Y, Huang C, Peng T, Chai W, et al. CTC1 deletion results in defective telomere replication, leading to catastrophic telomere loss and stem cell exhaustion. Embo j. 2012; 31: 2309-21.

47. Muramatsu M, Kinoshita K, Fagarasan S, Yamada S, Shinkai Y, Honjo T. Class switch recombination and hypermutation require activation-induced cytidine deaminase (AID), a potential RNA editing enzyme. Cell. 2000; 102: 553-63.
48. Gogola E, Duarte AA, de Ruiter JR, Wiegant WW, Schmid JA, de Bruijn R, et al. Selective Loss of PARG Restores PARylation and Counteracts PARP Inhibitor-Mediated Synthetic Lethality. Cancer cell. 2018; 33: 1078-93.e12.
49. Robinson MD, McCarthy DJ, Smyth GK. edgeR: a Bioconductor package for differential expression analysis of digital gene expression data. Bioinformatics. 2010; 26: 139-40.
50. Duarte AA, Gogola E, Sachs N, Barazas M, Annunziato S, J RdR, et al. BRCA-deficient mouse mammary tumor organoids to study cancer-drug resistance. Nat Methods. 2018; 15: 134-40.
51. Noordermeer SM, Adam S, Setiaputra D, Barazas M, Pettitt SJ, Ling AK, et al. The shieldin complex mediates 53BP1-dependent DNA repair. Nature. 2018; 560: 117-21.
52. Bhattacharjee A, Wang Y, Diao J, Price CM. Dynamic DNA binding, junction recognition and G4 melting activity underlie the telomeric and genome-wide roles of human CST. Nucleic Acids Res. 2017; 45: 12311-24.
53. Lue NF, Zhou R, Chico L, Mao N, Steinberg-Neifach O, Ha T. The telomere capping complex CST has an unusual stoichiometry, makes multipartite interaction with G-Tails, and unfolds higher-order G-tail structures. PLoS Genet. 2013; 9: e1003145.
54. Barazas M, Gasparini A, Huang Y, Küçükosmanoğlu A, Annunziato S, Bouwman P, et al. Radiosensitivity Is an Acquired Vulnerability of PARPi-Resistant BRCA1-Deficient Tumors. Cancer research. 2019; 79: 452-60.
55. Evers B, Drost R, Schut E, de Bruin M, van der Burg E, Derksen PW, et al. Selective inhibition of BRCA2-deficient mammary tumor cell growth by AZD2281 and cisplatin. Clinical cancer research : an official journal of the American Association for Cancer Research. 2008; 14: 3916-25.

## Supplementary Materials and Methods

*Cell culture*

KB1P and KB2P mouse mammary tumor cell lines were cultured in DMEM/F-12 medium (Life Technologies) in the presence of 10% FCS, penicillin/streptomycin (Gibco), 5µg/mL insulin (Sigma), 5ng/mL epidermal growth factor (Life Technologies) and 5ng/mL cholera toxin (Gentaur) under low oxygen conditions (3% $O_2$, 5% $CO_2$ at 37°C). SUM149PT cells were cultured in Ham's F12 medium (Gibco) supplemented with 5% FCS, 5 µg/ml insulin, 1 µg/mL hydrocortisone (Sigma-Aldrich, St. Louis, MI, USA). Mouse ES cells with a selectable conditional *Brca1* deletion (*R26*$^{CreERT2/wt}$*;Brca1*$^{SCo/\Delta}$ and *R26*$^{CreERT2}$*;Brca1*$^{SCo/\Delta}$*; Pim1*$^{DR\text{-}GFP/wt}$) [1, 2] were cultured on gelatin-coated plates in 60% buffalo red liver (BRL) cell conditioned medium supplied with 10% fetal calf serum, 0.1 mM β-mercaptoethanol (Merck) and $10^3$ U/ml ESGRO LIF (Millipore) under normal oxygen conditions (21% $O_2$, 5% $CO_2$, 37°C). *Trf2*$^{-/-}$*p53*$^{-/-}$ TRF2ts MEFs were grown in DMEM with 100U penicillin, 0.1 mg/ml streptomycin, 2mML-glutamine and 10%FBS. TRF2ts MEFs were maintained at the permissive temperature of 32 °C and only grown at 39°C to induce telomere uncapping through inactivation of TRF2 [3]. CH12F3 cell lines were cultured in RPMI supplemented with 5 % NCTC-109 medium, 10% FCS, 100 U/ml penicillin, 100 ng/ml streptomycin and 2 mM L-glutamine at 37°C with 5% $CO_2$ under ambient oxygen conditions. KB1P4 3D tumor organoid cells were seeded in Basement Membrane Extract Type 2 (BME, Trevigen) on 24-well suspension plates (Greiner Bio-One) and cultured in AdDMEM/F12 supplemented with 1 M HEPES (Sigma), GlutaMAX (Invitrogen), penicillin/

streptomycin (Gibco), B27 (Gibco), 125 µM N-acetyl-L- cysteine (Sigma), 50 ng/mL murine epidermal growth factor (Invitrogen).

*Transfection-based genome editing*

Transfection in KB1P-G3 cells was performed using TransIT-LT1 (Mirus) reagents following manufacturer's recommendations. In brief, 150,000 cells were plated in 6-well format 1 day before transfection with 1 µg DNA. The medium was refreshed 24 hours after transfection and transfected cells were selected with puromycin for three days. CRISPR/SpCas9 targeted SUM149PT cells were generated with editR crRNA (Dharmacon, Lafayette, CO, USA).

*Lentiviral transduction-based genome editing*

Cell lines targeted with the pGSC_Cas9_Neo and pLenti-sgRNA-tetR-T2A-Puro system were generated by lentiviral transduction. Lentivirus was produced in HEK293FT cells as described previously [4] and mouse KB1P-G3 or *Brca1*$^{-/-}$;*p53*$^{-/-}$ mES cells were infected overnight using polybrene (8 µg/mL). The medium was refreshed after 12 hours and transduced cells were selected with puromycin (3 µg/mL) and blasticidin (500 µg/mL) for five consecutive days. KB1P4 tumor organoids were transduced using spinoculation as described previously [5, 6]. Expression of the sgRNA was induced by incubation with 3 µg/ml doxycycline (Sigma) for at least five days.

*Plasmids*

pGSC_Cas9_Neo and pLenti-sgRNA-tetR-T2A-Puro were described previously [7]. Genome- wide mouse lentiviral CRISPR sgRNA library was a gift from Kosuke Yusa (Addgene #50947). Human Improved Genome-wide Knockout CRISPR Library v1 was a gift from Kosuke Yusa (Addgene #67989). pX330-U6- Chimeric_BB-CBh-SpCas9 was a gift from Feng Zhang (Addgene plasmid #42230). pLentiCRISPRv2 was a gift from Feng Zhang (Addgene plasmid # 52961). The MCherry/I-SceI plasmid has been described previously [2].

*Generation of CRISPR/SpCas9 plasmids*

Unless otherwise stated, KB1P-G3 experiments were performed using a modified version of the pX330 backbone [8] in which a puromycin resistance ORF was cloned under the hPGK promoter [9]. sgRNA sequences were cloned in the pX330puro backbone using custom DNA oligos (IDT) which were melted, annealed and subsequently ligated with quick-ligase (NEB) into BbsI-digested backbone. A similar procedure was used for cloning into the pLenti-sgRNA-tetR-T2A-Puro vector, but using

BfuAI-digested backbone. All constructs were sequence verified by Sanger sequencing. sgRNA sequences are provided in Supplementary Table S2.

*Genomic DNA isolation, PCR amplification and TIDE analysis*

Target loci were amplified by PCR using the following conditions: (1) 98 °C, 30 s, (2) 30 cycles of 98 °C for 10 s, 61 °C for 20 s and 72 °C for 30 s, (3) 72 °C, 5 min. Reaction mix consisted of 0.75 µl DMSO, 5 µl GC Phusion Buffer 5X, 0.5 µl 2 mM dNTPs, 0.125 µl 100 µM Fwd oligo, 0.125 µl 100 µM Rev oligo, 0.25 µl Phusion polymerase in 25 µl total volume. Amplified products were diluted 50X in $dH_2O$ and 2 µl of diluted product was submitted for Sanger sequencing.

*CRISPR library screens*

The first PARPi resistance screen was performed in the KB1P-G3 tumor cell line, which was previously established from a KB1P tumor [10]. This cell line is BRCA1- and p53-deficient through large intragenic deletions and shows sensitivity to PARPi treatment in the nanomolar range. The DDR sgRNA library was generated based on the gene list from Thanos Halazonetis (University of Geneva) described before [11, 12] and the NCBI search (terms: "DNA repair", "DNA damage response", "DNA replication", "telomere- associated genes"). See Table S1 for the full library details. This search resulted in a DDR-related gene list comprising a total of 1,752 genes (Supplementary Table S1). *Tp53bp1* was specifically removed from this list in anticipation that loss of 53BP1 might dominate the screen results and thereby obscure the effects of other genes. sgRNAs targeting the 1,752 DDR-related genes were synthesized (MYcroarray) and cloned into the pLenti-sgRNA-tetR-T2A-PuroR vector, which allows for doxycycline inducible expression of the sgRNA [7]. KB1P-G3-SpCas9 expressing cells were generated by transduction with the pGSC_SpCas9_Neo vector and transduced cells were selected by 500 µg/mL G418. The pLenti-sgRNA-tetR-T2A-Puro-DDR library was introduced at 100x coverage. Next, doxycycline was added to the medium for 5 days to mutagenize the population. Cells were subsequently plated in a clonogenic growth format in the presence of the PARP inhibitors olaparib or AZD2461 [13] at the approximate IC90 concentration for 14 days. Cells were harvested before and after PARPi treatment for genomic DNA isolation. Subsequently, sgRNA sequences were amplified from genomic DNA by two rounds of PCR amplification as described [5] and sequenced with the HiSeq 2500, using the following barcodes: GTAGCC, TACAAG, CTCTAC, GCGGAC, TTTCAC, GGCCAC. Sequencing reads were aligned to the reference sequences using edgeR software [14]. The screening data were processed by the MAGeCK algorithm [15], and results were sorted on MAGeCK-based positive selected gene ranks to allow comparison across screens.

The second PARPi resistance screen was performed in BRCA1- and p53-deficient, SpCas9-expressing mouse embryonic stem (mES) cells infected with a genome-wide lentiviral sgRNA library targeting 19,150 genes [16]. The screen was performed at 75x coverage in two independent transductions (MOI 0.5) and cells were first selected with puromycin and subsequently treated with olaparib at a concentration of 15 nM for 10 days. Surviving populations were harvested and processed as described previously [16], using the following barcodes CGTGAT, ACATCG, GCCTAA, TGGTCA, CACTGT, ATTGGC, GATCTG, TCAAGT, CTGATC, AAGCTA, GTAGCC, TACAAG, TTGACT, GGAACT. The screening data were processed similar to the screen in KB1P-G3 cells.

A third PARPi resistance screen was performed in the SUM149PT human breast cancer cell line. This cell line harbors the *BRCA1*$^{2288delT}$ mutation and LOH [17]. A derivative of SUM149PT with an integrated tetracycline-inducible SpCas9 was lentivirally infected with a genome-wide sgRNA library designed to target 18,010 genes [18] using a multiplicity of infection of 0.3 and infecting >1000 cells per sgRNA. After puromycin selection (3 µg/ml) to remove non-tranduced cells, a sample was removed (time or t=0); remaining cells were cultured in the presence or absence of doxycycline plus 100 nM talazoparib, a concentration which normally results in complete inhibition of the cell population. No cells survived in the absence of doxycycline. After two weeks of selection, genomic DNA from the remaining cells in the doxycycline-treated sample was recovered. The sgRNA sequences from this genomic DNA were PCR amplified using barcoded and tailed primers and deep sequenced as previously described [16] to identify sgRNAs in the talazoparib-resistant population. Read counts were normalized for coverage by converting to parts per ten million (pptm) reads and fold change between starting and resistant population was calculated for each guide. Fold change values were log- and Z- transformed and plotted based on z-rank [19].

*Clonogenic survival assay*

*Ctc1*, *Stn1* and *Ten1* were targeted in *R26*$^{CreERT2}$*;Brca1*$^{SCo/\Delta}$ mouse embryonic stem (mES) cells using pLentiCRISPRv2 vectors, Cre-mediated inactivation of the endogenous mouse *Brca1*$^{SCo}$ allele was achieved by overnight incubation of cells with 0.5 µmol/L 4-OHT (Sigma) [1]. Four days after switching, cells were seeded in triplicate at 10,000 cells per well in 6-well plates for clonogenic survival assay. For experiments with *R26*$^{CreERT2/wt}$*; Brca1*$^{SCo/\Delta}$ p53-null cells, cells were plated without treatment or in the presence of olaparib 2.5 nM. Cells were stained with 0.1% crystal violet one week later, and scanned with the Gelcount (Oxford Optronix). Automated quantification of colony counts was performed using the Gelcount colony counter software.

Clonogenic survival assay with PARPi (olaparib) were performed as described previously with minor modifications [12]. CRISPR/SpCas9 transfected KB1P-G3 cells were seeded in triplicate at 5 x $10^3$ cells per well into 6-well plates on day 0, and

then olaparib or AZD2461 was added at the indicated concentrations. On day 6, the untreated group was fixed, the other groups were fixed on day 9 and stained with 0.1% crystal violet. Plates were scanned with the Gelcount (Oxford Optronix). Quantifications were performed by solubilizing crystal violet using 10% acetic acid and the absorbance at 562nm was measured using the Tecan plate reader. The experiment was performed three times.

SUM149PT-SpCas9 cells were transfected with *CTC1* targeting crRNA and tracrRNA using the EditR system (Life Technologies), plated into 48 well plates and then treated with 50 nM talazoparib. Medium was replaced with fresh drug-containing medium as indicated. Images were taken to measure viability of cells in each well every 12 hours using the IncuCyte system. After two weeks, final viability was assessed using CellTiter Glo (Promega).

*Competition assays*

Competition assays were performed in KB1P-G3 SpCas9 expressing cells, transduced with pLenti-sgRNA-tetR- T2A-Puro vectors containing the indicated sgRNAs. Cells were selected with puromycin (3 µg/mL) for three days and allowed to recover from selection. A sample was harvested for gDNA isolation at t = 0, and 5,000 cells were plated in 6-well plates in triplicate per condition, with or without AZD2461 (250 nM). After 10 days of treatment, cells were harvested, counted and re-plated at 5,000 cells per 6-well two times (total treatment time of 30 days). On the last time point, each condition was plated as technical duplicate. At the end point, one technical duplicate well was fixed and stained with crystal violet and the other was used to isolate gDNA. Allele distributions were determined from gDNA samples by PCR followed by Sanger sequencing and TIDE analysis, as described above. Competition assays in KB2P-3.4 cells were performed similarly, except 2,000 cells were seeded per 6-well and cells were treated with olaparib (50 nM).

*Growth curves*

Growth curves were generated for CRISPR/SpCas9 transfected KB1P-G3 cells by seeding 1,000 cells per well in 96-well plates, seeding 6 technical replicates per experiment and the well confluency was recorded every 4 hours for 120 hours using an IncuCyte Zoom Live – Cell Analysis System (Essen Bioscience). The images were analyzed using IncuCyte Zoom software. Data were normalized to the confluency at 20h after seeding.

*Alpha track assay*

Experiments were performed as described previously [12] with small modifications. CRISPR/SpCas9 transfected KB1P-G3 cells were seeded on coverslips overnight, washed

with PBS and covered with a mylar foil, allowing α-particle irradiation from above, through mylar. Irradiation was done using a $^{241}$Am point- source by moving the source over the coverslip for 30s per area, cells were incubated for 1 hour at 37 ˚C and washed with ice- cold PBS. Subsequently, cells were extracted with cold CSK buffer (10 mM HEPES-KOH, pH 7.9, 100 mM NaCl, 300 mM sucrose, 3 mM MgCl2, 1 mM EGTA, 0.5% (v/v) Triton X-100) and cold CSS buffer (10 mM Tris, pH 7.4, 10 mM NaCl, 3 mM MgCl2, 1% (v/v) Tween20, 0.5% (w/v) sodium deoxycholate) for 5 min each before fixation in 4% PFA in PBS for 30 min at room temperature. Fixed cells were washed 2 times for 10 minutes in PBS (0.1% Triton X-100) and washed for 30 minutes in blocking solution (0.5% BSA and 0.15% glycine in PBS). Primary antibodies were diluted in blocking buffer and incubated overnight at 4 ˚C. Hereafter, cells were washed 2 times for 10 minutes in PBS (0.1% Triton X-100) and 1 time shortly in blocking buffer. Secondary antibodies were diluted in blocking buffer and cells were incubated for at least 1 hour at room temperature in the dark. Finally, cells were washed 2 times in PBS and coverslips were mounted using Vectashield with DAPI. Quantification was done as described previously. Primary antibodies used in this study were as follows: rabbit anti-53BP1 (NB100-304, Novus), 1:1000 dilution; mouse anti-RPA34-20 (Ab-3, CalBiochem), 1:1000 dilution; MRE11 antibody [20], 1:250 dilution. Secondary antibodies used in this study were as follows: Alexa Fluor 594 goat anti-rabbit IgG (A 31631, Invitrogen), Alexa Fluor 488 goat anti-mouse IgG (Thermo Fisher Scientific Cat# A-11001, RRID: AB_2534069), 1:1000 dilution.



*Foci formation experiments*

RAD51 immunofluorescence in CRISPR/SpCas9 transfected KB1P-G3 cells was performed as described previously, with minor modifications [12]. Cells were grown on 8-well chamber slides (Millipore). Ionizing-Radiation Induced Foci (IRIF) were induced by γ-irradiation (10 Gy) 3 hours prior to sample preparation. PARP inhibitor-induced foci were generated by treatment with 500 nM olaparib for 24h prior to sample preparation. Subsequently, cells were washed in PBS++ and fixed with 2% PFA/PBS++ for 20' on ice. Fixed cells were washed with PBS++ and were permeabilized for 20' in 0.2% Triton X-100/PBS++. All subsequent steps were performed in staining buffer (PBS++, BSA (2%), glycine (0.15%), Triton X-100 (0.1%)). Cells were washed 3x and blocked for 30' at RT, incubated with the 1$^{st}$ antibody for 2hrs at RT, washed 3x and incubated with the 2$^{nd}$ antibody for 1hr at RT. Antibodies were diluted in staining buffer. Last, cells were mounted and counterstained using Vectashield mounting medium with DAPI (H1500, Vector Laboratories). Primary antibodies used: rabbit-anti-RAD51; 70-001, BioAcademia, 1:1,000 dilution; rabbit-anti-53BP1; Abcam Ab21083, 1:2,000 dilution; rabbit-anti-RIF1 was a gift by Ross Chapman, 1:1,000 dilution; mouse anti yH2AX: Millipore JBW3O1, 1:1,000 dilution; Alexa fluor 568 F(ab')$_2$ Fragment goat anti-rabbit; A21069, Thermo Fisher Scientific,

1:400 dilution; Goat anti-Rabbit IgG (H+L) Cross-Adsorbed Secondary Antibody, Alexa Fluor 568 from Thermo Fisher Scientific, catalog # A-11011, RRID AB_143157; Goat anti-Mouse IgG (H+L) Cross-Adsorbed Secondary Antibody, Alexa Fluor 568 from Thermo Fisher Scientific, catalog # A-11004, RRID AB_2534072. Z-stack images were acquired using a confocal microscope (Leica SP5, Leica Microsystems GmbH) and multiple different confocal fields were imaged per sample (63x objective). Confocal images were analyzed automatically using an ImageJ script [12]. Briefly, the macro detects nuclei based on DAPI intensity and subsequently counts the number of foci within each nucleus.

*DR-GFP*

The DR-GFP assay was performed as described previously [2]. Genes were targeted using the pLentiCRISPRv2 system containing indicated sgRNAs.

*Assessment of telomere NHEJ*

*Trf2*$^{-/-}$*;Trp53*$^{-/-}$;TRF2ts MEFs (TRF2ts MEFs) were described before [3]. TRF2ts MEFs were targeted using the pX330puro system containing indicated sgRNAs at the permissive temperature of 32°C. Following selection and recovery, they were grown for 24 h at the non-permissive temperature of 39°C to inactivate TRF2 and induce NHEJ dependent chromosome end to end fusions as a consequence of telomere uncapping. Cell harvesting, preparation of metaphase spreads and telomere FISH with an Alexa488-labeled C-rich Telomere probe (PN-TC060-005, Panagene/Eurogentec) for metaphase chromosome analysis was done as described before [21].

Digital images of metaphases were captured using the Metafer4/MSearch automated metaphase finder system (MetaSystems, Germany) equipped with an AxioImager Z2 microscope (Carl Zeiss, Germany). After scanning metaphase preparations at 10x magnification, high-resolution images of metaphases were acquired using a 'Plan-Apochromat' 63x/1,40 oil objective. The cell cycle distribution of TRF2ts MEFs with or without CRISPR/SpCas9 mediated disruption of *Ctc1* or *Tp53bp1* was determined by propidium-iodide staining, acquired on a FACSCalibur (Beckton Dickinson) and analyzed with FlowJo (TreeStar, Ashland, OR) software.

*CSR assay*

*Ctc1*-mutated CH12F3 cells were generated by nucleofection (Amaxa Nucleofector 2b, Lonza) with 2 µg of plasmid and Cell Line Nucleofector Kit R (Lonza), using program D-023. Isogenic cell clones were isolated by limiting dilution and mutated clones were identified by native PAGE resolution of PCR amplicons of the target site, and subsequent confirmation by Sanger sequencing. Immunoglobulin CSR

was performed as described previously [12]. Briefly, CH12 cells were either mock-treated or stimulated with agonist anti-CD40 antibody (0.5 mg/ml; eBioscience; HM40-3), mouse IL-4 (5 ng/ml; R&D Systems) and TGF-b1 (1.25 ng/ml; R&D Systems). Cell- surface IgA expression was determined by flow cytometry, immunostaining with biotinylated antimouse IgA antibody (eBioscience; 13-5994), and Alexa488-streptavidin conjugate (Life Technologies).

*Generation of RNA sequencing data*

To determine the effects of Ctc1, Ten1 and Stn1 on PARPi treatment *in vivo*, we used our RNASeq dataset generated from a cohort of PARPi-naive and -resistant KB1P and KB1PM tumors [10, 22]. Hereto, fresh-frozen tumor tissues were subjected to high-speed shaking in 2 ml microcentrifuge tubes containing 1 ml of TRIsure reagent (Bioline) and stainless-steel beads (TissueLyser LT, Qiagen; 10 min, 50 Hz, room temperature). Homogenized lysates were further processed for RNA isolation following TRIsure manufacturer's protocol. Quality and quantity of the total RNA was assessed by the 2100 Bioanalyzer using a Nano chip (Agilent, Santa Clara, CA). Total RNA samples having RIN>8 were subjected to library generation. Strand- specific libraries were generated using the TruSeq Stranded mRNA sample preparation kit (Illumina Inc., San Diego, RS-122-2101/2) according to the manufacturer's instructions (Illumina, Part # 15031047 Rev. E). The libraries were analyzed on a 2100 Bioanalyzer using a 7500 chip (Agilent, Santa Clara, CA), diluted and pooled equimolar into a 10 nM sequencing stock solution. Ilumina TruSeq mRNA libraries were sequenced with 50 base single reads on a HiSeq2000 using V3 chemistry (Illumina Inc., San Diego). The resulting reads were trimmed using Cutadapt v.1.12. The trimmed reads were aligned to the GRCm38 reference genome using STAR v.2.5.2b [23]. QC statistics from Fastqc v.0.11.5 (www.bioinformatics.babraham.ac.uk/projects/fastqc) and the above-mentioned tools were collected and summarized using Multiqc (v.0.8; [24]). Gene expression counts were generated by featureCounts (v.1.5.2; [25]) using gene definitions from Ensembl GRCm38 version 76. The genes with counts per million (CPM) larger than one at least 20% of total number of samples were taken and used for further analysis. Then, trimmed mean of M-value (TMM) normalization was performed to obtain normalized expression using edgeR [14].

*Generation of CNV sequencing data*

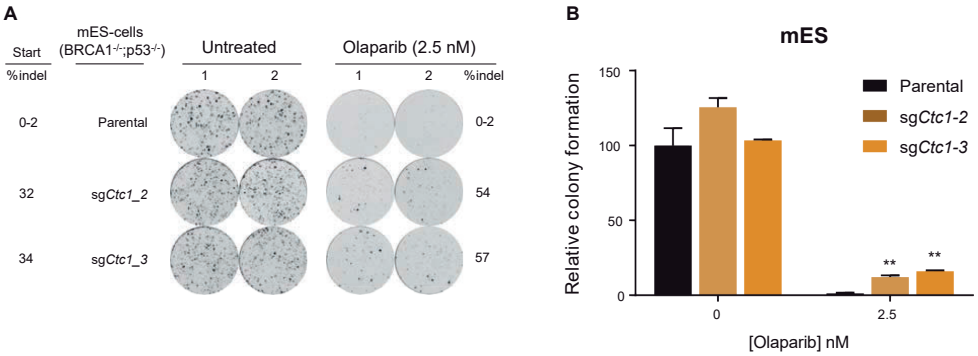
CNV-Seq was performed using double stranded DNA (dsDNA), quantified with the Qubit® dsDNA HS Assay Kit (Invitrogen, #Q32851). To obtain fragment sizes of 160–180 bp, 2 µg of dsDNA were fragmented by Covaris shearing and purified using 1.8X Agencourt AMPure XP PCR Purification beads according to manufacturer's protocol (Beckman Coulter, #A63881). Next, sheared DNA was quantified and qualified

on a BioAnalyzer system with the DNA7500 assay kit (Agilent Technologies, #5067-1506). Library preparation for Illumina sequencing was carried out with 1 µg of DNA and KAPA HTP Library Preparation Kit (KAPA Biosystems, #KK8234). HiSeq2500 machine in one lane of a single read 65 bp run, according to manufacturer's instructions. Sequencing reads were trimmed using Cutadapt (version 1.12) and reads shorter than 30 bp were removed. The trimmed reads were aligned to the GRCm38 reference genome using BWA (version 0.7.15; [26]). The resulting alignments were sorted and marked for duplicates using Picard tools (version 2.5.0). Copy number calls were generated using the QDNAseq and QDNAseq.mm10 [27] packages from Bioconductor (versions 1.8.0 and 1.4.0, respectively). Copy number calls of the resistant tumors were subtracted to those of matched naïve tumors for downstream analysis which examined the correlation between CNV and gene expression.

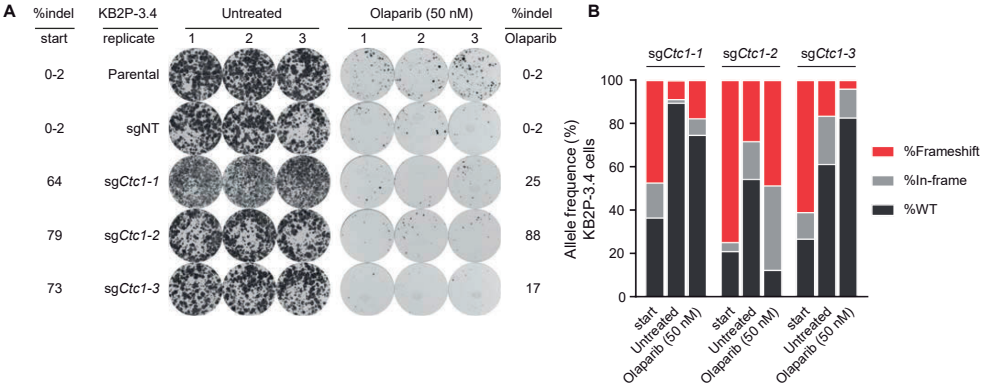
*In vivo studies*

Tumor organoids were collected, incubated with TripLE at 37°C for 5', dissociated into single cells, washed in PBS, resuspended in tumor organoid medium and mixed in a 1:1 ratio of tumor organoid suspension and BME in a cell concentration of $10^4$ cells per 40 µl. Subsequently, $10^4$ cells were transplanted in the fourth right mammary fat pad of 6–9-week-old NMRI nude mice. Mammary tumor size was measured by caliper measurements and tumor volume was calculated (0.5 x length x width$^2$). Treatment of tumor bearing mice was initiated when tumors reached a size of 50-100 mm$^3$, at which point mice were stratified into the untreated (n = 3) or olaparib treatment group (n = 7). Olaparib was administered at 100 mg/kg intraperitoneally for 56 consecutive days. Animals were sacrificed with $CO_2$ when the tumor reached a volume of 1,500 mm$^3$.

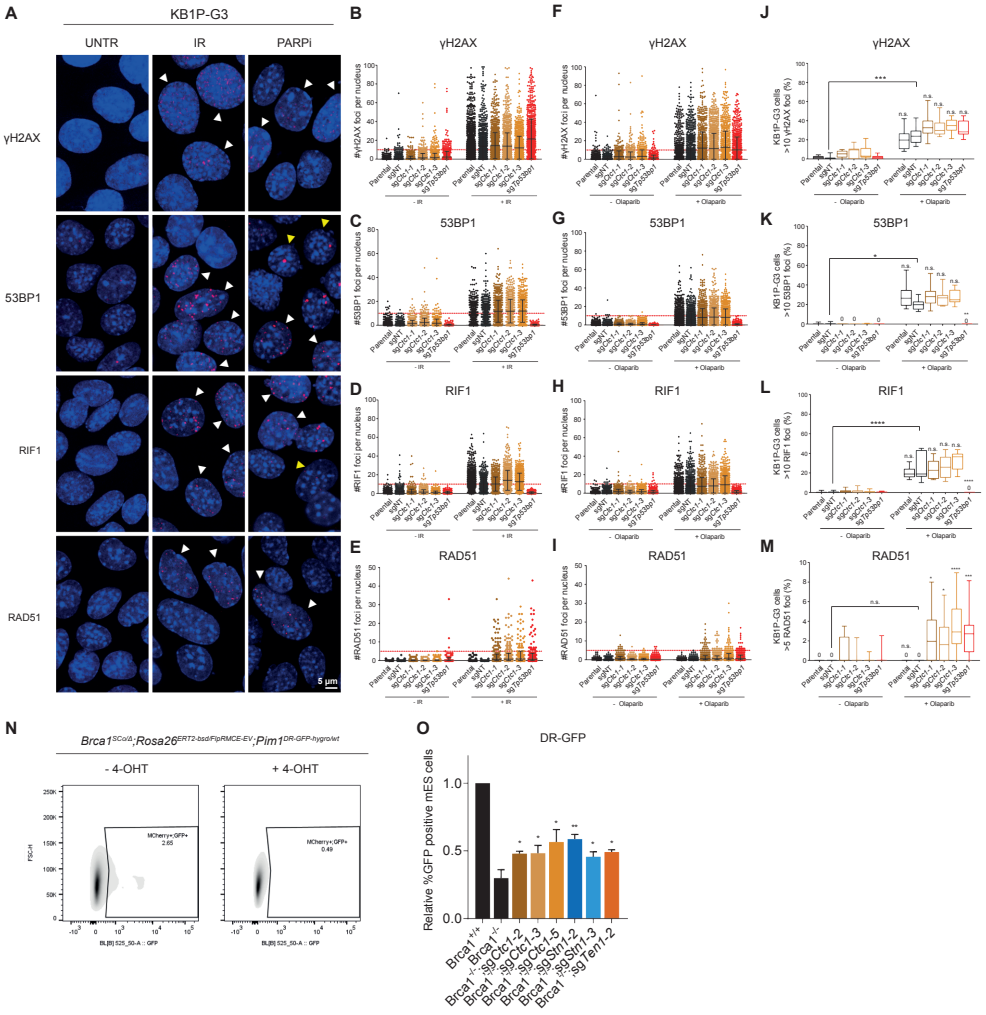
# Supplementary Figures and Tables




**SUPPLEMENTARY FIGURE S1 | Depletion of CTC1 induces PARPi resistance in *Brca1*$^{-/-}$;*p53*$^{-/-}$ mouse embryonic stem (mES) cells. Related to Figure 3.** *(A)* Parental and *Ctc1*-mutated *Brca1*$^{-/-}$;*p53*$^{-/-}$ mES cells were plated for clonogenic growth in the presence or absence of olaparib (2.5 nM) for 7 days before wells were fixed and stained with crystal violet. The experiment was performed in duplicate. *Ctc1* was mutated using the pLenti-sgRNA-tetR-T2A-PuroR vector containing the indicated gRNAs. Allele distributions were determined from the starting population and the surviving population after treatment. *(B)* Quantification of A. The number of colonies was determined using GelCount software. Data represent the relative number of colonies compared to the parental untreated mES cells. Data represent mean ± SD. P-values were determined by unpaired two-tailed students t-test (P = 0.0074 and P = 0.0017, respectively).

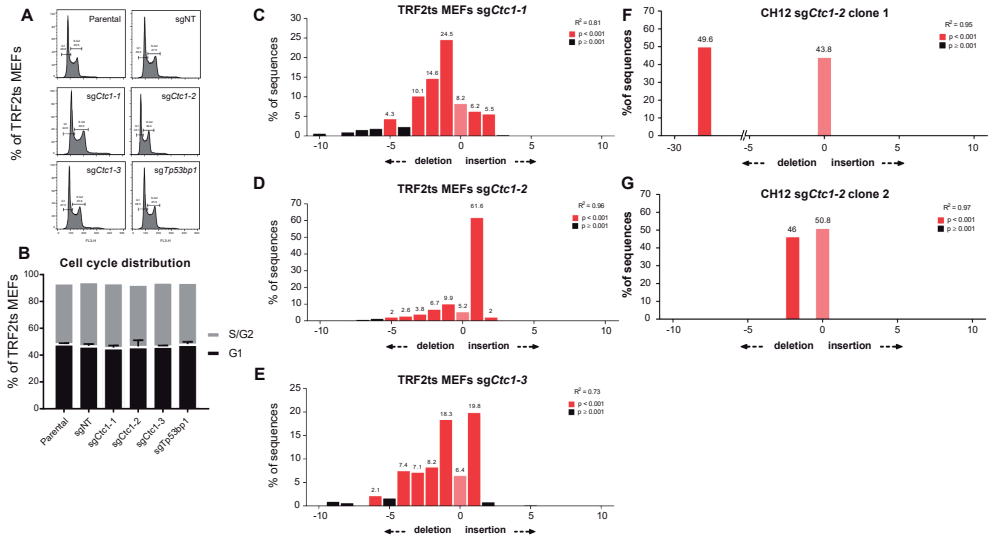



**SUPPLEMENTARY FIGURE S2 | Depletion of CTC1 does not improve PARPi survival in BRCA2-deficient cells. Related to Figure 3.** *(A-B)* Parental, sgNT or *Ctc1*-mutated KB2P-3.4 SpCas9 expressing cells were plated at 2,000 cells per 6-well for clonogenic growth in the presence or absence of olaparib (50 nM) for 10 days. Then, cells were harvested and re-plated at 2,000 cells per 6-well under the same treatment for 10 days, and this was repeated one more time (total treatment duration 30 days). *Ctc1* was mutated using the pLenti-sgRNA-tetR-T2A-PuroR vector containing the indicated gRNAs. Cells were selected with puromycin (3 µg/mL) and gRNA expression was induced with doxycycline (3 µg/mL) for 5 days. Allele distributions were determined from the starting, untreated and olaparib-treated populations and the percentage indel is shown and plotted in *B*.

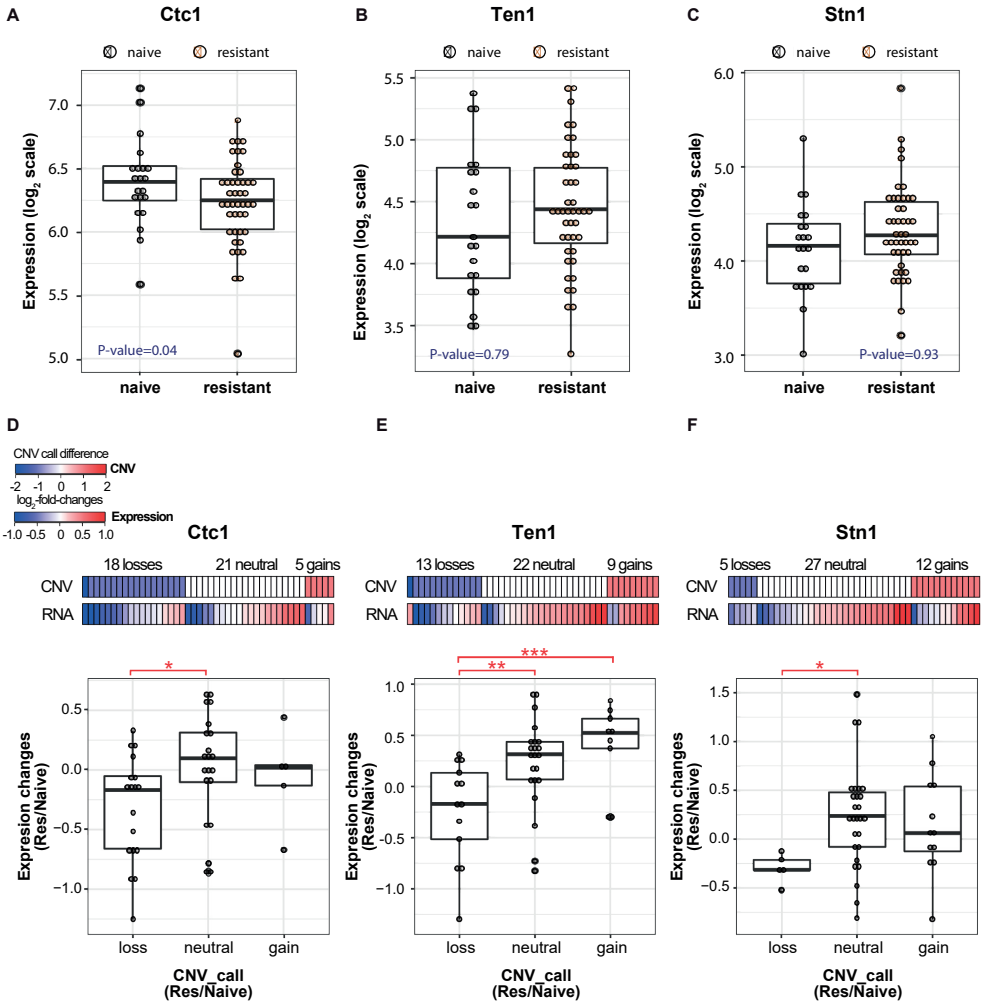



**SUPPLEMENTARY FIGURE S3 | CTC1 functions as a resection antagonist on non-telomeric DSBs. Related to Figure 4.** *(A)* Overview confocal images (63x magnification) of indicated proteins and treatments. White arrowheads indicate examples of positive cells, and yellow arrowheads indicate examples of negative cells containing nuclear bodies. *(B-E)* Quantifications of confocal images shown in Figure 4C. KB1P-G3 SpCas9 expressing cells of indicated genotype were irradiated (10 Gy) and harvested 3 hours later for immunofluorescence of indicated proteins. Data is plotted as #foci per nucleus for indicated proteins. *(F-M)* Immunofluorescence stainings were performed after 500nM olaparib treatment for 24h to induce DSBs. Data represent two independent experiments. *F-I* show quantifications of confocal images plotted as #foci per nucleus for indicated proteins, *J-M* quantification of confocal images, plotted as box and whiskers plot. The box represents the 25th to 75th percentiles and the whiskers show the min to max values. The experiment was performed at least two times and data is plotted as percentage of γH2AX, 53BP1 or RIF1-positive cells (>10 foci) or RAD51-positive cells (>5 foci) per field. Statistics was performed by Kruskal-Wallis non-parametric test followed by Dunn's multiple comparisons test. The indicated cell lines were compared to sgNT treated cells (**** = p-value < 0.0001). *Figure legend continues on next page.*

**SUPPLEMENTARY FIGURE S3 | CTC1 functions as a resection antagonist on non-telomeric DSBs. Related to Figure 4.** *Continued. (N-O)* CST complex members were depleted in *Brca1*$^{SCo/\Delta}$;*Rosa26*$^{ERT2\text{-}bsd/FlpRMCE\text{-}EV}$;*Pim1*$^{DR\text{-}GFP\text{-}hygro/wt}$ mES-cells using LentiCRISPRv2 vectors containing indicated sgRNAs. Cells were treated with 4-OHT to inactivate the *Brca1*$^{Sco}$ allele and subsequently transfected with mCherry/I-SceI constructs. HR activity was determined by flow cytometry and was calculated as the percentage of GFP+ cells in the mCherry+ population relative to BRCA1 proficient parental cells. The experiment was performed three times and the data are plotted as mean with SEM. Statistics was performed by unpaired one-tailed students t-test (* = p-value <0.05; ** = p-value <0.01).




**SUPPLEMENTARY FIGURE S4 | CTC1 facilitates cNHEJ at telomeric and non-telomeric DSBs. Related to Figure 5.** *(A-B)* Cell cycle distribution profiles were determined by flow cytometry from TRF2ts MEFs transfected with pX330puro vectors containing indicated sgRNAs. The experiment was performed two times. *(C-E)* TIDE plots of TRF2ts MEFs targeted by indicated sgRNAs. *(F-G)* TIDE plots of the two CH12 clones that were successfully targeted with sg*Ctc1-2*.




**SUPPLEMENTARY FIGURE S5 | Expression and copy number profiles for CST complex genes (*Ctc1*, *Ten1*, and *Stn1*) in matched KB1P(M) naïve- and PARPi-resistant tumors for which both RNA-seq and CNV-seq were available. In total, 21 naïve and 44 resistant tumors from 21 donors were used in this analysis. Related to Figure 6.** *(A-C)* mRNA expression levels (log2(CPM) of *Ctc1 (A)*, *Ten1 (B)*, and *Stn1 (C)*, between naïve and resistant tumors. P-values were obtained by one-tail t-test. *(D-F)* Correlation between mRNA levels and CNV for CST complex genes. CNV calling and gene expression levels of 44 resistant tumors were compared to those of corresponding naïve tumors. First heatmaps indicate copy number changes (red: copy number gain, blue: copy number loss) and second heatmaps indicate gene expression changes (red: upregulation, blue: downregulation) for the same tumors. Bottom boxplots indicate correlation between copy number changes and expression changes. Adjusted P-value were obtained by one-way anova and Tukey multiple pairwise-comparison. * Adj. P-value < 0.1, ** Adj. P-value < 0.05, *** Adj. P-value <0.01.

**SUPPLEMENTARY TABLE S1 | Details of the Focused Mouse DDR Library, Related to Supplementary Materials and Methods can be accessed via the online version of this article.**

**SUPPLEMENTARY TABLE S2 | sgRNA and crRNA sequences. Related to Supplementary Materials and Methods.**

| Mouse gene name | Mouse sgRNA name | sgRNA sequence |
|---|---|---|
| Non-targeting | sgNT | TGATTGGGGGTCGTTCGCCA |
| *Ctc1* | sg*Ctc1-1* | CTTGAAGCCGAACAGTGCCA |
| *Ctc1* | sg*Ctc1-2* | CACGAGTTGCTCATACAAGG |
| *Ctc1* | sg*Ctc1-3* | CTGGTCGAATAACCCGCCTG |
| *Stn1* | sg*Stn1-1* | ATGATATCTACCCGCCTTAT |
| *Stn1* | sg*Stn1-2* | CAACGGGCATCCAATAAGGC |
| *Ten1* | sg*Ten1* | CTGCGAACATTTGGCAGGTA |
| *Tp53BP1* | sg*Tp53BP1* | GAACAATCTGCTGTAGAACA |
| **Human gene name** | **Human crRNA name** | **crRNA sequence** |
| Non-targeting | crNT-1 | AAAACACGATGACGTCTCT |
| Non-targeting | crNT-2 | AAACGAGAAGTTTGTACTA |
| *CTC1* | cr*CTC1-1* | TGCCAACTCAATCGCCGCC |
| *CTC1* | cr*CTC1-2* | TAGGCTGTACCAGGCCGAA |
| *CTC1* | cr*CTC1-3* | ACAGACCTATCGGCAGACT |
| *TP53BP1* | cr*TP53BP1-1* | TCTAGTGTGTTAGATCAGG |
| *TP53BP1* | cr*TP53BP1-2* | GGGGGTTTTCTAACTCCAC |
| *TP53BP1* | cr*TP53BP1-3* | GACTGCTAGGAACGATAAA |

**SUPPLEMENTARY TABLE S3 | PCR primer sequences. Related to Supplementary Materials and Methods.**

| sgRNA name | FW PCR primer | RV PCR primer | Source |
|---|---|---|---|
| sgNon-targeting | N.A. | N.A. | Duarte et al., 2017 |
| sg*Ctc1-1* | TGTTCCAGACAGGGATTTTCCAA | AGGAGAGGGTTGCTTCAGGA | This paper |
| sg*Ctc1-2* | TGTTCCAGACAGGGATTTTCCAA | AGGAGAGGGTTGCTTCAGGA | This paper |
| sg*Ctc1-3* | ATTATGGTTAAGGGCGGGGGT | TGGCTACTGTTTCTCCACCAT | This paper |
| sg*Stn1-1* | GCATTTCAATTCTTCCACGGCT | CACTTGCCAAGGACTGACTC | This paper |
| sg*Stn1-2* | GCATTTCAATTCTTCCACGGCT | CACTTGCCAAGGACTGACTC | This paper |
| sg*Ten1* | GCCAGCTAGTCTTCCAAATGT | CAGCGTATGGTTCTCACTACC | This paper |
| sg*Tp53BP1* | TGAGAAATGGAGGCAACACCA | TGCAAATGTGGGCTACTGGG | This paper |
| *Brca1-Sco* allele | CACCTGCTCTGGCTGATG | AGGTCTGCCTGCCTCTACTTC | Bouwman et al., 2013 |
| *Brca1-DelSco* allele | GTGGGCTTGTACTCGGTCAT | GCTGTTCTCCTCTTCCTCATC | Bouwman et al., 2013 |
| iKRUNC sequencing primer | AAAGAATAGTAGACATAATAGC | N.A. | This paper |

## Supplementary References


1. Bouwman P, Aly A, Escandell JM, Pieterse M, Bartkova J, van der Gulden H, et al. 53BP1 loss rescues BRCA1 deficiency and is associated with triple-negative and BRCA-mutated breast cancers. Nat Struct Mol Biol. 2010; 17: 688-95.
2. Bouwman P, van der Gulden H, van der Heijden I, Drost R, Klijn CN, Prasetyanti P, et al. A high-throughput functional complementation assay for classification of BRCA1 missense variants. Cancer Discov. 2013; 3: 1142-55.
3. Peuscher MH, Jacobs JJ. DNA-damage response and repair activities at uncapped telomeres depend on RNF8. Nat Cell Biol. 2011; 13: 1139-45.
4. Follenzi A, Ailles LE, Bakovic S, Geuna M, Naldini L. Gene transfer by lentiviral vectors is limited by nuclear translocation and rescued by HIV-1 pol sequences. Nat Genet. 2000; 25: 217-22.
5. Duarte AA, Gogola E, Sachs N, Barazas M, Annunziato S, J RdR, et al. BRCA-deficient mouse mammary tumor organoids to study cancer-drug resistance. Nat Methods. 2018; 15: 134-40.
6. Koo BK, Stange DE, Sato T, Karthaus W, Farin HF, Huch M, et al. Controlled gene expression in primary Lgr5 organoid cultures. Nat Methods. 2011; 9: 81-3.
7. Prahallad A, Heynen GJ, Germano G, Willems SM, Evers B, Vecchione L, et al. PTPN11 Is a Central Node in Intrinsic and Acquired Resistance to Targeted Cancer Drugs. Cell Rep. 2015; 12: 1978-85.
8. Cong L, Ran FA, Cox D, Lin S, Barretto R, Habib N, et al. Multiplex genome engineering using CRISPR/Cas systems. Science. 2013; 339: 819-23.
9. Harmsen T, Klaasen S, van de Vrugt H, Te Riele H. DNA mismatch repair and oligonucleotide end-protection promote base-pair substitution distal from a CRISPR/Cas9-induced DNA break. Nucleic Acids Res. 2018; 46: 2945-55.
10. Jaspers JE, Kersbergen A, Boon U, Sol W, van Deemter L, Zander SA, et al. Loss of 53BP1 causes PARP inhibitor resistance in Brca1-mutated mouse mammary tumors. Cancer Discov. 2013; 3: 68-81.
11. Costantino L, Sotiriou SK, Rantala JK, Magin S, Mladenov E, Helleday T, et al. Break-induced replication repair of damaged forks induces genomic duplications in human cells. Science. 2014; 343: 88-91.
12. Xu G, Chapman JR, Brandsma I, Yuan J, Mistrik M, Bouwman P, et al. REV7 counteracts DNA double-strand break resection and affects PARP inhibition. Nature. 2015; 521: 541-4.
13. Oplustil O'Connor L, Rulten SL, Cranston AN, Odedra R, Brown H, Jaspers JE, et al. The PARP Inhibitor AZD2461 Provides Insights into the Role of PARP3 Inhibition for Both Synthetic Lethality and Tolerability with Chemotherapy in Preclinical Models. Cancer research. 2016; 76: 6084-94.
14. Robinson MD, McCarthy DJ, Smyth GK. edgeR: a Bioconductor package for differential expression analysis of digital gene expression data. Bioinformatics. 2010; 26: 139-40.
15. Liu X, Holstege H, van der Gulden H, Treur-Mulder M, Zevenhoven J, Velds A, et al. Somatic loss of BRCA1 and p53 in mice induces mammary tumors with features of human BRCA1-mutated basal-like breast cancer. Proc Natl Acad Sci U S A. 2007; 104: 12111-6.
16. Koike-Yusa H, Li Y, Tan EP, Velasco-Herrera Mdel C, Yusa K. Genome-wide recessive genetic screening in mammalian cells with a lentiviral CRISPR-guide RNA library. Nat Biotechnol. 2014; 32: 267-73.
17. Elstrodt F, Hollestelle A, Nagel JH, Gorin M, Wasielewski M, van den Ouweland A, et al. BRCA1 mutation analysis of 41 human breast cancer cell lines reveals three new deleterious mutants. Cancer research. 2006; 66: 41-5.
18. Tzelepis K, Koike-Yusa H, De Braekeleer E, Li Y, Metzakopian E, Dovey OM, et al. A CRISPR Dropout Screen Identifies Genetic Vulnerabilities and Therapeutic Targets in Acute Myeloid Leukemia. Cell Rep. 2016; 17: 1193-205.
19. Wang G, Zimmermann M, Mascall K, Lenoir WF, Moffat J, Angers S, et al. Identifying drug-gene interactions from CRISPR knockout screens with drugZ. bioRxiv. 2017: 232736.
20. de Jager M, Dronkert ML, Modesti M, Beerens CE, Kanaar R, van Gent DC. DNA-binding and strand-annealing activities of human Mre11: implications for its roles in DNA double-strand break repair pathways. Nucleic Acids Res. 2001; 29: 1317-25.
21. Boersma V, Moatti N, Segura-Bayona S, Peuscher MH, van der Torre J, Wevers BA, et al. MAD2L2 controls DNA repair at telomeres and DNA breaks by inhibiting 5' end resection. Nature. 2015; 521: 537-40.

22. Gogola E, Duarte AA, de Ruiter JR, Wiegant WW, Schmid JA, de Bruijn R, et al. Selective Loss of PARG Restores PARylation and Counteracts PARP Inhibitor-Mediated Synthetic Lethality. Cancer cell. 2018; 33: 1078-93.e12.
23. Dobin A, Davis CA, Schlesinger F, Drenkow J, Zaleski C, Jha S, et al. STAR: ultrafast universal RNA-seq aligner. Bioinformatics. 2013; 29: 15-21.
24. Ewels P, Magnusson M, Lundin S, Käller M. MultiQC: summarize analysis results for multiple tools and samples in a single report. Bioinformatics. 2016; 32: 3047-8.
25. Liao Y, Smyth GK, Shi W. featureCounts: an efficient general purpose program for assigning sequence reads to genomic features. Bioinformatics. 2014; 30: 923-30.
26. Li H, Durbin R. Fast and accurate long-read alignment with Burrows-Wheeler transform. Bioinformatics. 2010; 26: 589-95.
27. Scheinin I, Sie D, Bengtsson H, van de Wiel MA, Olshen AB, van Thuijl HF, et al. DNA copy number analysis of fresh and formalin-fixed specimens by shallow whole-genome sequencing with identification and exclusion of problematic regions in the genome assembly. Genome Res. 2014; 24: 2022-32.

## Abstract

The defect in homologous recombination (HR) found in BRCA1-associated cancers can be therapeutically exploited by treatment with DNA-damaging agents and poly (ADP-ribose) polymerase (PARP) inhibitors. We and others previously reported that BRCA1-deficient tumors are initially hypersensitive to the inhibition of topoisomerase I/II and PARP but acquire drug resistance through restoration of HR activity by the loss of end-resection antagonists of the 53BP1-RIF1-REV7-Shieldin-CST pathway. Here we identify radiotherapy as an acquired vulnerability of 53BP1;BRCA1-deficient cells *in vitro* and *in vivo*. In contrast to the radioresistance caused by HR restoration through BRCA1 reconstitution, HR restoration by 53BP1 pathway inactivation further increases radiosensitivity. This highlights the relevance of this pathway for the repair of radiotherapy-induced damage. Moreover, our data show that BRCA1-mutated tumors that acquire drug resistance due to BRCA1-independent HR restoration can be targeted by radiotherapy.

# Cancer Chess: Molecular Insights Into PARPi Resistance

## Radiotherapy Is An Acquired Vulnerability of PARPi-Resistant BRCA1-Deficient Tumors

# Chapter 7

*Adapted from:*

***Marco Barazas**, Alessia Gasparini, Yike Huang, Asli Küçükosmanoğlu, Stefano Annunziato, et al.*

*Cancer Research. 2019; 79(3): 452-60.*

## Introduction

Most of the currently used anticancer therapies include applications that target the DNA such as topoisomerase inhibitors, DNA-crosslinking agents, and radiotherapy. In recent years, it has become clear that alterations in the DNA damage response (DDR) provide a useful explanation for the initial drug sensitivity. Most cancers have lost a critical DDR pathway during cancer evolution [1], and therefore respond to clinical interventions that cause DNA damage. To further exploit defects in the DDR, targeted therapies have been developed using the "synthetic lethal" approach [2]. Tumors that have lost specific DDR pathways rely more heavily on the remaining pathways, whereas normal tissues still have all DDR pathways available. Thus, inhibition of a critical backup pathway in DDR-deficient cells will cause lethality in tumor cells while not harming the normal cells. A prime example is the selective toxicity of PARP inhibitors (PARPi) to cancer cells that are defective in homologous recombination (HR) due to dysfunctional BRCA1/2 proteins [3]. Indeed, PARPi's provide an opportunity to achieve a major benefit for patients with HR-deficient cancers, if the hurdle of drug resistance can be overcome [3]. Besides resistance mechanisms that involve restoration of BRCA1/2 protein function, there are a number of BRCA1-independent roads to PARPi resistance. Most notably, we and others have found that the loss of end-resection antagonists of the 53BP1/RIF1/REV7/SHLD/CST DNA repair pathway partially restores HR activity and causes PARPi resistance in BRCA1-deficient cells [4-9]. Loss of the 53BP1 pathway has recently been identified in breast cancer explants from BRCA1 mutation carriers [10]). In this study, we demonstrate that these PARPi-resistant tumor cells show increased radiosensitivity. This finding was spurred by our initial observation that, in contrast to PARPi resistance, acquired radioresistance in *K14cre;Brca1*$^{F/F}$*;p53*$^{F/F}$ (KB1P) mouse mammary tumors with irreversible deletions in *Brca1* was not mediated by the loss of 53BP1, nor by restoration of HR. Further *in vitro* and *in vivo* examination of the genetic interaction between BRCA1 and the 53BP1 pathway on therapy response established radiosensitivity as an acquired vulnerability of KB1P tumor cells that have inactivated the 53BP1 pathway and thereby provides insight in new treatment strategies to target PARPi-resistant tumors.

## Results

*KB1P tumors acquire radioresistance independent of HR restoration*

To test whether the loss of the 53BP1 pathway–mediated radioresistance in the *K14cre;Brca1*$^{F/F}$*;p53*$^{F/F}$ (KB1P) mouse model of hereditary breast cancer, we treated mice bearing KB1P mammary tumors with radiotherapy using a high-precision small-animal irradiator equipped with a cone-beam CT scanner (Fig. 1A; [11]). This enabled us to deliver focused radiotherapy to the tumor, while sparing normal tissue and to apply clinically relevant high-dose radiotherapy regimens (e.g., 36 Gy/9f in 3 weeks).

Compared with treatment-naïve *K14cre;p53*$^{F/F}$ (KP-N) tumors, treatment-naïve KB1P- (KB1P-N) tumors were more sensitive to radiotherapy, highlighting the role of BRCA1-mediated DNA repair in response to radiotherapy (Fig. 1B). Resistance to radiotherapy was induced in KB1P-N tumors by halting treatment when either >90% or >40% to 60% tumor eradication was measured, followed by treatment reinitiation when tumors relapsed to the starting volume. This was repeated until tumors eventually stopped responding (Fig. 1C; Supplementary Fig. S1A). Notably, these radioresistant KB1P (KB1P-RR) tumors showed stable radioresistance, as serially transplanted KB1P-RR tumors were significantly less responsive to radiotherapy than their treatment-naïve counterparts (Fig. 1C; Supplementary Fig. S1A). The tumor growth rates of KB1P-RR and KB1P-N tumors were similar (Supplementary Fig. S1B). Interestingly, the KB1P-RR tumors were cross-resistant to olaparib and topotecan, which is indicative of enhanced DNA damage repair in KB1P-RR tumors (Supplementary Fig. S1B). Because these drug-response profiles are consistent with restored HR and resemble KB1P tumors that have lost 53BP1 [8, 12], we analyzed 53BP1 expression by IHC in a panel of KB1P-RR tumors. Interestingly, while PARPi resistance was mediated by loss of 53BP1 expression in 12 of 79 KB1P(M) tumors [8], all 26 KB1P-RR tumors retained 53BP1 expression ($P$ = 0.0253, binomial test; Supplementary Fig. S2A and S2B).

We next scored the capacity of KB1P-RR tumors to form ionizing radiation (IR)-induced foci of RAD51 as a measure of their HR status. Hereto, KB1P-RR tumors and their matched KB1P-N counterparts were orthotopically transplanted into syngeneic FVB/N mice. Established tumors (>1,000 mm$^3$) were treated with 15 Gy radiotherapy treatment and stained for RAD51 by immunofluorescence. We showed previously that HR restoration is frequently observed in PARPi-resistant KB1P tumors [8, 9]. Strikingly, none of the 5 tested KB1P-RR tumors scored as RAD51-IRIF positive, demonstrating that restoration of HR was not a major resistance mechanism in response to radiotherapy (P = 0.0165, binomial test; Fig. 1D; Supplementary Fig. S2C and S2D). Thus, BRCA1-deficient KB1P tumors, which have an increased radiosensitivity compared with BRCA1-proficient tumors, did not show HR restoration upon acquisition of radiotherapy resistance. This finding seems at odds with the observed partial HR restoration in PARPi-resistant tumors and is suggestive of an adverse effect of partial HR restoration on radiotherapy survival.

*BRCA1-independent restoration of HR induces hypersensitivity to radiotherapy*

To explore the radiotherapy response of BRCA1-deficient tumor cells harboring BRCA1-independent genetic events that restore HR, we focused on 53BP1. Drug-response profiles were investigated in the KB1P-G3 tumor cell line in which *Trp53bp1* was knocked out using CRISPR/SpCas9 technology as evidenced by allele disruption and protein knockout (Supplementary Fig. S3A and S3B). KB1P-G3 tumor cells that were reconstituted with human BRCA1 (KB1P-G3 *BRCA1*-rec) were included as a control for HR proficiency. We measured the clonogenic growth of KB1P-G3-parental, KB1P-G3-sg*Trp53bp1*,

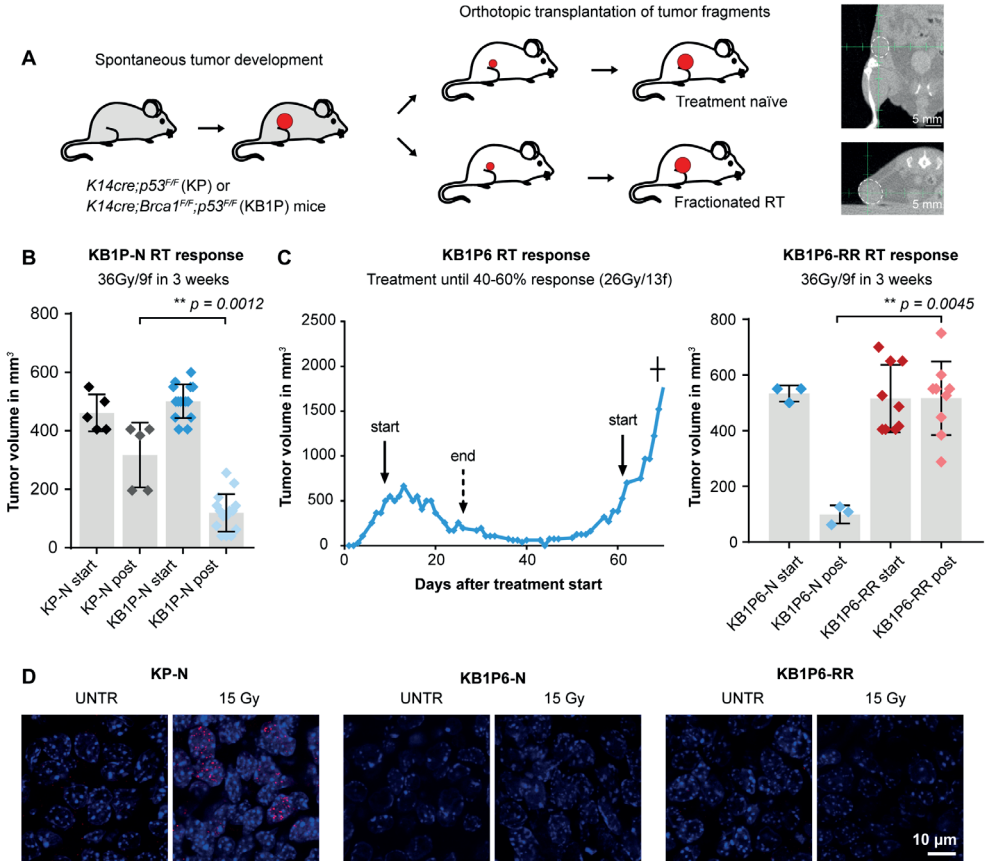



**FIGURE 1 | Radioresistance in KB1P tumors is not accompanied by HR restoration. See also Supplementary Figs. S1 and S2.** *(A)* Schematic overview of the serial transplantation model to test the radiotherapy sensitivity. Tumors derived from the spontaneous KP or KB1P tumor model were allografted in syngeneic FVB mice and treated with fractionated radiotherapy when tumors reached 500 $mm^3$. Radiotherapy was delivered locally using a high-precision irradiator dedicated for mice and equipped with a cone-beam CT scanner. This allowed accurate localization and treatment of the tumor. Example images are shown with the tumor highlighted by a white dashed line. *(B)* Radiotherapy response of KB1P compared with KP tumors. Radiotherapy was delivered to established tumors as 36 Gy/9fr in 3 weeks. Tumor volumes were compared at the end of treatment. Data are plotted as mean ± SD. Significance was calculated by unpaired two-tailed Student *t* test. *(C)* Example of a KB1P6 tumor in which radiotherapy resistance was induced by continuous treatment until 40%–60% response was measured (13fr/2 Gy). Treatment was reinitiated when the tumor had regrown to its starting volume, and this was repeated until the tumor stopped responding (KB1P-RR). KB1P-RR and its matched KB1P-N tumors were allografted in syngeneic FVB mice and treated with fractionated radiotherapy when tumors reached 500 $mm^3$ (36 Gy/9fr in 3 weeks). The volume posttreatment was compared with the volume at the start of treatment and are plotted as mean ± SD. Significance was calculated by unpaired two tailed Students *t* test. *(D)* Example immunofluorescence images of RAD51 IRIF formation on KP-N, KB1P-N, and KB1P-RR tumors before or after 15 Gy of IR. RT, radiotherapy; ns, nonsignificant.

KB1P-G3-*BRCA1*-rec, and KB1P-G3-sgEmpty control cells in response to PARPi (olaparib, AZD2461), topotecan, doxorubicin, and cisplatin. In line with previous studies [8, 12], loss of 53BP1 or reexpression of BRCA1 induced resistance to these treatments (Supplementary Fig. S3C, S3D and S4). However, upon radiotherapy treatment, depletion of 53BP1 resulted in a significant reduction in the surviving fraction compared with KB1P-G3-sgEmpty control cells. Similarly, depletion of *Rif1* or *Rev7*/*Mad2l2*, two downstream factors of 53BP1, also reduced the survival of KB1P-G3 cells upon radiotherapy treatment (Fig. 2A; Supplementary Fig. S3A and S3B). Although consistent with the absence of restoration of HR in KB1P-RR tumors, it was surprising to find that restoration of HR via loss of the 53BP1 pathway did not provide a survival benefit to radiotherapy treatment. Indeed, in line with our findings that BRCA1-deficient tumors were more sensitive to radiotherapy compared with BRCA1-proficient tumors, restoration of HR by restoring BRCA1 expression in KB1P-G3 tumor cells did increase resistance to radiotherapy (Fig. 2A), underscoring the role of the HR repair pathway in response to radiotherapy treatment.

Because repair via HR is restricted to DNA regions that undergo replication, we tested whether loss of 53BP1 might have opposing effects on cells in $G_1$ versus cells in S–$G_2$. Hereto, the FUCCI system was introduced in KB1P-G3-parental, KB1P-G3-sgEmpty, KB1P-G3-sg*Trp53bp1,* and KB1P-G3-*BRCA1*-rec cells. Cells were plated and irradiated directly after FACS to study clonogenic survival in response to radiotherapy treatment as a function of each cell-cycle phase (Fig. 2B). Although reconstitution of BRCA1 enhanced the viability upon radiotherapy treatment in S-phase populations, loss of 53BP1 sensitized KB1P-G3 tumor cells to radiotherapy treatment in all phases of the cell cycle (Fig. 2C). Notably, the radiosensitivity induced by loss of 53BP1 is likely mediated because of its role in c-NHEJ repair because the addition of a DNA-PK inhibitor (NU7441) sensitized parental and sg*Trp53bp1*-targeted cells to similar levels (Supplementary Fig. S5). Moreover, we confirmed the increased radiosensitivity induced by 53BP1 inactivation in tumor cell lines derived from a KB1PM treatment-naïve and its matched olaparib-resistant tumor that acquired genetic inactivation of *Trp53bp1* (Supplementary Fig. S6; [8]). These data show that the 53BP1 pathway plays an important role in the repair of radiotherapy treatment–induced DNA damage throughout the cell cycle, and that its loss in BRCA1-deficient cells is not compensated by the restoration of the HR pathway. Importantly, these data uncover a vulnerability of BRCA1-deficient cells that have restored HR via loss of the 53BP1 pathway.

To test whether radiotherapy can be applied to deplete PARPi-resistant cells within a mixed population of PARPi-resistant and -sensitive cells, we monitored the evolution of polyclonal populations of KB1P-G3 tumor cells targeted for *Trp53bp1, Rev7*/*Mad2l2, Rif1,* and *Ctc1* (Fig. 3A). The CST complex member CTC1 was included as we recently showed that loss of CTC1 restored HR and promoted PARPi resistance in BRCA1-deficient cells [4]. KB1P-G3 tumor cells were transduced with an inducible CRISPR/Cas9 system to achieve approximately 50% modified alleles as quantified by Sanger sequencing followed by TIDE

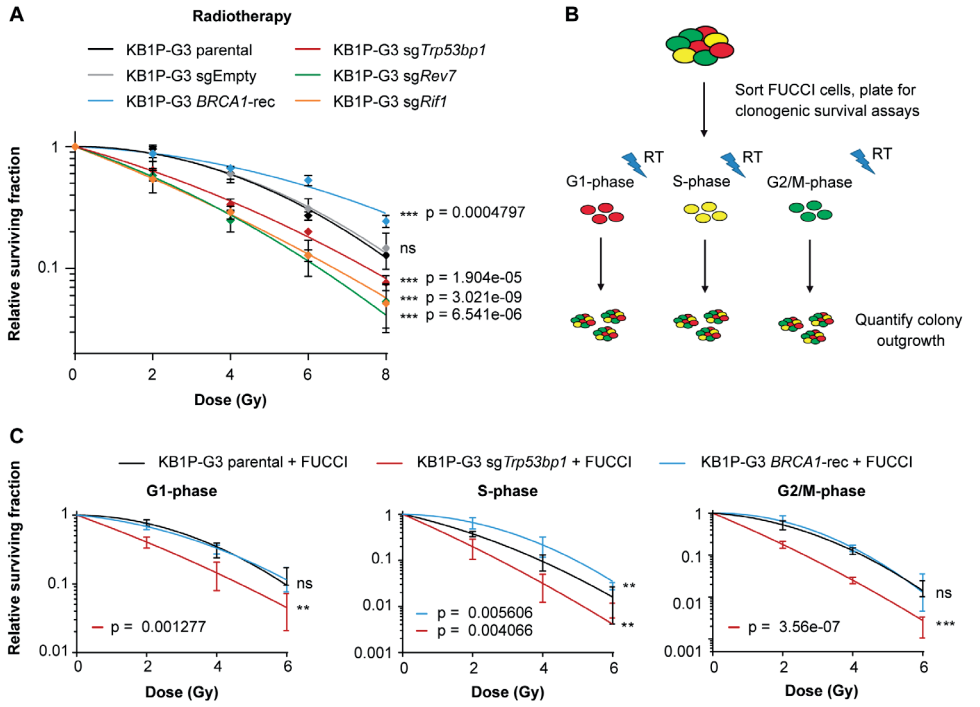



**FIGURE 2 | 53BP1 pathway inactivation in KB1P-G3 tumor cells enhances radiosensitivity. See also Supplementary Figs. S3 and S4.** *(A)* Radiotherapy response of CRISPR/spCas9–targeted KB1P-G3 tumor cell lines as determined by a clonogenic survival assay. Cells were plated as single cells, irradiated with the indicated dose immediately after plating, and fixed and stained 10 days later. The number of colonies was counted manually using an inverted microscope. Quantifications were performed blinded. Data represent at least two independent experiments and were plotted as mean ± SD and fitted to the LQ-model using GraphPad Prism software. Statistics were calculated using CFAssay in R. *(B)* Schematic overview of the FUCCI experiment in which the radiotherapy response was analyzed per stage of the cell cycle. Cells were FACS sorted, plated, and irradiated directly after plating. *(C)* The radiotherapy response of sorted KB1P-G3 parental, sg*Trp53bp1*-targeted, or BRCA1-reconstituted tumor cells in which the FUCCI system was introduced. Plates were fixed and quantified 10 days later as in *A*. Data represent three independent experiments and were plotted as in *A*. Statistics were calculated as in *A*. RT, radiotherapy; ns, nonsignificant.

analysis [13]. These polyclonal populations were subsequently plated for clonogenic growth and treated with olaparib, fractionated radiotherapy (3fr/week/4 Gy/1wk), or left untreated. All populations were harvested after 10 days and replated three times in equal cell amounts, followed by quantification of the allele distribution of the surviving populations. As expected, PARPi-resistant populations were readily selected out upon targeting of members of the 53BP1 pathway or CTC1. The surviving populations mainly comprised cells enriched for disrupted alleles compared with untreated populations (Fig. 3B). In stark contrast, the abundance of targeted alleles in cells subjected to fractionated radiotherapy was markedly reduced compared with untreated populations, further underscoring the notion that restoration of HR through loss of the 53BP1 pathway creates a therapeutically exploitable vulnerability to radiotherapy.

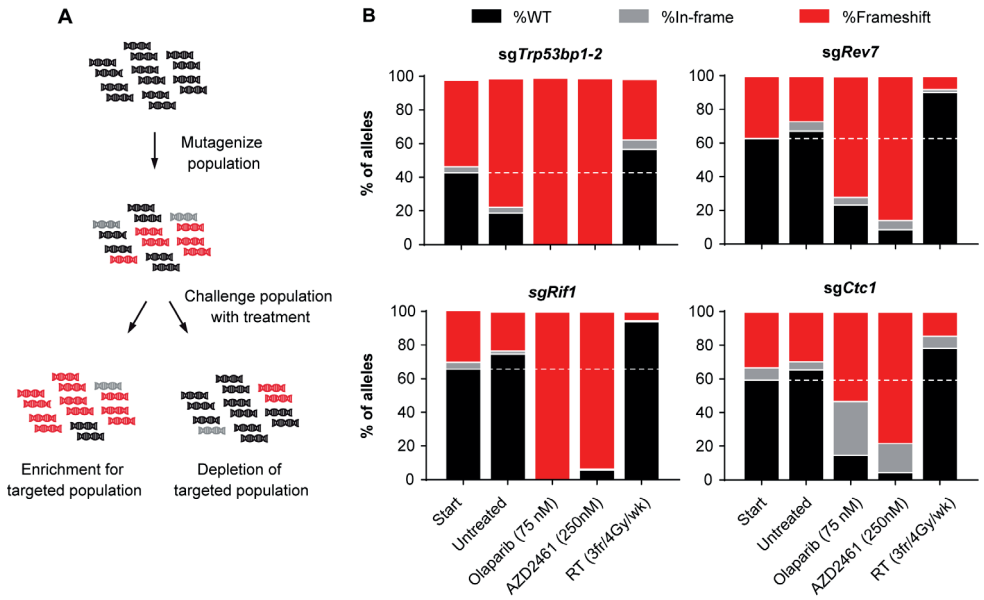



**FIGURE 3 | PARPi-resistant KB1P-G3 tumor cells can be depleted by radiotherapy.** *(A)* Schematic overview of the competition assay using polyclonal CRISPR/SpCas9–targeted starting populations. The allele distribution was quantified by TIDE before and after treatment with olaparib (75 nmol/L), AZD2461 (250 nmol/L), or IR (3fr/4 Gy/wk). Cells were passaged and replated in equal cell amounts every 10 days for a total of 30 days. Untreated populations were taken along to assess the evolution in a neutral setting. *(B)* TIDE quantifications of the indicated targeted populations at treatment initiation and after the last indicated treatment (day 30).

7

*Loss of 53BP1 IN KB1P mouse mammary tumor–derived organoids enhances the sensitivity to radiotherapy in vivo*

We next examined whether the therapeutic vulnerability exposed by 53BP1 loss is exploitable *in vivo* using our recently established tumor organoid model [12]. Hereto, KB1PM7-N tumor–derived organoids were transduced with a control or a *Trp53bp1*-targeting sgRNA and subsequently allografted in mice. Fractionated radiotherapy consisting of five consecutive fractions of 4 Gy per week for 2 weeks was initiated on mice bearing established tumors (50–100 $mm^3$), and the effect on tumor volume was evaluated at the end of treatment (Fig. 4A). Hereby, the growth of KB1PM7-N sg*NT* tumors could be contained (Fig. 4B). Although radiotherapy extended the survival of all treated mice, depletion of 53BP1 significantly enhanced the response, resulting in markedly reduced tumor volume at the end of treatment ($P$ = 0.0081, $t$ test.) and a prolonged time to relapse, defined as five times the original treatment volume ($P$ = 0.0117, log-rank test; Fig. 4C). Remarkably, the abundance of 53BP1-deficient cells was strongly depleted in KB1PM7-N sg*Trp53bp1* tumors by RT (Fig. 4D; Supplementary Table S1), in line with our *in vitro*

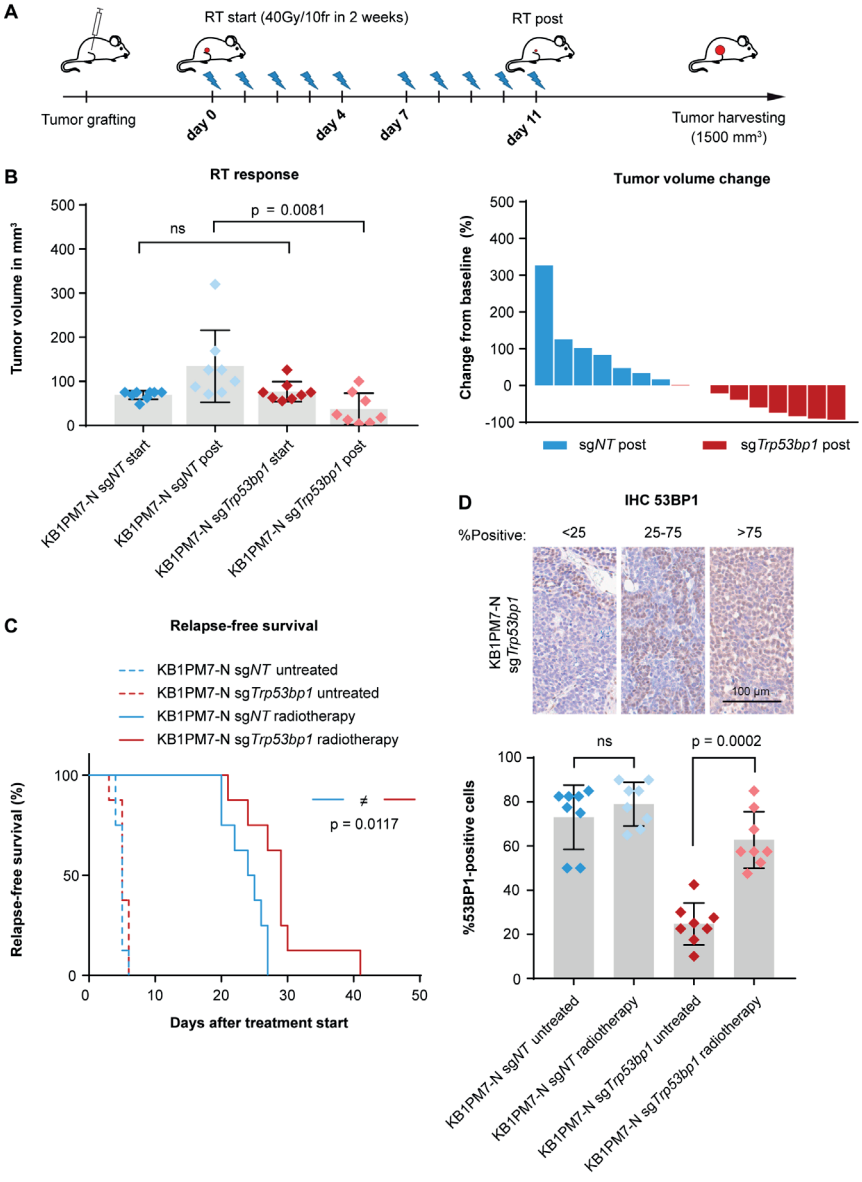
findings. Together, these data demonstrate that KB1P tumors that have lost 53BP1 expression are sensitized to radiotherapy, despite being unresponsive to PARPi treatment [12].

## Discussion

Acquired resistance to anticancer therapy may introduce new vulnerabilities, a concept known as collateral sensitivity [14]. In this study, we demonstrate that this concept also applies to anticancer therapy targeting DDR defects. We identified radiosensitivity as a therapeutically exploitable vulnerability of PARPi-resistant BRCA1-deficient cells that have restored HR via loss of the 53BP1 pathway. 53BP1 and its pathway member RIF1 have a known role in promoting double-strand break (DSB) repair via NHEJ. However, while loss of 53BP1 or RIF1 in BRCA1-proficient cells has been associated with increased radiotherapy treatment sensitivity [6, 15], the interaction between 53BP1 and BRCA1 on radiotherapy treatment response has remained unexplored. Collectively, our findings establish this interaction as a two-edged sword: loss of the 53BP1 pathway in BRCA1-deficient cells drives PARPi and topoisomerase inhibitor resistance at the expense of an acquired vulnerability to radiotherapy. These opposing responses to different DNA-damaging agents might be reconciled by the context in which DNA damage arises; olaparib and topoisomerase inhibitors cause DSBs primarily during replication by inhibiting single-strand break repair and/or promoting PARP1/TOP1 trapping on the DNA, which ultimately results in replication fork collapse and the formation of one-sided DSBs [3]. Therefore, a template for HR is in close proximity when a DSB arises, possibly explaining the strong effect of 53BP1 pathway inactivation on driving PARP- or topoisomerase inhibitor resistance. In contrast, acute DSB induction by radiotherapy treatment is inflicted independent of the cell cycle and is more dependent on repair via the NHEJ pathway. Indeed, inhibition of NHEJ repair, for instance by knocking out KU70/80, was previously shown to sensitize cells to radiotherapy treatment [16]. We provide evidence that loss of the 53BP1 pathway also confers sensitivity to radiotherapy treatment in a BRCA1-deficient context, which is dependent on NHEJ activity. Our

**FIGURE 4 | KB1PM7-N sg*Trp53bp1*–targeted tumors show an enhanced radiotherapy response.** *(A)* Schematic overview depicting the radiotherapy treatment schedule. *(B)* KB1PM7-N sg*NT* and KB1PM7-N sg*Trp53bp1*–targeted tumor pieces were orthotopically transplanted in mice and were treated with radiotherapy (40 Gy/10fr in 2 weeks) when tumors reached 50–100mm$^3$. The tumor volume at the end of treatment was compared with the volume at the start of treatment. Data are plotted as mean ± SD. Significance was calculated by unpaired two tailed Student *t* test. Right, the data are presented in a Waterfall plot as relative change in tumor volume after treatment compared with treatment start. *(C)* Kaplan–Meier curve showing that sg*Trp53bp1*-targeted KB1PM7-N tumors have a prolonged time to relapse upon radiotherapy treatment, defined as five times the tumor volume compared with treatment initiation. Significance was calculated by log-rank (Mantel–Cox) test in GraphPad Prism. *(D)* IHC for 53BP1 on KB1PM7-N sg*NT* and sg*Trp53bp1*-targeted end-stage tumors that were left untreated or received radiotherapy. The percentage of 53BP1-positive cells was quantified by two independent animal pathologists and the average percentage is plotted per tumor. Significance was calculated by Mann–Whitney *U* test. See also Supplementary Table S1. RT, radiotherapy; ns, nonsignificant.

data show that this acquired vulnerability can be exploited both *in vitro* and *in vivo* to constrain BRCA1-deficient cells that have acquired PARPi resistance via disruption of the 53BP1 pathway. Given the plethora of factors involved in the 53BP1 pathway and the pressing problem of clinical resistance to PARPi treatment, it will be important to determine the frequency of 53BP1/RIF1/REV7/Shieldin/CST pathway inactivation in PARPi-resistant tumors. Our findings also reemphasize the importance of identifying



the mechanistic basis of BRCA1-deficient tumors that have restored HR activity. For example, assessment of HR status by scoring for RAD51 IRIF formation may not provide sufficient detail to make informed treatment decisions because this assay does not discriminate BRCA1-dependent from BRCA1-independent restoration of HR. Given their hypersensitivity to radiotherapy, the latter tumors might have different treatment options from tumors in which BRCA1 expression has been restored.

## Materials and Methods

*In vivo studies*

All animal experiments were approved by the Animal Ethics Committee of The Netherlands Cancer Institute (Amsterdam, the Netherlands) and performed in accordance with the Dutch Act on Animal Experimentation (November 2014).

Radiosensitivity responses were evaluated by allografting previously harvested tumor pieces derived from the *K14cre;Trp53*$^{F/F}$ (KP) and *K14cre;Brca1*$^{F/F}$*;Trp53*$^{F/F}$ (KB1P) genetically engineered mouse model [17]. The tumor volume was determined using the egg formula (length × width$^2$ × 0.5). Established tumors (>500 mm$^3$) were irradiated daily using a high-precision small-animal irradiator equipped with a cone-beam CT scanner (X-RAD 225Cx). The dosing schedule consisted of 36 Gy/9f in 3 weeks. Radioresistant tumors were generated by allografting KB1P tumor pieces in 6- to 9-week-old syngeneic female mice followed by daily treatment with 2, 4, or 8 Gy, until a predetermined response was achieved, at which point the treatment was halted. The treatment was reinitiated when the tumor relapsed to the starting volume, and this was repeated until the tumor eventually stopped responding (KB1P-RR). KB1P-RR tumors were harvested and collected in formalin or DMSO for downstream analysis.

The stability of radioresistance and cross-resistance profiles was determined by allografting KB1P-RR and matched treatment-naïve (KB1P-N) tumor pieces in 6- to 9-week-old syngeneic female mice. Radiotherapy was given to established tumors (>500 mm$^3$) and consisted of 36 Gy/9f in 3 weeks. The cross-resistance study was carried out on established tumors (>200 mm$^3$), at which point mice were stratified into the different treatment arms. Treatments consisted of olaparib (50 mg/kg drug i.p. on 28 consecutive days; [18]), topotecan (4 mg/kg drug i.p. on days 0–4 and 14–18; [19]), cisplatin (6 mg/kg drug i.v. single dose; [18]), or untreated. To assess the radiotherapy response in isogenic *Trp53bp1*-knockout or control tumors (sg*NT*), previously generated and validated tumor organoids were allografted in 6- to 9-week-old NMRI nude female mice, as described previously [12]. Briefly, tumor organoids were collected, incubated with TripLE at 37°C for 5 minutes, dissociated into single cells, washed in PBS, resuspended in tumor organoid medium, and mixed in a 1:1 ratio of tumor organoid suspension and BME in a cell concentration of $10^4$ cells per 40 μL. Subsequently, $10^4$ cells were transplanted in the fourth right mammary fat pad of 6- to 9-week-old NMRI nude female

mice. Treatment of tumor-bearing mice was initiated when tumors reached a size of 50–100 $mm^3$, at which point mice were stratified into the untreated or radiotherapy treatment group. The dosing schedule consisted of 40 Gy/10f in 2 weeks. Animals were sacrificed with $CO_2$ when the tumor reached a volume of 1,500 $mm^3$.

*Tumor analysis*

IHC to detect 53BP1 expression in tumor tissues was performed as described previously [8]. The percentage of 53BP1-positive cells was scored blinded by two independent animal pathologists and the average score taken for plotting and analysis. RAD51 immunofluorescence on tumors was performed as described previously [9]. Briefly, ionizing radiation–induced foci (IRIF) were induced by irradiation (15 Gy) 2 hours prior to tumor harvesting and fixation in formalin. The staining was performed on FFPE slides using a noncommercial antibody for RAD51 provided by R. Kanaar (1:5,000) and goat anti-rabbit IgG (H+L) cross-adsorbed secondary antibody, Alexa Fluor 568 from Thermo Fisher Scientific, catalog no. A-11011, RRID AB_143157 and mounted and counterstained using VectaShield mounting medium with DAPI (H1500, Vector Laboratories). Samples were imaged by confocal microscope (Leica SP5, Leica Microsystems GmbH) using a 63× oil objective. Multiple different Z-stacks were imaged per sample. The number of foci per nucleus was analyzed automatically using an ImageJ script [9].

*Cell culture*

The KB1P-G3 and KB1PM5 tumor derived cell lines were previously established from a *K14cre;Brca1$^{F/F}$;Trp53$^{F/F}$* (KB1P) and *K14cre;Brca1$^{-/-}$;p53$^{-/-}$;Mdr1a/b$^{-/-}$* (KB1PM) mouse mammary tumor, respectively, and cultured as described previously [8]. The KB1PM5-158 cell line was derived from the treatment-naïve tumor and the KB1PM5-177 and KB1PM5-178 were established from a matched olaparib-resistant tumor due to an inactivating duplication event in *Trp53bp1*, which was described previously [8]. Briefly, cells were cultured in DMEM/F-12 medium (Life Technologies) in the presence of 10% FCS, penicillin/streptomycin (Gibco), 5 µg/mL insulin (Sigma), 5 ng/mL EGF (Life Technologies), and 5 ng/mL cholera toxin (Gentaur) under low-oxygen conditions (3% $O_2$, 5% $CO_2$ at 37°C). The KB1PM7-N 3D tumor organoid lines were previously established from a KB1PM mouse mammary tumor and cultured as described previously [12]. Briefly, KB1PM7-N 3D tumor organoid cells were seeded in Basement Membrane Extract Type 2 (BME, Trevigen) on 24-well suspension plates (Greiner Bio-One) and cultured in AdDMEM/F12 supplemented with 1 mol/L HEPES (Sigma), GlutaMAX (Invitrogen), penicillin/streptomycin (Gibco), B27 (Gibco), 125 µmol/L N-acetyl-L-cysteine (Sigma), 50 ng/mL murine EGF (Invitrogen). Cell authentication was not conducted. All cell lines were kept at low passage and testing for *Mycoplasma* contamination was performed on a regular basis using the MycoAlert Mycoplasma Detection Kit (Lonza).

*Plasmids, genome editing, and sequence analysis*

Unless otherwise stated, CRISPR/SpCas9-targeted KB1P-G3 tumor cell lines were generated using a modified version of the pX330 backbone [20] in which a puromycin-resistant ORF was cloned under the hPGK promoter [21]. sgRNA sequences were cloned in the pX330puro backbone as described previously (15) and sequence verified by Sanger Sequencing (Eurofins). KB1P-G3 tumor cells were transfected using TransIT-LT1 (Mirus) reagents according to manufacturer's protocol and using conditions as described previously [4]. Briefly, $1.5 \times 10^5$ cells were seeded in 6-well plates 1 day prior to transfection with 1 μg DNA. Twenty-four hours later, the medium was refreshed with puromycin (3 μg/mL) containing medium and cells were selected for 3 days. KB1P-G3 BRCA1–reconstituted cells were generated by transfecting KB1P-G3 cells with a human *BRCA1* cDNA expression construct [22] using Lipofectamine 2000 (Thermo Fisher Scientific). One day after transfection, cells were passaged and cultured with 300 μg/mL G418 (Thermo Fisher Scientific) to select for human *BRCA1*-complemented colonies. G418-resistant colonies were tested for human *BRCA1* integration by PCR with human *BRCA1* exon 11–specific primers: forward, 5'-TCCAGGAAATGCAGAAGAGG-3'; reverse, 5'-ACTGGAGCCCACTTCATTAG-3'.

Lentivirus production in HEK293T cells was performed as described previously [23]. KB1P-G3 cells were transduced with the FUCCI plasmids mKO2-hCdt1(30/120) and mAG-hGem(1/110; [24]) and were sorted for red fluorescence and green fluorescence in two subsequent sorting rounds to ensure the presence of both constructs in each cell. Cell lines targeted with the pGSC_Cas9_Neo and pLenti-sgRNA-tetR-T2A-Puro system [25] were generated by lentiviral transduction. sgRNA sequences were cloned in the pLenti-sgRNA-tetR-T2A-Puro backbone using the *Bfu*AI (NEB) restriction enzyme. Following transduction and selection with puromycin (3 μg/mL) and blasticidin (500 μg/mL) for 5 days, cells were cultured in the presence of 3 μg/mL doxycycline (Sigma) for at least 5 days to induce sgRNA expression. Doxycycline was removed from the medium prior to starting the competition assay. The KB1PM7-N 3D tumor organoid line derivatives KB1PM7-N sg*NT* and KB1PM7-N sg*Trp53bp1* were established previously [12]. sgRNA sequences used in this study are as follows [12]: sg*Trp53bp1*: 5'-GAACAATCTGCTGTAGAACA-3', sg*Trp53bp1-2*: 5'-TACCGGGCTGTACTGTAACA-3', sg*Rif1*: 5'-GACAATCCTGAGGTAATTCT-3', sg*Rev7*: 5'-GCGCAAGAAGTACAACGTGC-3' and sg*Ctc1*: 5'-CTTGAAGCCGAACAGTGCCA-3'. Targeting efficiencies were determined by genomic DNA isolation (Gentra Puregene, Qiagen) followed by PCR amplification of the target loci and subsequent Sanger Sequencing (Eurofins). Sequences were analyzed using the TIDE algorithm [13], using parental cells as a reference. The following PCR primers were used: sg*Trp53bp1*: forward, 5'-TGAGAAATGGAGGCAACACCA-3' and reverse, 5'-CTCGATCTCACACTTCCGCC-3'; sg*Trp53bp1-2*: forward, 5'-GAGAGCGCACGCACAGTAAG-3' and reverse, 5'-TGGGCTGGCTCTGATACTTTG-3'; sg*Rif1*: forward, 5'-GACGGACGCCTACCTAACTC-3' and reverse, 5'-AAAGGCCCTTGACATCTAGCC-3'; sg*Rev7*: forward, 5'-TAGCCCGGTCGTAGATTGGA-3' and reverse, 5'-CTGTC-

CGCTATCAGCCTCTG-3'; and sg*Ctc1*: forward, 5'-TGTTCCAGACAGGGATTTTCCAA-3' and reverse, 5'-AGGAGAGGGTTGCTTCAGGA-3'.

The exon 25–26 duplication specifically in the KB1PM5-177 and KB1PM5-178 cell lines was confirmed by PCR. Hereto, RNA was isolated from cell pellets according to the manufacturer's protocol (Bioline) and cDNA was generated using the cDNA Kit (Bioline) according to the manufacturer's protocol, making use of the polydT primer. Subsequently, the cDNA was used for PCR using the following primers to detect the exon 25–26 duplication event: forward, 5'- CGGACCAGCACTGTCGAACCC-3', reverse, 5'- GGGCTTCATTGAAGTCTTCAAG-3' and the following primers to detect exon 25: forward, 5'-TCCCAAATGCCATTCTTCCTGTT-3', reverse, 5'- TAGCCGGAAGGTGGGGTACT-3'. Expected bands (262 bp and 562 bp, respectively) were gel extracted (Bioline) according to manufacturer's protocol and submitted for Sanger Sequencing (Eurofins).

*Western blot analysis*

Western blot analysis for 53BP1, RIF1, and REV7 was performed as described previously [9]. Briefly, cells were plated in equal amounts and the next day cells were washed with PBS and lysed with RIPA lysis buffer supplemented with protease inhibitors. The protein concentration was determined using the Pierce BCA Protein Assay Kit (Thermo Fisher Scientific) according to manufacturer's protocol. Samples were heated at 70°C for 10 minutes and loaded on 3%–8% Tris-acetate (53BP1 and RIF1) or 4%–12% Bis-Tris gradient gels (REV7). Following SDS-PAGE separation, proteins were transferred to nitrocellulose membranes for 53BP1 and RIF1 (Invitrogen), or to polyvinylidene difluoride membrane (Millipore) for REV7. Membranes were blocked in 5% milk with Tris-buffered saline Triton X-100 buffer (100 mmol/L Tris, pH 7.4, 500 mmol/L NaCl, 0.1% TritonX-100; TBS-T0.1%), and all antibody incubations were performed in the same buffer. Primary antibody incubations were performed overnight at 4°C; secondary antibody incubations were performed for 1 hour at room temperature and proteins were visualized by ECL. Antibodies used were as follows: rabbit anti-53BP1 (ab21083, Abcam), 1:1,000 dilution; rabbit anti-RIF1 (SK1316; ref. 5); mouse anti-REV7 (612266, BD Biosciences), 1:5,000 dilution; mouse anti-α-tubulin (T6074, Sigma), 1:5,000 dilution; polyclonal rabbit anti-mouse immunoglobulins/HRP (P0161, Dako), 1:10,000 dilution; polyclonal swine anti-rabbit immunoglobulins/HRP (P0217, Dako), 1:10,000 dilution.

*In vitro drug response profiles*

Clonogenic growth assays with PARPis (olaparib and AZD2461), topoisomerase inhibitors (topotecan and doxorubicin), and the alkylating agent cisplatin were performed as described previously [4]. Briefly, on day 0, $5 \times 10^3$ KB1P-G3 cells were seeded per 6 well, and drugs were added in the indicated concentrations. Untreated cells were fixed on day 6, and treated cells were fixed on day 9. After fixation, cells were stained with 0.1%

crystal violet, and plates were scanned with the Gelcount (Oxford Optronix). Crystal violet was solubilized using 10% acetic acid, and the absorbance at 562nm was measured using a Tecan plate reader. The experiment was performed three times. Dose–response curves with PARPis were generated similarly, but $1 \times 10^3$ KB1P-G3 cells were seeded per 6 well, and all conditions were fixed on day 9. Clonogenic growth assays on KB1PM5 tumor-derived cell lines were performed as described above, but cells from all conditions were fixed and stained on day 7. Radiotherapy survival curves on KB1P-G3 cell lines were generated by seeding different amounts of cells (50, 100, 500, 1,000, and 5,000) per 6 well in technical duplicates, followed by irradiation with a single fraction of the indicated dose using the $^{137}$Cs-irradiation unit Gammacell 40 EXACTOR (Best Theratronics). FUCCI experiments were performed by sorting the different cell populations followed by immediate irradiation with a single fraction of the indicated dose. DNAPK-inhibitor experiments were performed by addition of 1 μmol/L NU7441 1 hour prior to a single fraction of the indicated dose. Plates were fixed and stained with 0.1% crystal violet on day 9. Colonies containing at least 50 cells were counted manually using an inverted microscope, selecting the wells in which <150 colonies were counted to restrict the quantifications to wells in which the colonies were still well separated. Plating efficiencies (PE) were calculated by dividing the number of colonies after treatment with the amount of cells that were originally plated. Surviving fractions were calculated for each KB1P-G3 cell line by dividing the PE after radiotherapy treatment to the PE of untreated cells and plotted using GraphPad Prism. Data were fitted to LQ model: Y=EXP(-(A*X + B*X^2)). The experiment was performed at least two times. Radiotherapy survival curves on KB1PM5-158 and KB1PM5-177 cell lines 1,000, 2,000, or 4,000 cells were plated. For the KB1PM5-178 cell lines, 100, 500, or 1,000 cells were plated. Analysis was performed as described above. The experiment was performed three times.

Competition assays were performed as described previously [4]. Briefly, KB1P-G3 SpCas9–expressing cells were transduced with pLenti-sgRNA-tetR-T2A-Puro vectors in which the indicated sgRNAs were cloned. Following selection with puromycin (3 μg/mL) for 3 days and recovery from selection, 5,000 cells were plated in 6-well plates in triplicate per condition, with or without olaparib (75 nmol/L), AZD2461 (250 nmol/L), or radiotherapy (3fr/4Gy/1wk). After 10 days of treatment, cells were harvested, counted, and replated at 5,000 cells per 6 well two times (total treatment time of 30 days). Cells were harvested for gDNA isolation and target loci analysis was done at day 0 and after treatment.

Growth curves were generated as described previously [4]. KB1P-G3 cells were seeded at 1,000 cells per well in 96-well plates. In each experiment, 6 technical replicates were seeded and the well confluency was recorded every 4 hours using an IncuCyte Zoom Live-Cell Analysis System (Essen Bioscience). The images were analyzed using IncuCyte Zoom software. The experiment was performed three times.

*Quantification and statistical analysis*

Statistical analysis was performed using GraphPad Prism software and R software. Significance was calculated as indicated in the specific figure legends using unpaired two-tailed Student *t* test, CFAssay Bioconductor version 3.7, Kruskal–Wallis nonparametric test, log-rank (Mantel–Cox) test, one-way ANOVA with Dunnett multiple comparison test, Mann–Whitney *U* test, binomial test, and using observed distributions of PARPi-resistant KB1P(M) tumors for comparison [8].

## Disclosure of Potential Conflicts of Interest

No potential conflicts of interest were disclosed.

## Author Contributions

*Conception and design*: M. Barazas, G.R. Borst, S. Rottenberg. *Development of methodology*: M. Barazas, A. Gasparini, G.R. Borst, S. Rottenberg. *Acquisition of data (provided animals, acquired and managed patients, provided facilities, etc.)*: M. Barazas, A. Gasparini, Y. Huang, A. Küçükosmanoğlu, S. Annunziato, P. Bouwman, W. Sol, N. Proost, R. de Korte-Grimmerink, J. Jonkers, G.R. Borst, S. Rottenberg. *Analysis and interpretation of data (e.g., statistical analysis, biostatistics, computational analysis)*: M. Barazas, S. Annunziato, G.R. Borst, S. Rottenberg. *Writing, review, and/or revision of the manuscript*: M. Barazas, J. Jonkers, G.R. Borst, S. Rottenberg. *Administrative, technical, or material support (i.e., reporting or organizing data, constructing databases)*: M. Barazas, A. Gasparini, A. Küçükosmanoğlu, A. Kersbergen, N. Proost, R. de Korte-Grimmerink, M. van de Ven, S. Rottenberg. *Study supervision*: J. Jonkers, G.R. Borst, S. Rottenberg.



## Acknowledgements

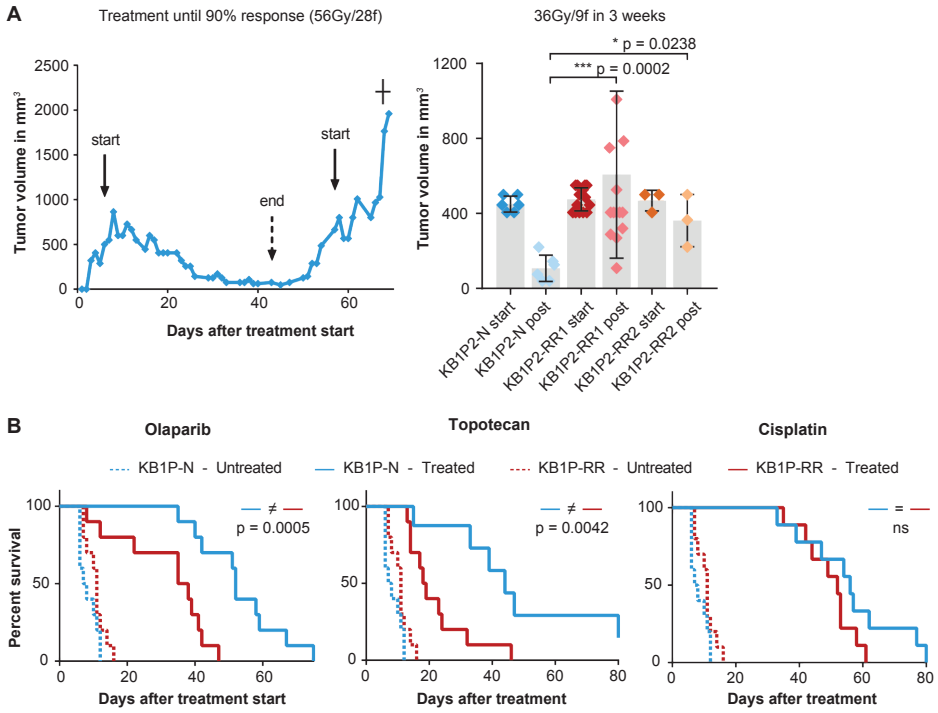
We wish to thank Piet Borst for critical reading of the manuscript and the members of the Preclinical Intervention Unit of the Mouse Clinic for Cancer and Aging (MCCA) at the Netherlands Cancer Institute (NKI) for their technical support with the animal experiments. We are grateful to the NKI animal facility, animal pathology facility, and flow cytometry facility for their excellent service and Sjoerd Klarenbeek for the independent scoring of the 53BP1 IHC. This work was supported by grants from the Dutch Cancer Society (KWF 2011-5220 and 2014-6532 to S. Rottenberg and J. Jonkers), the Netherlands Organization for Scientific Research (VICI 91814643, NGI 93512009, Cancer Genomics Netherlands, and a National Roadmap Grant for Large-Scale Research Facilities to J. Jonkers), the Swiss National Science Foundation (310030_179360 to S. Rottenberg), the Swiss Cancer League (KLS-4282-08-2017 to S. Rottenberg; ERC CoG-681572 to S. Rottenberg; and ERC Synergy Grant 319661 to J. Jonkers).

## References

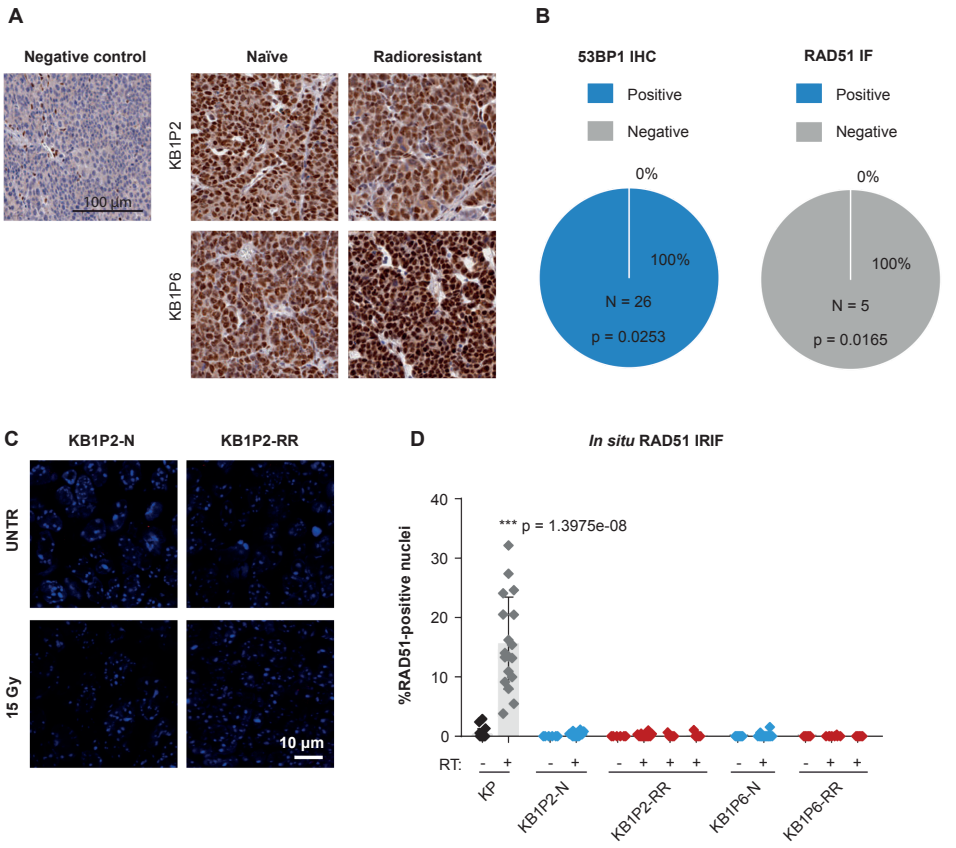

1. Knijnenburg TA, Wang L, Zimmermann MT, Chambwe N, Gao GF, Cherniack AD, et al. Genomic and Molecular Landscape of DNA Damage Repair Deficiency across The Cancer Genome Atlas. Cell Rep. 2018; 23: 239-54.e6.
2. Kaelin WG, Jr. The concept of synthetic lethality in the context of anticancer therapy. Nat Rev Cancer. 2005; 5: 689-98.
3. Lord CJ, Ashworth A. PARP inhibitors: Synthetic lethality in the clinic. Science. 2017; 355: 1152-8.
4. Barazas M, Annunziato S, Pettitt SJ, de Krijger I, Ghezraoui H, Roobol SJ, et al. The CST Complex Mediates End Protection at Double-Strand Breaks and Promotes PARP Inhibitor Sensitivity in BRCA1-Deficient Cells. Cell Rep. 2018; 23: 2107-18.
5. Bunting SF, Callén E, Wong N, Chen HT, Polato F, Gunn A, et al. 53BP1 inhibits homologous recombination in Brca1-deficient cells by blocking resection of DNA breaks. Cell. 2010; 141: 243-54.
6. Chapman JR, Barral P, Vannier JB, Borel V, Steger M, Tomas-Loba A, et al. RIF1 is essential for 53BP1-dependent nonhomologous end joining and suppression of DNA double-strand break resection. Mol Cell. 2013; 49: 858-71.
7. Gupta R, Somyajit K, Narita T, Maskey E, Stanlie A, Kremer M, et al. DNA Repair Network Analysis Reveals Shieldin as a Key Regulator of NHEJ and PARP Inhibitor Sensitivity. Cell. 2018; 173: 972-88.e23.
8. Jaspers JE, Kersbergen A, Boon U, Sol W, van Deemter L, Zander SA, et al. Loss of 53BP1 causes PARP inhibitor resistance in Brca1-mutated mouse mammary tumors. Cancer Discov. 2013; 3: 68-81.
9. Xu G, Chapman JR, Brandsma I, Yuan J, Mistrik M, Bouwman P, et al. REV7 counteracts DNA double-strand break resection and affects PARP inhibition. Nature. 2015; 521: 541-4.
10. Bruna A, Rueda OM, Greenwood W, Batra AS, Callari M, Batra RN, et al. A Biobank of Breast Cancer Explants with Preserved Intra-tumor Heterogeneity to Screen Anticancer Compounds. Cell. 2016; 167: 260-74.e22.
11. Clarkson R, Lindsay PE, Ansell S, Wilson G, Jelveh S, Hill RP, et al. Characterization of image quality and image-guidance performance of a preclinical microirradiator. Med Phys. 2011; 38: 845-56.
12. Duarte AA, Gogola E, Sachs N, Barazas M, Annunziato S, J RdR, et al. BRCA-deficient mouse mammary tumor organoids to study cancer-drug resistance. Nat Methods. 2018; 15: 134-40.
13. Brinkman EK, Chen T, Amendola M, van Steensel B. Easy quantitative assessment of genome editing by sequence trace decomposition. Nucleic Acids Res. 2014; 42: e168.
14. Hutchison DJ. Cross resistance and collateral sensitivity studies in cancer chemotherapy. Adv Cancer Res. 1963; 7: 235-50.
15. Nakamura K, Sakai W, Kawamoto T, Bree RT, Lowndes NF, Takeda S, et al. Genetic dissection of vertebrate 53BP1: a major role in non-homologous end joining of DNA double strand breaks. DNA Repair (Amst). 2006; 5: 741-9.
16. Smith GC, Jackson SP. The DNA-dependent protein kinase. Genes Dev. 1999; 13: 916-34.
17. Liu X, Holstege H, van der Gulden H, Treur-Mulder M, Zevenhoven J, Velds A, et al. Somatic loss of BRCA1 and p53 in mice induces mammary tumors with features of human BRCA1-mutated basal-like breast cancer. Proc Natl Acad Sci U S A. 2007; 104: 12111-6.
18. Rottenberg S, Jaspers JE, Kersbergen A, van der Burg E, Nygren AO, Zander SA, et al. High sensitivity of BRCA1-deficient mammary tumors to the PARP inhibitor AZD2281 alone and in combination with platinum drugs. Proc Natl Acad Sci U S A. 2008; 105: 17079-84.
19. Zander SAL, Kersbergen A, van der Burg E, de Water N, van Tellingen O, Gunnarsdottir S, et al. Sensitivity and Acquired Resistance of BRCA1;p53-Deficient Mouse Mammary Tumors to the Topoisomerase I Inhibitor Topotecan. Cancer research. 2010; 70: 1700-10.
20. Cong L, Ran FA, Cox D, Lin S, Barretto R, Habib N, et al. Multiplex genome engineering using CRISPR/Cas systems. Science. 2013; 339: 819-23.
21. Harmsen T, Klaasen S, van de Vrugt H, Te Riele H. DNA mismatch repair and oligonucleotide end-protection promote base-pair substitution distal from a CRISPR/Cas9-induced DNA break. Nucleic Acids Res. 2018; 46: 2945-55.

22. Chen J, Silver DP, Walpita D, Cantor SB, Gazdar AF, Tomlinson G, et al. Stable interaction between the products of the BRCA1 and BRCA2 tumor suppressor genes in mitotic and meiotic cells. Mol Cell. 1998; 2: 317-28.
23. Follenzi A, Ailles LE, Bakovic S, Geuna M, Naldini L. Gene transfer by lentiviral vectors is limited by nuclear translocation and rescued by HIV-1 pol sequences. Nat Genet. 2000; 25: 217-22.
24. Sakaue-Sawano A, Kurokawa H, Morimura T, Hanyu A, Hama H, Osawa H, et al. Visualizing spatiotemporal dynamics of multicellular cell-cycle progression. Cell. 2008; 132: 487-98.
25. Prahallad A, Heynen GJ, Germano G, Willems SM, Evers B, Vecchione L, et al. PTPN11 Is a Central Node in Intrinsic and Acquired Resistance to Targeted Cancer Drugs. Cell Rep. 2015; 12: 1978-85.

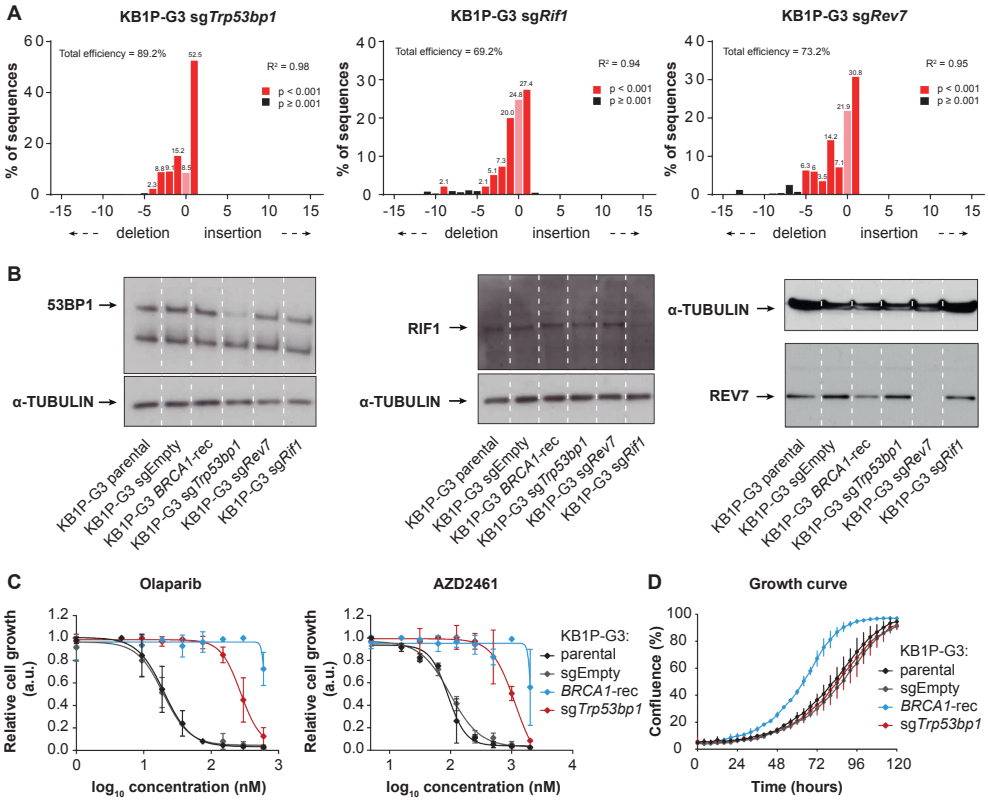
## Supplementary Figures & Table



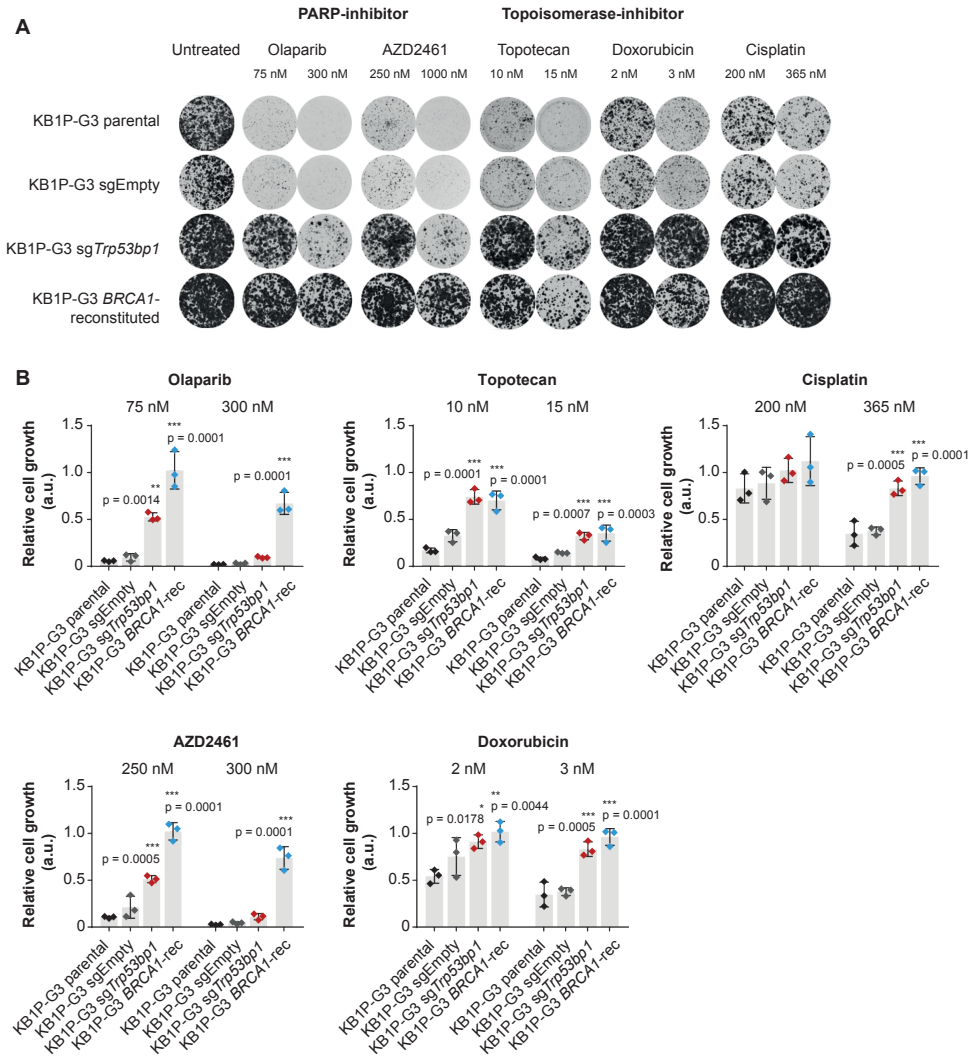

**SUPPLEMENTARY FIGURE S1 | KB1P-RR tumors have an activated DNA damage response. Related to Figure 1.** *(A)* Example of a KB1P2 tumor in which radiotherapy resistance was induced by continuous treatment until 90% response was measured (28fr/2Gy) followed by treatment continuation when the tumor relapsed to the starting volume. KB1P-RR and its matched KB1P-N tumors were allografted in syngeneic FVB mice and treated with fractionated radiotherapy when tumors reached 500 $mm^3$ (36Gy/9fr in 3 weeks), as in Fig. 1C. The volume post treatment was compared to the volume at treatment start and are plotted as mean ± SD. Significance was calculated by unpaired two-tailed students t-test. *(B)* Cross-resistance profiles of KB1P-N and KB1P-RR tumors. KB1P-N and KB1P-RR tumor pieces were orthotopically transplanted in FVB mice and mice were stratified into the treatment groups when tumors >200$mm^3$. Treatment consisted of olaparib (50 mg/kg drug i.p. on 28 consecutive days), topotecan (4 mg/kg drug i.p. on days 0-4 and 14-18), cisplatin (6 mg/kg drug i.v. single dose) or untreated. Data are plotted using Graphpad Prism software. Significance was calculated by Log-rank (Mantel Cox) test.



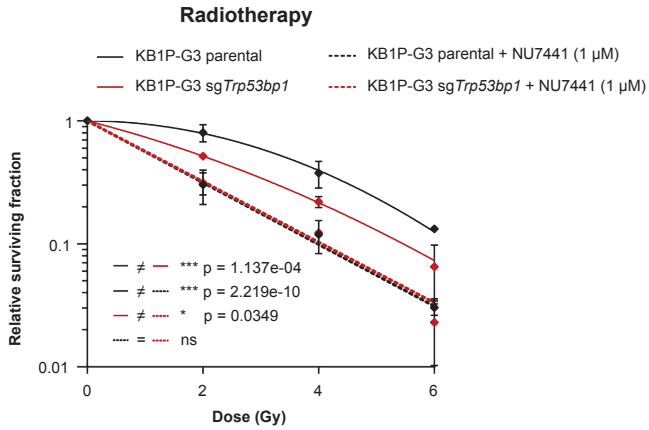

**SUPPLEMENTARY FIGURE S2 | 53BP1 and RAD51 profiling of KB1P-N and KB1P-RR tumors. Related to Figure 1.** *(A)* IHC of 53BP1 protein on matched KB1P-N and KB1P-RR tumors. *(B)* Pie-charts showing an overview of KB1P-RR tumors stained for 53BP1 by IHC (n = 26) or RAD51 IRIF formation by IF (n = 5). Significance was calculated by binomial test using distributions observed for KB1P-PARPi resistant tumors. *(C)* Example IF images of RAD51 IRIF formation on KB1P2-N and KB1P2-RR tumors before or after 15Gy of IR. *(D)* Quantification of C. Data are plotted as %RAD51 positive nuclei per field (>100 cells) and represent the mean ± SD. Significance was calculated by Kruskal Wallis non-parametric test followed by Dunn's multiple comparisons test. Each group was compared to its non-irradiated control.



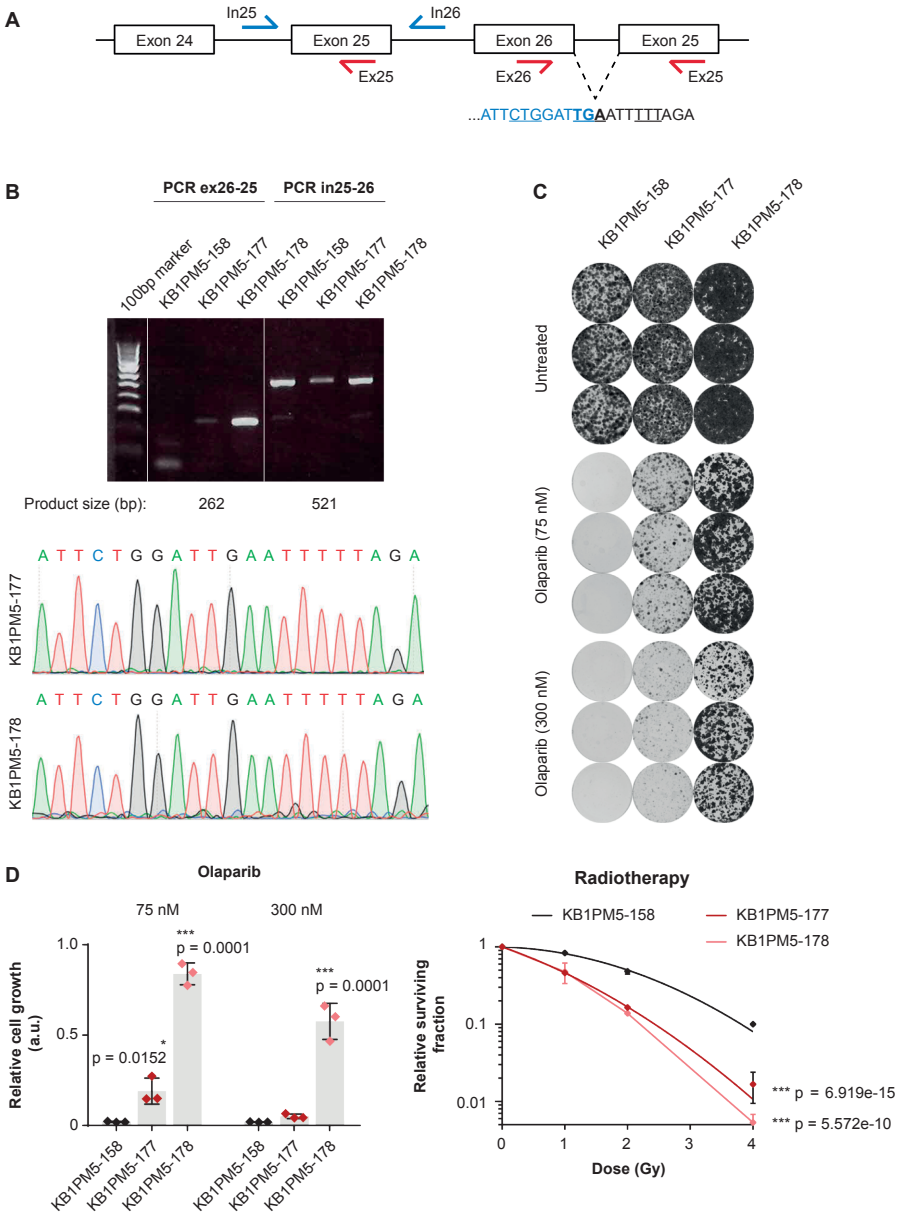

**SUPPLEMENTARY FIGURE S3 | *Trp53bp1*, *Rif1* and *Rev7* can be knocked out in KB1P-G3 tumor cells. Related to Figure 2.** *(A)* KB1P-G3 tumor cells were targeted for *Trp53bp1*, *Rif1* and *Rev7*, respectively. Corresponding target locations were amplified by PCR, submitted for Sanger sequencing and quantified by TIDE. Parental cells were used as control. *(B)* Western blot for 53BP1, RIF1 and REV7 on CRISPR/spCas9 targeted KB1P-G3 tumor cells. *(C)* Dose-response curves of parental, sgEmpty, sg*Trp53bp1* and *BRCA1*-reconstituted KB1P-G3 tumor cells treated with the PARPi olaparib or AZD2461. Cells were fixed and stained with crystal violet 10 days after plating, after which crystal violet was solubilized and measured using the Tecan spectrophotometer. *(D)* Growth curve of parental, sgEmpty, sg*Trp53bp1* and *BRCA1*-reconstituted KB1P-G3 tumor cells were measured using an Incucyte.




**SUPPLEMENTARY FIGURE S4 | 53BP1 pathway inactivation induces drug resistance in KB1P-G3 tumor cells. Related to Figure 2.** *(A)* Representative overview of clonogenic growth assay on indicated KB1P-G3 tumor cells treated with PARP inhibitors, topoisomerase inhibitors or cisplatin at the indicated doses. Cells were fixed and stained with crystal violet at the end of treatment. *(B)* Quantification of A. Crystal violet was solubilized and measured using a Tecan spectrophotometer. Data were normalized to the untreated condition and represent three independent experiments, plotted as mean ± SD. Significance was determined by ordinary one-way ANOVA with Dunnett's multiple comparison test, comparing each group to the respective KB1P-G3 parental control.




**SUPPLEMENTARY FIGURE S5 | Radiosensitization of BRCA1 deficient cells by 53BP1 depletion is dependent on DNA-PK. Related to Figure 2.** KB1P-G3 parental and sg*Trp53bp1* cell lines were plated for clonogenic survival assay upon single-dose radiotherapy treatment in the presence or absence of the DNA-PK inhibitor NU7441 (1 μM). Results are the average of two independent experiments. Plotting and quantifications were performed similar to Figure 2A.


A
In25
In26
Exon 24
Exon 25
Exon 26
Exon 25
Ex25
Ex26
Ex25
...ATTCTGGATTGAATTTTTAGA
B
PCR ex26-25
PCR in25-26
100bp marker
KB1PM5-158
KB1PM5-177
KB1PM5-178
KB1PM5-158
KB1PM5-177
KB1PM5-178
Product size (bp):
262
521
A T T C T G G A T T G A A T T T T T A G A
KB1PM5-177
A T T C T G G A T T G A A T T T T T A G A
KB1PM5-178
C
KB1PM5-158
KB1PM5-177
KB1PM5-178
Untreated
Olaparib (75 nM)
Olaparib (300 nM)
D
Olaparib
75 nM
300 nM
Relative cell growth (a.u.)
1.0
0.5
0
p = 0.0152
*
***
p = 0.0001
***
p = 0.0001
KB1PM5-158
KB1PM5-177
KB1PM5-178
KB1PM5-158
KB1PM5-177
KB1PM5-178
Radiotherapy
KB1PM5-158
KB1PM5-177
KB1PM5-178
Relative surviving fraction
1
0.1
0.01
0
1
2
3
4
Dose (Gy)
*** p = 6.919e-15
*** p = 5.572e-10

**SUPPLEMENTARY FIGURE S6 | Acquired inactivation of 53BP1 in KB1PM5 tumor-derived cell lines enhances radiosensitivity. Related to Figure 2.** *(A)* Schematic overview of the inactivating duplication event in *Trp53bp1* in an olaparib- resistant KB1PM5 tumor, adapted from (6). KB1PM5-158 was derived from the naïve tumor, whereas KB1PM5-177 and KB1PM5-178 were derived from the matched olaparib resistant tumor. Exon 25 and exon 26 are duplicated after exon 26, creating a new splice junction between exon 26-25 encoding for a stop-codon. Primers used to amplify exon 25 or duplication specific cDNA are indicated by the blue and red arrows, respectively. *(B)* PCR for exon 25 or duplication specific cDNA of *Trp53bp1*. Expected band sizes were extracted and sent for Sanger Sequencing. The duplication specific band was not observed in the naïve KB1PM5-158 cell line. *(C)* KB1PM5-158, KB1PM5- 177 and KB1PM5-178 cell lines were plated for clonogenic growth assays and were untreated or treated with olaparib at a concentration of 75 or 300 nM. The experiment was performed three times, and each independent experiment consisted of three technical replicates per condition. One representative technical replicate is shown per biological replicate. *(D)* Quantification, plotting and statistics of the olaparib response or radiotherapy response was performed as in Supplementary Figure S4B and Figure 2A, respectively.

**SUPPLEMENTARY TABLE S1 | IHC scoring for 53BP1-positive cells by two blinded observers. Related to Fig. 4D.**

| Mouse# | Treatment | Genotype | Blinded observer 1 %53BP1-Positive | Blinded observer 2 %53BP1-Positive | Average %53BP1-Positive |
|---|---|---|---|---|---|
| 1563673 | Untreated | sg*Trp53bp1* | 25 | 30 | 27.5 |
| 1563697 | Untreated | sg*Trp53bp1* | 25 | 20 | 22.5 |
| 1563698 | Untreated | sg*Trp53bp1* | 15 | 20 | 17.5 |
| 1563685 | Untreated | sg*Trp53bp1* | 20 | 30 | 25 |
| 1563695 | Untreated | sg*Trp53bp1* | 25 | 20 | 22.5 |
| 1563665 | Untreated | sg*Trp53bp1* | 30 | 30 | 30 |
| 1563668 | Untreated | sg*Trp53bp1* | 35 | 50 | 42.5 |
| 1563667 | Untreated | sg*Trp53bp1* | 10 | 10 | 10 |
| 1563709 | Untreated | sg*NT* | 75 | 90 | 82.5 |
| 1563682 | Untreated | sg*NT* | 70 | 80 | 75 |
| 1563677 | Untreated | sg*NT* | 75 | 90 | 82.5 |
| 1563705 | Untreated | sg*NT* | 75 | 80 | 77.5 |
| 1563706 | Untreated | sg*NT* | 70 | 30 | 50 |
| 1563684 | Untreated | sg*NT* | 70 | 30 | 50 |
| 1563710 | Untreated | sg*NT* | 80 | 90 | 85 |
| 1563712 | Untreated | sg*NT* | 75 | 90 | 82.5 |
| 1563674 | Radiotherapy | sg*Trp53bp1* | 45 | 70 | 57.5 |
| 1563678 | Radiotherapy | sg*NT* | 75 | 70 | 72.5 |
| 1563669 | Radiotherapy | sg*Trp53bp1* | 45 | 60 | 52.5 |
| 1563696 | Radiotherapy | sg*Trp53bp1* | 45 | 70 | 57.5 |
| 1563666 | Radiotherapy | sg*Trp53bp1* | 75 | 80 | 77.5 |
| 1563681 | Radiotherapy | sg*NT* | 80 | 100 | 90 |
| 1563680 | Radiotherapy | sg*NT* | 75 | 80 | 77.5 |
| 1563711 | Radiotherapy | sg*NT* | 80 | 90 | 85 |
| 1563672 | Radiotherapy | sg*Trp53bp1* | 45 | 50 | 47.5 |
| 1563671 | Radiotherapy | sg*Trp53bp1* | 65 | 50 | 57.5 |
| 1563670 | Radiotherapy | sg*Trp53bp1* | 80 | 90 | 85 |
| 1563675 | Radiotherapy | sg*NT* | 80 | 90 | 85 |
| 1563676 | Radiotherapy | sg*NT* | 55 | 80 | 67.5 |
| 1563679 | Radiotherapy | sg*NT* | 50 | 80 | 65 |
| 1563683 | Radiotherapy | sg*NT* | 80 | 100 | 90 |
| 1563699 | Radiotherapy | sg*Trp53bp1* | 55 | 80 | 67.5 |

*“Logic will get you from A to B,*
*imagination will take you everywhere“*

(Albert Einstein)

# Cancer Chess: Molecular Insights Into PARPi Resistance

## General Discussion and Future Perspectives

Chapter 8

## General Discussion and Future Perspectives

Personalized medicine is aimed at improving cancer treatment by defining the genetic background of a tumor and tailoring the treatment to exploit tumor-specific characteristics. However, the complexity of cancer genomes poses researchers and clinicians with the challenge to extract the information that is of clinical relevance. In addition to direct targeting of cancer cell proliferation and survival, tumors may also be targeted by exploiting the concept of synthetic lethality (SL). A synthetic lethal (SL) interaction is an interaction between two genes in which inactivation of either of the single gene has no or little effect on cell survival, whereas simultaneous inactivation of both genes is highly lethal [1-3]. While the concept of SL was first described almost a century ago, its clinical utility for cancer treatment has been long-awaited. Indeed, the initial discovery that chemical inhibition of poly(ADP-ribose) polymerase (PARP)1/2 (PARPi) is selectively toxic to cells that are defective for the double-strand break (DSB) repair mechanism homologous recombination (HR) was received with great enthusiasm as it provided a strong rationale for the targeted treatment of BRCA1/2 deficient tumors [4, 5]. Mechanistically, PARPi treatment is believed to induce one-sided DSBs upon replication fork collapse which in the absence of HR become substrates for toxic canonical non-homologous end joining (c-NHEJ), driving radial chromosome formation and ultimately cell death [4] – a model which still stands today (Fig. 1). However, despite encouraging clinical responses initially, the majority of patients are eventually faced with a recurrent tumor that has become refractory to PARPi treatment [6]. Thus, it is evident that (acquired) resistance remains a major hurdle which must be overcome to achieve long-lasting responses in more patients, even when exploiting SL genetic interactions. This unsatisfactory outcome drives the interest to map molecular mechanisms that may explain PARPi resistance with the ultimate goal to translate this knowledge into strategies that may increase PARPi efficacy in more patients. This thesis contributes to these efforts by describing the identification of several new factors that modulate PARPi sensitivity in BRCA1 deficient cells, namely DYNLL1 (Chapter 4), the Shieldin (SHLD) complex (Chapter 5) and the CTC1-STN1-TEN1 (CST) complex (Chapter 6). This thesis also describes that 53BP1 pathway inactivation creates a new treatment vulnerability in the form of radiotherapy (Chapter 7). At the same time, the study of PARPi resistance mechanisms is providing unprecedented insights in the DNA damage response.

DYNLL1, SHLD and CST were found to be linked to the 53BP1-RIF1-MAD2L2/REV7 pathway in DSB repair [7-12], a pathway that is presumed to promote repair via c-NHEJ by protecting DSB ends from resection and is normally counteracted by BRCA1 (reviewed in [13, 14]). It is well-described that inactivation of the 53BP1 pathway in BRCA1 deficient cells partially restores end resection and HR activity [15-24], providing an explanation for PARPi resistance. However, since neither 53BP1 nor RIF1 nor MAD2l2/REV7 is known to possess direct DNA binding properties, it has remained elusive how end protection may be achieved by this pathway. The identification of two novel single-stranded DNA

(ssDNA) binding complexes that function downstream in the 53BP1 pathway, SHLD and CST, provides valuable mechanistic insights: active recruitment of ssDNA binding complexes may 'shield' the DSB end from further resection. At the same time, the involvement of ssDNA binding complexes in the 53BP1 pathway raises new questions about the nature of the DSB end on which this pathway is engaged. Indeed, it hints to the generation of DSB intermediates that comprise a 3' ssDNA tail. At first sight, this seems at odds with the hitherto presumed role of 53BP1 in DSB end protection. However, this seeming paradox could also imply that 53BP1 mediated end protection is a more finely regulated process.

## 53BP1 Mediated DSB End Protection Revisited

The notion that the 53BP1 pathway facilitates c-NHEJ is supported by a number of assays that serve as a proxy for c-NHEJ activity, including IR sensitivity assays [25], plasmid

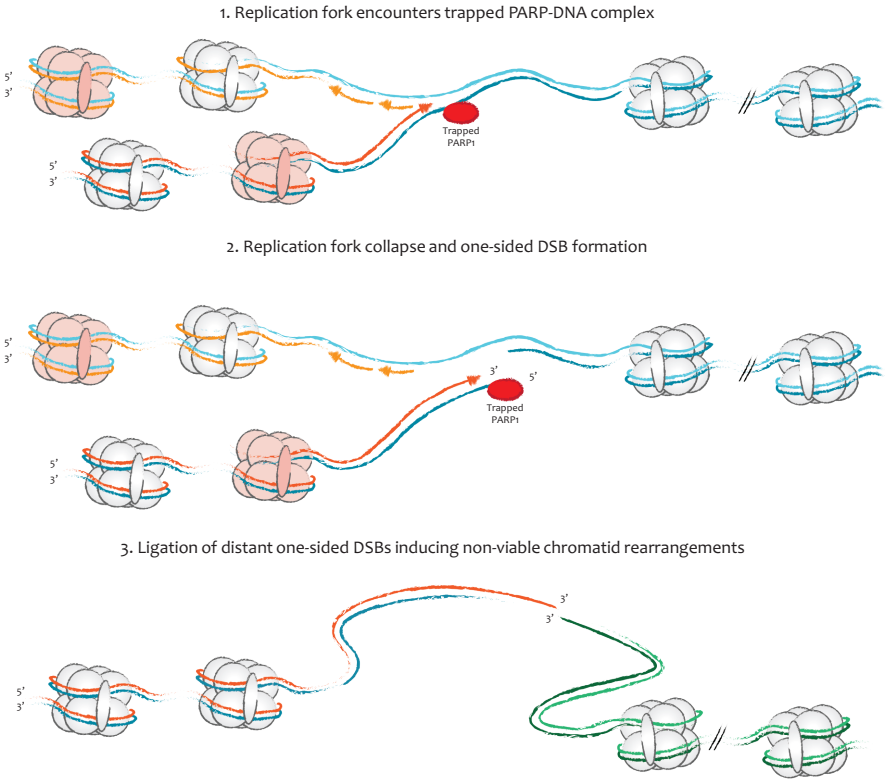



**FIGURE 1 |** Simplified model for the generation of non-viable chromatid rearrangements upon PARPi treatment in BRCA1 deficient cells. When a trapped PARP-DNA complex is encountered by a replication fork, a one-sided DSB is formed, which in the absence of BRCA1 is prone to 53BP1 pathway mediated ligation with distant one-sides DSBs.

integration assays [17], CSR assays [26, 27], and the fusion of uncapped telomeres [28]. These assays strongly rely on KU70/80, XRCC4 or LIG4 activity and 53BP1 acts epistatic with these factors. Moreover, cells in which the 53BP1 pathway is suboptimal become increasingly dependent on alternative end joining (a-EJ) pathways such as alternative non-homologous end joining (a-NHEJ) and polymerase-theta mediated end joining (TMEJ) to repair DSBs, which demonstrates that the 53BP1 pathway does not function in a-NHEJ or TMEJ [29, 30]. The observation that DSB end resection is enhanced upon 53BP1 depletion [15, 16] provides a plausible explanation for why repair may be shuttled towards these alternative repair pathways, which require ssDNA overhangs, and corroborates the hypothesis that the 53BP1 pathway facilitates c-NHEJ by inhibiting end resection.

However, several peculiarities emphasize that the 53BP1 pathway is not essential for c-NHEJ. For example, the IR sensitivity that is observed upon depletion of 53BP1 pathway factors is relatively mild compared to core c-NHEJ factors, suggesting that not all IR induced DSBs require the 53BP1 pathway for its repair ([25], this thesis). Moreover, the role of the 53BP1 pathway in other c-NHEJ driven processes such as V(D)J recombination is limited [31]. Together, these findings argue that the 53BP1 pathway acts as a positive regulator of c-NHEJ in a subset rather than in all DSB contexts, although it is unclear how this substrate is defined.

It has been shown that when DSB ends are directly compatible for end joining, c-NHEJ can be executed efficiently and proceeds primarily by the activities of KU70/80, XRCC4 and LIG4 [32]. The role of the 53BP1 pathway in the repair of blunt DSB ends or DSB ends with short overhangs (<4 nts) may thus be limited, although 53BP1 induced changes in the chromatin environment and enhancement of DSB end mobility may enhance the efficacy of the repair process [28, 33, 34]. It also seems unlikely that the ssDNA binding complexes SHLD and CST would be required for the repair of 'clean' breaks due to the limited length or absence of ssDNA overhangs. However, more complex breaks that are not amenable for direct ligation and/or contain (protein) blocks on DSB ends may require additional processing and in this context one can speculate about a role for the 53BP1 pathway and ssDNA binding complexes.

*The 53BP1 pathway at DSB ends - protection from or by resection?*

The findings described in this thesis may be incorporated in the accepted model, which proposes that an important function of the 53BP1 pathway is to regulate DSB repair pathway choice by controlling end resection. As outlined in more detail in the introduction (Chapter 1), the widespread abundance of the H4K20me2 chromatin mark primes the chromatin for rapid recruitment of 53BP1 to DSBs following ATM/MRN activation and seems consistent with such a coordinating role [35-38]. Once 53BP1 is engaged, however, rather than inducing a block to resection the role of the 53BP1 pathway may be more versatile.

It is conceptually tempting to speculate that the 53BP1 pathway may allow limited resection to proceed in a resection dependent c-NHEJ sub-pathway. This sub-pathway might resemble the slow component of c-NHEJ [39], which is LIG4 dependent and thus differs from a-NHEJ. In contrast to resection in S/G2, which requires the endonuclease activity of MRN, resection dependent c-NHEJ was previously shown to depend on the exonuclease activity of MRN and EXO1 [40]. However, it is possible that distinct DSB lesions might be subjected to endonucleolytic rather than exonucleolytic resection by MRN in G1, and a protein block (i.e. TOP2 or KU) at the DSB end has been suggested as a candidate [41-43]. Here, MRE11 initiated endonucleolytic cleavage followed by 3' – 5' resection towards the DSB end resembles MRN activity in G2 and provides a means to remove the protein block, leaving behind a free 3' ssDNA overhang in the process (Fig. 2). This scenario is analogous to the removal of covalently bound SPO11 during meiotic recombination, which also requires MRE11 nuclease activity [44, 45]. Subsequent binding of SHLD or CST could be an effective way to occlude the ssDNA tail from 5' – 3' nuclease access and/or to shorten the resected overhang by a POLA mediated fill-in reaction (discussed below). Future studies are required to unravel the precise PARPi induced DSB substrate and how it is generated. Possibly, the trapping of PARP1 on the DNA by PARPi is also processed as a protein block by MRN. The high sensitivity of BRCA1 deficient cells to both PARPi and topoisomerase inhibitors, together with the finding that 53BP1 pathway inactivation induces cross-resistance to both treatments corroborates this possibility [this thesis, [23, 46, 47]]. However, it cannot be excluded that the 3' ssDNA tail results from incomplete DNA synthesis at a collapsed replication fork or upon fork reversal [48], in which case MRN mediated resection would not be required for the loading of SHLD-CST on PARPi induced DSBs.

*The 53BP1 pathway at DSB ends – competition for the overhang?*

Although the identification of SHLD and CST may be incorporated in the accepted model of end protection by the 53BP1 pathway, a number of implications on DSB end metabolism remain obscure. Both SHLD and CST are RPA like complexes that bind ssDNA through their OB-fold domains [8, 49]. However, whilst RPA binding to ssDNA is an intermediate step in HR, SHLD-CST binding facilitates repair via c-NHEJ. How the biochemical properties of SHLD-CST binding to ssDNA compare to RPA remains to be investigated. The affinity of the heterotrimeric RPA complex for ssDNA has been shown to depend on its conformation and on the OB-fold domains that make contact with ssDNA (reviewed in [50], [51]). In its low-affinity mode, RPA binds 8-10 nucleotides of ssDNA, while 30-nts are bound per complex in its high-affinity mode. As such, RPA may progressively 'unroll' on a short ssDNA overhang. This bimodal distribution of RPA is believed to be important for the regulation of its interacting proteins (reviewed in [52]). While it is currently unknown if SHLD also adopts different conformations, this has been suggested in the literature for CST [53]. Furthermore, it has been shown that 18-nt of

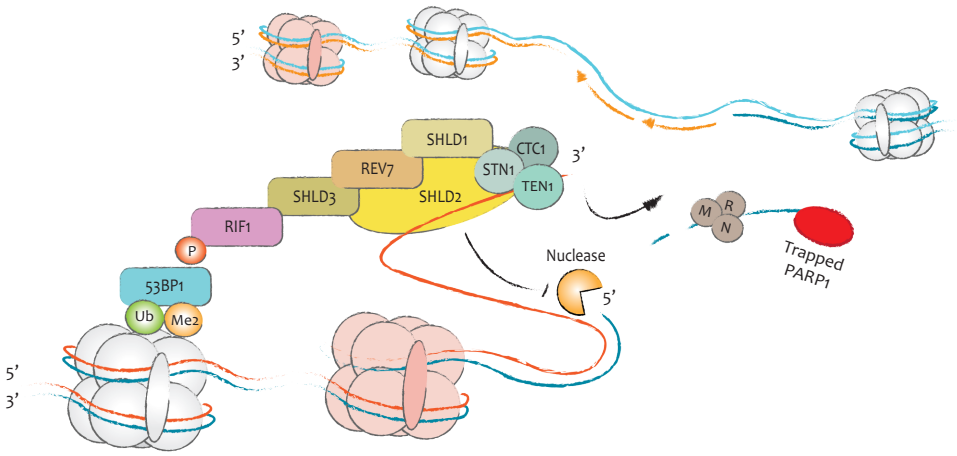



**FIGURE 2 |** A speculative model in which the MRN-mediated exonucleolytic activity followed by 3' to 5' resection towards the DSB end removes a trapped PARP-DNA complex. SHLD-CST is subsequently loaded on the 3' ssDNA tail to occlude nuclease access and thereby protect the DSB end from extensive resection.

G-rich ssDNA is sufficient for CST binding, although this sequence specificity may be diminished for longer stretches of ssDNA [49, 53, 54]. It has also been shown that CST is stabilized at the ssDNA-dsDNA junction and that a 10-nt overhang is sufficient for binding [55]. Notably, these ssDNA lengths are in the same ballpark as the ~20-35nt ssDNA overhang that is initially generated by MRE11 mediated endonucleolytic resection on blocked dsDNA ends [43, 56]. Thus, although limited, the insights into the biochemical properties of SHLD-CST binding to ssDNA may be consistent with a proposed role of the 53BP1 pathway downstream of MRN. It would be useful to learn more about the characteristics of the overhangs that engage SHLD and CST, which may help understand how the overhang is generated. Such data may also provide insights into whether SHLD is exchanged for CST, or if both complexes coexist on ssDNA overhangs.

Regardless of its generation, it seems evident that the ssDNA overhang can in principle be bound by both RPA and SHLD-CST, implying a direct competition between these protein complexes for ssDNA binding. The relatively low abundance of SHLD and CST suggests that these complexes require the 53BP1 pathway for efficient loading on resected DNA. Thereby, active recruitment further distinguishes SHLD-CST from RPA. Upon DNA binding, it is possible that the subsequent antagonizing effect of SHLD-CST on end resection is explained solely by steric hindrance of resection nucleases. However, additional consequences on DNA repair cannot be excluded as ssDNA-RPA has been shown to activate ATR signaling [57, 58]; terminate EXO1 mediated resection [59]; and is exchanged for RAD51 during HR [60, 61]. Future work is required to investigate if these processes are affected by SHLD-CST coated ssDNA.

*The 53BP1 pathway at DSB ends – is POLA involved?*

It is noteworthy that while SHLD and CST could be expected to act redundantly in the processes described above, depletion of either SHLD or CST alone is sufficient to inactivate the 53BP1 pathway [7-12]. This dual requirement for the ssDNA binding complexes SHLD and CST in modulating end protection is enigmatic. The finding that CST is recruited to DSB ends by SHLD [12] suggests that CST might perform a function that cannot be executed by SHLD alone. The previously described activities of CST in other DNA contexts provide food for thought to speculate on such function. The preference of CST for binding G-rich DNA and its demonstrated ability to unfold G-quadruplexes [55, 62] raise the possibility that CST aids SHLD specifically in the protection of G-rich ssDNA. This would imply that the requirement for CST is sequence dependent, providing a testable hypothesis. Alternatively, the recognition of the ssDNA-dsDNA junction by CST [55] may aid in coordinating end capture or in providing a tighter restriction against resection nucleases. However, a more exciting hypothesis stems from the described role of CST at resected telomeres, where it recruits POLA to mediate a fill-in reaction as a way to buffer resection length and thereby limit telomere erosion [63]. This would extend the analogy between end protection at telomeres by shelterin and at DSB ends by shieldin [8]. Interestingly, resection at telomeres is mediated by EXO1 [63], demonstrating that POLA has the capacity to counteract substantially resected telomeric ends. Although the evidence that CST mediates a similar reaction at resected DSB ends is limited [12], it may provide the most appealing explanation for the requirement of CST beyond SHLD (Fig. 3). Indeed, the ability of CST to bind ssDNA substrates dynamically and to recognize the ssDNA-dsDNA junction seems most appropriate for mediating a fill-in reaction via sequential extension [55].

The prospect of active fill-in at resected DSB ends certainly warrants further investigation as it could invoke a paradigm shift. Depending on the processivity – i.e. whether fill-in is limited to the terminal nucleotides or if it may proceed over longer distances – initiation of long-range end resection might be a reversible process and commitment to HR repair might be revoked by active fill-in. Similarly, it raises the possibility that the length of the 3' overhang may be buffered by POLA mediated fill-in synthesis during end resection. Capturing this process *in vivo*, however, is challenging due to the error-free nature of fill-in. Hence, differentiation between a sequence that has never been resected versus a sequence that has been resected and subsequently filled-in is problematic, at least on the sequence level. The essential role of POLA in lagging-strand replication further complicates experiments directed at demonstrating a role of POLA at DSB ends. Fiddling with POLA activity may not be tolerated by cells, and care must be taken to separate fill-in synthesis during DSB repair from fill-in during replication. Conducting experiments in arrested cells, or using mutants that impair POLA binding to CST [64] may provide a solution to circumvent these issues.

If fill-in of resected DSB ends can be unequivocally demonstrated, the next question that arises is how these filled-in ends are subsequently processed. It seems unlikely that the RNA primer from which a fill-in reaction is initiated invariably binds the terminus of the ssDNA overhang; hence the fill-in reaction possibly leaves behind an ssDNA overhang that is too short to initiate a new round of fill-in. Furthermore, the faith of the RNA primer requires further study. Since the majority of 53BP1 driven DSB substrates require LIG4 for their repair, it is tempting to believe that LIG4 is ultimately responsible for the ligation of filled-in ends. This is compatible with the observation that LIG4 retains activity on DSB ends with short overhangs [32]. A possible physiological role for 53BP1-RIF1-SHLD-CST-POLA could thus be to allow the removal of end blocking lesions through MRN mediated resection, whilst protecting these ends from engaging long-range resection and simultaneously mediating fill-in synthesis to channel repair through c-NHEJ. Future studies are required to determine if fill-in indeed occurs at DSBs, which DSB substrate is amenable for fill-in, and how a filled-in DSB end is subsequently processed.

*The 53BP1 pathway at DSB ends – convergence with other DSB repair pathways on ssDNA?*

The finding that the 53BP1 pathway acts on DSB substrates that entail an ssDNA tail also raises new questions for the regulation of DSB repair pathway choice. DSB repair pathway choice is commonly referred to as the choice between NHEJ and HR, depending on whether end resection is initiated or not. The finding that a short ssDNA tail may be the actual substrate that is protected from extensive resection by the 53BP1 pathway raises the possibility that this pathway competes with polymerase theta (POLQ).

POLQ was recently described to join 3' ssDNA overhangs that share ≥2 bp homology at or near the break end, by using these overhangs as a template for DNA synthesis (extensively reviewed in [65]). This activity is prone to generate deletions with microhomology and templated insertions, making TMEJ an intrinsically mutagenic repair pathway. The possibility that 53BP1 and POLQ act on the same DSB substrate is supported by the observation that 53BP1 and POLQ are synthetic lethal [30]. Moreover, c-NHEJ and TMEJ function synergistically in response to IR [66]. Thus, c-NHEJ and TMEJ are each exclusively involved in the repair of a subset of DSBs, while acting redundantly on others. This may be interpreted such that POLQ is able to take over the repair of at least a subset of DSB ends that would otherwise have been repaired via the 53BP1 pathway. Since repair via the 53BP1 pathway appears to ultimately require LIG4 rather than POLQ for completion, this may implicate that the 53BP1 pathway somehow obstructs the engagement of POLQ. How this may be achieved, however, is puzzling, since the helicase domain of POLQ has been shown to facilitate the removal of RPA from ssDNA overhangs [67] and thus may similarly be able to strip off SHLD-CST. Perhaps the anchor to 53BP1-RIF1 sufficiently enforces SHLD-CST protection of ssDNA such that POLQ is disfavored in the presence of 53BP1.

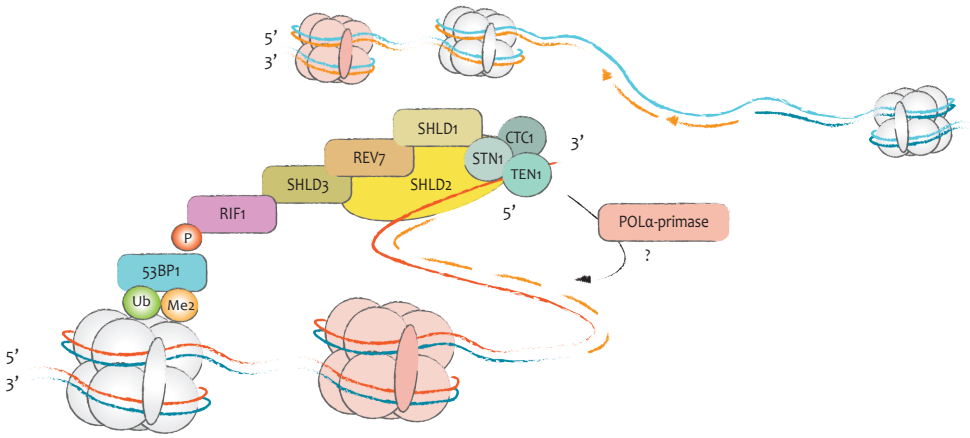



**Figure 3 |** POLA mediated fill-in synthesis may further reduce the length of the 3' ssDNA tail to allow ligation via LIG4.

Interestingly, TMEJ has also been shown to be essential for the survival of cells in which HR is compromised [68, 69]. The finding that BRCA1 deficient tumors are characterized by genetic scars that are typical for TMEJ activity provides a solid case for its significance [70]. It is hypothesized that TMEJ is required to rescue cells from toxic DSB repair intermediates that are generated when HR is initiated but cannot be completed [65, 71]. Similar to the 53BP1 pathway, this implies that the HR pathway may somehow preclude POLQ from acting on its substrate.

Together, these studies hint towards a potential competition between TMEJ, c-NHEJ and HR. How the engagement of these pathways is coordinated remains to be investigated.

*The 53BP1 pathway at DSB ends – an inconvenient observation*

Throughout this thesis, 3D organoid technology was used to evaluate the effect of genetic depletion of the 53BP1 pathway on PARPi response in BRCA1 deficient mouse mammary tumors. Hereby, previous data on 53BP1 and REV7/MAD2L2 were confirmed, and it was demonstrated for the first time that loss of RIF1, DYNLL1, SHLD or CST drives PARPi resistance *in vivo* (this thesis). The tumor data for 53BP1, RIF1 and REV7/MAD2L2 were generated in the same experiment and therefore resemble a direct isogenic comparison (Chapter 3 - addendum). Interestingly, genetic depletion of different 53BP1 pathway members showed different potencies in driving PARPi resistance. Although a technical explanation cannot be excluded, it is peculiar that the time before resistant tumors emerged matched the hierarchy of the 53BP1 pathway. Indeed, PARPi treated mice bearing 53BP1 depleted tumors had a median survival of only 8 days, which did not differ significantly from tumor-bearing mice that were left untreated. PARPi treated mice bearing RIF1 depleted tumors had a significantly longer median survival of

25 days, whereas PARPi treated mice with REV7/MAD2l2 depleted tumors had an even longer median survival of approximately 41 days. Although it remains unclear how these differences should be interpreted, it could be that loss of these downstream factors is not fully epistatic with loss of 53BP1. Perhaps the physical presence of 53BP1 also interferes with HR directly, even when the downstream pathway members are depleted. Alternatively, 53BP1 might perform RIF1 independent functions that influence PARPi toxicity. This is not unlikely, since 53BP1 has been described to enhance chromatin mobility [33, 34] and additional effector proteins have been identified, including PTIP [18, 72].

PTIP forms the other known branch of the 53BP1 pathway [18, 72]. Even though PTIP has been implicated in the 53BP1 pathway for several years and is also thought to stimulate DSB end protection, its precise role is still poorly understood. Moreover, besides its role in DSB end protection, PTIP has been shown to regulate replication fork (RF) stability in an MLL3/4-CHD4-MRE11 dependent manner [73]. In the model proposed by Chaudhuri et al., the collision of a replication fork with trapped PARP-DNA causes fork stalling. Stalled forks are normally protected from degradation by BRCA1/2 [74, 75], but become substrates for MRE11 mediated degradation of the nascent strands in the absence of BRCA1/2. Loss of PTIP was shown to rescue RFs from MRE11 mediated degradation by preventing MRE11 recruitment to stalled RFs [73]. RF protection by PTIP loss was sufficient to induce resistance to therapeutics that cause RF stalling (such as PARPi) in BRCA1 /2 deficient cells, without restoring HR. In light of the observation that 53BP1 depletion may be more potent *in vivo* than depletion of the downstream factors of the RIF1 branch, it would be interesting to test if dual depletion of the RIF1- and PTIP axis recapitulates the full extent of 53BP1 depletion on PARPi resistance *in vivo*. Admittedly, the plethora of genome-wide CRISPR screens for PARPi resistance adequately picked up the RNF8-RNF168-53BP1-RIF1-REV7-SHLD-CST pathway [8, 9, 11], while the PTIP axis was conspicuous by its absence. Direct testing of two PTIP targeting sgRNAs in KB1P and KB2P mammary tumor cell lines also did not show a notable effect on PARPi sensitivity *in vitro*, although it must be noted that these sgRNAs were not validated for protein knockout (data not shown). Certainly, the extent to which PTIP loss and/or replication fork protection contributes to PARPi resistance requires further study.

Whilst the components of the 53BP1 pathway seem set with the identification of the SHLD and CST complexes, it is clear that several questions regarding its spatiotemporal regulation and its precise substrate remain to be addressed.

## On the Origin of PARPi Induced DSBs

The prevailing model for PARPi induced toxicity holds that DSBs are formed when replication forks collide with trapped PARP1-DNA complexes, resulting in replication fork stalling and collapse. However, the model of fork stalling and fork collapse has been challenged by Maya-Mendoza et al., who rather proposed that PARPi accelerates

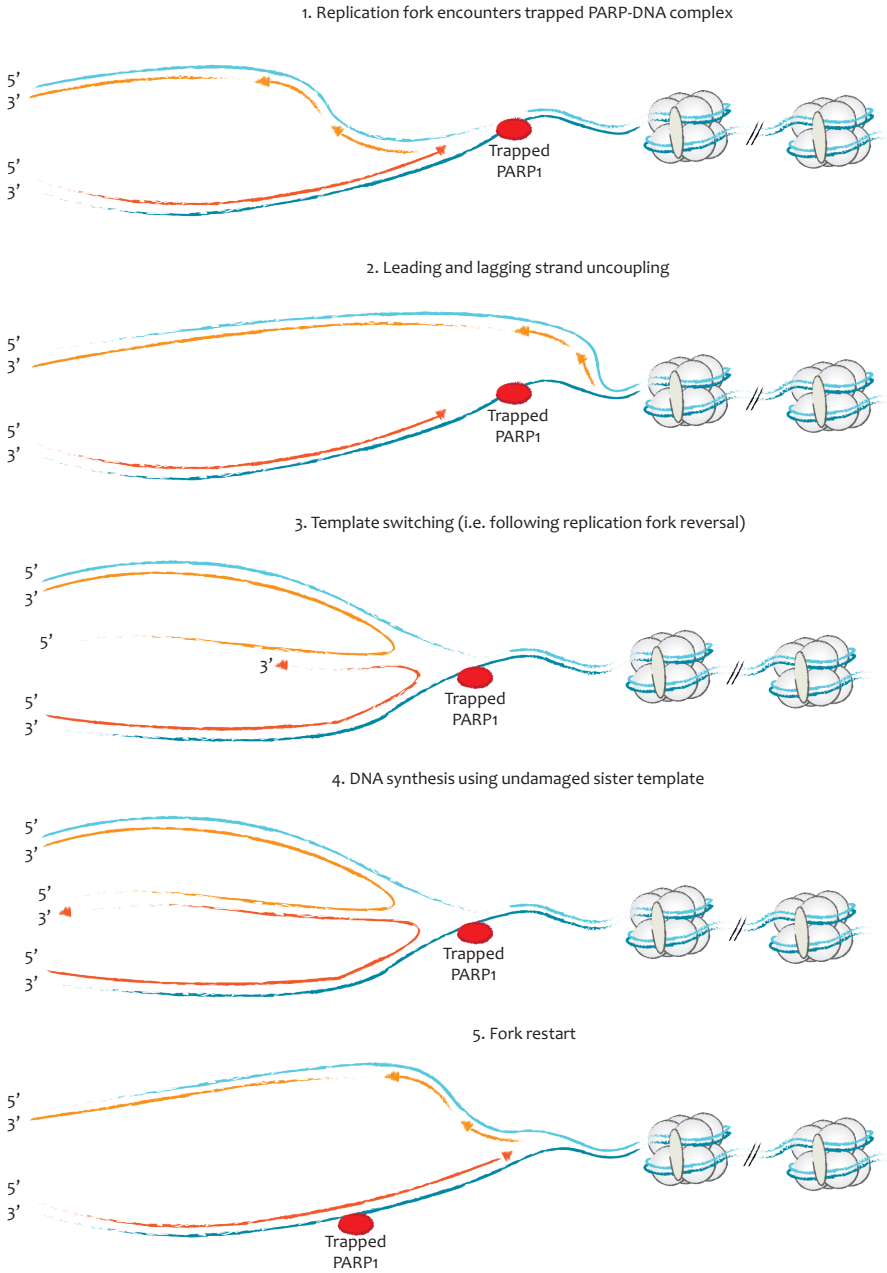



**FIGURE 4 |** a hypothetical model for template switching to continue replication upon collision of a replication fork with a PARP-DNA complex. Uncoupling of the leading and the lagging strand followed by fork stabilization and template switching might allow the use of the nascent strand as a template for replication.

replication fork progression and that cells accumulate ssDNA gaps as a result [76]. Unfortunately, the authors have not attempted to unify their model with existing data on the 53BP1-BRCA1 interaction. Indeed, the strong influence of the 53BP1 pathway on the PARPi response in BRCA1 deficient cells is adequately explained by the formation of PARPi induced DSBs, presumably resulting from fork collapse. Moreover, PARPi resistance in BRCA1/2 deficient cells due to restoration of replication fork stability was explained by the generation of a reversed fork intermediate upon PARPi treatment [73]. If PARPi treatment does not lead to fork reversal and/or collapse [76], alternative explanations for the 53BP1-BRCA1 interaction on PARPi sensitivity must be found. Moreover, the possibility that ssDNA gaps induce fork collapse in the next round of replication has not been investigated, which would only be a minor deviation from the accepted model. The study is also subject to certain limitations, as the experiments were performed under high concentrations of PARPi (10 µM), while PARPi toxicity in BRCA1/2 deficient cells is already observed in the nM range – a dose at which Maya-Mendoza et al. describe no effect on fork speed [76]. Moreover, a 10 µM concentration of the PARPi olaparib was previously shown to release the PARP mediated break on RECQ1 mediated fork restart, providing an alternative explanation for the finding that PARPi accelerates fork progression [48, 77]. Lastly, Maya-Mandoza et al. describe that accelerated elongation was dependent on the p21-p53 axis, which is known to be impaired in the majority of BRCA1/2 deficient tumors. Therefore, the relevance of these findings for the clinical utility of PARPi requires further study.

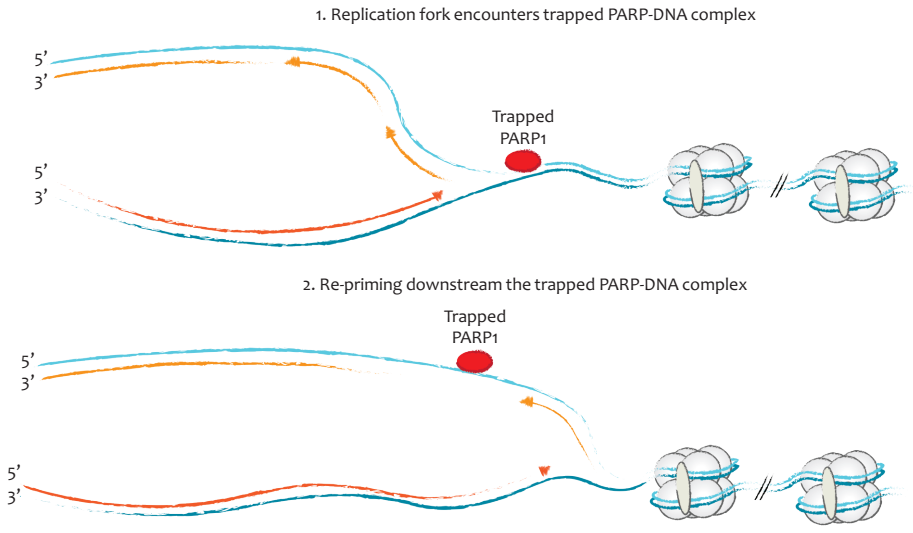



**FIGURE 5 |** a hypothetical model for re-priming downstream a trapped PARP-DNA complex as a way to avoid replication fork collapse.

The previous section illustrates the poor understanding of the cellular response that is initiated when a replication fork encounters a trapped PARP1-DNA complex. Besides the possibility of fork reversal and/or collapse, it is unclear if the replication machinery may be able to replicate past PARP1-DNA complexes by the use of template switching (Fig. 4). Collision of an ongoing replication fork with a PARP1-DNA complex might result in leading-lagging strand uncoupling. Thereby, replication might continue on the undamaged strand. Although not absolutely required for the model, the exposure of ssDNA on the damaged strand could trigger fork reversal to stabilize the replication fork. DNA synthesis might subsequently continue using the nascent strand as a template, after which the fork could be restarted to proceed with replication. This process might also explain how increased fork stabilization leads to chemoresistance in HR deficient cells. Similarly, it would be interesting to investigate if re-priming downstream of PARP1-DNA complexes occurs as it would allow replication to proceed at the expense of ssDNA gaps (Fig. 5). Interestingly, replication fork uncoupling and re-priming would both lead to increased levels of ssDNA gaps [76]. At the same time, it is questionable if such strategies are viable in the long-term since the PARP1-DNA complex is not removed and thus continues to pose a barrier for transcription and replication.

## Checking in on PARPi

In the last decade, a number of mechanisms have been described that may affect the responsiveness of tumors to PARPi treatment. Functional restoration of the genetic alteration underlying the HR defect and PARPi sensitivity is a major resistance mechanism and remains the only clinically validated mechanism to date (reviewed in [6]). A surprising number of ways by which this is achieved in tumor cells have been described (reviewed in Chapter 2 [78]).

In case functional restoration of BRCA1 is not possible (e.g. due to large, irreversible deletions as is the case in the BRCA1 deficient mouse tumor model that was used throughout this thesis), disruption of the 53BP1 pathway appears to be a dominant route to PARPi resistance. The absence of clinical data has thus far precluded full validation of the mechanisms described in this thesis, although the existence of disruptive mutations in 53BP1 and REV7/MAD2L2 has been identified in breast explants [79]. These explants were derived from BRCA1 germline mutation carriers and were refractory to PARPi treatment when transplanted in mice; however, a causal relation cannot be confirmed.

Restoration of HR via BRCA1/2 re-expression or disruption of the 53BP1 pathway is not the only route to resistance that has been described. PARPi resistance may also occur independently of HR restoration, for example due to replication fork protection [73]. Additionally, certain PARP inhibitors, such as olaparib (Lynparza) were found to be a substrate for the drug efflux-transporter MDR1 [80]. Overexpression of MDR1 reduces intracellular levels of these drugs, thereby alleviating toxicity. Although this was found to be a prominent resistance mechanism in mouse models, clinical

indications of this mechanism occurring in patients remain limited. The most compelling evidence comes from the finding that approximately 8% of chemoresistant high-grade serous carcinoma had upregulated MDR1 [81, 82]. However, it is not known if this was causal for the lack of response, nor that MDR1 was specifically upregulated by PARPi treatment since these tumors were heavily pre-treated. Finally, the drug target of PARPi may also be modulated. Indeed, it was shown that PARP1 depletion alleviates PARPi toxicity in wildtype and BRCA1 deficient cells [83, 84]. PARPi cytotoxicity can also be relieved by depleting PAR glycohydrolase (PARG) [85], the enzyme responsible for degrading PAR chains. Hereby, the residual catalytic activity of PARP1 is thought to be sufficient to mediate the recruitment of downstream DDR factors and to mediate its release from the DNA in the presence of PARPi. Collectively, these and future studies will provide a 'roadmap' of routes that tumors follow to alleviate PARPi toxicity. The next step will be to capitalize on this knowledge by identifying new treatment options for resistant tumors.

*From bench to bedside*

Since resistance mechanisms evolve to provide a survival advantage in the presence of therapy pressure, this may be accompanied by a fitness cost in other settings [86, 87]. The existence of such an acquired vulnerability or Achilles' heel in PARPi resistant clones that have inactivated the 53BP1 pathway is described in Chapter 7 [9, 46]. Resistance to PARPi came at the cost of an enhanced sensitivity to IR, which could be exploited to deplete these PARPi resistant cells from mouse tumors *in vivo* (Fig. 6) [46]. Thus, radiotherapy may be effective in such cases. Similar studies need to be employed for each known mechanism of resistance in order to provide actionable solutions to combat resistant tumors.

The identification of new vulnerabilities in resistant tumors also advocates that the molecular cause of resistance must be evaluated in the clinic. Hereto, carefully designed studies are required that directly compare each resistant tumor to its matched treatment-naïve counterpart. Ideally, these matched tumors are compared on the genetic level to pinpoint the alteration(s) that may be causal for resistance. Hopefully, these and equivalent studies will provide sufficient incentive to address the lack of clinical validation in the future.

*Hypothesis-driven questions for the clinic*

Several propositions follow from the resistance mechanisms that have been described. Certain HR deficient/PARPi sensitive genetic backgrounds might be more prone to developing resistance than others. This can be deduced from the number of resistance mechanisms that accompany each gene defect. For example, loss of the 53BP1 pathway renders BRCA1 deficient cells resistant to PARPi, thus providing a number of genes that

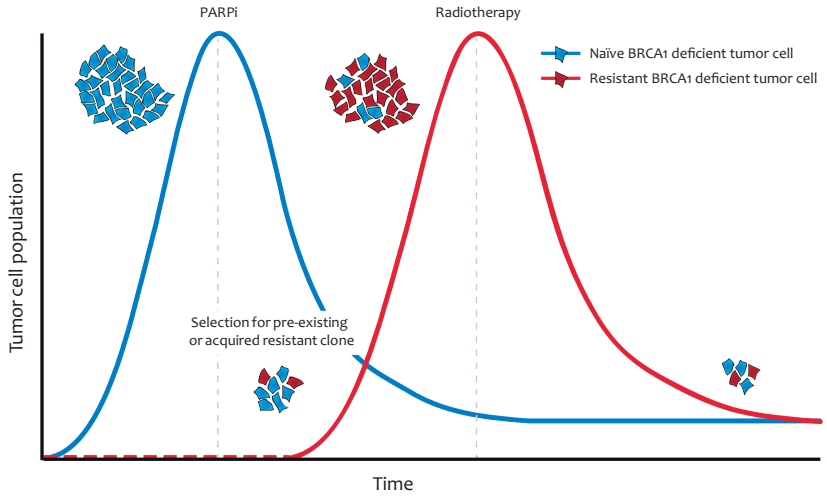



**FIGURE 6 |** Certain resistance mechanisms might expose a new treatment vulnerability which can be therapeutically exploited. For example, loss of the 53BP1 pathway renders BRCA1 deficient cells resistant to PARPi leading to their enrichment. These cells may subsequently be depleted from the population by radiotherapy.

may induce synthetic viability when inactivated. However, these same genes have no effect on BRCA2 deficient cells. Therefore, BRCA1 deficient tumors might have more options to acquire resistance and therefore might show a less durable response to PARPi. Similarly, ATM mutations induce PARPi sensitivity, but this is alleviated when members of the c-NHEJ pathway or the BRCA1-A complex are inactivated [88]. This shows that resistance mechanisms may vary per genetic background. Therefore, the ongoing efforts to evaluate PARPi efficacy in other HR deficient backgrounds should be met with, ideally saturating, screens to pinpoint the genetic contexts that rescue the synthetic lethal interaction with PARPi. This becomes more complex if an HR defect can be implied on the basis of a BRCAness "scar", while no causal gene disruption can be identified [70]. Thus, besides testing whether such tumors are responsive to PARPi treatment, it will be pivotal to eventually pinpoint the underlying cause of the HR defect and to investigate which mechanisms may rescue its SL interaction with PARPi.

Not only alterations in different HR genes might affect PARPi efficacy; different mutations in the same HR gene may also affect the outcome. Mutations in essential domains could be expected to carry a lower potential for functional restoration by secondary mutations, since large in-frame deletions would render the protein non-functional and thereby preclude these events from driving resistance. Although it remains speculative if specific mutations indeed influence clinical outcome, it has been described that BRCA1null alleles cause embryonic lethality at E7.5-9.5, whilst C-terminal truncating BRCA1 mutations show delayed lethality at E9.5-E10.5 [89]. Similarly, it has been shown that a subset of inactivating mutations in BRCA1 or BRCA2 can be

by-passed with splice-variants that possess hypomorphic activity [90-93]. Inactivating events that cause synthetic viability may also depend on the expression of such allelic variants. This is most evident from PARP1 inactivation as a means to alleviate the toxicity by PARP trapping, which is tolerated if cells possess residual BRCA1 activity [84]. A dependency on BRCA1-Δ11q expression was recently also described for 53BP1 pathway inactivation [94]. However, this finding warrants further study as 53BP1 pathway inactivation potently induced resistance in the KB1P mouse model, which develops mammary tumors that lack Brca1 exons 5-13 and do not express BRCA1-Δ11q [8, 11, 22, 23, 47]. Regardless, the existence of allelic variants must be considered if we are to fully understand the genetic network that determines PARPi sensitivity.

*An alternative strategy to enhance PARPi efficacy*

An interesting new angle to PARPi was provided by the recent finding that BRCA1/2 deficient tumors are prone to activating the cGAS-STING pathway [95, 96]. This pathway normally functions as an antiviral defense mechanism by activating the immune system in response to cytosolic dsDNA of viral origin [97, 98]. It was found that this pathway is also triggered by cytoplasmic dsDNA arising from faulty mitosis, which may be enhanced in HR deficient tumors due to their genomic instability [95]. The use of PD-L1 and CTLA4 immune-checkpoint inhibitors (ICI) might work synergistically in this context by unleashing cytotoxic T-cells to boost immune cell activity against tumor cells. Not mutually exclusive, tumors with unstable genomes might be more likely to create neo-antigens, which could subsequently elicit an immune response. This may be boosted further by treatment, and PARPi seem ideal for this task as they have few side effects and are likely to be more tumor-specific than conventional chemotherapy [99-101]. This concept is supported by the observation that PD-1/PD-L1 activation limits the activity of PARPi in HR deficient mouse tumors, which can be diminished by co-administration of a PD-L1 inhibitor with PARPi [100]. Furthermore, preclinical work using the KB1P transplantation model has shown that PARPi treatment enhances the activation of the cGAS/STING pathway, triggering cytotoxic CD8+ T-cell recruitment and an antitumor immune response [101]. It was further demonstrated that this response was more pronounced in BRCA deficient cells compared to BRCA proficient cells, which is significant from a translational perspective. These prospects have drawn PARPi therapy closer to the field of immunotherapy, which has already achieved promising clinical responses for several tumor types [102]. Indeed, the clinical utility of combinations of PARPi with ICI is currently being investigated in several clinical trials [103]. The notion that the immune system may eradicate genomically unstable tumor cells also predicts that immune-modulation may play a role in PARPi resistance and this certainly calls for further study. Here, genetically engineered mouse models may provide a shortcut to test the role of the immune system in modulating PARPi response. In this respect, it is

intriguing that a matched treatment-naïve and treatment-resistant KB1P tumor-derived organoid model did not recapitulate PARPi resistance *in vitro* but maintained resistance *in vivo*, indicating that PARPi resistance in this tumor may be driven by a cancer cell-extrinsic mechanism (Chapter 3). Although many explanations for this discrepancy could be pursued, an obvious difference between *in vitro* and *in vivo* culture systems is the lack of an immune system. Perhaps it is not that the resistant organoid model does not recapitulate its resistance *in vitro*, but that the naïve organoid model does not recapitulate its sensitivity *in vitro*. Perhaps *in vivo* the naïve tumor cells are efficiently eradicated by the immune system upon PARPi treatment. A straightforward experiment would be to test the response of these matched models in NMRI/Nude mice, which lack a cytotoxic T-cell response. If this hypothesis were true one would predict to observe no differences in PARPi response between this naïve and resistance organoid model in athymic NMRI/Nude mice. In line with this thought, Pantelidou et al. indeed observed an enhanced antitumor response upon PARPi treatment when KB1P tumor pieces were engrafted in syngeneic FVB mice compared to immunodeficient SCID mice [101].

***Although it is clear that PARPi may not immediately put the tumor in checkmate, the game of chess is far from over.***

## References


1. Kaelin WG, Jr. The concept of synthetic lethality in the context of anticancer therapy. Nature reviews Cancer. 2005; 5: 689-98.
2. Dobzhansky T. Genetics of natural populations; recombination and variability in populations of Drosophila pseudoobscura. Genetics. 1946; 31: 269-90.
3. Hartwell LH, Szankasi P, Roberts CJ, Murray AW, Friend SH. Integrating genetic approaches into the discovery of anticancer drugs. Science. 1997; 278: 1064-8.
4. Farmer H, McCabe N, Lord CJ, Tutt ANJ, Johnson DA, Richardson TB, et al. Targeting the DNA repair defect in BRCA mutant cells as a therapeutic strategy. Nature. 2005; 434: 917.
5. Bryant HE, Schultz N, Thomas HD, Parker KM, Flower D, Lopez E, et al. Specific killing of BRCA2-deficient tumours with inhibitors of poly(ADP-ribose) polymerase. Nature. 2005; 434: 913-7.
6. Lord CJ, Ashworth A. PARP inhibitors: Synthetic lethality in the clinic. Science. 2017; 355: 1152-8.
7. Gupta R, Somyajit K, Narita T, Maskey E, Stanlie A, Kremer M, et al. DNA Repair Network Analysis Reveals Shieldin as a Key Regulator of NHEJ and PARP Inhibitor Sensitivity. Cell. 2018; 173: 972-88.e23.
8. Noordermeer SM, Adam S, Setiaputra D, Barazas M, Pettitt SJ, Ling AK, et al. The shieldin complex mediates 53BP1-dependent DNA repair. Nature. 2018.
9. Dev H, Chiang TW, Lescale C, de Krijger I, Martin AG, Pilger D, et al. Shieldin complex promotes DNA end-joining and counters homologous recombination in BRCA1-null cells. Nature cell biology. 2018; 20: 954-65.
10. Ghezraoui H, Oliveira C, Becker JR, Bilham K, Moralli D, Anzilotti C, et al. 53BP1 cooperation with the REV7-shieldin complex underpins DNA structure-specific NHEJ. Nature. 2018; 560: 122-7.
11. Barazas M, Annunziato S, Pettitt SJ, de Krijger I, Ghezraoui H, Roobol SJ, et al. The CST Complex Mediates End Protection at Double-Strand Breaks and Promotes PARP Inhibitor Sensitivity in BRCA1-Deficient Cells. Cell Rep. 2018; 23: 2107-18.
12. Mirman Z, Lottersberger F, Takai H, Kibe T, Gong Y, Takai K, et al. 53BP1–RIF1–shieldin counteracts DSB resection through CST- and Polα-dependent fill-in. Nature. 2018.
13. Panier S, Boulton SJ. Double-strand break repair: 53BP1 comes into focus. Nature reviews Molecular cell biology. 2014; 15: 7-18.
14. Zimmermann M, de Lange T. 53BP1: pro choice in DNA repair. Trends in Cell Biology. 2014; 24: 108-17.

15. Bouwman P, Aly A, Escandell JM, Pieterse M, Bartkova J, van der Gulden H, et al. 53BP1 loss rescues BRCA1 deficiency and is associated with triple-negative and BRCA-mutated breast cancers. Nat Struct Mol Biol. 2010; 17: 688-95.
16. Bunting SF, Callen E, Wong N, Chen HT, Polato F, Gunn A, et al. 53BP1 inhibits homologous recombination in Brca1-deficient cells by blocking resection of DNA breaks. Cell. 2010; 141: 243-54.
17. Escribano-Diaz C, Orthwein A, Fradet-Turcotte A, Xing M, Young JT, Tkac J, et al. A cell cycle-dependent regulatory circuit composed of 53BP1-RIF1 and BRCA1-CtIP controls DNA repair pathway choice. Mol Cell. 2013; 49: 872-83.
18. Callen E, Di Virgilio M, Kruhlak MJ, Nieto-Soler M, Wong N, Chen HT, et al. 53BP1 mediates productive and mutagenic DNA repair through distinct phosphoprotein interactions. Cell. 2013; 153: 1266-80.
19. Chapman JR, Barral P, Vannier JB, Borel V, Steger M, Tomas-Loba A, et al. RIF1 is essential for 53BP1-dependent nonhomologous end joining and suppression of DNA double-strand break resection. Mol Cell. 2013; 49: 858-71.
20. Di Virgilio M, Callen E, Yamane A, Zhang W, Jankovic M, Gitlin AD, et al. Rif1 prevents resection of DNA breaks and promotes immunoglobulin class switching. Science. 2013; 339: 711-5.
21. Zimmermann M, Lottersberger F, Buonomo SB, Sfeir A, de Lange T. 53BP1 regulates DSB repair using Rif1 to control 5' end resection. Science. 2013; 339: 700-4.
22. Xu G, Chapman JR, Brandsma I, Yuan J, Mistrik M, Bouwman P, et al. REV7 counteracts DNA double-strand break resection and affects PARP inhibition. Nature. 2015; 521: 541-4.
23. Jaspers JE, Kersbergen A, Boon U, Sol W, van Deemter L, Zander SA, et al. Loss of 53BP1 causes PARP inhibitor resistance in Brca1-mutated mouse mammary tumors. Cancer discovery. 2013; 3: 68-81.
24. Boersma V, Moatti N, Segura-Bayona S, Peuscher MH, van der Torre J, Wevers BA, et al. MAD2L2 controls DNA repair at telomeres and DNA breaks by inhibiting 5' end resection. Nature. 2015; 521: 537-40.
25. Nakamura K, Sakai W, Kawamoto T, Bree RT, Lowndes NF, Takeda S, et al. Genetic dissection of vertebrate 53BP1: a major role in non-homologous end joining of DNA double strand breaks. DNA repair. 2006; 5: 741-9.
26. Manis JP, Morales JC, Xia Z, Kutok JL, Alt FW, Carpenter PB. 53BP1 links DNA damage-response pathways to immunoglobulin heavy chain class-switch recombination. Nature immunology. 2004; 5: 481-7.
27. Ward IM, Reina-San-Martin B, Olaru A, Minn K, Tamada K, Lau JS, et al. 53BP1 is required for class switch recombination. The Journal of cell biology. 2004; 165: 459-64.
28. Dimitrova N, Chen YC, Spector DL, de Lange T. 53BP1 promotes non-homologous end joining of telomeres by increasing chromatin mobility. Nature. 2008; 456: 524-8.
29. Bothmer A, Robbiani DF, Feldhahn N, Gazumyan A, Nussenzweig A, Nussenzweig MC. 53BP1 regulates DNA resection and the choice between classical and alternative end joining during class switch recombination. The Journal of experimental medicine. 2010; 207: 855-65.
30. Wyatt David W, Feng W, Conlin Michael P, Yousefzadeh Matthew J, Roberts Steven A, Mieczkowski P, et al. Essential Roles for Polymerase θ-Mediated End Joining in the Repair of Chromosome Breaks. Molecular Cell. 2016; 63: 662-73.
31. Difilippantonio S, Gapud E, Wong N, Huang CY, Mahowald G, Chen HT, et al. 53BP1 facilitates long-range DNA end-joining during V(D)J recombination. Nature. 2008; 456: 529-33.
32. Chang HHY, Watanabe G, Gerodimos CA, Ochi T, Blundell TL, Jackson SP, et al. Different DNA End Configurations Dictate Which NHEJ Components Are Most Important for Joining Efficiency. The Journal of biological chemistry. 2016; 291: 24377-89.
33. Lottersberger F, Bothmer A, Robbiani DF, Nussenzweig MC, de Lange T. Role of 53BP1 oligomerization in regulating double-strand break repair. Proceedings of the National Academy of Sciences of the United States of America. 2013; 110: 2146-51.
34. Lottersberger F, Karssemeijer Roos A, Dimitrova N, de Lange T. 53BP1 and the LINC Complex Promote Microtubule-Dependent DSB Mobility and DNA Repair. Cell. 2015; 163: 880-93.
35. Fradet-Turcotte A, Canny MD, Escribano-Diaz C, Orthwein A, Leung CC, Huang H, et al. 53BP1 is a reader of the DNA-damage-induced H2A Lys 15 ubiquitin mark. Nature. 2013; 499: 50-4.
36. Botuyan MV, Lee J, Ward IM, Kim JE, Thompson JR, Chen J, et al. Structural basis for the methylation state-specific recognition of histone H4-K20 by 53BP1 and Crb2 in DNA repair. Cell. 2006; 127: 1361-73.

37. Mallette FA, Mattiroli F, Cui G, Young LC, Hendzel MJ, Mer G, et al. RNF8- and RNF168-dependent degradation of KDM4A/JMJD2A triggers 53BP1 recruitment to DNA damage sites. The EMBO journal. 2012; 31: 1865-78.
38. Acs K, Luijsterburg MS, Ackermann L, Salomons FA, Hoppe T, Dantuma NP. The AAA-ATPase VCP/p97 promotes 53BP1 recruitment by removing L3MBTL1 from DNA double-strand breaks. Nat Struct Mol Biol. 2011; 18: 1345-50.
39. Riballo E, Kühne M, Rief N, Doherty A, Smith GCM, Recio Ma-J, et al. A Pathway of Double-Strand Break Rejoining Dependent upon ATM, Artemis, and Proteins Locating to γ-H2AX Foci. Molecular Cell. 2004; 16: 715-24.
40. Biehs R, Steinlage M, Barton O, Juhasz S, Kunzel J, Spies J, et al. DNA Double-Strand Break Resection Occurs during Non-homologous End Joining in G1 but Is Distinct from Resection during Homologous Recombination. Mol Cell. 2017; 65: 671-84.e5.
41. Shibata A, Jeggo P, Löbrich M. The pendulum of the Ku-Ku clock. DNA repair. 2018; 71: 164-71.
42. Hartsuiker E, Neale MJ, Carr AM. Distinct requirements for the Rad32(Mre11) nuclease and Ctp1(CtIP) in the removal of covalently bound topoisomerase I and II from DNA. Mol Cell. 2009; 33: 117-23.
43. Reginato G, Cannavo E, Cejka P. Physiological protein blocks direct the Mre11–Rad50–Xrs2 and Sae2 nuclease complex to initiate DNA end resection. Genes & Development. 2017; 31: 2325-30.
44. Neale MJ, Pan J, Keeney S. Endonucleolytic processing of covalent protein-linked DNA double-strand breaks. Nature. 2005; 436: 1053-7.
45. Garcia V, Phelps SEL, Gray S, Neale MJ. Bidirectional resection of DNA double-strand breaks by Mre11 and Exo1. Nature. 2011; 479: 241-4.
46. Barazas M, Gasparini A, Huang Y, Küçükosmanoğlu A, Annunziato S, Bouwman P, et al. Radiosensitivity is an acquired vulnerability of PARPi-resistant BRCA1-deficient tumors. Cancer research. 2018: canres.2077.18.
47. Duarte AA, Gogola E, Sachs N, Barazas M, Annunziato S, J RdR, et al. BRCA-deficient mouse mammary tumor organoids to study cancer-drug resistance. Nat Methods. 2018; 15: 134-40.
48. Zellweger R, Dalcher D, Mutreja K, Berti M, Schmid JA, Herrador R, et al. Rad51-mediated replication fork reversal is a global response to genotoxic treatments in human cells. The Journal of cell biology. 2015; 208: 563-79.
49. Miyake Y, Nakamura M, Nabetani A, Shimamura S, Tamura M, Yonehara S, et al. RPA-like mammalian Ctc1-Stn1-Ten1 complex binds to single-stranded DNA and protects telomeres independently of the Pot1 pathway. Mol Cell. 2009; 36: 193-206.
50. Iftode C, Daniely Y, Borowiec JA. Replication protein A (RPA): the eukaryotic SSB. Crit Rev Biochem Mol Biol. 1999; 34: 141-80.
51. Bochkareva E, Korolev S, Lees-Miller SP, Bochkarev A. Structure of the RPA trimerization core and its role in the multistep DNA-binding mechanism of RPA. The EMBO journal. 2002; 21: 1855-63.
52. Fanning E, Klimovich V, Nager AR. A dynamic model for replication protein A (RPA) function in DNA processing pathways. Nucleic acids research. 2006; 34: 4126-37.
53. Bhattacharjee A, Stewart J, Chaiken M, Price CM. STN1 OB Fold Mutation Alters DNA Binding and Affects Selective Aspects of CST Function. PLoS Genet. 2016; 12: e1006342.
54. Chen LY, Redon S, Lingner J. The human CST complex is a terminator of telomerase activity. Nature. 2012; 488: 540-4.
55. Bhattacharjee A, Wang Y, Diao J, Price CM. Dynamic DNA binding, junction recognition and G4 melting activity underlie the telomeric and genome-wide roles of human CST. Nucleic Acids Res. 2017; 45: 12311-24.
56. Anand R, Ranjha L, Cannavo E, Cejka P. Phosphorylated CtIP Functions as a Co-factor of the MRE11-RAD50-NBS1 Endonuclease in DNA End Resection. Molecular Cell. 2016; 64: 940-50.
57. Zou L, Elledge SJ. Sensing DNA damage through ATRIP recognition of RPA-ssDNA complexes. Science. 2003; 300: 1542-8.
58. Zou L, Liu D, Elledge SJ. Replication protein A-mediated recruitment and activation of Rad17 complexes. Proceedings of the National Academy of Sciences of the United States of America. 2003; 100: 13827-32.
59. Myler LR, Gallardo IF, Soniat MM, Deshpande RA, Gonzalez XB, Kim Y, et al. Single-Molecule Imaging Reveals How Mre11-Rad50-Nbs1 Initiates DNA Break Repair. Molecular Cell. 2017; 67: 891-8.e4.
60. Golub EI, Gupta RC, Haaf T, Wold MS, Radding CM. Interaction of human rad51 recombination protein with single-stranded DNA binding protein, RPA. Nucleic acids research. 1998; 26: 5388-93.

61. Sugiyama T, Kowalczykowski SC. Rad52 protein associates with replication protein A (RPA)-single-stranded DNA to accelerate Rad51-mediated displacement of RPA and presynaptic complex formation. The Journal of biological chemistry. 2002; 277: 31663-72.
62. Lue NF, Zhou R, Chico L, Mao N, Steinberg-Neifach O, Ha T. The telomere capping complex CST has an unusual stoichiometry, makes multipartite interaction with G-Tails, and unfolds higher-order G-tail structures. PLoS Genet. 2013; 9: e1003145.
63. Wu P, Takai H, de Lange T. Telomeric 3' overhangs derive from resection by Exo1 and Apollo and fill-in by POT1b-associated CST. Cell. 2012; 150: 39-52.
64. Ganduri S, Lue NF. STN1–POLA2 interaction provides a basis for primase-pol α stimulation by human STN1. Nucleic Acids Research. 2017; 45: 9455-66.
65. Schimmel J, van Schendel R, den Dunnen JT, Tijsterman M. Templated Insertions: A Smoking Gun for Polymerase Theta-Mediated End Joining. Trends in Genetics. 2019; 35: 632-44.
66. Schimmel J, Kool H, van Schendel R, Tijsterman M. Mutational signatures of non-homologous and polymerase theta-mediated end-joining in embryonic stem cells. The EMBO journal. 2017; 36: 3634-49.
67. Mateos-Gomez PA, Kent T, Deng SK, McDevitt S, Kashkina E, Hoang TM, et al. The helicase domain of Poltheta counteracts RPA to promote alt-NHEJ. Nat Struct Mol Biol. 2017; 24: 1116-23.
68. Ceccaldi R, Liu JC, Amunugama R, Hajdu I, Primack B, Petalcorin MIR, et al. Homologous-recombination-deficient tumours are dependent on Polθ-mediated repair. Nature. 2015; 518: 258-62.
69. Mateos-Gomez PA, Gong F, Nair N, Miller KM, Lazzerini-Denchi E, Sfeir A. Mammalian polymerase theta promotes alternative NHEJ and suppresses recombination. Nature. 2015; 518: 254-7.
70. Nik-Zainal S, Davies H, Staaf J, Ramakrishna M, Glodzik D, Zou X, et al. Landscape of somatic mutations in 560 breast cancer whole-genome sequences. Nature. 2016; 534: 47-54.
71. Wood RD, Doublié S. DNA polymerase θ (POLQ), double-strand break repair, and cancer. DNA repair. 2016; 44: 22-32.
72. Wang J, Aroumougame A, Lobrich M, Li Y, Chen D, Chen J, et al. PTIP associates with Artemis to dictate DNA repair pathway choice. Genes Dev. 2014; 28: 2693-8.
73. Chaudhuri AR, Callen E, Ding X, Gogola E, Duarte AA, Lee JE, et al. Replication fork stability confers chemoresistance in BRCA-deficient cells. Nature. 2016; 535: 382-7.
74. Ray Chaudhuri A, Nussenzweig A. The multifaceted roles of PARP1 in DNA repair and chromatin remodelling. Nature reviews Molecular cell biology. 2017; 18: 610-21.
75. Rickman K, Smogorzewska A. Advances in understanding DNA processing and protection at stalled replication forks. 2019: jcb.201809012.
76. Maya-Mendoza A, Moudry P, Merchut-Maya JM, Lee M, Strauss R, Bartek J. High speed of fork progression induces DNA replication stress and genomic instability. Nature. 2018; 559: 279-84.
77. Berti M, Ray Chaudhuri A, Thangavel S, Gomathinayagam S, Kenig S, Vujanovic M, et al. Human RECQ1 promotes restart of replication forks reversed by DNA topoisomerase I inhibition. Nat Struct Mol Biol. 2013; 20: 347-54.
78. Annunziato S, Barazas M, Rottenberg S, Jonkers J. Genetic Dissection of Cancer Development, Therapy Response, and Resistance in Mouse Models of Breast Cancer. Cold Spring Harbor symposia on quantitative biology. 2016; 81: 141-50.
79. Bruna A, Rueda OM, Greenwood W, Batra AS, Callari M, Batra RN, et al. A Biobank of Breast Cancer Explants with Preserved Intra-tumor Heterogeneity to Screen Anticancer Compounds. Cell. 2016; 167: 260-74.e22.
80. Rottenberg S, Jaspers JE, Kersbergen A, van der Burg E, Nygren AO, Zander SA, et al. High sensitivity of BRCA1-deficient mammary tumors to the PARP inhibitor AZD2281 alone and in combination with platinum drugs. Proceedings of the National Academy of Sciences of the United States of America. 2008; 105: 17079-84.
81. Patch AM, Christie EL, Etemadmoghadam D, Garsed DW, George J, Fereday S, et al. Whole-genome characterization of chemoresistant ovarian cancer. Nature. 2015; 521: 489-94.
82. Christie EL, Pattnaik S, Beach J, Copeland A, Rashoo N, Fereday S, et al. Multiple ABCB1 transcriptional fusions in drug resistant high-grade serous ovarian and breast cancer. Nature communications. 2019; 10: 1295.

83. Pettitt SJ, Rehman FL, Bajrami I, Brough R, Wallberg F, Kozarewa I, et al. A genetic screen using the PiggyBac transposon in haploid cells identifies Parp1 as a mediator of olaparib toxicity. PloS one. 2013; 8: e61520.
84. Pettitt SJ, Krastev DB, Brandsma I, Drean A, Song F, Aleksandrov R, et al. Genome-wide and high-density CRISPR-Cas9 screens identify point mutations in PARP1 causing PARP inhibitor resistance. Nature communications. 2018; 9: 1849.
85. Gogola E, Duarte AA, de Ruiter JR, Wiegant WW, Schmid JA, de Bruijn R, et al. Selective Loss of PARG Restores PARylation and Counteracts PARP Inhibitor-Mediated Synthetic Lethality. Cancer Cell. 2018; 33: 1078-93.e12.
86. Hutchison DJ. Cross Resistance and Collateral Sensitivity Studies in Cancer Chemotherapy. Advances in cancer research: Academic Press; 1963. p. 235-350.
87. Wang L, Leite de Oliveira R, Huijberts S, Bosdriesz E, Pencheva N, Brunen D, et al. An Acquired Vulnerability of Drug-Resistant Melanoma with Therapeutic Potential. Cell. 2018; 173: 1413-25.e14.
88. Balmus G, Pilger D, Coates J, Demir M, Sczaniecka-Clift M, Barros AC, et al. ATM orchestrates the DNA-damage response to counter toxic non-homologous end-joining at broken replication forks. Nature communications. 2019; 10: 87.
89. Evers B, Jonkers J. Mouse models of BRCA1 and BRCA2 deficiency: past lessons, current understanding and future prospects. Oncogene. 2006; 25: 5885-97.
90. Drost R, Dhillon KK, van der Gulden H, van der Heijden I, Brandsma I, Cruz C, et al. BRCA1185delAG tumors may acquire therapy resistance through expression of RING-less BRCA1. The Journal of clinical investigation. 2016; 126: 2903-18.
91. Wang Y, Bernhardy AJ, Cruz C, Krais JJ, Nacson J, Nicolas E, et al. The BRCA1-Delta11q Alternative Splice Isoform Bypasses Germline Mutations and Promotes Therapeutic Resistance to PARP Inhibition and Cisplatin. Cancer research. 2016; 76: 2778-90.
92. Drost R, Bouwman P, Rottenberg S, Boon U, Schut E, Klarenbeek S, et al. BRCA1 RING function is essential for tumor suppression but dispensable for therapy resistance. Cancer Cell. 2011; 20: 797-809.
93. Mesman RLS, Calléja F, de la Hoya M, Devilee P, van Asperen CJ, Vrieling H, et al. Alternative mRNA splicing can attenuate the pathogenicity of presumed loss-of-function variants in BRCA2. Genetics in medicine : official journal of the American College of Medical Genetics. 2020; 22: 1355-65.
94. Nacson J, Krais JJ, Bernhardy AJ, Clausen E, Feng W, Wang Y, et al. BRCA1 Mutation-Specific Responses to 53BP1 Loss-Induced Homologous Recombination and PARP Inhibitor Resistance. Cell Reports. 2018; 24: 3513-27.e7.
95. Heijink AM, Talens F, Jae LT, van Gijn SE, Fehrmann RSN, Brummelkamp TR, et al. BRCA2 deficiency instigates cGAS-mediated inflammatory signaling and confers sensitivity to tumor necrosis factor-alpha-mediated cytotoxicity. Nature communications. 2019; 10: 100.
96. Parkes EE, Walker SM, Taggart LE, McCabe N, Knight LA, Wilkinson R, et al. Activation of STING-Dependent Innate Immune Signaling By S-Phase-Specific DNA Damage in Breast Cancer. Journal of the National Cancer Institute. 2017; 109.
97. Li T, Chen ZJ. The cGAS–cGAMP–STING pathway connects DNA damage to inflammation, senescence, and cancer. The Journal of experimental medicine. 2018; 215: 1287.
98. Chen Q, Sun L, Chen ZJ. Regulation and function of the cGAS–STING pathway of cytosolic DNA sensing. Nature immunology. 2016; 17: 1142.
99. Shen J, Zhao W, Ju Z, Wang L, Peng Y, Labrie M, et al. PARPi Triggers the STING-Dependent Immune Response and Enhances the Therapeutic Efficacy of Immune Checkpoint Blockade Independent of BRCAness. Cancer research. 2019; 79: 311-9.
100. Ding L, Kim HJ, Wang Q, Kearns M, Jiang T, Ohlson CE, et al. PARP Inhibition Elicits STING-Dependent Antitumor Immunity in Brca1-Deficient Ovarian Cancer. Cell Rep. 2018; 25: 2972-80.e5.
101. Pantelidou C, Sonzogni O, De Oliveria Taveira M, Mehta AK, Kothari A, Wang D, et al. PARP Inhibitor Efficacy Depends on CD8(+) T-cell Recruitment via Intratumoral STING Pathway Activation in BRCA-Deficient Models of Triple-Negative Breast Cancer. Cancer discovery. 2019; 9: 722-37.
102. Seidel JA, Otsuka A, Kabashima K. Anti-PD-1 and Anti-CTLA-4 Therapies in Cancer: Mechanisms of Action, Efficacy, and Limitations. Front Oncol. 2018; 8: 86-.
103. Stewart RA, Pilié PG, Yap TA. Development of PARP and Immune-Checkpoint Inhibitor Combinations. Cancer research. 2018; 78: 6717-25.

*"The greatest enemy of knowledge is not ignorance, it is the illusion of knowledge"*

*(Stephen Hawking)*

# Cancer Chess:

**Addendum**

# Molecular Insights

# Into PARPi Resistance

Summary

Nederlandse Samenvatting

Curriculum Vitae

List of Publications

Acknowledgements

- & -

## Summary

Personalized medicine has great potential to improve cancer treatment. The premise of defining the genetic background of a tumor and tailoring the treatment to exploit specific tumor characteristics is especially powerful when applied to synthetic lethal interactions. Synthetic lethality occurs when the perturbation of two genes individually exerts no effect on cell survival, while simultaneous perturbation of the same two genes is highly lethal. A prime example is the BRCA/Poly (ADP-Ribose) Polymerase (PARP) paradigm in which a defect in the *BRCA1/2* genes (i.e. *BRCA1/2* mutation carriers and subsequent loss-of-heterozygosity of the remaining wild type allele) results in a remarkable sensitivity to PARP inhibition (PARPi). The clinical exploitation of this synthetic lethal interaction has achieved durable responses in a subset of patients, illustrating the potency of this interaction for cancer treatment. However, sustained responses are not universal, as tumors frequently develop resistance towards PARPi. The mechanisms that allow BRCA1 deficient cells to tolerate PARPi induced DNA damage are poorly understood. The current understanding is that PARPi induces double-strand breaks (DSBs) indirectly through replication fork collapse. The preferred route to repair these DSBs is via the error-free DSB repair pathway homologous recombination (HR). A critical step in the HR pathway is DSB end resection, which is promoted by BRCA1. In the absence of BRCA1, cells rely on error-prone repair of DSBs via non-homologous end joining (NHEJ) at the expense of an increased risk to generate toxic genomic DNA rearrangements which can subsequently lead to cell death. It is this synthetic lethal interaction that is exploited by PARPi.

Recently, the 53BP1 pathway has emerged as a key component in the response to PARPi induced DSBs by antagonizing end resection. Its loss in BRCA1 deficient cells results in the partial restoration of HR activity and drives PARPi resistance. However, since neither 53BP1 nor its downstream factors RIF1 or REV7/MAD2L2 have DNA-binding capacity, it remains elusive how this pathway blocks end resection. This framework is explained in more detail in the introductory **Chapter 1** and forms the basis for the rest of this thesis, which aims to provide insight into mechanisms that allow BRCA1 deficient cells to tolerate PARPi induced DNA damage and to find new vulnerabilities of these PARPi resistant cells. Ultimately, this knowledge might offer a rationale to act on resistance as it emerges, or ideally to anticipate on resistance prior to its appearance.

Genetically engineered mouse models (GEMMs) are invaluable in cancer research. In **Chapter 2** the major technological advancements that have been made in GEMMs of breast cancer in the last years are reviewed. This review is focused on the biological insights in cancer development that have been obtained from such model systems, and describes how these models have been used to study therapy response and resistance. The evolutionary process contained in GEMM tumors faithfully recapitulates the patient tumor setting and allows tumors to acquire resistance in an unbiased manner. However, the practical use of GEMMs has been hampered by the low success rates to

generate *in vitro* cell line systems from GEMM tumors and vice versa, the inefficiency to establish *in vivo* tumors from these cell lines. These limitations were eliminated by applying established 3D culture conditions on mammary tumor cells derived from the *K14cre;Brca1*$^{F/F}$*;p53*$^{F/F}$ (KB1P) mouse model. Hereby, it was possible to generate tumor organoids derived from KB1P mouse tumors at a high success rate. This work is described in **Chapter 3** and, since tumor organoids could be genetically modified *ex vivo* and re-transplanted orthotopically without compromising the tumor forming potential, allowed time- and labor-efficient examination of genetic interactions with therapy response. This is exemplified by the systematic interrogation of known factors of the 53BP1 pathway presented in this chapter. This technique was used in the forthcoming chapters, including for the *in vivo* validation of ASCIZ (**Chapter 4**). The ASCIZ-DYNLL axis promotes 53BP1 oligomerisation and recruitment to DSB ends, and thereby 53BP1 mediated NHEJ. Its depletion induces PARPi resistance in BRCA1 deficient cells.

Novel PARPi resistance mechanisms were identified by employing (genome-wide) CRISPR/SpCas9 loss-of-function screens in BRCA1 deficient cells using survival in the presence of PARPi as a readout. These screens yielded a number of interesting new factors that provided new insight into end resection regulation and metabolism. **Chapter 5** describes the identification of a novel trimeric single-stranded DNA (ssDNA) binding complex, composed of C20ORF196 (SHLD1), FAM35A (SHLD2) and FLJ26957/CTC534A2.2 (SHLD3) together forming the Shieldin complex. Shieldin was shown to be recruited to sites of DNA damage by REV7/MAD2L2 and its loss phenocopied the loss of 53BP1 pathway members. The tethering of the Shieldin complex to the upstream factor RNF8 eliminated the requirement for 53BP1-RIF1-REV7 and prohibited restoration of HR in the absence of 53BP1; unequivocally demonstrating that Shieldin is the downstream effector complex of the 53BP1 pathway. The genetic screens also implicated another trimeric ssDNA binding complex, the CST complex, as a modulator of the PARP1/BRCA1 synthetic lethal interaction. The CST complex is composed of CTC1, STN1 and TEN1 and has previously been described to regulate telomere length by counteracting resection of telomeres via the recruitment of POLA and subsequent fill-in DNA synthesis. The validation of this hit is the focus of **Chapter 6.** The loss of CST in BRCA1 deficient tumors partially restored HR activity and was a driver of PARPi resistance *in vitro* and *in vivo*. Moreover, CST promoted NHEJ activity on dysfunctional telomeres and facilitated NHEJ driven class-switch recombination. These data demonstrated that CST, besides its role on telomeres, also functions on non-telomeric DSBs, although the requirement for POLA fill-in DNA synthesis requires further study. Together, **Chapters 5** and **6** delineate the hitherto missing links between the 53BP1 pathway and DSB end metabolism.

In **Chapter 7** the knowledge on PARPi resistance mechanisms was utilized to identify and exploit new vulnerabilities of PARPi resistant BRCA1 deficient cells. The existence of such vulnerabilities was expected since the 53BP1 pathway is implicated in DSB repair via NHEJ. BRCA1 deficient cells that have lost the 53BP1 pathway are cross-resistant to topoisomerase inhibition, which, analogous to PARPi, generates DSBs

through replication fork collapse. However, these cells displayed increased sensitivity to radiotherapy (RT). This highlighted that the partial restoration of HR did not outweigh the loss of the 53BP1 pathway. Indeed, radiotherapy resistant BRCA1 deficient tumors did not restore HR activity underscoring that, despite the hypersensitivity to RT that was imposed by BRCA1 deficiency; BRCA1 independent (partial) restoration of HR was not beneficial in the context of RT. This vulnerability was exploited *in vitro* and *in vivo* to deplete PARPi resistant cells demonstrating a potential therapeutic option to treat recurrent tumors in which the 53BP1 pathway has been inactivated.

Given the encouraging response rates to PARP inhibition in the clinic and the urge to ultimately tackle clinical resistance, it is no surprise that the BRCA1/PARP1 paradigm receives great attention in the field. The high number of independent publications on PARPi resistance mechanisms testifies to the rapid pace at which the field is advancing. This thesis concludes with a general discussion of the remaining questions related to the repair of PARPi induced DNA damage and DSB end regulation in **Chapter 8**. Finally, strategies to improve the clinical utilization of PARPi are discussed. Together, this thesis provides insights into the game of cancer chess in the context of PARPi treatment of BRCA1 deficient tumors.

## Nederlandse Samenvatting

Behandeling-op-maat heeft veel potentie om de effectiviteit van kankertherapie te verbeteren. Door vooraf de genetische achtergrond van een tumor te bepalen kan de behandeling worden afgestemd op de specifieke eigenschappen en kwetsbaarheden van de tumor. Dit kan onder andere worden gedaan door gebruik te maken van synthetisch letale interacties. Synthetische letaliteit wil zeggen dat de uitschakeling van één van twee genen afzonderlijk geen effect heeft op de overleving van de cel, maar dat celdood ontstaat wanneer deze beide genen tegelijkertijd worden uitgeschakeld. Een goed voorbeeld van synthetische letaliteit is de interactie tussen BRCA en Poly (ADP-Ribose) Polymerase (PARP), waarbij door een defect in het *BRCA1* of *BRCA2* gen een aanzienlijke gevoeligheid ontstaat voor de remming van PARP (PARPi). Zowel in dragers als in niet-dragers van een BRCA1/2 mutatie is deze gevoeligheid specifiek voor tumorcellen door het verlies van het tweede wild type allel in tumorcellen. De therapeutische potentie van deze interactie wordt geïllustreerd door de fractie van tumoren die een langdurige respons vertonen. Echter, deze langdurige responses zijn niet universeel aangezien er in een substantiële fractie van de tumoren resistentie ontstaat tegen PARPi. De kennis over mechanismen die kunnen verklaren waardoor sommige BRCA1-deficiënte cellen de gevolgen van PARPi kunnen tolereren is beperkt. Volgens het huidige model ontstaan er door PARPi indirect dubbel-strengs breuken (DSB) in het DNA. De meest precieze manier om deze DSBs te repareren is via het foutloze DSB-reparatiemechanisme homologe recombinatie (HR). Een belangrijke stap in HR is eind-resectie van DSBs: het "opeten" van één streng DNA, waardoor er een enkelstrengs DNA overhang ontstaat. Deze resectie wordt gestimuleerd door BRCA1, en maakt het mogelijk om twee DSB-uiteinden nauwkeurig aan elkaar te koppelen door gebruik te maken van homologie tussen het enkelstrengs DNA aan het uiteinde en intact DNA. In afwezigheid van BRCA1 zijn cellen echter afhankelijk van het meer foutgevoelige DSB-reparatiemechanisme niet-homologe eind-ligatie (NHEJ). Eind-ligatie is het "aan elkaar plakken" van twee DSB-uiteinden. Wanneer dit incorrect gebeurt, bijvoorbeeld door twee niet aan elkaar horende uiteinden te koppelen, kunnen er toxische herschikkingen ontstaan in het DNA die uiteindelijk tot celdood kunnen leiden. Hiervan wordt gebruik gemaakt om tumorcellen te doden door middel van PARPi.

Recentelijk is aangetoond dat in BRCA1-deficiënte cellen het 53BP1-complex een belangrijke rol speelt in het ontstaan van toxische herschikkingen van PARPi-geïnduceerde DSBs door eind-resectie te blokkeren. Normaal wordt ongewenste 53BP1 activiteit beperkt door BRCA1. Door het 53BP1-pad te inactiveren in BRCA1-deficiënte cellen (BRCA1;53BP1-deficiënt) wordt HR-activiteit deels herstelt en ontstaat er resistentie tegen PARPi. Echter, aangezien noch 53BP1 noch de andere factoren in het 53BP1-pad (RIF1 en REV7/MAD2L2) direct DNA kunnen binden is het lang onduidelijk gebleven hoe eind-resectie geblokkeerd wordt. Deze achtergrond wordt verder uitgelegd in het introducerende **Hoofdstuk 1** en vormt de basis voor de rest van dit

proefschrift, dat tot doel heeft om meer inzicht te verschaffen in de mechanismen die ervoor zorgen dat BRCA1-deficiënte cellen ongevoelig worden voor de door PARPi-geïnduceerde DNA-schade. Het proefschrift heeft tevens tot doel om mogelijke nieuwe kwetsbaarheden van deze PARPi-resistente cellen in kaart te brengen. Dit zou uiteindelijk tot een rationele aanpak kunnen leiden om resistente tumoren te behandelen, of idealiter, te anticiperen op resistentie nog voordat dit verschijnt.

Genetische muis modellen (GEMMs) zijn zeer belangrijk in het kankeronderzoek. **Hoofdstuk 2** geeft een overzicht van de technologische vooruitgang die is geboekt in GEMMs van borstkanker. Dit overzicht richt zich tevens op de biologische inzichten die door middel van GEMMs zijn verkregen, onder andere met betrekking tot het ontstaan van kanker, alsmede hoe deze kankermodellen worden gebruikt om de respons op therapie en het ontstaan van resistentie te bestuderen. Bij dit laatste is de evolutionaire component die GEMMs bevatten cruciaal aangezien dit het ontstaan van resistentie in humane tumoren nabootst. Echter, het in GEMMs uitschakelen en bestuderen van de invloed van individuele genen op therapierespons wordt bemoeilijkt door het lage slagingspercentage om *in vitro* cellijnen te creëren uit GEMM-tumoren, en vice versa, de ineffectiviteit van deze cellijnen om *in vivo* tumoren te genereren. Deze beperkingen werden weggenomen door eerder beschreven 3D-kweekcondities toe te passen op borstkankercellen uit het *K14cre;Brca1*$^{F/F}$*;p53*$^{F/F}$ (KB1P) muismodel. Hiermee was het mogelijk om tumor-organoïden te groeien uit KB1P muistumoren. Dit wordt beschreven in **Hoofdstuk 3**. Het genetisch aanpassen van deze tumor-organoïden en terugplaatsing hiervan in muizen, maakte het mogelijk om tijds- en arbeidseffectief het effect van individuele genen op therapierespons te bestuderen. Dit is geïllustreerd door de systematische uitschakeling van bekende factoren uit het 53BP1-pad, wat in dit hoofdstuk is gepresenteerd. Deze techniek wordt tevens gebruikt in de navolgende hoofdstukken, waaronder voor de *in vivo* validatie van de rol van ASCIZ (**Hoofdstuk 4**). De ASCIZ-DYNLL1 as stimuleert de oligomerisatie en rekrutering van 53BP1 naar DSB-uiteinden, en daarmee 53BP1-gedreven NHEJ. Uitschakeling van deze as resulteert in verminderde gevoeligheid van BRCA1-deficiënte cellen voor PARPi.

Om nieuwe PARPi resistentiemechanismen te ontdekken zijn (genoom-brede) CRISPR/SpCas9 screens uitgevoerd in BRCA1-deficiënte cellen, hierbij gebruikmakend van cel overleving onder druk van PARPi als eindpunt. Deze screens hebben meerdere interessante factoren opgeleverd, waardoor nieuwe inzichten zijn verkregen in de regulatie van eind-resectie en DSB-metabolisme. **Hoofdstuk 5** beschrijft een nieuw complex dat enkelstrengs DNA kan binden en wat bestaat uit drie factoren, C20ORF196 (SHLD1), FAM35A (SHLD2) en FLJ26957/CTC534A2.2 (SHLD3), die gezamenlijk het Shieldin-complex vormen. Er is aangetoond dat het Shieldin-complex naar plekken van DNA-schade wordt gebracht door 53BP1-RIF1-REV7 en verlies van Shieldin bootst de fenotypen na die beschreven zijn voor andere factoren uit het 53BP1-pad. Directe koppeling van het Shieldin-complex aan RNF8 maakte de rol van 53BP1-RIF1-REV7 overbodig en verhinderde de reactivering van HR in BRCA1;53BP1-deficiënte cellen. Dit

toonde aan dat Shieldin de effector is in van het 53BP1-complex. De genetische screens identificeerde nog een ander ssDNA bindend complex die de interactie tussen BRCA1 en PARP1 beïnvloedt, te weten het CST-complex. Het CST-complex bestaat uit CTC1, STN1 en TEN1 en is bekend als regulator van de lengte van telomeren. Het gaat de eind-resectie van telomeren tegen door POLA te rekruteren en vervolgens een DNA-synthese reactie te starten. De validatie van deze hit is het onderwerp van **Hoofdstuk 6**. Het uitschakelen van CST in BRCA1-deficiënte tumorcellen herstelde (ten dele) HR-activiteit en leidde tot PARPi-resistentie *in vitro* en *in vivo*. Bovendien stimuleerde CST de activiteit van NHEJ op disfunctionele telomeren en faciliteerde het door NHEJ-gedreven klasse-switch recombinatie. Deze data demonstreren dat CST ook actief is op DSBs buiten telomeren. Gezamenlijk beschrijven hoofdstuk 5 en 6 de tot dusver ontbrekende schakel tussen het 53BP1-pad en de regulatie van DSB eind-metabolisme.

In **Hoofdstuk 7** wordt de kennis over resistentiemechanismen benut om naar nieuwe kwetsbaarheden van PARPi-resistente BRCA1-deficiënte cellen te zoeken. Het mogelijk bestaan van een kwetsbaarheid was verwacht gezien de rol van het 53BP1-pad in de reparatie van DSBs via NHEJ. BRCA1;53BP1-deficiënte cellen zijn kruisresistent tegen onder andere topoisomerase-remmers, welke, analoog aan PARP-remmers, indirect DSBs genereren. Echter, dit hoofdstuk laat zien dat BRCA1;53BP1-deficiënte cellen een verhoogde gevoeligheid hebben voor radiotherapie (RT). Dit benadrukt dat in de context van RT de partiële restoratie van HR niet opweegt tegen het verlies van het 53BP1-pad. In overeenstemming hiermee bleek HR-activiteit niet hersteld te zijn in een cohort radiotherapie-resistente BRCA1-deficiënte GEMM-tumoren, ondanks het feit dat BRCA1-deficiëntie leidde tot hypergevoeligheid tegen RT. De verhoogde gevoeligheid voor RT van BRCA1;53BP1-deficiënte cellen ten opzichte van BRCA1-deficiënte cellen is dusdanig dat *in vitro* en *in vivo* modellen aantoonden dat in gemengde populaties de aanwezigheid van BRCA1;53BP1-deficiënte tumorcellen afneemt ten opzichte van BRCA1-deficiënte tumorcellen. Dit laat zien dat er mogelijkheden zijn om PARPi-resistente BRCA1-deficiënte tumoren waarin het 53BP1-pad is uitgeschakeld te behandelen.

Gezien de veelbelovende klinische respons op PARPi en de noodzaak om resistentie in de kliniek te behandelen, wordt de BRCA1/PARP1 interactie veel bestudeerd. Het hoge aantal onafhankelijke publicaties omtrent PARPi-resistentiemechanismen getuigen van de snelheid waarin het veld vordert. Het proefschrift eindigt met een algemene discussie over de uitstaande vragen omtrent de reparatie van door PARPi ontstane DNA-schade en DSB-eind-regulatie in **Hoofdstuk 8**. Tot slot worden strategieën beschreven om de toepassing van PARPi verder te verbreden en verbeteren. Samenvattend biedt dit proefschrift inzicht in het schaakspel tegen kanker in de context van PARPi-behandeling van BRCA1-deficiënte tumoren.

## List of Publications

1. Tannous BA, Kerami M, Van der Stoop PM, Kwiatkowski N, Wang J, Zhou W, Kessler AF, Lewandrowski G, Hiddingh L, Sol N, Lagerweij T, Wedekind L, Niers JM, **Barazas M**, Nilsson RJ, Geerts D, De Witt Hamer PC, Hagemann C, Vandertop WP, Van Tellingen O, Noske DP, Gray NS, Würdinger T. *'Effects of the selective MPS1 inhibitor MPS1-IN-3 on glioblastoma sensitivity to antimitotic drugs.'* J Natl Cancer Inst. 2013; 105(17): 1322-31.

2. Xu G, Chapman JR, Brandsma I, Yuan J, Mistrik M, Bouwman P, Bartkova J, Gogola E, Warmerdam D, **Barazas M**, Jaspers JE, Watanabe K, Pieterse M, Kersbergen A, Sol W, Celie PHN, Schouten PC, van den Broek B, Salman A, Nieuwland M, de Rink I, de Ronde J, Jalink K, Boulton SJ, Chen J, van Gent DC, Bartek J, Jonkers J, Borst P, Rottenberg S. *'REV7 counteracts DNA double-strand break resection and affects PARP inhibition.'* Nature. 2015; 521(7553): 541-544.

3. Annunziato S, **Barazas M**, Rottenberg S, Jonkers J. *'Genetic Dissection of Cancer Development, Therapy Response, and Resistance in Mouse Models of Breast Cancer.'* Cold Spring Harb Symp Quant Biol. 2016; 81:141-150.

4. Teng J, Hejazi S, Hiddingh L, Carvalho L, de Gooijer MC, Wakimoto H, **Barazas M**, Tannous M, Chi AS, Noske DP, Wesseling P, Wurdinger T, Batchelor TT, Tannous BA. *'Recycling drug screen repurposes hydroxyurea as a sensitizer of glioblastomas to temozolomide targeting de novo DNA synthesis, irrespective of molecular subtype.' Neuro Oncol. 2018; 20(5): 642-654.*

5. Duarte AA, Gogola E, Sachs N, **Barazas M**, Annunziato S, R de Ruiter J, Velds A, Blatter S, Houthuijzen JM, van de Ven M, Clevers H, Borst P, Jonkers J, Rottenberg S. *'BRCA-deficient mouse mammary tumor organoids to study cancer-drug resistance.'* Nat Methods. 2018; 15(2): 134-140.

6. Becker JR, Cuella-Martin R*****, **Barazas M***, Liu R*****, Oliveira C, Oliver AW, Bilham K, Holt AB, Blackford AN, Heierhorst J, Jonkers J, Rottenberg S, Chapman JR. *'The ASCIZ-DYNLL1 axis promotes 53BP1-dependent non-homologous end joining and PARP inhibitor sensitivity.'* Nat Commun. 2018; 9(1): 5406.

7. Gogola E, Duarte AA, de Ruiter JR, Wiegant WW, Schmid JA, de Bruijn R, James DI, Guerrero Llobet S, Vis DJ, Annunziato S, van den Broek B, **Barazas M**, Kersbergen A, van de Ven M, Tarsounas M, Ogilvie DJ, van Vugt M, Wessels LFA, Bartkova J, Gromova I, Andújar-Sánchez M, Bartek J, Lopes M, van Attikum H, Borst P, Jonkers J, Rottenberg S. *'Selective Loss of PARG Restores PARylation and Counteracts PARP Inhibitor-Mediated Synthetic Lethality.'* Cancer Cell. 2018; 33(6): 1078-1093.

8. Noordermeer SM*, Adam S*, Setiaputra D*, **Barazas M**, Pettitt SJ, Ling AK, Olivieri M, Álvarez-Quilón A, Moatti N, Zimmermann M, Annunziato S, Krastev DB, Song F, Brandsma I, Frankum J, Brough R, Sherker A, Landry S, Szilard RK, Munro MM, McEwan A, Goullet de Rugy T, Lin ZY, Hart T, Moffat J, Gingras AC, Martin A, van Attikum H, Jonkers J, Lord CJ, Rottenberg S, Durocher D. *'The shieldin complex mediates 53BP1-dependent DNA repair.'* Nature. 2018; 560(7716): 117-121.

**9.** **Barazas M**, Annunziato S, Pettitt SJ, de Krijger I, Ghezraoui H, Roobol SJ, Lutz C, Frankum J, Song FF, Brough R, Evers B, Gogola E, Bhin J, van de Ven M, van Gent DC, Jacobs JJL, Chapman R, Lord CJ, Jonkers J, Rottenberg S. *'The CST Complex Mediates End Protection at Double-Strand Breaks and Promotes PARP Inhibitor Sensitivity in BRCA1-Deficient Cells.'* Cell Rep. 2018; 23(7): 2107-2118.

**10.** **Barazas M**, Gasparini A, Huang Y, Küçükosmanoğlu A, Annunziato S, Bouwman P, Sol W, Kersbergen A, Proost N, de Korte-Grimmerink R, van de Ven M, Jonkers J, Borst GR, Rottenberg S. *'Radiosensitivity Is an Acquired Vulnerability of PARPi-Resistant BRCA1-Deficient Tumors.'* Cancer Res. 2019; 79(3): 452-460.

&

## Curriculum Vitae

Marco Barazas was born in 1988, Hoorn, the Netherlands. In 2006, he enrolled into the Life Science Bachelor program at Hogeschool Inholland Alkmaar. After receiving his propaedeutic diploma in 2007, he continued his Bachelor program at Hogeschool Leiden. His interest in molecular biology with a translational angle led to his participation in several courses organized by the Molecular Biology and Animal Experimentation programs. He then put this combination in practice during an internship on the DNA repair gene *p53* in the lab of Prof. Dr. Hein te Riele at the Netherlands Cancer Institute – Antoni van Leeuwenhoek Hospital (NKI-AVL), which was concluded by a Bachelor thesis and Article 12 of the *Wet op de Dierproeven* (WOD, Experiments on Animals Act) in 2009. Later that year, he started the Master's program Oncology at the VU university. He performed his first internship in the lab of Prof.Dr. Tom Würdinger at the VUmc Cancer Center Amsterdam (CCA), where he worked on the establishment of a mouse model for diffuse intrinsic pontine glioma (DIPG). In 2011, he performed his second internship in the lab of Dr. Bakhos Tannous at the Harvard Medical School/Massachussetts General Hospital (HMS/MGH) in Boston. It was here where he first combined his interest in molecular biology with cancer therapy using high-throughput screening technology in a project aimed to identify sensitizers to temozolomide in glioblastoma. He graduated Cum Laude in December 2012. In February 2013, Marco returned to the NKI-AVL when he joined the lab of Prof.Dr. Sven Rottenberg. During his PhD, he further pursued his interest in combining molecular biology to improve cancer therapy this time with a focus on BRCA1-deficient breast cancer. Here, he could take advantage of his previous experience in the DNA repair field and functional high-throughput screening technology. The major findings of this research are described in this thesis. From January 2019, he holds a post-doc position in the lab of Prof.Dr. Marcel Tijsterman at the Leiden University Medical Center (LUMC).

## Acknowledgements

This thesis concludes what has been a great period of my career. Of course, I could not have done the work presented in this thesis if it wasn't for the fantastic support that I received over the years, so to everyone who has been involved in this work – a big thank you, your help has always been greatly appreciated!

In particular I would like to thank:
*My promotor, Prof.dr. Jos Jonkers* and *co-promotor Prof.dr. Sven Rottenberg*, for allowing me the opportunity to dive into this fascinating subject where I could combine my scientific interests. The move of the *Rottenberg*-lab to Switzerland came as a surprise to me, but I could not have wished for a smoother integration within the *Division of Molecular Pathology* and the *Jonkers*-lab. It later turned out we were ahead of the curve with our online meetings. I have learned a great deal in the lab, have participated in inspiring collaborations and attended (inter)national meetings, and foremost I have been able to develop myself as an independent researcher, all under your guidance. *Dr. Piet Borst*, when it comes to the importance of critical thinking and careful thought about controls, I could not have had a better teacher. Together, *Sven*, *Jos* and *Piet*, you provide a case-in-point of the strength of collaboration and team effort. I would also like to thank my national and international collaborators *Dr. Gerben Borst*, *Dr. Jacqueline Jacobs, Dr. Dik van Gent, Dr. Ross Chapman*, *Prof. Dr. Daniel Durocher* and *Prof. Dr. Chris Lord* for their valuable feedback, supportive attitude and fruitful collaborations.

All members of the *Rottenberg*-lab, although it hasn't always been easy to stay connected between the two locations, I have enjoyed our shared meetings and Lab outings. *Ewa,* we both started and ended our work at the NKI around the same time. While we have had our challenges, your passion for science cannot be denied and I wish you great success.

All colleagues of the *Division of Molecular Pathology*, I have enjoyed the atmosphere in the department. *Stefano*, it has been a real pleasure to collaborate with you on many projects. Your can-do and let's-do work ethos has stimulated many experiments. I cannot thank you, and *Sjors, Koen, Chiara, Julian, Anne Paulien, Arne, Ellen, Ingrid, Hanneke, Peter, Catrin, Guotai, Asli, Hanneke, Wendy, Sohvi, Nora, Inge and my students Yike and Julia* enough for the positive environment we created and that always made work enjoyable.

&

All the *facilities of the NKI*, although you may not always end up in the spot lights there is no question about the importance of your contributions. Your expert knowledge and collaborative attitude forms the foundation of many complex experiments. A special thanks to the colleagues of the *Mouse Cancer Clinic Amsterdam (MCCA) Preclinical Intervention Unit* (*Marieke* and the team). I have experienced the time "without" and "with" the MCCA, and can only conclude that you have transformed the way of doing mouse experiments for researchers. It has been great working together with you.

*Papa, Mama, Familie, Vrienden* en natuurlijk *Tessa*, bedankt voor alle steun. Mijn nieuwsgierigheid is van jongs af aan al gestimuleerd en daar ben ik dankbaar voor. Jullie hebben mij altijd aangemoedigd om het beste uit mezelf te halen en dit heeft ontegenzeggelijk bijgedragen aan de totstandkoming van dit proefschrift.

